

# **MOF-808 and UTSA-120a based mixed matrix membranes for carbon dioxide separations**

MOF-808 en UTSA-120a als vulmateriaal in polymeermembranen voor koolstofdioxidescheidingen

Promotor:

Prof. Ivo Vankelecom

Departement Microbiële en Moleculaire Systemen

Centrum voor Membraanscheidingen, Adsorptie, Katalyse  
en Spectroscopie voor Duurzame Oplossingen

Masterproef voorgedragen

tot het behalen van het diploma van

Master of Science in de bio-ingenieurswetenschappen:

katalytische technologie

**Daan Van Havere**

juni 2020

*"Dit proefschrift is een examendocument dat na de verdediging niet meer werd gecorrigeerd voor eventueel vastgestelde fouten. In publicaties mag naar dit proefwerk verwezen worden mits schriftelijke toelating van de promotor, vermeld op de titelpagina."*

## Acknowledgements

This thesis concludes a five year long amazing journey towards obtaining my degree in bioscience engineering. First of all, I would like to thank my daily supervisor Raymond Thür for guiding me through this process. Thank you, for introducing me to the world of membrane gas separations and academic research. Thank you, for assisting me in writing this thesis in a scientifically correct way. Thank you, for supporting me in being creative. Thank you for an amazing, interesting, enlightening and fun year!

Next, I would like to thank Prof. Ivo Vankelecom for supporting me throughout this thesis year, by following up the progression of this thesis as well as by giving support with his expertise when necessary. I would also like to express my gratitude for letting me take part in UMASS 2019, which was an utmost interesting and educative experience. Furthermore, I would like to thank the PhD students and staff members of the Membrane Technology Group for the many interesting and fun lunches we had throughout the year.

In particular I would like to thank Maarten Bastin of the Membrane Technology Group for taking the SEM pictures and conducting the EDX measurement of the MOFs developed in this work. I would also like to thank Niels Van Velthoven and Simon Smolders of the Prof. Dirk De Vos group for conducting the NMR and CO<sub>2</sub> adsorption experiments crucial to this work.

In general, I would like to thank all of the professors and other members of the educative team of the bioscience engineering faculty of both the KU Leuven and the University of Antwerp for enthusing me day to day to become a successful bioscience engineer and scientist.

I would also like to express my gratitude towards my parents and brother for their unwavering support. Further, I want to thank my friends of '97, the Piekploeg and Babier for helping me relax throughout this year. Especially, I would like to thank 'de Sas' for the various interesting discussions and amazing experiences we had together.

Finally, I would like to thank Ayla De Schepper for the numerous amazing, fun and relaxing moments we had together the last years. Thank you, for always listening to me and for always believing in me, even when I doubted myself.

Thank you!

## Abstract

Both for mitigation of anthropogenic carbon dioxide (CO<sub>2</sub>) emissions and the treatment of industrial energy streams, there is a need for efficient CO<sub>2</sub> separations. Membrane gas separation is a promising approach for these separations, offering low energy consumption, modular design and a low environmental impact. However, traditional polymeric membranes are limited by a trade-off between selectivity and permeability. A possible strategy to overcome this setback is the incorporation of fillers (e.g. metal organic frameworks (MOFs)) with gas separation enhancing properties in a polymer, resulting in mixed matrix membranes (MMM). By modification of the filler MOF-808, this thesis aims at developing new MOF fillers as well as understanding which filler properties result in enhanced MMM gas separation performance.

A post-synthetic modification strategy was developed to modify pre-formed MOF-808 with various functionalizing agents. First, MOF-808 was modified with serine, to investigate the potential of amino acid modification for enhancing MMM performance. MOF-Ser showed a 62% increase in CO<sub>2</sub> uptake compared to the parent MOF-808. However, Matrimid/MOF-Ser MMM displayed only marginally better CO<sub>2</sub>/N<sub>2</sub> gas separation performance compared to Matrimid/unfunctionalized MOF-808 MMM. This discrepancy gave rise to the question which MOF parameters correlate with the MMM gas separation performance. To answer this question, a series of MOF-808 were functionalized, using various functionalizing agents hypothesized to increase the CO<sub>2</sub>-affinity of the MOF. All functionalized MOFs had a reduced CO<sub>2</sub> uptake compared to the parent MOF-808. The effect on the isosteric heat of CO<sub>2</sub> adsorption ( $Q_{st}$ ) varied, with some MOFs showing an increase in  $Q_{st}$  and others a decrease. The highest  $Q_{st}$  was recorded for MOF-808 functionalized with trifluoroacetic acid (TFA). Functionalization altered the gas separation performance of Matrimid MMM of the functionalized MOFs as well. Both MMM of MOF-808 functionalized with TFA and benzoic acid showed respectively a 72% and 52% increase in permeability and a 32% and 26% increase in separation factor compared to pure Matrimid membranes, for a 50/50 CO<sub>2</sub>/N<sub>2</sub> gas mixture. Furthermore, they outperformed the MMM based on the parent MOF-808. Contrary to literature, no clear correlation was found between CO<sub>2</sub> uptake and either permeability or separation factor.  $Q_{st}$  showed a poor correlation with the separation factor as well, but correlated strongly with the CO<sub>2</sub> permeability.

The potential of the MOF UTSA-120a, as filler material for MMM was evaluated as well. UTSA-120a/6FDA-DAM MMM showed an increase in separation factor of 7% compared to the pure 6FDA-DAM membranes for a 50/50 CO<sub>2</sub>/CH<sub>4</sub> gas mixture, but a 32% decrease in permeability. Presumably, these changes are the result of polymer rigidification.

## Samenvatting

Zowel voor het reduceren van de antropogene CO<sub>2</sub>-uitstoot als voor de behandeling van industriële energiestromen zijn efficiënte CO<sub>2</sub>-scheidingen nodig. Gasscheidingsmembranen zijn een veelbelovende technologie voor deze scheidingen door hun laag energieverbruik, relatief beperkte milieu-impact en modulair design. Traditionele polymere membranen kampen echter met een trade-off tussen selectiviteit en permeabiliteit. Een manier om deze trade-off te omzeilen is het toevoegen van vulmaterialen met sterke gasscheidingscapaciteit aan polymeren, om zo mixed matrix membranen (MMM) te bekomen. Deze thesis heeft als doel nieuwe MMM-vulmaterialen te ontwikkelen en inzicht te krijgen in materiaalkenmerken die resulteren in verbeterde MMM-gasscheidingseigenschappen, door het modifieren van de vuller MOF-808.

Een post-synthetische functionalisatiemethode (PSF) werd ontwikkeld om modificaties uit te voeren op vooraf gesynthetiseerde MOF-808 (MOF-FA). Vooreerst werd het potentieel van aminozuur gefunctionaliseerde MOF-808 als MMM vuller onderzocht door de MOF te modifieren met serine (MOF-Ser). MOF-Ser vertoonde een 62% hogere CO<sub>2</sub>-opslagcapaciteit vergeleken met het niet-gemodificeerde startmateriaal MOF-FA. Matrimid/MOF-ser MMM hadden echter slechts triviaal verbeterde CO<sub>2</sub>/N<sub>2</sub>-gasscheidingseigenschappen. Deze tegenstelling resulteerde in de vraag welke eigenschappen van een vulmateriaal correleren met MMM gasscheidingseigenschappen. Om dit te onderzoeken werd dezelfde PSF gebruikt om MOF-808 te functionaliseren met een reeks moleculen die mogelijk de CO<sub>2</sub>-affiniteit van de MOF verhogen. Elke gefunctionaliseerde MOF had een lagere CO<sub>2</sub>-opslagcapaciteit dan MOF-FA, terwijl de isostere adsorptiewarmte van CO<sub>2</sub> ( $Q_{st}$ ) zowel toe- als afnam afhankelijk van de gebruikte functionalisator. MOF-808 gefunctionaliseerd met trifluoroazijnzuur (TFA) had de hoogste  $Q_{st}$ . Functionalisatie beïnvloedde ook de CO<sub>2</sub>/N<sub>2</sub>-gasscheidingseigenschappen van Matrimid MMM van de gefunctionaliseerde vulmaterialen. MOF-808 gefunctionaliseerd met TFA en benzoëzuur vertoonden een 72% en 52% hogere permeabiliteit en een 32% en 26% hogere separatiefactor. De gasscheidingseigenschappen van deze MMM waren ook beter dan die van MMM gebaseerd op MOF-FA. De CO<sub>2</sub>-opslagcapaciteit van de MOFs vertoonde geen duidelijk lineair verband met de MMM gasscheidingseigenschappen. Daarentegen correleerde  $Q_{st}$  wel sterk met CO<sub>2</sub> permeabiliteit, maar eveneens slecht met de separatiefactor.

De MOF, UTSA-120a, werd eveneens als nieuw vulmateriaal in MMM onderzocht. De 6FDA-DAM MMM van UTSA-120a hadden een 7% hogere separatiefactor in vergelijking met puur 6FDA-DAM membranen voor CO<sub>2</sub>/CH<sub>4</sub> scheidingen, maar een 32% lagere CO<sub>2</sub>-permeabiliteit. Vermoedelijk zijn beide observaties het resultaat van verstarring van de polymere ketens.

## List of abbreviations

$^1\text{H NMR}$	Proton nuclear magnetic resonance
6FDA	Hexafluoro isopropylidene diphtalic anhydride
A	Membrane surface area
ANOVA	One-way analysis of variance
ATR-FTIR	Attenuated total reflection Fourier transform infrared spectroscopy
b	Langmuir constant
$b_1$	Langmuir constant site 1
$b_2$	Langmuir constant site 2
BA	Benzoic acid
BDC	Benzenedicarboxylic acid
BET	Brunauer-Emmet and Teller
BTC	Benzenetricarboxylic acid
BTDA	3,3'-4,4'-benzophenone tetracarboxylic dianhydride
BTEX	Benzene, toluene, ethylbenzene and xylene
c	Amount of gas adsorbed in the polymer
CA	Cellulose acetate
CCS	Carbon capture and storage
$c_H'$	Saturation sorption concentration
$\text{CH}_4$	Methane
$c_{\text{Henry}}$	Amount of gas adsorbed in Henry sites
$c_{\text{Langmuir}}$	Amount of gas adsorbed in Langmuir sites
CMS	Carbon molecular sieves
$\text{CO}_2$	Carbon dioxide
$\text{CuSiF}_6$	Copper hexafluorosilicate
D	Diffusivity coefficient
DABA	3,5-aminobenzoic acid
DMF	N,N-dimethylformamide
DMSO	Dimethyl sulfoxide
dobdc	2,5-dioxido-1,4-benzenedicarboxylate
dpa	4-4'-dipyridylacetylene
dpt	3,6-di(4-pyridyl)-1,2,4,5-tetrazine

DSC	Differential scanning calorimetry
EDX	Energy dispersive X-ray analysis
EtOH	Ethanol
FA	Formic acid
FFV	Fractional free volume
GA	Glycolic acid
GPU	Gas permeation units
HCl	Hydrochloric acid
His	Histidine
HTGS	High throughput gas separation
IAST	Ideal adsorbed solution theory
ICP-OES	Inductive coupled plasma - optical emission spectroscopy
IR	Infrared
J	Flux
$K_D$	Henry constant
L	Membrane thickness
$Li_2SO_4$	Lithium sulfate monohydrate
Matrimid	Matrimid®
MEA	Monoethanolamine
MeOH	methanol
MMM	Mixed matrix membranes
MOF	Metal organic framework
MOF-BA	Benzoic acid functionalized MOF-808 (MOF-808 from upscaled recipe)
MOF-FA	Formic acid modulated MOF-808 (normal recipe)
MOF-FA-u	Formic acid modulated MOF-808 (upscaled recipe)
MOF-GA	glycolic acid functionalized MOF-808 (MOF-808 from upscaled recipe)
MOF-His	Histidine functionalized MOF-808 (MOF-808 from upscaled recipe)
MOF- $Li_2SO_4$	Lithium sulfate monohydrate functionalized MOF-808 (MOF-808 from upscaled recipe)
MOF-Ser	Serine functionalized MOF-808 (MOF-808 from normal recipe)

MOF-SO <sub>4</sub>	Sulfuric acid functionalized MOF-808 (MOF-808 from upscaled recipe)
MOF-TFA	Trifluoroacetic acid functionalized MOF-808 (MOF-808 from upscaled recipe)
MOF-TFBA	4-(trifluoromethyl)benzoic acid functionalized MOF-808 (MOF-808 from upscaled recipe)
N	Amount of adsorbed gas
N <sub>2</sub>	Nitrogen
N <sub>m,1</sub>	Amount of adsorbed gas at saturation for site 1
N <sub>m,2</sub>	Amount of adsorbed gas at saturation for site 2
NU	Northwestern University
OECD	Organization for economic cooperation and development
P	Permeability
p	Pressure
PALS	Positronium annihilation lifetime spectroscopy
PBI	Polybenzimidazoles
PBO	Polybenzoxazoles
PDMS	Polydimethylsiloxane
PEO	Polyethylene oxide
PES	Polyethersulfone
PIM	Polymer of intrinsic microporosity
PMDA	Pyromellitic dianhydride
PSF	Post-synthetic functionalization
Q <sub>st</sub>	Isosteric heat of CO <sub>2</sub> adsorption
R	Gas constant
S	Solubility (sorption) coefficient
SCXRD	Single crystal X-ray diffraction
SD	Solution-diffusion
SEM	Scanning electron microscopy
Ser	Serine
SI	International system of units
SiF <sub>6</sub> <sup>2-</sup>	Hexafluorosilicate anion
SIFSIX	Hexafluorosilicate

SO <sub>4</sub>	Sulfuric acid
STP	Standard temperature and pressure
T	Temperature
TFA	Trifluoroacetic acid
TFBA	4-(trifluoromethyl)benzoic acid
T <sub>g</sub>	Glass transition temperature
THF	Tetrahydrofuran
TR	Thermally rearranged
UiO	Universitetet I Oslo
UiO-66-NH <sub>2</sub>	UiO-66 with a 2-amino benzenedicarboxylic acid linker
UiO-66-NH <sub>2</sub> -ABA	UiO-66-NH <sub>2</sub> with 4 aminobenzoic acid used as modulator
UTSA	University of Texas at San Antonio
v	Specific volume of the polymer
v <sub>0</sub>	Volume occupied by the polymer chains
x	Mole fraction of a component in the feed gas mixture
XRD	X-ray diffraction
y	Mole fraction of a component in the permeate
ZIF	Zeolitic imidazole framework
Zr <sub>6</sub> cluster	Zirconium oxide cluster of MOF-808/UiO-66
ZrOCl <sub>2</sub> .8H <sub>2</sub> O	Zirconyl chloride octahydrate
α	Selectivity
α*	Separation factor
β	Parameter in mathematical description Robeson upper bound
γ	Parameter in mathematical description Robeson upper bound
Δp	Pressure difference over the membrane
Δt	Time interval

## List of tables

Table 1: Chemical composition of natural gas reservoirs around the world. Copied from ref. [10].	3
Table 2: Constituents of biogas originating from different waste streams. Copied from ref. [12].	4
Table 3: Typical composition of flue gas originating from different sources. Copied from ref. [16].	5
Table 4: Permeability (Barrer) and selectivity of some polymeric membranes studied for CO <sub>2</sub> /CH <sub>4</sub> gas separations. Data used from ref. [32,38,39,45,48,52,61,62].	16
Table 5: Performance requirements for gas separation membranes to be an economically feasible alternative to conventional gas separation technologies. Copied from ref. [1].	26
Table 6: Physical properties together with MOF gas uptake and selectivity of various members of the SIFSIX family, including UTSA-120a. Data were taken from ref [157] and [163].	40
Table 7: Synthesis conditions explored in in-situ MOF functionalization. (a) Water (or DMF) was added until the total volume of the reaction mixture was 5 mL. (b) in this recipe UiO-66 was synthesized and thus a BDC linker was used instead of BTC. (c) For these recipes DMF was used instead of H <sub>2</sub> O.	42
Table 8: Parameters evaluated for in-situ amino acid modulation of MOF-808.	48
Table 9: Cluster composition of MOF-FA and MOF-Ser as determined by <sup>1</sup> H NMR.	51
Table 10: Particle size distribution with standard deviation for each of the functionalized MOF frameworks.	57
Table 11: Cluster composition of functionalized MOF-808 determined by <sup>1</sup> H NMR.	58
Table 12: Elemental composition of MOF-Li <sub>2</sub> SO <sub>4</sub> , determined using EDX.	59
Table 13: CO <sub>2</sub> uptake of the MOFs at 50 mbar and 1000 mbar for a temperature of 0 °C, 20°C and 40°C.	65
Table 14: Calculated correlation coefficients for MOF parameters and MMM gas separation performance ( $\alpha$ = selectivity, $a^*$ = separation factor, P = CO <sub>2</sub> permeability).	72
Table A 1: Dual-site Langmuir fit parameters of the adsorption isotherms measured at 0 °C, 20 °C and 40 °C for each of the functionalized MOFs.	111

## List of figures

Figure 1: Schematic representation of membrane gas separation. $P_{\text{feed}}$ , $P_{\text{permeate}}$ and $L$ respectively represent the feed pressure, permeate pressure and membrane thickness. Copied from ref. [25].	7
Figure 2: Chemical structure of cellulose triacetate. copied from ref. [31].	10
Figure 3: a) Chemical structure of Matrimid 5218. Adapted from ref.[41] b) Chemical structure of ethylene glycol crosslinked 6FDA-DABA. Adapted from ref. [38,39] and c) Chemical structure of P84®. copied from ref. [35].	12
Figure 4: Chemical structure of bisphenol-A polysulfone. copied from ref [43].	12
Figure 5: Chemical structure of Celazole®. copied from ref. [47].	13
Figure 6: a) Chemical structure of PIM-1. copied from ref. [48]. b) Molecular model of a fragment of PIM-1 showing its rigid, contorted structure. Copied from ref. [48].	13
Figure 7: Chemical structure of TR-1. Copied from ref. [52].	15
Figure 8: Chemical structure of PEBAX® MH1657 with $x$ the percentage of polyamide and $y$ the percentage of polyether segments. Copied from ref. [60].	15
Figure 9: Polymer free volume plotted against temperature. The occupied volume ( $v_o$ ) represents the volume occupied by the polymer chains. The difference between this volume and the specific volume ( $v$ ) of the polymer represents the free volume within the polymer matrix. $T_g$ represents the glass transition temperature of the polymer. Copied from ref. [21].	18
Figure 10: Solubility and diffusion coefficients for various gasses in a group of polymers from the same family. Copied from refs. [21,63].	19
Figure 11: Illustration of the dual-sorption model discerning between both Langmuir and Henry absorption behavior and their contribution to total sorption for different gas pressures. Copied from ref. [21].	20
Figure 12: Simulation of diffusion of a $\text{CO}_2$ molecule in a 6FDA-4PDA polymer matrix showing the molecules jump from cavity to cavity. Copied from ref. [21,66].	21
Figure 13: a) Dependence of the dichloroethane diffusion coefficient on the volume fraction of dichloroethane in the polymer matrix. Copied from ref. [21,67]. b) Influence of FFV of various polymers on the $\text{CO}_2$ diffusion coefficients. Copied from ref. [26].	22

Figure 14: CO <sub>2</sub> /CH <sub>4</sub> gas separation performance of various classes of polymer materials reported in literature together with the 1991 and 2008 Robeson upper bound. TR polymers (black), PIMs (green), Perfluoropolymers (red), polyimides (yellow) and poly-room temperature ionic liquids (blue). Copied from ref. [6].	23
Figure 15: a) Visualization of polymer plasticization resulting in a swollen polymer matrix. Adapted from ref. [76] b) Effect of CO <sub>2</sub> feed pressure on CO <sub>2</sub> permeability in a glassy polymer (Polysulfone) and a rubbery polymer (Polyethylene oxide, PEO). Copied from ref. [72].	25
Figure 16: Effect of physical aging on the normalized CH <sub>4</sub> permeability (P/P <sub>0</sub> ) for Matrimid membranes of varying thickness. Copied from ref. [1].	26
Figure 17: Illustration of a mixed matrix membrane.	27
Figure 18: Visualization of the volume accessible to a permeating component in the transition state theory. When the permeant moves to another cavity it has to pass through a neck with a noticeably smaller accessible volume. Copied from ref. [94].	28
Figure 19: a) molecular sieve with rigid (ultra-) micropores. b) semi-rigid polymer containing permanent porosity and flexible zones. c) flexible polymer with varying gap size due to segmental packing and motion. In all figures the yellow areas represent permanent porosity and the green areas mobile segments, able to create voids necessary for diffusion. Copied from ref. [95].	29
Figure 20: a) Continuous gas transport, gas pathways can bridge the membrane by only passing through the filler phase. b) discontinuous gas transport, gas pathways always pass through the polymer phase. Adapted from ref. [82].	30
Figure 21: Illustration of the different interactions between filler and polymer. a) Case I: rigidified polymer layer, b) Case II: sieve-in-a-cage morphologie. c) Case III: sieve-in-a-cage with size-selective gaps between polymer and filler. d) Case IV: pore blocking. e) Effect of the a good interface and case I-IV on permeability and selectivity. The dot represents the properties of the pure polymeric membrane. Adapted from ref. [98].	31
Figure 22: Isoreticular series based on the MOF-5 framework (IRMOF series). On the left sides the different linkers connecting the nodes are shown. On the right side the resulting MOF frameworks are shown. The numbers connect the MOF structures with their respective linkers. Adapted from ref. [120].	34
Figure 23: a) Structure of the node of UiO-66. b) Crystal structure of UiO-66. c) Structure of the node of MOF-808. d) Crystal structure of MOF-808. (grey = C, red = O, green = Zr) copied from refs. [150,151].	37

Figure 24: Crystal structure of a) SIFSIX-Cu-i, b) SIFSIX-Cu(Zn)-3 and c) UTSA-120a. In all figures the octahedra present Cu clusters, the structure attached to this cluster represents the $\text{SiF}_6^{2-}$ group and the other species the linker of the framework. The chemical structure of the framework linker is shown below (dpa, pyrazine and dpt respectively) Copied from refs. [157,159].	39
Figure 25: Chemical structure of formic acid (left), glycine (middle) and proline (right).	48
Figure 26: XRD diffractogram of the obtained material for the MOF-808 amino acid modulation synthesis mixture with a modulator/cluster ratio of 1 and a HCl/modulator ratio of 1.	48
Figure 27: UiO-66 and MOF-808 synthesized using the recipe described by Marshall et al. for amino acid modulated UiO-66 synthesis. a) UiO-66-proline, b) MOF-808-proline, c) UiO-66-glycine, d) MOF-808-proline.	49
Figure 28: Chemical structure of MEA (left) and Serine (right).	50
Figure 29: XRD diffractogram of MOF-FA and MOF-Ser, scaled to the peak situated at a $2\theta$ value of $4.3^\circ$ .	51
Figure 30: $\text{CO}_2$ adsorption isotherms of MOF-FA (red triangles) and MOF-Ser (green circles) measured at $0^\circ\text{C}$ for a pressure range of 0-1000 mbar.	52
Figure 31: a) $\text{CO}_2/\text{N}_2$ mixed gas separation performance of Matrimid, Matrimid + MOF-FA and Matrimid + MOF-Ser MMM for a 50/50 $\text{CO}_2/\text{N}_2$ gas mixture measured at 5 bar and $35^\circ\text{C}$ .	53
Figure 32: Hypothesized coordination of the functionalizing agents to the MOF cluster. The hypothesized coordination is based on results obtained by Furukawa et al. and Baek et al. [148,164]. The coordination of $\text{Li}^+$ is not shown on the figure.	54
Figure 33: XRD diffractograms of the various functionalized MOFs together with the calculated XRD pattern of MOF-808, stacked and scaled to the peak situated around $4.3^\circ$ .	55
Figure 34: SEM pictures of the functionalize MOFs. Images are taken at a magnification (x20000), a scale bar is represented at the bottom of each figure.	56
Figure 35: ATR-FTIR spectra of the functionalized MOFs. Wavenumbers associated with the MOF cluster and BTC linker are respectively marked with red and blue arrows.	60
Figure 36: Specific sections out of the ATR-FTIR spectra of each of the functionalized MOFs compared to the spectrum of MOF-FA-u. Characteristic functionalizing agent wavenumbers are indicated with arrows. a) MOF-His, b) MOF-TFA, c) MOF-GA, d) MOF-BA and e) MOF- $\text{Li}_2\text{SO}_4$ .	61

Figure 37: ATR-FTIR adsorption spectrum of MOF-His, Matrimid and Matrimid + MOF-His MMM. Spectra were scaled to an identical intensity for the most intense absorption peak for clarity.....	62
Figure 38: Comparison of the CO <sub>2</sub> adsorption isotherms for each of the functionalized MOFs for the entire pressure range up to 1000 mbar at a temperature of a) 0°C, b) 20°C and c) 40°C. The initial uptake in the low pressure region is also shown for a temperature of d) 0°C, e) 20 °C and f) 40 °C. ....	64
Figure 39: Q <sub>st</sub> values of the functionalized MOFs calculated using the Clausius-Clapeyron method.....	66
Figure 40: CO <sub>2</sub> permeability of the functionalized MOFs in Matrimid MMM for a 15/85 and 50/50 gas mixture and pure CO <sub>2</sub> gas. All measurements were conducted at a pressure of 5 bar and temperature of 35 °C. The shown permeability values are an average value calculated from data of 3 membrane coupons, except for MOF-GA where only 2 coupons were measured.....	68
Figure 41: CO <sub>2</sub> /N <sub>2</sub> separation factor of the functionalized MOFs in Matrimid MMM for a 15/85 and 50/50 gas mixture together with the ideal CO <sub>2</sub> /N <sub>2</sub> selectivity. All measurements were conducted at a pressure of 5 bar and temperature of 35 °C. The shown selectivity and separation factor values are an average value calculated from data of 3 membrane coupons, except for MOF-GA where only 2 coupons were measured....	70
Figure 42: XRD diffractogram of UTSA-120a. ....	74
Figure 43: ATR-FTIR spectrum of UTSA-120a.....	75
Figure 44: Gas separation performance of 6FDA-DAM pure polymer and 6FDA-DAM + UTSA-120a for a 15/85 CO <sub>2</sub> /N <sub>2</sub> gas mixture and a 50/50 CO <sub>2</sub> /CH <sub>4</sub> gas mixture, measured at an upstream pressure of 5 bar and temperature of 35 °C. ....	76
Figure 45: CO <sub>2</sub> /N <sub>2</sub> Robeson upper bound plot for MMM of Matrimid/functionalized MOF-808[69]. Data for the 15/85 CO <sub>2</sub> /N <sub>2</sub> mixture are shown for all MMM and Matrimid, except for MOF-Ser MMM where data for the 50/50 CO <sub>2</sub> /N <sub>2</sub> mixture is shown.....	76
Figure A 1: XRD diffractogram of MOF-FA-u. ....	102
Figure A 2: XRD diffractogram of MOF-His. ....	102
Figure A 3: XRD diffractogram of MOF-TFA. ....	103
Figure A 4: XRD diffractogram of MOF-GA.....	103
Figure A 5: XRD diffractogram of MOF-BA. ....	104
Figure A 6: XRD diffractogram of MOF-Li <sub>2</sub> SO <sub>4</sub> . ....	104

Figure A 7: SEM images of MOF-FA-u, MOF-GA, MOF-TFA and MOF-BA taken at a magnification (x50000). For MOF-His and MOF-Li <sub>2</sub> SO <sub>4</sub> no SEM images were recorded at this magnification.....	105
Figure A 8: EDX spectrum of MOF-Li <sub>2</sub> SO <sub>4</sub> .....	105
Figure A 9: ATR-FTIR absorbance spectrum of MOF-FA-u.....	106
Figure A 10: ATR-FTIR absorbance spectrum of MOF-His.....	106
Figure A 11: ATR-FTIR absorbance spectrum of MOF-TFA.....	107
Figure A 12: ATR-FTIR absorbance spectrum of MOF-GA.....	107
Figure A 13: ATR-FTIR absorbance spectrum of MOF-BA.....	108
Figure A 14: ATR-FTIR absorbance spectrum of MOF-Li <sub>2</sub> SO <sub>4</sub> .....	108
Figure A 15: ATR-FTIR absorbance spectrum of MOF-FA-u, Matrimid and Matrimid + MOF-FA-u MMM. Spectra were scaled to an identical intensity for the most intense absorption for clarity.....	109
Figure A 16: ATR-FTIR absorbance spectrum of MOF-TFA, Matrimid and Matrimid + MOF-TFA MMM. Spectra were scaled to an identical intensity for the most intense absorption for clarity.....	109
Figure A 17: ATR-FTIR absorbance spectrum of MOF-GA, Matrimid and Matrimid + MOF-GA MMM. Spectra were scaled to an identical intensity for the most intense absorption for clarity.....	110
Figure A 18: ATR-FTIR absorbance spectrum of MOF-BA, Matrimid and Matrimid + MOF-BA MMM. Spectra were scaled to an identical intensity for the most intense absorption for clarity.....	110
Figure A 19: ATR-FTIR absorbance spectrum of MOF-Li <sub>2</sub> SO <sub>4</sub> , Matrimid and Matrimid + MOF-Li <sub>2</sub> SO <sub>4</sub> MMM. Spectra were scaled to an identical intensity for the most intense absorption for clarity.....	111
Figure A 20: CO <sub>2</sub> /CH <sub>4</sub> Robeson plot for 6FDA-DAM and UTSA-120a 6FDA-DAM MMM[69,229]. The datapoints for a 50/50 CO <sub>2</sub> /CH <sub>4</sub> feed gas mixture are shown.....	112
Figure A 21: CO <sub>2</sub> /N <sub>2</sub> Robeson plot for 6FDA-DAM and UTSA-120a 6FDA-DAM MMM[69]. The datapoints for a 15/85 CO <sub>2</sub> /N <sub>2</sub> gas mixture are shown.....	112

# Table of contents

Acknowledgments.....	I
Abstract.....	II
Samenvatting.....	III
List of abbreviations.....	IV
List of tables.....	VIII
List of figures.....	IX
Table of content.....	XIV
Adapted planning due to Coronavirus measures.....	XVIII
1 General introduction and objectives .....	1
1.1 General introduction.....	1
1.2 Thesis objectives.....	2
2 Literature review.....	3
2.1 Carbon dioxide separations .....	3
2.1.1 CO <sub>2</sub> removal from natural gas and biogas .....	3
2.1.2 CO <sub>2</sub> removal from flue gas .....	4
2.1.3 CO <sub>2</sub> removal from syngas.....	5
2.2 Membrane technology .....	6
2.2.1 History of membrane gas separations .....	6
2.2.2 Basic concepts of membrane transport .....	7
2.2.3 Measuring membrane performance .....	8
2.2.3.1 Flux, permeability and permeance.....	8
2.2.3.2 Ideal selectivity and separation factor .....	9
2.2.4 Polymeric membranes.....	10
2.2.4.1 State of the art of polymeric CO <sub>2</sub> gas separation membranes .....	10
2.2.4.2 Mass transport in polymeric membranes.....	16
2.2.4.2.1 Solution-diffusion model.....	16
2.2.4.2.2 Free volume theory.....	17
2.2.4.3 Challenges of polymeric membranes .....	22
2.2.4.3.1 Permeability/Selectivity trade-off .....	22
2.2.4.3.2 Plasticization .....	24

2.2.4.3.3	Physical aging .....	25
2.2.5	Mixed matrix membranes .....	26
2.2.5.1	Introduction .....	27
2.2.5.2	Mass transport in MMM.....	27
2.2.5.3	Challenges of creating MMM.....	30
2.2.5.3.1	Polymer-filler interface .....	30
2.2.5.3.2	Dispersion.....	32
2.2.5.3.3	Mechanical stability .....	33
2.2.6	Metal organic framework mixed matrix membranes.....	33
2.2.6.1	Introduction .....	33
2.2.6.2	Advantages of MOF fillers .....	34
2.2.6.3	MOF fillers used in MMM CO <sub>2</sub> gas separations.....	36
3	Materials and methods .....	41
3.1	Materials .....	41
3.2	MOF-808-FA synthesis .....	41
3.3	MOF-808 functionalization strategies .....	42
3.3.1	In-situ functionalization .....	42
3.3.2	Post-synthetic functionalization.....	42
3.3.2.1	Method 1 .....	42
3.3.2.2	Method 2.....	43
3.3.2.3	Method 3.....	43
3.4	UTSA-120a synthesis .....	43
3.5	Membrane synthesis .....	43
3.6	X-ray diffraction (XRD).....	44
3.7	Nuclear magnetic resonance (NMR) .....	44
3.8	Attenuated total reflection Fourier transform infrared spectroscopy (ATR-FTIR)...	44
3.9	Scanning electron microscopy (SEM) and energy dispersive X-ray analysis (EDX)	45
3.10	CO <sub>2</sub> adsorption measurements.....	45
3.11	High-throughput gas separation measurements (HTGS).....	46
4	Results and discussion .....	47
4.1	Introduction .....	47
4.2	Amino acid functionalization of MOF-808 .....	47

4.2.1	In-situ functionalization of MOF-808 with amino acids .....	47
4.2.2	Post-synthetic functionalization of MOF-808 with serine.....	50
4.2.2.1	Characterization of MOF-Ser .....	50
4.2.2.2	Gas separation performance of MOF-Ser.....	52
4.3	Platform MOF-808: correlation of MOF parameters with MMM gas separation performance .....	53
4.3.1	XRD .....	55
4.3.2	SEM .....	56
4.3.3	NMR .....	57
4.3.4	EDX .....	58
4.3.5	ATR-FTIR.....	59
4.3.6	CO <sub>2</sub> physisorption.....	63
4.3.6.1	CO <sub>2</sub> uptake.....	63
4.3.6.2	Comparison of MOF-FA and MOF-FA-u .....	65
4.3.6.3	Isosteric heat of CO <sub>2</sub> adsorption.....	66
4.3.7	Gas separation performance.....	67
4.3.7.1	CO <sub>2</sub> permeability .....	68
4.3.7.2	CO <sub>2</sub> /N <sub>2</sub> selectivity and separation factor .....	69
4.3.8	Correlation of MOF parameters with MMM performance.....	72
4.4	MMM based on UTSA-120a.....	73
4.4.1	XRD .....	73
4.4.2	ATR-FTIR.....	74
4.4.3	Gas separation performance.....	75
4.5	Comparison of MMM with the Robeson upper bound.....	76
5	General conclusion and Future work .....	77
5.1	Amino acid functionalization of MOF-808 .....	77
5.2	Platform MOF-808: correlation of MOF parameters with MMM gas separation performance .....	77
5.3	MMM based on UTSA-120a.....	78
5.4	Future work.....	79
5.4.1	Additional characterization.....	79
5.4.2	Additional experiments .....	80

References.....	81
Appendix.....	102
Risk analysis.....	113
Popularized summary.....	124

## Adapted planning due to Coronavirus measures

The planning of this thesis was influenced by the coronavirus measures adopted by the KU Leuven. Starting from 16/3/2020 all lab activities were suspended. As a result, some experiments required for this thesis could not be carried out. This section provides a list of all cancelled experiments, together with the dates they were planned.

- N<sub>2</sub> physisorption measurements
  - o All functionalized MOFs (30/3-1/4)
  - o UTSA-120a (20/4-21/4)
- CO<sub>2</sub> physisorption measurements of UTSA-120a (20/4-21/4)
- Thermogravimetric analysis of UTSA-120a (not planned yet)
- X-ray diffraction measurements of MOF-808 functionalized with 4-(trifluoromethyl) benzoic acid (MOF-TFBA) (16/3)
- <sup>19</sup>F NMR of MOF-TFA and MOF-TFBA (not planned yet)
- Scanning electron microscopy measurements of:
  - o UTSA-120a (26/3)
  - o Mixed-matrix membranes (MMM) of UTSA-120a (26/3)
- ICP-OES of MOF-Li<sub>2</sub>SO<sub>4</sub> (not planned yet)
- Gas separation measurements
  - o MMM of MOF-GA (20/3-25/3)
    - The initial measurements for these MMM showed large deviations between the three measured membranes. Extra measurements were planned to improve the dataset.
  - o MMM of MOF-TFBA (20/3-25/3)
  - o MMM of UTSA-120a (16/3-18/3)
    - 50/50 CO<sub>2</sub>/N<sub>2</sub> and pure gas CO<sub>2</sub>, N<sub>2</sub> and CH<sub>4</sub>

Together with the promotor and daily supervisor of this thesis, it was concluded sufficient experimental data was obtained to write and hand in this manuscript.

# 1 General introduction and objectives

## 1.1 General introduction

Carbon dioxide (CO<sub>2</sub>) is an important greenhouse gas and strong contributor to global warming[1,2]. The intergovernmental panel on climate change stated in their 2018 report significant changes in the global industrial and energy consumption practices are required to maintain global warming below the 1.5°C target[2]. Evidence of the global concern about CO<sub>2</sub> emissions can be found in the stronger regulations both on a local and international level (e.g. EU Emissions Trading System), as well as in various projects such as the European Green Deal and the Moonshot project for a CO<sub>2</sub>-neutral Flanders in 2050[3–5]. CO<sub>2</sub> capture from power plants and industrial exhaust gas streams (CO<sub>2</sub>/N<sub>2</sub> separations) aims at significantly reducing anthropogenic CO<sub>2</sub> emissions[2]. Next to environmental reasons, CO<sub>2</sub> removal from energy streams, such as natural gas and biogas (e.g. CO<sub>2</sub>/CH<sub>4</sub> separation), is imperative in industry to prevent transport infrastructure corrosion and to maintain high caloric value specifications of the produced methane[6].

Although conventional separation technologies for these applications (such as cryogenic distillation and amine scrubbing) definitely have their respective advantages, they are often highly energy-intensive and have a relatively large environmental footprint[6]. Membrane-based gas separation is considered a viable alternative for the traditional technologies as it offers lower energy consumption, reduced environmental impact and a modular design, which allows retrofitting in existing plants[6]. Therefore, membrane based CO<sub>2</sub> gas separations have gained increasing attention over the past years, both in industry and academia[1,6]. Current state-of-the-art polymeric membranes for the well-established natural and biogas market mostly consist of cellulose acetate and polyimide. They typically show rather low CO<sub>2</sub>/CH<sub>4</sub> selectivity combined with medium gas permeance, which significantly impacts operational and capital costs[1]. Academic research has mainly focused on engineering membrane materials for performance improvement. Various new promising polymeric membranes were developed, yet with this development, a trade-off between desirable membrane properties was discovered: membranes with high selectivities generally show low permeabilities and vice versa[1].

Nonetheless, some membrane classes managed to surpass this trade-off limit and one of these new, promising membrane materials are mixed-matrix membranes (MMM)[1]. These type of membranes combine the properties of organic polymers and inorganic fillers, aiming at high selectivities and permeabilities with the processability and ease of operation of polymeric

membranes[1]. Specifically, MMM with metal-organic frameworks (MOFs) as filler materials have shown exceptional gas separation performance and are therefore a ‘hot topic’ in membrane gas separation[1].

## **1.2 Thesis objectives**

A multitude of challenges, societal as well as industrial, give rise to a need for efficient CO<sub>2</sub> separations. Membrane gas separation is a promising technology to aid in overcoming this challenges. However, traditional polymeric membranes are limited by a trade-off between desirable membrane properties. A possible strategy to circumvent this setback is the incorporation of various filler materials with separation enhancing properties in a polymer, resulting in so called MMM. The aim of this thesis is to develop new MOF materials to be used as fillers in MMM, resulting in enhanced CO<sub>2</sub> gas separation performance. Simultaneously, the relationship between characteristic properties of these materials and the resulting gas separation performance of the MMM will be investigated. In a first part, the scientific background surrounding this research is framed. An overview of the relevant CO<sub>2</sub> separation processes is provided, along with the current state of the art polymeric gas separation membranes. Next, the theoretical principles and theories surrounding gas transport in both polymeric and mixed matrix membranes are elaborated upon, along with challenges both fields face. To conclude this section, a short introduction to MOFs in general and specifically the MOFs relevant to this thesis is provided.

Functionalization of MOF-808 has recently been proven to be an effective strategy in enhancing the performance of MMM. This work aims to extend this functionalization strategy to other types of organic molecules. First of all, amino acid functionalization will be investigated. Amino acids are of particular interest since they contain functional groups known to interact well with CO<sub>2</sub>. Additionally, they are relatively cheap and can be considered as ‘green’ chemicals. Two strategies will be used to incorporate amino acids: an in-situ functionalization method, where amino acids are used to modulate the synthesis of MOF-808 and a post-synthetic functionalization method, where amino acids will be exchanged with other molecules coordinating to the cluster of a pre-synthesized MOF-808. Next, this functionalization strategy will be extended to a broad range of potential functionalizing agents. These functionalized MOFs will be thoroughly characterized and evaluated for their MMM gas separation performance and the relationship between MOF characteristic ‘parameters’ and MMM performance will be evaluated. Finally, the MOF UTSA-120a will be evaluated as a new filler material in MMM for CO<sub>2</sub>/N<sub>2</sub> and CO<sub>2</sub>/CH<sub>4</sub> separations.

## 2 Literature review

### 2.1 Carbon dioxide separations

Various industrial processes require separation of CO<sub>2</sub> from a feed gas stream. Some examples are the removal of CO<sub>2</sub> from natural gas and biogas or CO<sub>2</sub> separations for the production of H<sub>2</sub> gas. Similarly CO<sub>2</sub> capture from flue gas streams might become increasingly important in industry in the future[1,2]. This section gives an overview of some relevant CO<sub>2</sub> separations.

#### 2.1.1 CO<sub>2</sub> removal from natural gas and biogas

The global consumption of natural gas has increased from 2.2 trillion cubic meters in 1998 to 3.8 trillion cubic meters in 2018, mainly due to an increase in natural gas power stations for electricity generation[7,8]. Natural gas power stations could conceivably function as a support for renewable energy resources, which suffer from load balancing problems. These power plants are flexible due to their ability to quickly ramp up their production capacity and have a relatively low greenhouse gas emissions compared to other fossil fuel based electricity generation plants[9]. Furthermore, natural gas based power installations offer good compatibility with renewable fuels, such as biogas[9].

The composition of natural gas varies strongly depending on the location of extraction. Some examples of raw natural gas extracted from reservoirs in various locations are shown in Table 1[10]. Often, a distinction is made between wet and dry gas depending on the hydrocarbon constituents of the gas mixture. Wet gas contains more than 10 vol% of C<sub>2+</sub> constituents, whereas dry gas contains little C<sub>2+</sub> constituents[11]. Another classification which is often used is the distinction between sour and sweet gas based on the H<sub>2</sub>S content, with gas containing more than 5 mg/Nm<sup>3</sup> being classified as sour[11]. Next to the constituents listed in Table 1 raw natural gas often contains small amounts of helium and argon and trace amounts of radon, krypton and xenon[11]. Biogas can be used as well in gas based power installations. The composition of biogas generated from different waste sources is listed in Table 2[12].

Table 1: Chemical composition of natural gas reservoirs around the world. Copied from ref. [10].

(%vol)	Groningen (Netherlands)	Ardjuna (Indonesia)	Uthmaniyah (Saudi Arabia)	Lacq (France)	Uch (Pakistan)
CH <sub>4</sub>	81.3	65.7	55.5	69	27.3
C <sub>2</sub> H <sub>6</sub>	2.9	8.5	18	3	0.7
C <sub>3</sub> H <sub>8</sub>	0.4	14.5	9.8	0.9	0.3
C <sub>4</sub> H <sub>10</sub>	0.1	5.1	4.5	0.5	0.3
C <sub>5+</sub>	0.1	0.8	1.6	0.5	–
N <sub>2</sub>	14.3	1.3	0.2	1.5	25.2
H <sub>2</sub> S	–	–	1.5	15.3	–
CO <sub>2</sub>	0.9	4.1	8.9	9.3	46.2

Table 2: Constituents of biogas originating from different waste streams. Copied from ref. [12].

Component (vol%)	Agricultural waste	Landfills	Industrial waste
CH <sub>4</sub>	50–80	50–80	50–70
CO <sub>2</sub>	30–50	20–50	30–50
H <sub>2</sub> S	0.7	0.1	0.8
H <sub>2</sub>	0–2	0–5	0–2
N <sub>2</sub>	0–1	0–3	0–1
O <sub>2</sub>	0–1	0–1	0–1
CO	0–1	0–1	0–1
NH <sub>3</sub>	Traces	Traces	Traces
Siloxanes	Traces	Traces	Traces
H <sub>2</sub> O	Saturation	Saturation	Saturation

As can be seen in Table 1 and Table 2, natural gas and biogas can contain up to 50% CO<sub>2</sub> depending on the location of gas extraction or the waste source it is generated from respectively. CO<sub>2</sub> is a noncombustible gas and therefore reduces the heating value of the gas mixture. In addition, the presence of the gas can cause corrosion in the transport pipelines[11]. Therefore the CO<sub>2</sub> content of raw natural gas has to be reduced (to  $\leq 2\%$  to meet U.S. pipeline grid requirements)[13]. CO<sub>2</sub> removal from natural gas (CO<sub>2</sub>/CH<sub>4</sub> separation) is mostly done using amine absorption. Membrane technology is an interesting alternative which at the moment occupies 10% of the natural gas separation market[1]. Membranes offer the advantage of more effectively treating high CO<sub>2</sub> content feed streams and a simpler operation[13]. Expansion of the market share of membranes is mainly limited by the relatively higher CH<sub>4</sub> loss compared to amine absorption. Therefore, membranes with higher selectivities and permeances under real industrial conditions would be required to expand the market share of membranes in this separation[1].

### 2.1.2 CO<sub>2</sub> removal from flue gas

In 2016, the generation of 1 kWh electricity in Europe was accompanied by the emission of 295.8 kg CO<sub>2</sub>[14]. The total global amount of CO<sub>2</sub> emitted from fuel combustion reached 32.8 billion tons in 2018[15]. Furthermore, recent data of the International Environmental Agency show an ever increasing demand for energy. Especially non-OECD (Organization for economic cooperation and development) countries have strongly increasing CO<sub>2</sub> emissions. In 2017, the average non-OECD emission increased by 472 megaton[15]. A possible approach to reduce CO<sub>2</sub> emissions originating from electricity generation and industry could be its capture and storage(CCS). In order for this technology to be adopted at large scales, efficient CO<sub>2</sub>/N<sub>2</sub> separation technology is required. Various technologies have been considered for CCS, such as chemical or physical absorption and cryogenic distillation[1,16,17]. Membrane separations

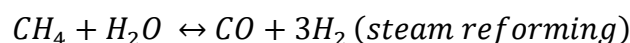
could be a viable technology for CCS as well, offering advantages such as compactness, modular design, ease of installation and often lower capital costs[16,17]. Furthermore, they generally have a lower energy consumption and require less chemicals during operation[16,17]. However, better membranes are needed[1]. As flue gas generally contains a low concentration of CO<sub>2</sub> and is often emitted at near atmospheric pressure, the major challenge for this separation is to create sufficient driving force (Table 3). These low pressures result in a high compressor cost rendering the economic feasibility of such a process low[16]. Therefore, development of membranes which combine high CO<sub>2</sub> permeance with reasonable CO<sub>2</sub>/N<sub>2</sub> selectivity is most desired. Additionally, these membranes should display good thermal and chemical stability[1,16]. Due to the ever increasing energy demand and concomitant CO<sub>2</sub> emissions the development of environmentally friendly CCS technology will become increasingly important and membrane technology could be an important contributor to achieve this[2].

Table 3: Typical composition of flue gas originating from different sources. Copied from ref. [16].

Stream sources	CO <sub>2</sub> concentration %vol (dry)	Pressure range	CO <sub>2</sub> partial pressure (bar)
Gas turbines	3–4	Atmospheric	0.03–0.04
Fired boilers of oil refinery and petrochemical plant	8	“	0.08
Natural gas fired boiler	7–10	“	0.07–0.10
Oil fired boilers	11–13	“	0.11–0.13
Coal fired boilers	12–14	“	0.12–0.14
IGCC after combustion	12–14	“	0.12–0.14
Blast furnace (after combustion)	27	“	0.27
Cement process	14–33	“	0.14–0.33

### 2.1.3 CO<sub>2</sub> removal from syngas

Global hydrogen production reached 70 million tons in 2018[18]. Up to three quarters of the hydrogen is produced from natural gas and as a result hydrogen production is accountable for 6% of the global natural gas use[18]. Hydrogen is produced out of natural gas using steam reforming followed by a water-gas shift reaction. Both reactions are shown below[19]:



In this second step, CO and water react to form CO<sub>2</sub> and H<sub>2</sub>. As a result, the produced hydrogen will be mixed with CO<sub>2</sub> which has to be removed prior to hydrogen use. At the moment, CO<sub>2</sub> capture from syngas (CO en H<sub>2</sub> mixture) is mainly done using physical absorption for high

pressure streams and amine absorption for low pressure streams (below 20 bar), however membranes are an interesting alternative[1,20]. H<sub>2</sub> as well as CO<sub>2</sub> selective membranes are interesting for this application. The advantages of membranes in this process are the relatively simple mode of operation and potential higher energy efficiency. The main challenge for membranes to take over from conventionally used absorption processes is a higher mixed-gas selectivity, which is required to improve process economics[1,20].

## **2.2 Membrane technology**

### **2.2.1 History of membrane gas separations**

The first systematic studies of membrane-based gas separation were carried out by J. K. Mitchell, who studied the permeation rates of ten gasses through natural rubber. Mitchell observed permeation rates diverging up to a factor 100 between the slowest permeating gas, carbon monoxide and the fastest permeating gas, ammonium. In addition, he observed that the natural rubber adsorbed a portion of CO<sub>2</sub> and associated this solubility behavior with the high permeability of CO<sub>2</sub>[21,22]. The next milestone towards gas separation membranes was marked by the publication of a paper by Thomas Graham in 1866. In this paper, he first proposed the basis of the nowadays universal used solution-diffusion (SD) model. Graham studied porous membranes, eventually leading to the formulation of Graham's law of diffusivity, which would later be used during the Manhattan project for the enrichment of uranium[21,22]. This was the first time gas separation membranes were applied on industrial scale. In 1879, von Wroblewski experimentally determined the permeation rate of gasses in a rubber is proportional to the product of gas solubility and the diffusion coefficient of the gas, building on previous results obtained by Exner and Stefan[22]. In the 1940s and 1950s, other scientists modernized the SD model and other theories on gas transport through membranes. So far, studies had mainly focused on polymers above their glass transition temperature. Maeres was in 1954 the first to observe the discontinuity in Arrhenius plots at the glass transition temperature in polymers and to describe permeation of gasses in glassy polymers with the dual-sorption model. Michaels, Vieth and Barrie elaborated on his work and first demonstrated the dual-sorption in 1963 and discussed its effect on membrane transport[21,23]. Up until this point, there were no large-scale industrial applications of gas separation membranes. This changed in 1961 with Loeb and Sourirajan's discovery of the first semi-permeable asymmetric membranes by phase inversion, developed for the desalination of seawater. These membranes yielded higher fluxes at comparable salt rejection compared to the existing, isotropic membranes at that time[21,23]. Permea used this phase inversion technique for the production of asymmetric gas separation

membranes. Together with the development of large surface area membrane modules, this made the first commercial membrane-based gas separation application possible: the hydrogen-separating Prism® membranes of Permea (now Air Products), which were launched in 1980. These membranes were mainly used for the separation of hydrogen from purge gas streams in ammonia plants[21,23]. Shortly after this first application, other companies developed commercial membranes for CO<sub>2</sub>/CH<sub>4</sub> and N<sub>2</sub>/O<sub>2</sub> separations. Membrane separation of oxygen and nitrogen strongly expanded after optimization by Dow, Ube and Du Pont/Air Liquide. Alongside these big applications, some smaller scale applications of gas separation developed, such as dehydration of air and natural gas or vapor removal from air and nitrogen streams[21]. Nowadays, the separation of CO<sub>2</sub> from natural gas and the separation of N<sub>2</sub> from air are the two largest contributors to the global membrane gas separation market, with approximate yearly revenues of 300 million and 800 million dollars respectively[1]. Different applications are still being developed, for example CO<sub>2</sub>/H<sub>2</sub> and olefin/paraffin separations[1].

### 2.2.2 Basic concepts of membrane transport

Membrane separations are based on a difference in permeation rate of the individual components of a mixture through the membrane[21]. Figure 1 shows the specific example of a membrane-based gas separation. Three streams are discerned in the gas separation process, a feed stream consisting of the raw gas to be separated, a permeate stream comprised of the gas molecules actually permeating through the membrane and finally the molecules retained at the feed side of the membrane, which form the retentate stream[21,24]. The driving force in a membrane separation process is a gradient in chemical potential across the membrane, expressed in terms of a gradient in pressure, temperature, electric potential and/or concentration[21,24].

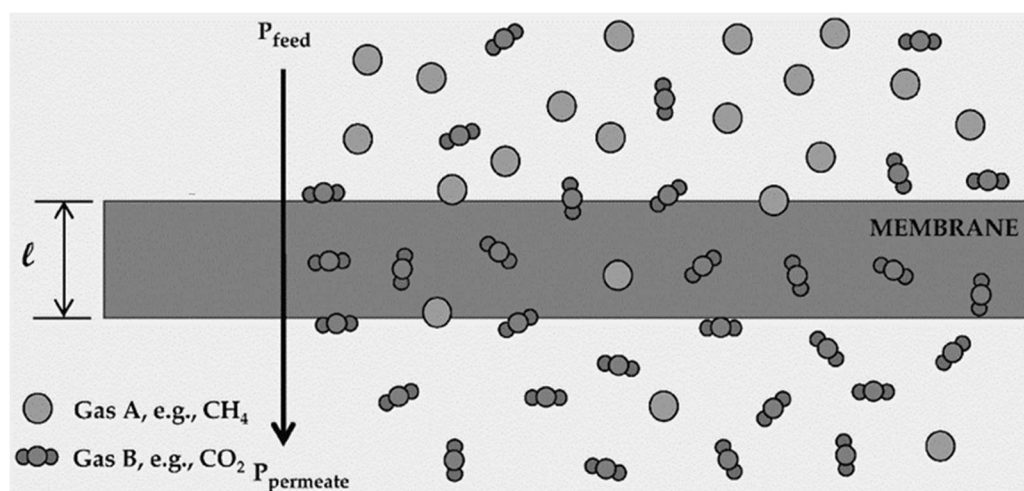


Figure 1: Schematic representation of membrane gas separation.  $P_{feed}$ ,  $P_{permeate}$  and  $L$  respectively represent the feed pressure, permeate pressure and membrane thickness. Copied from ref. [25].

### 2.2.3 Measuring membrane performance

In order to optimize membranes for different applications, evaluation criteria for membrane performance are required. In lab-scale membrane development research, permeability/permeance and selectivity/separation factor are predominantly considered[24].

#### 2.2.3.1 Flux, permeability and permeance

Flux is defined as the volume flowing through a membrane per unit of surface area and unit of time. The flux is proportional to the driving force of the membrane process, in the case of gas separations this is the pressure difference across the membrane. The flux ( $\text{m}^3/\text{m}^2\cdot\text{s}$ ) through a membrane can thus be described using the formula[21,24]:

$$J = \frac{V}{A \cdot \Delta t} \quad (1)$$

With A the membrane surface area ( $\text{m}^2$ ), V ( $\text{m}^3$ ) the volume of the permeate and  $\Delta t$  (s) the time interval during which a volume V permeates through the membrane.

Flux does not allow for the comparison of the intrinsic transport properties of different membrane materials because it does not consider differences in thickness or applied driving force. Therefore, permeability (P) of a gas is defined as the pressure and thickness normalized gas flux through a membrane[26].

$$P_i = \frac{J_i \times L}{\Delta p} \quad (2)$$

Where  $P_i$  represents the permeability of component i, L (m) the thickness of the membrane and  $\Delta p$  (Pa) the pressure gradient over the membrane.

Permeability is expressed in SI units (International System of Units) as[26]:

$$P = \frac{\text{mol}}{\text{m s Pa}} \quad (3)$$

However, Barrer is a more widely used unit for permeability. The unit Barrer at standard temperature and pressure (STP) is defined as[26]:

$$1 \text{ Barrer} = 10^{-10} \times \frac{\text{cm}^3(\text{STP}) \text{ cm}}{\text{cm}^2 \text{ s cmHg}} \quad (4)$$

In practice, the thickness of the thin, selective layer of industrially used asymmetric or thin film composite membranes is difficult to measure due to small chemical contrast between this layer and the underlying support. Therefore, gas permeance of a gas through a membrane is defined as the pressure normalized gas flux. It is mostly expressed in Gas Permeation Units (GPU). A

permeance of 1 GPU corresponds to a membrane with a selective layer thickness of 1  $\mu\text{m}$  and an intrinsic permeability of 1 Barrer[26].

$$1 \text{ GPU} = 10^{-6} \times \frac{\text{cm}^3(\text{STP})}{\text{cm}^2 \text{ s cmHg}} \quad (5)$$

### 2.2.3.2 Ideal selectivity and separation factor

The ideal selectivity ( $\alpha$ ) defines the efficiency of the separation. It is a measure of the effectiveness of the membrane to discern between the different components in the feed[26]. The ideal selectivity is defined as:

$$\alpha_{AB} = \frac{P_A}{P_B} \quad (6)$$

Where  $P_A$  and  $P_B$  are, respectively, the pure gas permeabilities of component A and B. In more complex separations, the permeation of one component influences the transport of the other component through the membrane. Therefore, the ideal ‘pure-gas’ selectivity can deviate from the selectivity measured when gas mixtures are considered. Consequently, the separation factor  $\alpha_{AB}^*$  is determined measuring the performance of the membrane when a feed gas mixture is used[26].

$$\alpha_{AB}^* = \frac{\gamma_A / x_A}{\gamma_B / x_B} \quad (7)$$

Where  $\gamma_A$  and  $\gamma_B$  represent, respectively, the mole fractions of component A and B in the permeate and  $x_A$  and  $x_B$  the mole fractions of component A and B respectively in the feed. This separation factor or ‘mixed-gas’ selectivity can be linked to the ideal ‘pure gas’ selectivity via Equation 8, indicating that the separation factor also depends on process parameters such as pressure and gas composition, with  $p_1$  (Pa) representing the downstream pressure and  $p_2$  (Pa) the upstream pressure[26].

$$\alpha_{AB}^* = \alpha_{AB} \frac{p_2 - p_1 \left( \frac{\gamma_A}{x_A} \right)}{p_2 - p_1 \left( \frac{\gamma_B}{x_B} \right)} \quad (8)$$

## 2.2.4 Polymeric membranes

### 2.2.4.1 State of the art of polymeric CO<sub>2</sub> gas separation membranes

Different types of polymeric membranes have been studied for their performance in CO<sub>2</sub> membrane separations. Despite this extensive research, up to 90% of commercial gas separation membranes consist of 10 different polymer materials[27]. A brief overview of the conventional polymer families used in industrial CO<sub>2</sub> gas separations and research is provided in this section, combined with a discussion on some promising new families of membrane materials for CO<sub>2</sub> gas separations.

#### *Cellulose acetate*

Traditionally, asymmetric cellulose acetate (CA) based membranes make up the bulk of the polymeric membranes applied for CO<sub>2</sub>/CH<sub>4</sub> gas separations due to their relatively low production cost[6]. They consist of a cellulose polymer chain with varying degree of acetylation, which determines the separation properties of the membrane[1,6,27–30]. The chemical structure of this polymer is shown in Figure 2, while Table 4 shows its ideal gas selectivity. However, CA membranes are susceptible to plasticization by CO<sub>2</sub> and hydrocarbons of the C<sub>2</sub> to C<sub>6</sub> fractions, including BTEX (benzene, toluene, ethylbenzene and xylenes) aromatics. Plasticization results in an increase in polymer chain mobility which reduces the selectivity of the membranes[1,28,30]. Additionally, the plasticization behavior of CA membranes speeds up physical ageing, the time-dependent decrease in membrane gas separation performance[1,28,30]. Furthermore, membranes with a higher selectivity are required to increase the competitiveness of membrane-based natural gas treatment[1,27].

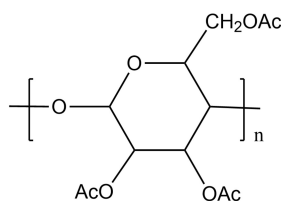


Figure 2: Chemical structure of cellulose triacetate. copied from ref. [31].

#### *Polyimides*

Polyimides are used in different gas separation applications such as hydrogen recovery, N<sub>2</sub> production and natural gas treatment[1,6]. Polyimide membranes generally have a high mechanical strength and thermal resistance and can be easily processed and shaped into thin membranes. These properties make them interesting for different applications, even despite their relatively high prices[6,32]. Matrimid® (Matrimid) is a commercially available polyimide

membrane consisting of a 3,3'-4,4'-benzophenone tetracarboxylic dianhydride (BTDA) and a diaminophenylindane (DAPI) unit (Figure 3a), showing a reasonable combination of selectivity and permeability for CO<sub>2</sub>/CH<sub>4</sub> gas streams[6]. However, commonly, Matrimid and other polyimides are highly susceptible to CO<sub>2</sub> plasticization and plasticization by other minor components in the raw gas stream (e.g. small hydrocarbons and BTEX)[1,6,27,28,33]. Another commercially available polyimide membrane used in CO<sub>2</sub>/CH<sub>4</sub> separations is the P84® membrane created by Evonik(Figure 3c). It is a copolyimide consisting of BTDA and 80% methyl phenylene diamine/20% methylene diamine. P84® has a lower CO<sub>2</sub> permeability than Matrimid, but a higher selectivity. P84® membranes are industrially relevant due to their high thermal and chemical stability and reasonable selectivity in mixed gas feed conditions[34–36]. The CO<sub>2</sub>/CH<sub>4</sub> gas separation performance of Matrimid and P84® can be found in Table 4.

A broad range of structural variants of polyimide membranes have been studied and evaluated for their gas separation properties[6,28,34]. One of these variants are fluorinated polyimides. These are often based on pyromellitic dianhydride (PMDA) and hexafluoro isopropylidene diphtalic anhydride monomer (6FDA) combined with varying other monomers[6]. PMDA based polyimides showed enhanced CO<sub>2</sub>/CH<sub>4</sub> selectivities compared to other polyimides with similar permeabilities. This increase was attributed to (1) the fluor groups which interact strongly with CO<sub>2</sub> enhancing the solubility selectivity and (2) an increase in stiffness of the polymer chain as a result of the backbone chemical structure, which increases the diffusivity selectivity of the polymer[37]. 6FDA based polyimides even surpassed the performance of their PMDA based counterparts. Their larger chain stiffness further reduced segmental mobility and thus enhanced the diffusivity selectivity of the polymers. Simultaneously, the -C(CF<sub>3</sub>)- groups in the backbone are suggested to disturb chain packing, which is hypothesized to contribute to their enhanced permeability[37]. The hexafluoro-substituted polyimides are however also susceptible to plasticization under relevant industrial conditions[27].

Mitigation of plasticization in polyimides mainly consists of thermal, chemical or UV crosslinking methods. Current generation fluorinated polyimides show permeation properties close the Robeson 2008 upper bound[6,34]. An example of such a polyimide is 6FDA-DABA (DABA = 3,5-diaminobenzoic acid). Membranes of this polyimide can be crosslinked through chemical crosslinking, using ethylene glycol to connect two DABA units(Figure 3b)[38]. The crosslinked membrane showed excellent separation performance which can be found in Table 4[27,39]. Adam *et al.* showed that 6FDA-DABA (2:1) can be thermally crosslinked as well[40].

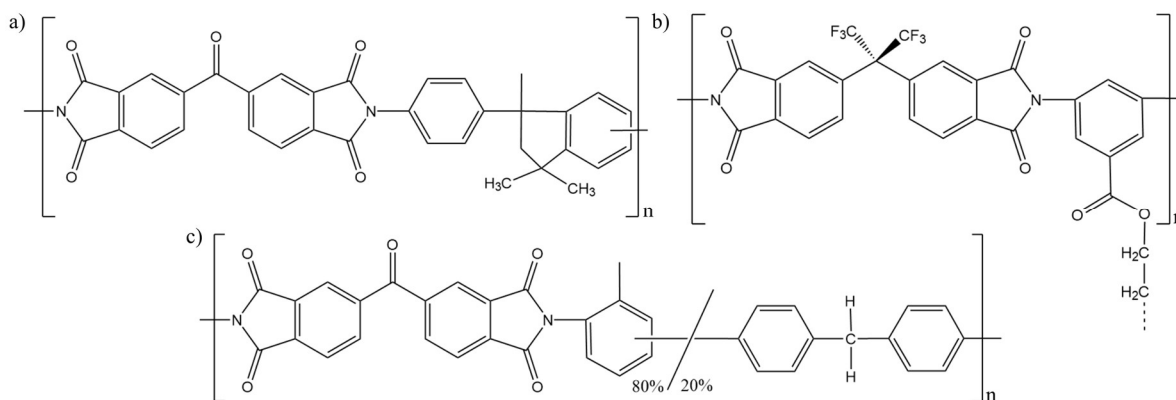


Figure 3: a) Chemical structure of Matrimid 5218. Adapted from ref.[41] b) Chemical structure of ethylene glycol crosslinked 6FDA-DABA. Adapted from ref. [38,39] and c) Chemical structure of P84®. copied from ref. [35].

### Polysulfone

Polysulfones are glassy polymers with a diphenylene sulfone repeat unit and are known for their chemical and thermal stability and easy processability[6,30,32]. As a result, these membranes are used in  $N_2/O_2$  and  $H_2/CO_2$  separations[27]. Polysulfone membranes have as well been evaluated for their  $CO_2/CH_4$  separation performance. The selectivity of polysulfone gas separation membranes for this separation is lower than the selectivity of their CA counterparts. However, they are more resistant to  $CO_2$  plasticization[33,42]. Traditionally, tetramethyl bisphenol-A analogs of polysulfone are used, which have lower permeabilities but higher selectivities towards  $CO_2$ [6,42]. Various polysulfone membrane manufacturing modifications and polysulfone chemical structure modifications have been extensively studied in order to increase their permeation properties[6,42]. The permeability and selectivity of bisphenol-A-polysulfone and its tetramethyl form are given in Table 4. The chemical structure of bisphenol-A polysulfone can be found in Figure 4[32,43].

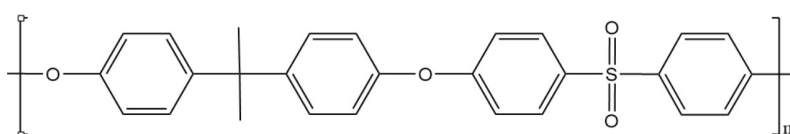


Figure 4: Chemical structure of bisphenol-A polysulfone. copied from ref [43].

### Polybenzimidazoles

Polybenzimidazoles (PBIs) are a class of glassy polymers consisting of heterocyclic ring structures and have outstanding thermal, chemical and mechanical stability[44,45]. They have been studied for  $H_2/CO_2$  separations. Celazole® is a commercially available PBI, which has been investigated thoroughly. It has a  $H_2/CO_2$  selectivity of 19 and a  $H_2$  permeance of 500 GPU at a temperature of  $250^\circ C$ . Its chemical structure can be found in Figure 5[46,47]. Celazole®

H<sub>2</sub> permeabilities at 35°C were calculated by Stevens *et al.* and found to be ranging from 0.6 to 3.4 Barrer[46].

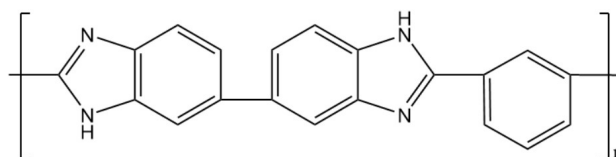


Figure 5: Chemical structure of Celazole®. copied from ref. [47].

### Polymers of intrinsic micro-porosity

In 2005, a group of newly developed polymeric membranes called polymers of intrinsic micro-porosity (PIMs) showed gas separation properties surpassing the 1991 Robeson upper bound[6,48]. PIM-1 films displayed a CO<sub>2</sub>/CH<sub>4</sub> ideal selectivity of 18.4 combined with a CO<sub>2</sub> permeability of 2300 Barrer[48]. The good separation performance of PIMs originates from their rigid backbone, which has no rotational freedom, combined with spiro-centres at well-defined intervals that contort the polymer backbone (Figure 6a and b). The resulting inflexible polymers with a ‘kinked’ backbone have large amounts of free volume, which is reflected in high BET surfaces of 700-900 m<sup>2</sup>g<sup>-1</sup>[1,6,48]. Their microporous structure together with the presence of polar groups results in the high solubilities of gasses in PIMs compared to other polymer materials. Therefore, their high permeability originates from a combined high gas solubility and diffusivity[1,6,48]. The sorption behavior of most gasses in PIMs is similar, resulting in a modest solubility selectivity. The observed selectivity of the PIMs is thus mainly attributed to differences in gas molecule diffusivities[1,6,48]. Various other PIMS with different functionalities and have been synthesized, with some surpassing the 2008 Robeson upper bound[1,49]. Another advantage of this class of polymers is that they dissolve well in organic solvents which makes them easily processable in thin films[1,50]. However a major setback is their high susceptibility to physical aging and plasticization[1,50,51].

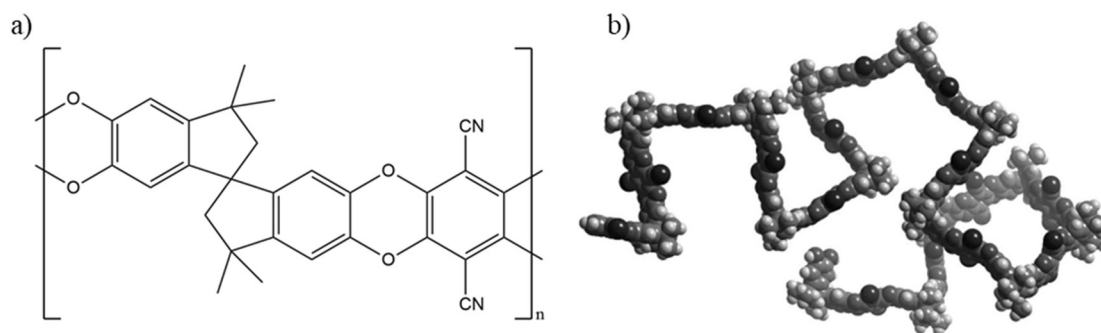


Figure 6: a) Chemical structure of PIM-1. copied from ref. [48]. b) Molecular model of a fragment of PIM-1 showing its rigid, contorted structure. Copied from ref. [48].

### *Thermally rearranged polymers*

Polybenzoxazoles (PBO) are another interesting class of materials for CO<sub>2</sub> gas separation due to their stiff ring units in a flat configuration which pack efficiently[1,6,52]. However due to their low solubility in common solvents the processing of these polymers in membranes for gas separations proved to be difficult. Park *et al.* circumvented the solubility problem by a post-synthetic treatment of easily processable imide membranes[1,6,52]. Their thermally rearranged (TR) polymers were formed by subjecting an aromatic polyimide precursor containing an ortho-positioned functional hydroxyl group to a high temperature treatment (350-450 °C). Due to the high temperature of the synthesis, a decarboxylation reaction takes place between the phthalic imide moiety and functionalized phenylene ring and PBO are formed. TR-1 showed CO<sub>2</sub> and CH<sub>4</sub> gas separation performances above the 1991 Robeson upper-bound. The chemical structure of TR-1 can be found in Figure 7 and its gas separation data are noted in Table 4[52]. The exceptional performance of PBO is a result of the rigid benzoxazole phenylene ring structure prevents torsional rotations between individual phenylene-heterocyclic rings and increases the cavity formation and stability[6,52]. Park *et al.* investigated the free volume of TR-1 with Positronium annihilation lifetime spectroscopy (PALS) and discovered that the amount of free volume elements present increases and their size distribution narrowed compared to the untreated polymer, resulting in superior gas separation performance of TR polymers. Upon increasing the treatment temperature, the size of the free volume elements increased concurrent with a decrease in their quantity. When temperatures were increased even further (450 °C), the free volume elements coalesce, forming hourglass shaped cavities. The small necks offer size selectivity whereas the large cavities contribute to the high gas permeabilities[6,52]. Surprisingly, TR polymers show high CO<sub>2</sub> permeabilities and selectivities in comparison to other size-sieving polymers, which generally show high selectivities combined with low permeabilities[52]. The high PBO permeabilities are mainly attributed to high diffusion coefficients, however solubility does increase as well upon thermal rearrangement[6,53]. Additionally, the TR membranes have shown excellent resistance to CO<sub>2</sub> induced plasticization[52]. Their gas separation can be improved by adding small acidic dopants to the TR, which can interact with the basic nitrogen atoms of the benzoxazole ring and successfully increase the CO<sub>2</sub>/CH<sub>4</sub> selectivity at the expense of permeability[52]. Although the TR polymers show excellent gas separation properties some face difficulties with mechanical properties due to overlap of the thermal degradation region and PBO formation region of the polymer[6]. Additional research towards commercially available precursors and physical properties such as physical aging of these interesting polymers is thus still required[6].

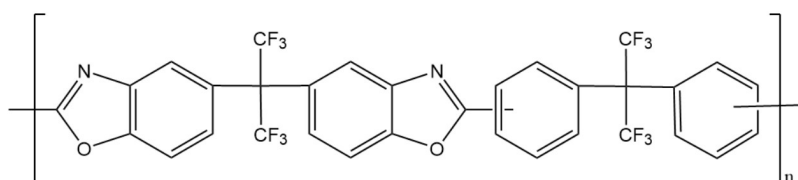


Figure 7: Chemical structure of TR-1. Copied from ref. [52].

### Block copolymers

Block copolymers consist of nanometer-sized repeating units of different homopolymers, covalently linked together. Due to the different chemical properties of the homopolymers, block copolymers tend to organize in ordered nanostructures, combining properties of different polymer materials, which makes these polymers interesting for polymeric gas separation membranes[54]. Generally rubbery segments provide high permeability whereas glassy parts provide mechanical strength and plasticization resistance[1,54]. A wide range of possible homopolymer combinations can be used, as well as a wide range of nanostructures[54]. A block copolymer of particular interest for CO<sub>2</sub> gas separations is PEBA, consisting of polyamide and polyether segments. It is commercially available as PEBAX®[55,56]. These membranes show good selectivities for separations of quadrupolar compounds from non-polar compounds (CO<sub>2</sub>/N<sub>2</sub> and CO<sub>2</sub>/H<sub>2</sub> separations). Their good separation performance for these separations results from a high solubility selectivity. Sorption and permeation results obtained by Bondar *et al.* showed that gas transport mainly occurs through the rubbery polyether phase, which strongly interacts with CO<sub>2</sub>. The hard polyamide blocks mainly contribute to the mechanical properties of the polymer[55,56]. The chemical structure of PEBAX® MH1657 can be found in Figure 8. Its separation performance can be found in Table 4[55]. A commercial gas separation membrane, which is hypothesized to have a similar structure to PEBAX® structure is the Polaris® membrane produced by MTR[57]. Another commercially available block copolymer investigated in CO<sub>2</sub> separations is the Polyactive™ membrane consisting of butylene terephthalate and ethylene oxide[54,58,59].

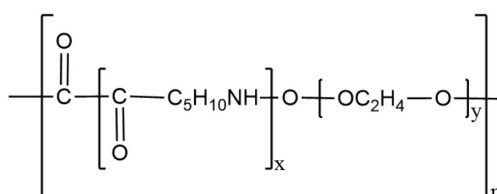


Figure 8: Chemical structure of PEBAX® MH1657 with  $x$  the percentage of polyamide and  $y$  the percentage of polyether segments. Copied from ref. [60].

Table 4: Permeability (Barrer) and selectivity of some polymeric membranes studied for CO<sub>2</sub>/CH<sub>4</sub> gas separations. Data used from ref. [32,38,39,45,48,52,61,62].

Polymer	Permeability (Barrer)		Selectivity ( $\alpha$ )	Reference
	CO <sub>2</sub>	CH <sub>4</sub>	CO <sub>2</sub> /CH <sub>4</sub>	
Cellulose acetate	6.3	0.21	30.0	Chen <i>et al.</i> [61]
Matrimid®	6.5	0.19	34.0	Chen <i>et al.</i> [61]
P84®	1.2	0.02	50.0	Chen <i>et al.</i> [61]
Bisphenol-A-Polysulfone	5.6	0.25	22.4	Chen <i>et al.</i> [61]
Tetramethyl bisphenol-A polysulfone	21	0.95	22.0	Jeon <i>et al.</i> [32]
6FDA-DAM	370	17.6	21.0	Chen <i>et al.</i> [61]
6FDA-DABA	12.8	0.2	62.2	Qiu <i>et al.</i> [39]
6FDA-DABA (ethylene glycol crosslinked)	10.4	0.12	87.0	Staudt-Bickel <i>et al.</i> [38]
Celazole®	0.025	0.005	5.0	Li <i>et al.</i> [45]
PIM-1	2300	125	18.4	Budd <i>et al.</i> [48]
TR-1-450	1610	25.83	60	Park <i>et al.</i> [52]
PEBAX® MH-1657	70.1	4.1	17.2	Meshkat <i>et al.</i> [62]

#### 2.2.4.2 Mass transport in polymeric membranes

Throughout the history of membrane separations different models have been developed to describe mass transport through membranes[21]. Until the mid-1940's, the most popular model was the pore flow model. This model considers a convective, pressure-driven flow of permeants through pores in the membrane. Selectivity arises from the inability of certain species to pass through the membrane pores[21]. In the 1940's, the SD model was used to describe transport of gasses through polymeric membranes. The use of the SD model was by 1980 extended to describing reverse osmosis processes and pervaporation[21].

##### 2.2.4.2.1 Solution-diffusion model

Gas transport in polymeric membranes is generally described using the SD model. The model presumes gas molecules dissolve from the gas phase into the membrane, subsequently diffuse through the membrane and desorb at the permeate side of the membrane. A gradient in chemical potential between the high pressure feed side and the low pressure permeate side of the membrane drives this three step process. The model allows to compose a set of empiric rules to describe the relationship between the nature of a polymer and its transport properties[21].

The permeability of a gas in a specific membrane is expressed as the product of its diffusivity and solubility (equation 9). The solubility of a gas describes the relationship between the concentration of the gas in the fluid phase to the concentration of the gas in the membrane. It can be seen as the affinity of the gas for the polymer phase[21]. Diffusivity describes the effect of the chemical environment and the molecular motions of the permeating gas on the kinetics of gas transport[21].

$$P = DS \quad (9)$$

Where P represents the permeability (Barrer), D the diffusion coefficient ( $cm^2/s$ ) and S the solubility coefficient ( $cm^3(STP)/cm^3cmHg$ ).

High gas permeabilities are thus achieved by a high diffusion coefficient, a high solubility coefficient or a combination of both. The solubility and diffusivity of a gas are defined by the gas-polymer system[21]. Some examples of molecules with high D values are hydrogen and helium as a result of their small size. CO<sub>2</sub> is an example of a gas with a relatively high solubility coefficient, originating from its strong quadrupolar interactions. Water shows a high solubility, in hydrophilic polymers, combined with a small molecular diameter resulting in a high diffusivity coefficient and thus generally has high permeability values[21].

#### 2.2.4.2.2 Free volume theory

Knowledge of the relation between the structure of polymers and their permeation properties is essential to design or select the most suitable membrane for a certain application[21]. No quantitative structure-property relation has yet been found, however different theories allow to rationalize variation in permeation properties for structurally related polymers[21]. The most commonly used theory for gas separations is the free volume theory. Free volume can be considered the sum of all volume elements in between the polymer chains resulting from non-ideal packing[21]. It is often expressed as the fractional free volume (FFV), defined as[21]:

$$FFV = \frac{v - v_0}{v} \quad (10)$$

Where v is the specific volume of the polymer ( $cm^3/g$ ) and  $v_0$  ( $cm^3/g$ ) the volume occupied by the polymer molecules at 0 K[21].

Two types of free volume are generally considered: interstitial or equilibrium free volume and frozen or excess free volume[21,24]. The distinction between both types arises from the two temperature dependent states of a polymer: the glassy and rubbery state. Several physical properties of a membrane (specific volume, tensile modulus, specific heat, refractive index and permeability) are dependent on the polymer state. The glass transition temperature ( $T_g$ ) is defined as the transition temperature where these physical properties of a membrane and thus its state change[24]. For example, the change of polymer free volume as a function of temperature is represented in Figure 9[21]. For temperatures above  $T_g$  the polymer is in its rubbery state. At the molecular level, the polymer molecules have enough energy to allow rotations of the polymer chain around its backbone. If the temperature is reduced below  $T_g$  the

polymer enters its glassy state and now lacks sufficient energy to allow backbone rotation. However, rotations of sidechains can still occur[21,24]. In both glassy and rubbery state, the polymer has interstitial free volume, resulting from unoccupied spaces within the polymer matrix due to constant thermal motion of the polymer chain segments. This equilibrium free volume increases and decreases with temperature due to an increase or decrease in polymer chain mobility[21,24]. Upon transition from the rubbery to glassy state, a part of the free volume from the rubbery state will be kinetically frozen, i.e. no longer able to disappear due to the lack of backbone mobility. Consequently, two types of free volume (e.g. equilibrium free volume and excess free volume) are present in polymers in their glassy state. This phenomenon explains the discontinuity observed at the  $T_g$  in Figure 9. Due to the excess free volume, the specific volume decreases slower than would be expected when the temperature is reduced further below  $T_g$ [21,24]. Both types of free volume will help rationalize the differences in membrane separation properties of different materials.

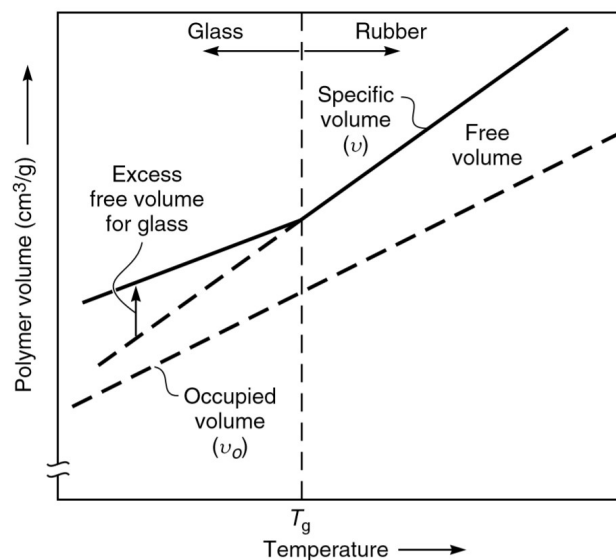


Figure 9: Polymer free volume plotted against temperature. The occupied volume ( $v_0$ ) represents the volume occupied by the polymer chains. The difference between this volume and the specific volume ( $v$ ) of the polymer represents the free volume within the polymer matrix.  $T_g$  represents the glass transition temperature of the polymer. Copied from ref. [21].

### Solubility

Figure 10 shows the sorption and diffusivity coefficients of various gasses in a group of polymers from the same family. Whereas differences in gas diffusion coefficients for a certain gas in various polymers can be orders of magnitude, solubility coefficients tend to vary maximally with a factor 10[21]. The gas solubility (sorption) coefficient is defined as the pressure normalized amount of gas adsorbed in the polymer matrix.

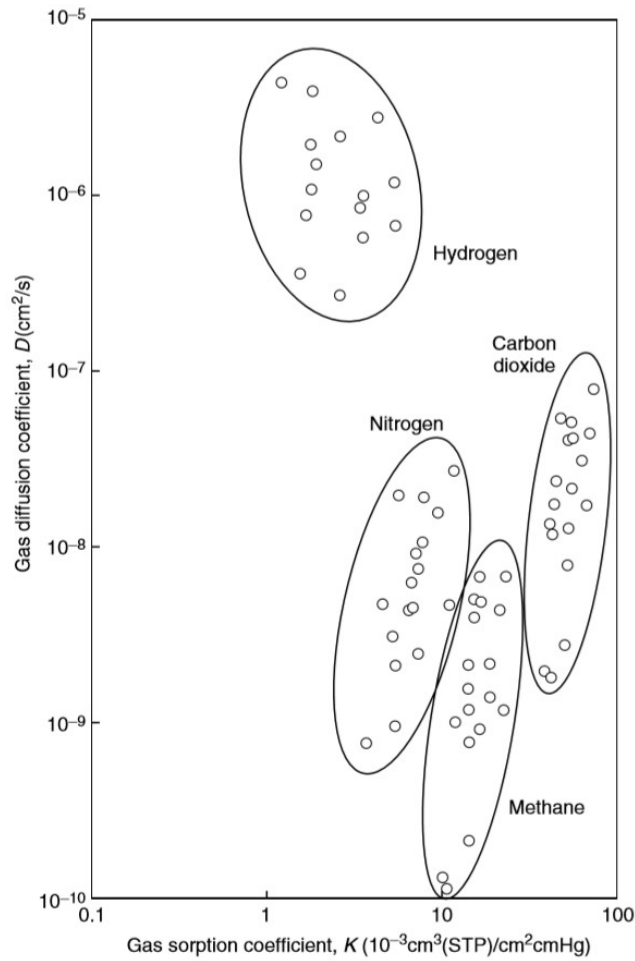


Figure 10: Solubility and diffusion coefficients for various gasses in a group of polymers from the same family. Copied from refs. [21,63].

Gases have relatively constant sorption coefficients because sorption in polymers behaves like sorption of a gas in an ideal fluid. Therefore sorption of gasses in an ideal polymer can be described with Henry's law[21,24,64]:

$$c = K_D p \quad (11)$$

With  $c$  the amount of gas adsorbed in the polymer ( $\text{cm}^3(\text{STP})/\text{cm}^3$ ),  $K_D$  ( $\text{cm}^3(\text{STP})/\text{cm}^3 \cdot \text{cmHg}$ ) the Henry constant and  $p$  ( $\text{cmHg}$ ) the pressure of the gas. As a result, the gas sorption coefficient is in this ideal case equal to the Henry constant.

Equation 11 can be used to describe gas adsorption in rubbery polymers. However, glassy polymers deviate from this ideal behavior, therefore the dual-sorption model was proposed by Barrer *et al.* to describe solubility of gasses in glassy polymers[21]. The dual-sorption model describes sorption in two distinct sites: gas sorption by dissolving gas molecules in the polymer matrix (equilibrium free volume) and gas sorption in excess free volume[21,26]. The first form of sorption occurs in both glassy and rubbery polymers and can be described by using Henry's

law for gas sorption, analogous to equation 11. The second form only occurs in glassy polymers and is described using the Langmuir model of gas sorption[21,26]. The amount of gas molecules absorbed increases with increasing pressure as is shown in Figure 11. At the saturation sorption concentration ( $c'_H$ ), all of the excess volume is filled and only the first form of gas sorption will contribute to the total amount of gas adsorbed. As a result,  $c'_H$  can be seen as a measure of the amount of non-equilibrium free volume[21,26,65]. The total amount of gas adsorbed ( $c$  ( $\text{cm}^3(\text{STP})/\text{cm}^3$ )) can be expressed as:

$$c = c_{\text{Henry}} + c_{\text{Langmuir}} = K_D p + \frac{c'_H b p}{1 + b p} \quad (12)$$

Where  $c_{\text{Henry}}$  ( $\text{cm}^3(\text{STP})/\text{cm}^3$ ) and  $c_{\text{Langmuir}}$  ( $\text{cm}^3(\text{STP})/\text{cm}^3$ ) represent the amount of gas adsorbed in the Henry and Langmuir sites respectively and  $K_D$  ( $\text{cm}^3(\text{STP})/\text{cm}^3 \cdot \text{cmHg}$ ),  $c'_H$  ( $\text{cm}^3(\text{STP})/\text{cm}^3$ ) and  $b$  ( $\text{cmHg}^{-1}$ ), respectively the Henry constant, the saturation adsorption concentration of the excess free volume and the Langmuir constant and. Finally  $p$  ( $\text{cmHg}$ ) represents the pressure.  $K_D$  and  $b$  are temperature dependent and are both correlated with the pure gas condensability. The dual-sorption model provides a good fit with experimental data, however, as it has no molecular foundation it cannot be used to make predictions without measurement data[21,26].

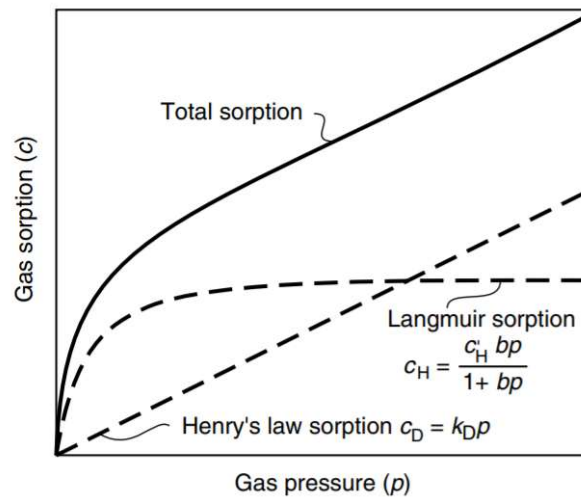


Figure 11: Illustration of the dual-sorption model discerning between both Langmuir and Henry absorption behavior and their contribution to total sorption for different gas pressures. Copied from ref. [21].

### Diffusivity

Diffusion coefficients of different gasses in a membrane can vary several orders of magnitude[21]. A quantitative link between the structure of a polymer and the permeation properties of a certain gas in that polymer has not yet been found[21]. However a semi-empirical approach using free volume theory makes it possible to rationalize a relationship

between differences in diffusivity for a gas diffusing through different membranes and between different gasses diffusing through a certain membrane and the polymer structure[21]. Diffusion rates of molecules are determined by the local environment of the diffusing molecule. Gas molecules move through a membrane by migrating through gaps in between the polymer chains. Due to thermal motion, these cavities constantly close and open. The diffusing molecule can only migrate further down its driving force gradient when polymer segmental motion moves the polymer in such a way that a large enough cavity is formed for the diffusing molecule[21]. This can be seen in Figure 12, which simulates the movement of a carbon dioxide molecule in a polyimide membrane in function of time using molecular dynamics. Initially, the CO<sub>2</sub> molecule moves around in the cavity, unable to migrate to a next cavity. After 100 picoseconds the collective motion of the surrounding polymer chains allows it to move to the next cavity where it is again entrapped[21].

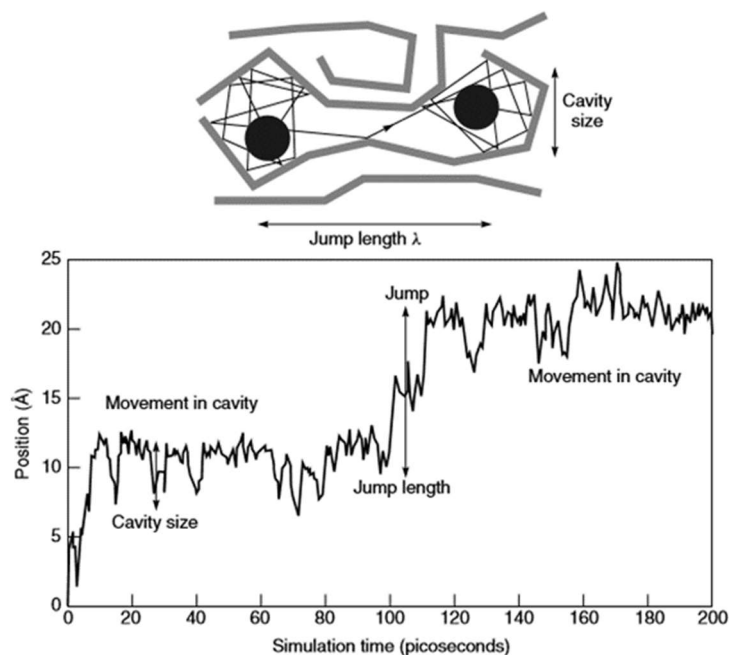


Figure 12: Simulation of diffusion of a CO<sub>2</sub> molecule in a 6FDA-4PDA polymer matrix showing the molecules jump from cavity to cavity. Copied from ref. [21,66].

Figure 13a shows the diffusion coefficients of dichloroethane in an ethyl cellulose polymer in function of the volume fraction of dichloroethane dissolved in the polymer matrix. Due to an increase in the volume fraction of dissolved dichloroethane, the polymer goes from a glassy to a rubbery and finally polymer gel state[21]. The polymer shows notably higher diffusion coefficients in a rubbery state. This is explained by the higher mobility of polymer chains in a rubbery material. As a result, these materials do not only have more free volume, but also a higher probability of a collective motion of the polymer chains surrounding the diffusing species allowing it to move to a next cavity[21,26]. On the other hand, in a glassy state the

polymer is more rigid. The polymer chains in this case cannot rotate freely and consequently, achieving the required collective motion of the chains is less likely. This results in generally lower diffusion coefficients for glassy polymers. Diffusion coefficients in both glassy and rubbery polymers increase with temperature due to the rise in thermal energy and thus a rise in polymer flexibility, including possible sidechain rotations[21,26].

If less free volume elements are present the diffusion coefficient will generally decrease[21,26]. Figure 13b shows how differences in polymer FFV influence gas diffusion coefficients. Parameters influencing the FFV such as side chain length and rigidity, polymer-polymer interactions and polymer stacking influence the diffusion coefficient as well, together with properties of the diffusing molecule[21,26]. Generally, larger molecules have smaller diffusion coefficients. This arises from a smaller amount of free volume elements large enough to house these molecules and a smaller chance of a collective motion of the polymer chains allowing the molecule to diffuse[26].

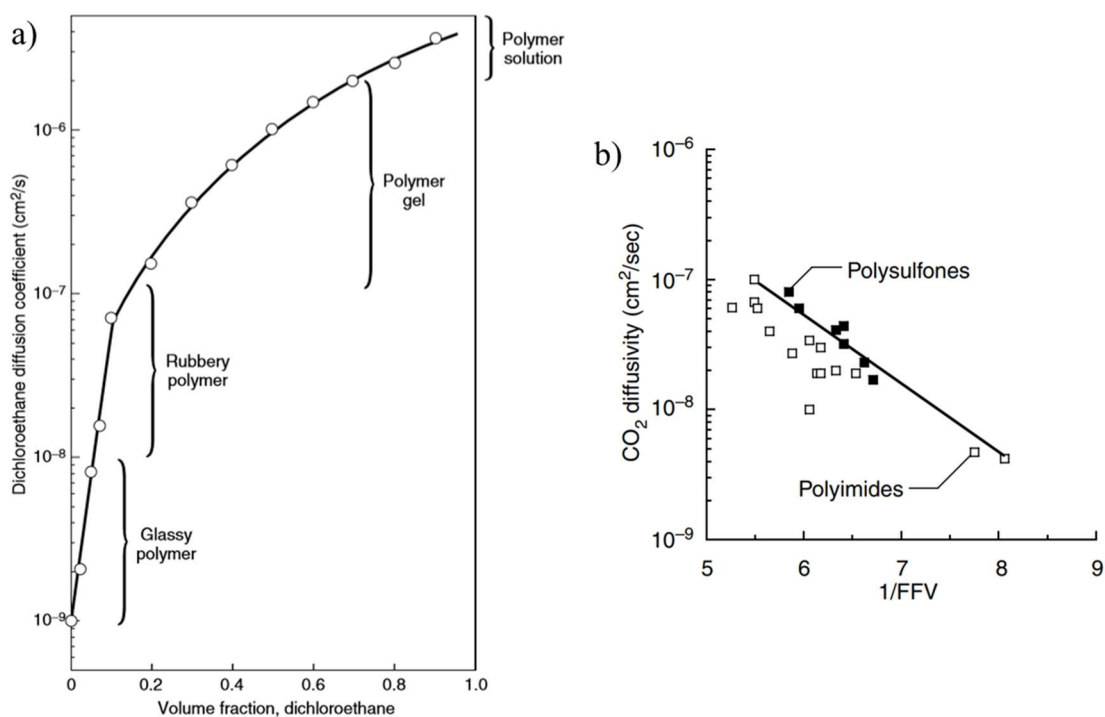


Figure 13: a) Dependence of the dichloroethane diffusion coefficient on the volume fraction of dichloroethane in the polymer matrix. Copied from ref. [21,67]. b) Influence of FFV of various polymers on the CO<sub>2</sub> diffusion coefficients. Copied from ref. [26].

### 2.2.4.3 Challenges of polymeric membranes

#### 2.2.4.3.1 Permeability/Selectivity trade-off

In membrane technology, there is a continuous striving to create membranes with higher permeabilities and selectivities. However, during the screening of possible membrane materials, it was noticed that an increase in membrane permeability was often accompanied by a lower

selectivity for a certain separation and vice versa. This permeability/selectivity trade-off behavior was first reported by Robeson in 1991[1,6,26,68–70]. Using extensive literature data available at that time, he defined the empirical upper bound for multiple gas separations. Figure 14 shows the CO<sub>2</sub>/CH<sub>4</sub> upper bound. Further developments in membrane research led to revision of the upper bound in 2008. The upper bound shifted upwards, but the trade-off relationship between permeability and selectivity remained relatively constant[1,6,26,68–70]. The upper bound is mainly defined by glassy polymers, because they have larger solubility coefficients than their rubbery counterparts when membranes with similar permeabilities are compared. The higher solubility is a result of the excess free volume in glassy polymers[64,70].

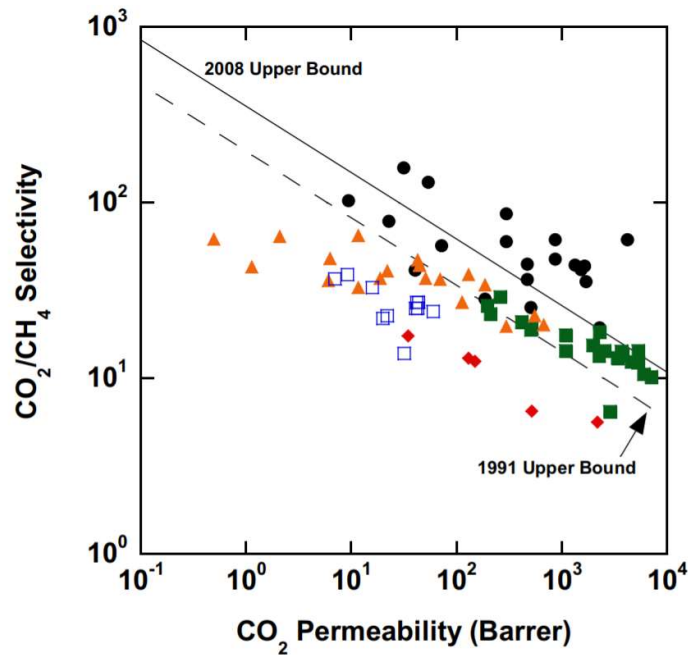


Figure 14: CO<sub>2</sub>/CH<sub>4</sub> gas separation performance of various classes of polymer materials reported in literature together with the 1991 and 2008 Robeson upper bound. TR polymers (black), PIMs (green), Perfluoropolymers (red), polyimides (yellow) and poly-room temperature ionic liquids (blue). Copied from ref. [6].

The upper bound follows a mathematic relationship:

$$\alpha_{ij} = \beta_{ij} P_i^{-\gamma_{ij}} \quad (13)$$

The subscripts i and j stand respectively for gas i and gas j.  $\beta_{ij}$  and  $\gamma_{ij}$  are parameters depending on the gas pair. These constants can be linked to the physical properties of the membrane and the permeating gasses. The parameter  $\gamma_{ij}$  depends on the ratio of the gas molecules kinetic diameters.  $\beta_{ij}$  depends on  $\gamma_{ij}$ , gas solubility and a constant which relates to the average distance between polymer chains and chain stiffness[26,70].

The free volume theory can help interpret the permeability/selectivity trade-off[26,70]. For example, to increase the permeability of a polymeric membrane either the diffusion coefficient

or the solubility coefficient can be increased. Since the diffusion coefficient varies over a larger range than the solubility coefficient, it is often considered to increase permeability. In order to increase this diffusion coefficient, the amount of free volume present in the polymer has to increase. Increasing the free volume is generally linked to a reduction in diffusivity selectivity due to the presence of larger free volume elements and a broader free volume element size distribution. As a result, by increasing the free volume, the permeability increases due to an increase in diffusivity and the overall selectivity is reduced due to the loss of diffusivity selectivity. Therefore, coupling an increase in free volume to a narrower free volume size distribution could allow to surpass the upper bound[26,70].

#### 2.2.4.3.2 *Plasticization*

Plasticization occurs when large concentrations of a highly condensable gas (such as CO<sub>2</sub>, water and hydrocarbon and other organic vapors) are adsorbed in the polymer matrix. The adsorbed gas will disrupt the polymer packing, resulting in a swollen polymer matrix. This is shown in Figure 15a[1,71–74]. Swelling increases segmental mobility of polymer chains and therefore free volume. The increase in polymer chain mobility can be seen as an artificial reduction of the T<sub>g</sub> of the polymer material. The polymer will behave as if it is in its rubbery state at temperatures below its T<sub>g</sub>. For rubbery as well as glassy polymers, the increase in free volume results in an increase of the diffusion coefficient and permeability of all components in the gas mixture[1,71–74]. For glassy polymers exhibiting some form of size selectivity, the increase in diffusion coefficients for all permeating components results in a concomitant loss in selectivity. Rubbery polymers generally suffer less from selectivity losses due to plasticization, because they mostly discriminate between different gasses based upon differences in solubility[1,71–74]. Plasticization is dependent on the condensation temperature of the solvable component, the partial pressure of this component in the feed mixture and the duration of exposure as well as the thickness and treatment/operation history of the membrane[75]. The susceptibility of a membrane towards plasticization is generally expressed using the plasticization pressure. This is the pressure at which permeability of glassy polymers starts to increase with increasing pressure[73]. The pressure permeation behavior of an exemplary glassy and rubbery polymer is shown in Figure 15b. The initial decrease in CO<sub>2</sub> permeability for the glassy polymer is due to saturation of the frozen free volume elements. At higher pressures the permeability increase due to plasticization overpowers the permeability decrease due to saturation. Different methods have been developed to reduce plasticization in gas separation membranes, such as crosslinking, thermal treatment and adding plasticization reducing additives[73].

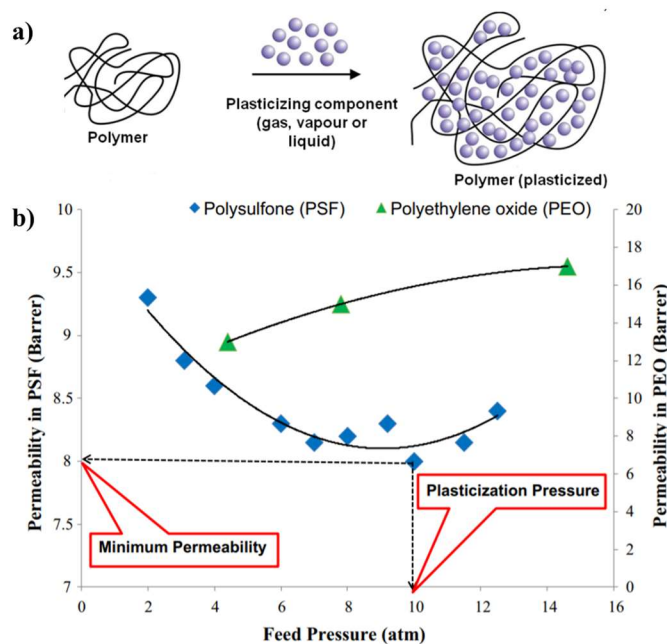


Figure 15: a) Visualization of polymer plasticization resulting in a swollen polymer matrix. Adapted from ref. [76] b) Effect of CO<sub>2</sub> feed pressure on CO<sub>2</sub> permeability in a glassy polymer (Polysulfone) and a rubbery polymer (Polyethylene oxide, PEO). Copied from ref. [72].

### 2.2.4.3.3 Physical aging

Glassy polymers can be considered to be intrinsically non-equilibrium materials below their  $T_g$ [1,72,77,78]. Their polymer chains lack sufficient free energy to allow backbone rotations and reach their thermodynamically most favorable packing. As mentioned before, the free volume associated with this phenomenon is called excess or frozen free volume and it is essential to increase gas diffusion coefficients and as a result permeability in glassy polymers. Over time, a gradual rearrangement of polymer chains towards their equilibrium packing occurs, resulting in a loss of excess free volume[1,72,77,78]. This process is called physical aging and makes membrane performance time-dependent. The time dependency of CH<sub>4</sub> permeability through Matrimid membranes of varying thickness is shown in Figure 16. In this figure a clear decrease in permeability is observed over time[1]. Diffusion of free volume elements towards the surface of the membrane has been suggested to cause the physical aging phenomenon[78]. Throughout the rearrangement free volume elements gradually shift towards the membrane surface and ‘disappear’ when they eventually reach it. The thickness of the membrane influences the diffusion of the free volume elements with thinner membranes aging faster[78]. The rate of physical aging depends on the polymer type, the conditions during polymer synthesis and the post-synthesis treatment of the membrane (temperature of annealing, annealing time) as well as the temperature of the membrane during the aging process[1,77,79]. Physical aging can be reduced by blending polymers, crosslinking them or blending polymers with nanomaterials[80].

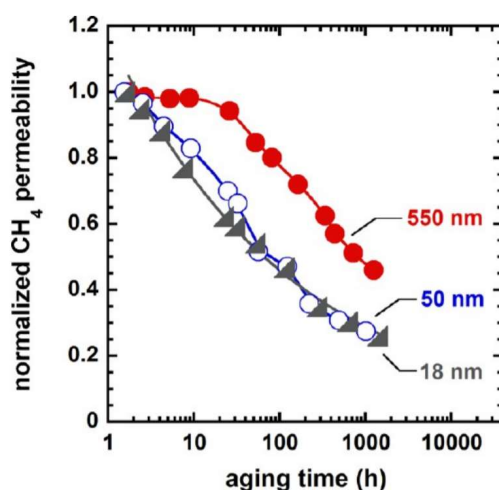


Figure 16: Effect of physical aging on the normalized  $CH_4$  permeability ( $P/P_0$ ) for Matrimid membranes of varying thickness. Copied from ref. [1].

### 2.2.5 Mixed matrix membranes

To be able to compete with other separation technologies, certain minimum requirements for membrane performance (selectivity and permeability) can be defined for each gas separation[1]. These requirements are shown for different commercial important gas separations in Table 5. The economically interesting region is often situated at permeability-selectivity combinations far past the upper bound limits defined for conventional polymeric membranes[1,81,82]. A series of new approaches have been proposed over the past years to surpass the upper bound, amongst others the use of new polymer materials (such as fluorinated polyimides, polybenzimidazoles, PIMs, TRs and block copolymers), facilitated transport membranes, inorganic membranes and mixed matrix membranes (MMM). For a more concise discussion on innovative polymer chemistries and inorganic membranes, extensive reviews can be found in open literature[1,29,70,83–85]. In the following section, MMM and their application potential for gas separations will be discussed in more detail.

Table 5: Performance requirements for gas separation membranes to be an economically feasible alternative to conventional gas separation technologies. Copied from ref. [1].

Application	Gas separation	Selectivity	Permeance (GPU)	Comments
CO <sub>2</sub> removal from natural gas	CO <sub>2</sub> /CH <sub>4</sub>	20–30	>100	already an established membrane application; goal would be to capture a portion of the much larger amine absorption market
olefin/paraffin separation	C <sub>2</sub> H <sub>4</sub> /C <sub>2</sub> H <sub>6</sub>	>5	>50	near-term market is reactor purge streams; larger application is processing steam cracker gas or fluid catalytic cracking unit (FCCU) off-gas
	C <sub>3</sub> H <sub>6</sub> /C <sub>3</sub> H <sub>8</sub>			
CO <sub>2</sub> capture	CO <sub>2</sub> /N <sub>2</sub>	30–50	1000–5000	CO <sub>2</sub> capture from power and industrial exhaust gases
	H <sub>2</sub> /CO <sub>2</sub>	>10	>200	syngas separations, coal or gas-to-chemical applications
	CO <sub>2</sub> /H <sub>2</sub>	>20		
vapor/vapor	H <sub>2</sub> O/ethanol, H <sub>2</sub> O/2-propanol	50–100	1000–3000	solvent dehydration, has to be done as a high temperature vapor to be commercially significant
	aromatic/aliphatic, polar/nonpolar	>10	>500	vapor/vapor separation to reduce cost and energy consumption of distillation

### 2.2.5.1 Introduction

MMM are hybrid membranes that combine the advantages of inorganic materials and polymeric membranes in order to increase membrane selectivity, permeability or both[1,86,87]. A schematic representation of such a MMM is shown in Figure 17. On the one hand, inorganic particles (e.g. zeolites, MOFs, carbon nanotubes,...) have well defined pore sizes, shapes and geometries, which allow them to effectively separate molecules based on diffusion selectivity[1,86,87]. They may also have specific chemical functionalities not present in conventional polymer membranes, allowing them to enhance solubility selectivity[1,86,87]. Furthermore, filler materials such as MOFs can be chemically tuned towards a certain application[88–90]. On the other hand, pure inorganic membranes are costly and often fragile and hard to produce in defect-free films[1,86]. Therefore, combining these materials with cheap and easy-to-process polymers can theoretically result in flexible hybrid membranes with enhanced separation performance[1,86].

One of the first reports on MMM date from the 1970's. Paul and Kemp reported a large increase in diffusion time lag of CO<sub>2</sub> and CH<sub>4</sub> in a zeolite 5A filled PDMS membrane[86,87,91]. Kulprathipanja *et al.* observed for the first time an enhanced gas separation performance of MMM compared to the pure polymer. They reported an increased O<sub>2</sub>/N<sub>2</sub> selectivity when silicalite was added to a CA matrix[86,87]. In the 1980's, more reports on enhanced separation properties of MMM with respect to their polymeric counterparts followed[86]. Since then, various porous materials such as zeolites, mesoporous silica, carbon molecular sieves (CMS), carbon nanotubes, carbon nanofibers, graphene-oxide and MOFs have been added to various polymers in order to enhance their separation performance[92].

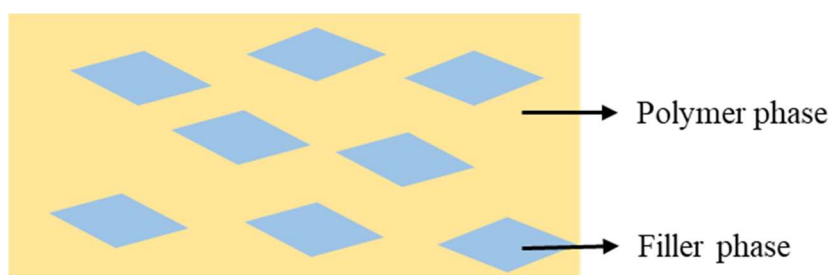


Figure 17: Illustration of a mixed matrix membrane.

### 2.2.5.2 Mass transport in MMM

In order to describe mass transport in MMM, a model combining mass transport in polymers and in the inorganic phase is required. Mass transport in the inorganic phase as well as in the mixed matrix membrane can be described using the previously discussed SD model[82,93].

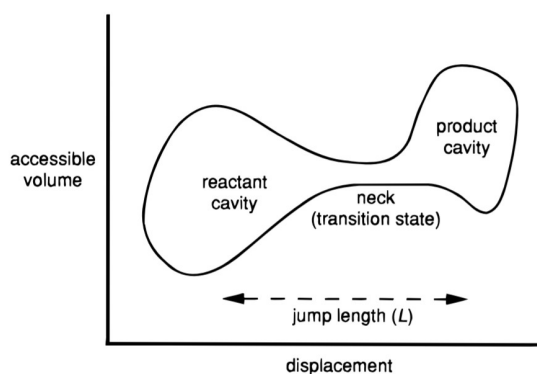


Figure 18: Visualization of the volume accessible to a permeating component in the transition state theory. When the permeant moves to another cavity it has to pass through a neck with a noticeably smaller accessible volume. Copied from ref. [94].

Diffusion selectivity in the inorganic fillers and the polymer matrix can be described by using the transition state theory of diffusion. According to this model, permeating components move through the polymer matrix by hopping from cavity to cavity through necks connecting these cavities (Figure 18)[81,94]. Energy is required to form the transition state in which the molecule can pass through the neck. While in its transition state, the molecule might lose some degrees of freedom with respect to its normal state. This is a result of the restrictions in movement imposed by the width and shape of the neck connecting both cavities. This loss of degrees of freedom corresponds to a loss in entropy and has to be compensated by an additional energy input into the molecule. Therefore, as more degrees of freedom are lost in the molecular transition state, it will become increasingly harder for it to diffuse. Finally, if the distance of the jump increases, it becomes more difficult to bridge the neck[81,94,95]. Using the transition state theory of diffusion, diffusion selectivity between two components can be expressed using the following formula[95]:

$$\frac{D_A}{D_B} = \left[ \frac{\lambda_A^2}{\lambda_B^2} \right] \exp(\Delta S_{D(A,B)}^*) \exp\left(-\frac{\Delta H_{D(A,B)}^*}{RT}\right) \quad (14)$$

Where the jump lengths of components A and B are represented respectively by  $\lambda_A$  and  $\lambda_B$ ,  $\Delta S_{D(A,B)}^*$  and  $\Delta H_{D(A,B)}^*$  are the differences between the diffusion transition state entropy and enthalpy of components A and B, R is the gas constant and T the temperature.

Transition state theory allows to interpret the size sieving properties of molecular sieves[95]. Due to their rigid and well-defined pores, molecular sieves have excellent diffusion selectivity. For example, when  $O_2$  and  $N_2$  are both permeating through a molecular sieve, the entropic selectivity will cause  $N_2$  to permeate slower.  $N_2$  is larger than  $O_2$  and therefore has some rotational and vibrational motions which will be suppressed in the transition state.  $O_2$  does not

experience this loss of degrees of freedom and therefore entropic selectivity favors O<sub>2</sub>. In flexible polymer chains (i.e. conventional glassy and rubbery polymers), there is a range of ‘pore apertures’[95]. Different free volume elements of varying sizes coexist and thermal motion of the polymer chain or side groups constantly reforms the void geometry. In these flexible materials, transition states generally do not experience hindered rotational and vibration degrees of freedom. Size selectivity in these membranes originates from the difference in transition state activation enthalpy, the energy required to shape a neck large enough to allow the permeating components to migrate to the next free volume element. Large enough necks are more readily formed for smaller permeating components[95]. Semi-rigid polymers (PIM and TRs) are situated somewhere in between the molecular sieves and flexible polymers and offer some degree of entropic selectivity. However, their structure still has some thermal mobility, which limits their entropic selectivity. The three cases are illustrated in Figure 19[95].

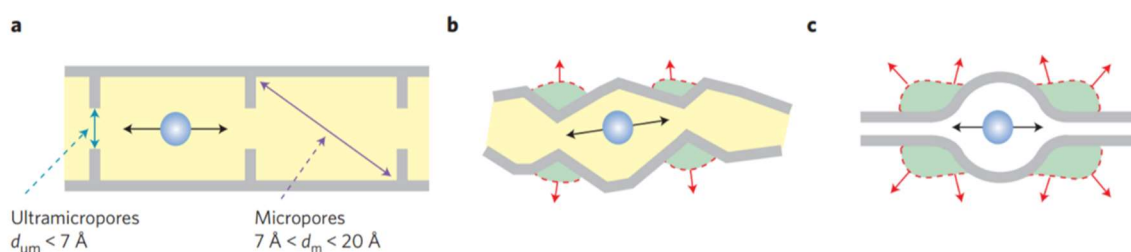


Figure 19: a) molecular sieve with rigid (ultra-) micropores. b) semi-rigid polymer containing permanent porosity and flexible zones. c) flexible polymer with varying gap size due to segmental packing and motion. In all figures the yellow areas represent permanent porosity and the green areas mobile segments, able to create voids necessary for diffusion. Copied from ref. [95].

MMM combine the properties of the inorganic phase and polymer matrix. Therefore, molecules permeating through such membranes can pass through two different phases. Two models have been proposed for describing permeation through MMM: the continuous and discontinuous model[82]. In the continuous model, the filler phase is considered continuous and the permeating component can permeate from the high pressure side to the low pressure side of the membrane without having to enter the polymer phase[82]. In the discontinuous model, permeating molecules move through the polymer matrix as well as the filler particles. Both models are shown in Figure 20[82]. Membrane performance of membranes for the continuous model is better, however, forming MMM with a high enough filler loading in order to achieve this proves to be difficult. As a result, mostly the discontinuous model is applied to MMM[82]. The Maxwell equation relates the MMM permeability to the permeability of the polymer, the permeability of the filler and the volume fraction of the filler in the MMM[1,87,93,95,96]. The equation assumes that the flow through the MMM follows the discontinuous model. Consequently, it is only applicable to low filler volume fractions. Moreover, it does not account

for the different forms of particle-matrix interfaces commonly found in MMM, which will be discussed in the next section. The model assumes perfect contact between the polymer matrix and filler particles[1,87,93,95,96].

$$P_{MMM} = P_c \left[ \frac{nP_d + (1 - n)P_c - (1 - n)\Phi_d(P_c - P_d)}{nP_d + (1 - n)P_c + n\Phi_d(P_c - P_d)} \right] \quad (15)$$

With  $P_{MMM}$ ,  $P_c$  and  $P_d$  the permeability of the mixed matrix membrane, the permeability of the continuous phase and the permeability of the discontinuous phase,  $\Phi_d$  the volume fraction of the filler and  $n$  a shape factor dependent on the geometry of the filler particles.

The Maxwell equation is often used to back-calculate the permeability of a certain filler from a measured MMM permeability since measuring pure filler permeabilities experimentally is often difficult[1,87,93,95,96]. Various other models have been developed for describing transport in MMM. However, these exceed the scope of this literature review, more information on them can be found in open literature[93].

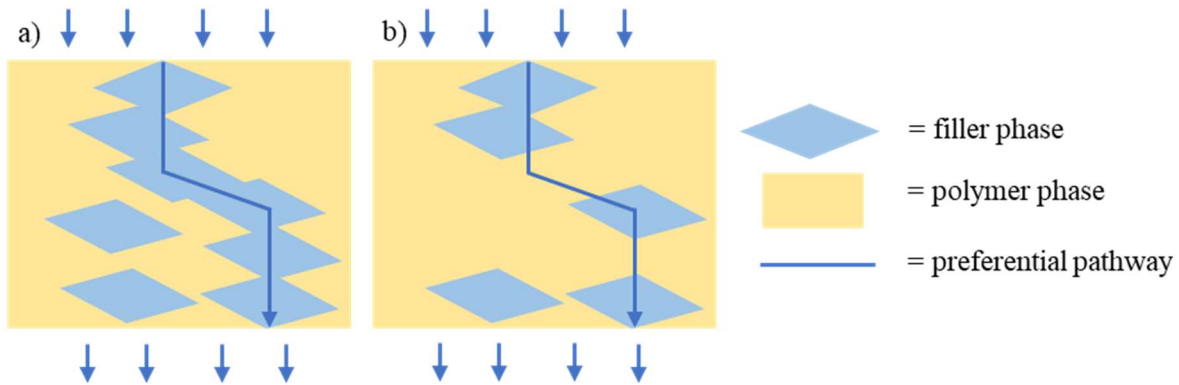


Figure 20: a) Continuous gas transport, gas pathways can bridge the membrane by only passing through the filler phase. b) discontinuous gas transport, gas pathways always pass through the polymer phase. Adapted from ref. [82].

### 2.2.5.3 Challenges of creating MMM

Incorporation of a filler within the polymer phase poses some additional challenges due to the differences in chemistry of both components. Compatibility of the polymer and the filler is required to achieve the desired mix in properties of the MMM[1]. Dispersion of filler particles within the polymer phase and the mechanical stability of the membranes can be challenging as well[1].

#### 2.2.5.3.1 Polymer-filler interface

Including an inorganic filler in a polymer matrix poses some challenges. Compatibility between the filler and polymer matrix can be low and the consequent impact on the MMM performance significant[86,93,97–99]. In the ideal case, the inorganic particles are perfectly ‘wetted’ by the

polymer phase, which means that the polymer surrounding the particle has no difference in physical properties compared to the pure polymer and there are no significant gaps situated at the interface between the polymer and filler particle. However, regularly the synthesis of the MMM and the often weak polymer-filler adhesion induce interface defects[86,93,97–99].

A possible explanation for the formation of interfacial defects is the result of stresses generated in the material due to solvent removal. Initially, the dissolved polymer phase and dispersed inorganic filler are in close contact due to high mobility of the polymer whilst solvated. When solvent is removed, the polymer phase will shrink. In a pure polymer, this shrinking would be isotropic but in the case of MMM, the polymer in contact with the more rigid filler phase will not be able to contract isotropically[93,97,98,100,101]. Additionally, upon removing solvent, the mobility of the polymer backbone is reduced and will eventually be lost when the polymer becomes glassy. After the transition of the polymer matrix into this glassy state interfacial stresses can arise when even more solvent is removed[93,97,98,100,101].

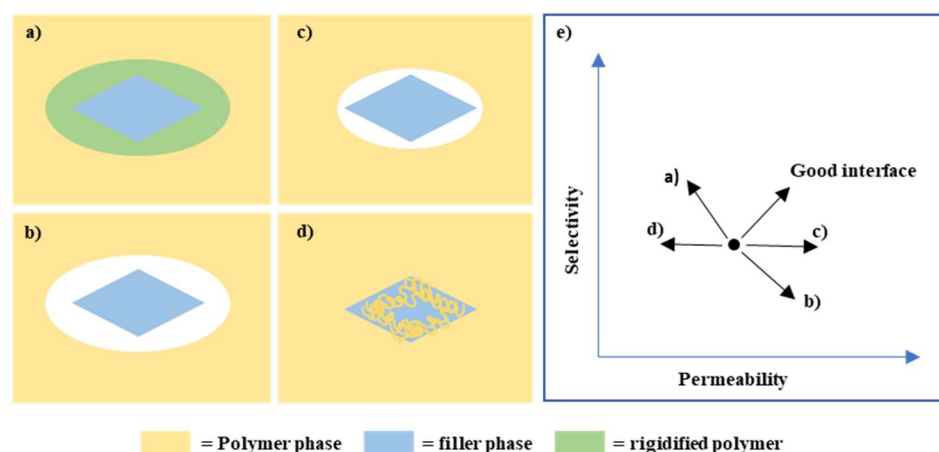


Figure 21: Illustration of the different interactions between filler and polymer. a) Case I: rigidified polymer layer, b) Case II: sieve-in-a-cage morphology. c) Case III: sieve-in-a-cage with size-selective gaps between polymer and filler. d) Case IV: pore blocking. e) Effect of the a good interface and case I-IV on permeability and selectivity. The dot represents the properties of the pure polymeric membrane. Adapted from ref. [98].

Figure 21 schematically represents the possible filler/polymer interfaces. If adhesion between the polymer and filler phase is good, the inward forces caused by interfacial stress will compress the polymer close to the filler particle. As a result, a layer of polymer is formed with a decreased amount of free volume. This process is called polymer rigidification and results in an increase in diffusion selectivity and a decrease in permeability (case I, Figure 21a). Polymer rigidification is often characterized by an increased  $T_g$  of the MMM compared to the pristine membrane[93,98,101–103]. In case II, the compatibility between both phases is low and the stressed polymer will detach from the particle. As a consequence, so-called interfacial voids form between the polymer and filler. These voids increase permeability significantly but reduce

the size selectivity of the polymer and renders the potential superior size sieving capacity of the filler (partially) useless[93,98,101–103]. Addition of the filler to the polymer matrix thus results in a ‘sieve-in-a-cage’ morphology. When the interfacial voids have a width in the range of the permeating gasses selectivity is only slightly reduced (case III). Permeability is still increased as a result of void formation that can be interpreted as an increase of free volume. Both cases are shown in Figure 21c[93,98,101–103].

Finally, filler particles can be completely blocked by the permeating components, residual solvent or due to blocking by interaction with the polymer chain. This results in a reduced permeability but does not change the selectivity of the membrane as compared to the pristine membrane (Figure 21d, case IV). The effect on the permeability and selectivity of these different interfaces on the performance of the MMM is shown in Figure 21e[93,98,99,101–103].

#### 2.2.5.3.2 Dispersion

The filler particles in MMM often tend to aggregate due to stronger inter-particle interactions than polymer-particle interactions. The agglomeration of the particles is non-ideal since a homogeneous mixing of both phases is required to effectively combine the gas separation properties of both[104,105]. Additionally, particle agglomeration could result in the formation of interfacial voids[104,105]. The effect of particle size on dispersion is inconclusive. Research by Sanchez-Lainez *et al.* demonstrated that larger particles are usually better dispersed because they have a smaller tendency towards agglomeration possibly due to their smaller specific surface area[106]. However, Thür *et al.* observed an increase in separation factor and permeability for a trifluoroacetic acid (TFA) modulated MOF-808 dispersed in Matrimid. The worse performance of the larger particles was in this case attributed to less successful incorporation within the polymer matrix[107].

In order to avoid particle agglomeration during MMM synthesis, priming of the filler suspension is often performed. This is a procedure wherein only a small amount of polymer is initially added to a filler containing suspension. As such, the low concentrated polymer forms a thin layer on the surface of the filler particle to avoid the formation of larger aggregates. Afterwards, more polymer is added stepwise to form the membrane. Before each addition step, the solution is sonicated to decompose potentially formed aggregates[104,105,108]. Drying of the filler after its synthesis, often results in particle agglomeration. Mixing the filler synthesis mixture with a membrane solution avoids this and thus helps to improve particle dispersion as well[109].

### 2.2.5.3.3 Mechanical stability

Another challenge associated with MMM is mechanical stability, which is paramount for the industrial application of the membranes. The incorporation of fillers within a polymer often results in a deterioration of the mechanical properties of the polymer. Mahdi *et al.* discovered that ZIF-8 nanoparticle loadings above 10-15 wt% in Matrimid reduces the stretchability, toughness and tensile strength of the membranes. The membranes with higher filler loadings were brittle. Furthermore, membrane properties deteriorated even further when membranes were treated at elevated temperatures[110]. A similar trend was observed when ZIF-90 nanoparticles were incorporated in a PVDF membrane[111]. These stability issues might become even more pronounced when asymmetric MMM, with a very thin selective MMM layer, are synthesized[104,112]. Some stable asymmetric MMM have been reported, however most upscaled asymmetric MMM production attempts still resulted in defect membranes [104,113,114].

## 2.2.6 Metal organic framework mixed matrix membranes

### 2.2.6.1 Introduction

MOFs are a class of microporous, crystalline materials. They consist of organic multidentate linkers, which connect inorganic metal atoms or clusters (nodes). MOFs generally exhibit great tunability, due to the wide variety of possible nodes and linkers, allowing for optimization of the MOF system to a certain application[1,113,115–120]. An example of this great tunability can be seen in Figure 22. This figure shows an isoreticular series of MOFs based on the MOF-5 topology. The series is referred to as isoreticular since all MOFs within the series have the same framework topology. Different linkers are used to connect the identical Zn-O-C clusters resulting in a different chemical environment within the pores of the MOF and changes in pore dimensions[120]. The large selection of possible linkers and nodes has resulted in a wide range of suggested applications for MOF materials such as catalysis, adsorption, sensors, drug delivery and membrane separations[1,113,115–120].

The first report of a MMM with MOF particle fillers dates from 2004. Yehia *et al.* reported a pure gas selectivity of 3.2 for a CO<sub>2</sub>/CH<sub>4</sub> separation using a Cu BPDC-TED/PAET MOF[115]. Since then, a wide range of MOFs were developed and, more importantly, a wide range of MOF/polymer combinations were tested for different gas separations, showing increases in membrane performance situated above the Robeson upper bound[115].

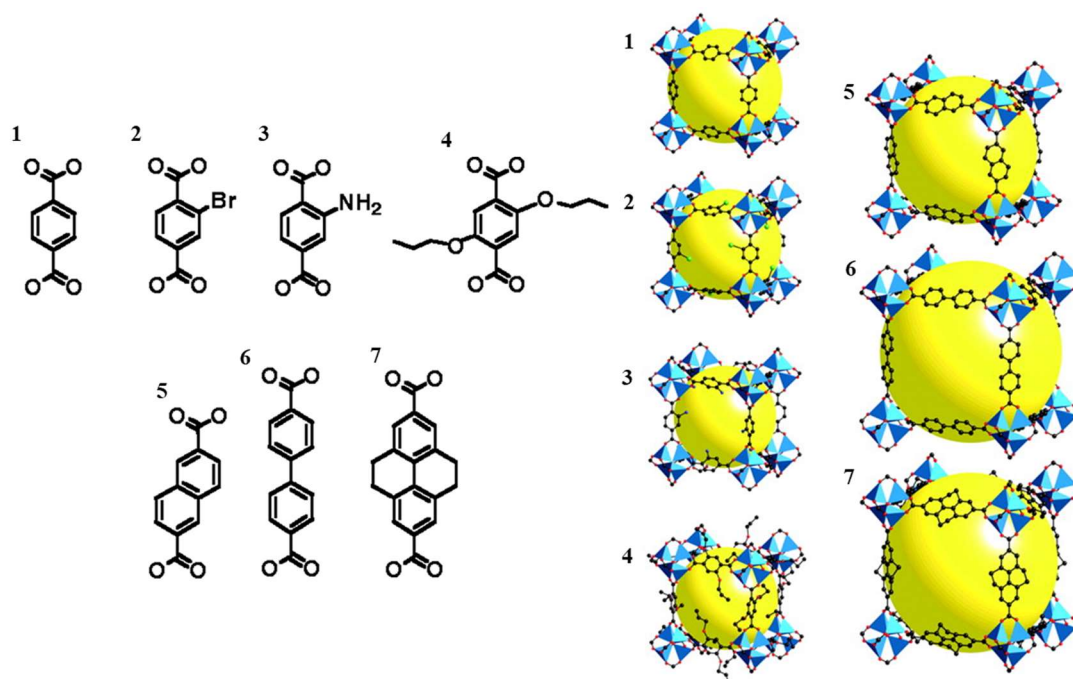


Figure 22: Isorecticular series based on the MOF-5 framework (IRMOF series). On the left sides the different linkers connecting the nodes are shown. On the right side the resulting MOF frameworks are shown. The numbers connect the MOF structures with their respective linkers. Adapted from ref. [120].

#### 2.2.6.2 Advantages of MOF fillers

The use of MOFs as a filler in MMM is particularly interesting due to their high tunability. As mentioned before, a wide range of nodes and linkers is available, resulting in different MOF structures. This can be used to modify the pore aperture of MOFs, resulting in size sieving abilities[121,122]. For example, Xue *et al.* synthesized and tuned an ftw-topology MOF by using an azobenzenetetracarboxylic acid linker, resulting in particles with a pore aperture of 5 Å. This MOF showed remarkable kinetic (size) separating properties as an adsorbent for propene/propane separations[123]. Size selectivity of MOFs has also been used in the development of MMM. For example, ZIF-8 based 6FDA-DAM MMM have been used for separating propylene from propylene/propane mixtures. The addition of ZIF-8 to the polymer matrix increased both the propylene/propane selectivity and propylene permeability significantly[1,124].

On the other hand, CO<sub>2</sub>-philic entities can be introduced in the MOF framework increasing the affinity of the MOF for CO<sub>2</sub> and/or its CO<sub>2</sub> storage capacity[125]. Various strategies have been adopted to include these entities and thus increase the CO<sub>2</sub> uptake or CO<sub>2</sub> selectivity over other gasses of MOFs when used as a physical adsorbent. One possible approach is the use of functionalized ligands in the MOF synthesis[125,126]. For example Cmarik *et al.* synthesized UiO-66 using ligands functionalized with an -NH<sub>2</sub> functional group. The corresponding UiO-

66-NH<sub>2</sub> showed a significantly higher CO<sub>2</sub> uptake compared to unfunctionalized UiO-66 at low CO<sub>2</sub> pressures[127]. Another approach to increase CO<sub>2</sub> affinity is the use of exposed metal cation sites in MOFs[125,128]. These exposed cations can interact with gas molecules such as CO<sub>2</sub> through its strong quadrupole moment. Bae *et al.* compared the CO<sub>2</sub> uptake of a carborane based MOF with free and solvent blocked metal sites. The framework with free metal sites showed a significant increase CO<sub>2</sub> uptake and in CO<sub>2</sub>/CH<sub>4</sub> selectivity[129]. Queen *et al.* showed for an isostructural series of M<sub>2</sub>(dobdc, 2,5-dioxido-1,4-benzenedicarboxylate) MOFs with various metal nodes (M) that the type of metal used as free cation site also influences the CO<sub>2</sub> adsorption behavior, with the Mg<sup>2+</sup>(dobdc) showing the highest CO<sub>2</sub> uptake per metal ion in their case[130]. Various MOFs make use of modulators in their synthesis[131]. In some cases the use of different modulators can be exploited to increase the CO<sub>2</sub> uptake of the MOF. Gutov *et al.* used amino acid modulation to synthesize various Zr-MOFs (Zirconium MOFs), which resulted in the inclusion of the amino acids in the MOF framework, simultaneously increasing their CO<sub>2</sub> uptake[122,132]. Finally, there are also various post-synthetic MOF functionalization strategies, capable of altering CO<sub>2</sub>-MOF interactions. One example is the modification of defect containing UiO-66 frameworks with various organic functionalizing agents. Defective UiO-66 modified with 3-aminobenzoic acid showed a significantly higher CO<sub>2</sub> uptake at 1 bar compared to the unfunctionalized UiO-66 material[133]. Similarly, Deria *et al.* reported a significant increase in CO<sub>2</sub> uptake at 150 mbar and isosteric heat of CO<sub>2</sub> adsorption at zero coverage for NU-1000 post-synthetically functionalized with various perfluoroalkanes[134]. This section only provides a very short overview of MOF development strategies for CO<sub>2</sub> capture with a few examples, a more extensive discussion is available in some great literature reviews[115,125,135]. Functionalization of MOFs also proved an effective strategy to increase the gas separation performance of MMM based on these MOFs. For example, Thür *et al.* incorporated a nitrogen functionality in UiO-67, using a bipyridine-based linker. This resulted in an increase in CO<sub>2</sub>/CH<sub>4</sub> separation factor of the MMM consisting of this MOF and Matrimid[89]. Similarly, Incorporation of an amine functionality in MOF-199 was found to enhance both the CO<sub>2</sub> ideal selectivity and permeability of 6FDA-ODA MMM based on this MOF compared to unmodified MOF-199/6FDA-ODA MMM[136].

Furthermore, MOF fillers generally have a better compatibility with the polymer matrix than their zeolite and CMS counterpart as a result of their partially organic structure[1,103,104]. Additionally their high tunability allows optimization of the linker-polymer interaction, further reducing compatibility issues[103]. For example UiO-66-NH<sub>2</sub> showed a superior interfacial

compatibility with various polymers compared to its unfunctionalized UiO-66 counterpart, supposedly through hydrogen bonding interactions[136,137]. More elaborate interface engineering strategies have been applied as well. For instance, post-synthetic modification of UiO-66-NH<sub>2</sub> through reaction of the -NH<sub>2</sub> group with the dianhydride end of 6FDA-durene oligomers allowed synthesis of 6FDA-durene/6FDA-durene modified UiO-66-NH<sub>2</sub> MMM showing good interfacial compatibilities for MOF loadings up to 40 wt%[138].

Moreover, some MOFs have been reported to be thermally stable up to temperatures ranging from 250-500 °C[139]. Chemical stability of MOFs poses a greater challenge. The bond between nodes and linkers is susceptible to hydrolysis in aqueous conditions. The hydrolysis reaction can be accelerated by the presence of acids and bases, respectively, promoting the formation of a protonated linker or hydroxylated node and as a result the associated dissociation of the MOF[139,140]. However, MOFs have been developed which are able to withstand extreme conditions (pH, solvents). For instance, UiO-66 showed to be resistant to a pH equal to 1 and an UiO-66 MOF with a NO<sub>2</sub> modified linker was stable in a pH of 13.6[139–141].

#### 2.2.6.3 MOF fillers used in MMM CO<sub>2</sub> gas separations

This section gives a more detailed description of three MOFs which are of high relevancy for this thesis. First, UiO-66 is described as it is one of the most reported MOFs in MMM literature. Next, two relatively new MOFs (MOF-808 and UTSA-120a) are introduced.

##### *UiO-66*

UiO-66 consists of a zirconium-oxide (Zr<sub>6</sub>O<sub>4</sub>(OH)<sub>4</sub>) cluster (Zr<sub>6</sub> cluster) linked by 1,4-benzenedicarboxylic acid (BDC) linkers. It has a pore structure built from octahedral and tetrahedral cages, which together form a triangular pore aperture of 6 Å[1]. The crystal structure of UiO-66 together with the structure of its node (Zr<sub>6</sub> cluster) is shown in Figure 23a and b.

In UiO-66, normally every cluster is coordinatively saturated with 12 linkers[89,142]. As a result, the structure remains relatively stable when a linker or cluster is missing. Bueken *et al.* reported a tolerance of up to 4.3 missing linkers per Zr-cluster, using a mixed linker approach followed by a degradation step of one of the linkers[142]. Different strategies to synthesis and optimize high-defect UiO-66 have been adopted. Missing linkers were found to increase the BET surface area and pore size of the MOF particles[143]. Additionally, these missing linkers expose unsaturated Zr<sub>6</sub> clusters which could possibly interact with gasses such as CO<sub>2</sub>. Wu *et al.* for instance reported higher CO<sub>2</sub> uptake capacities for a UiO-66 MOF with hydroxylated defects[144,145].

UiO-66 is reported to be thermally, chemically and mechanically stable, as well as highly tunable[141]. A wide range of variants to the standard UiO-66 have been synthesized, focusing on the enhancement of its sorption and separation properties[146]. MMM comprised of a 4-aminobenzoic acid modulated MOF UiO-66-NH<sub>2</sub> (UiO-66-NH<sub>2</sub>-ABA), which uses 2-aminoterephthalic acid as linker, and a Matrimid membrane showed an increase in permeability as well as selectivity for CO<sub>2</sub>/CH<sub>4</sub> gas separation[147]. Post-synthetic modifications of UiO-66 based MOFs have been reported as well. Jiang *et al.* succeeded in forming a UiO-66-NH<sub>2</sub>@ICA MOF by an amine condensation reaction between UiO-66-NH<sub>2</sub> and imidazole-2-carbaldehyde (ICA). The MMM formed by combining this MOF with Matrimid showed even higher permeability and selectivity than the UiO-66-NH<sub>2</sub>-ABA MMM[148].

Recent research by Reinsch *et al.* focused on the green synthesis of UiO-66. They succeeded in synthesizing MOF particles using water as a solvent instead of N,N-dimethylformamide which is commonly used in UiO-66 synthesis. The crystal structure of the particles showed similarities to the structure of UiO-66 but had a lower symmetry and different unit cell parameters. The synthesis of these MOFs under industrially feasible, green conditions is an important step towards large scale MOF applications[149].

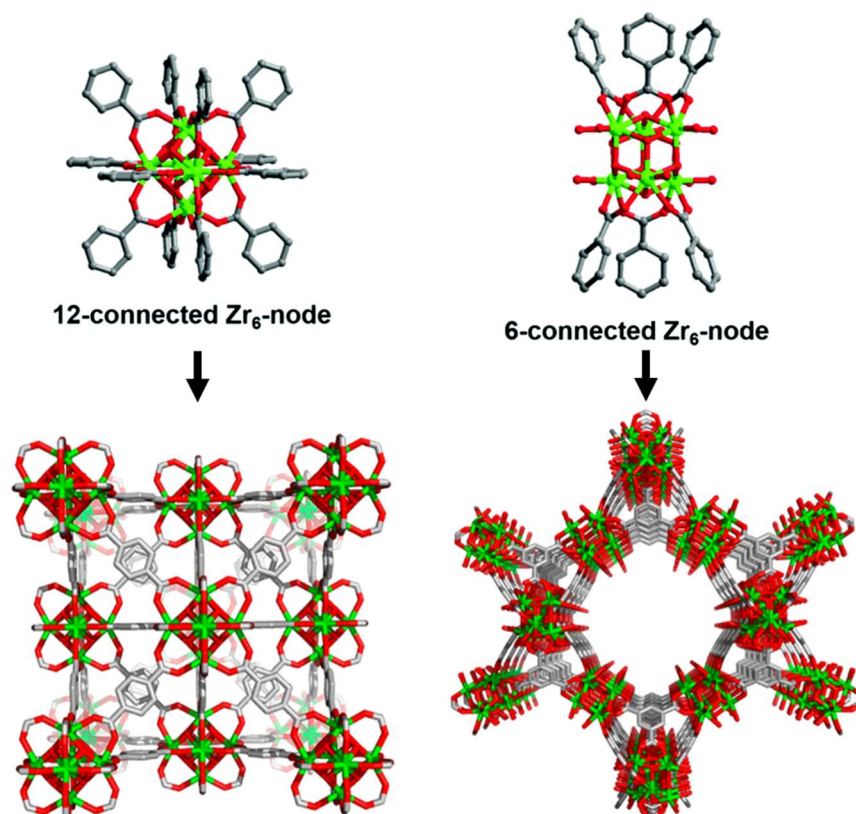


Figure 23: a) Structure of the node of UiO-66. b) Crystal structure of UiO-66. c) Structure of the node of MOF-808. d) Crystal structure of MOF-808. (grey = C, red = O, green = Zr) copied from refs. [150,151].

### MOF-808

Another  $Zr_6$  cluster based MOF of interest is MOF-808. In the case of MOF-808, the clusters are linked by benzenetricarboxylic acid (BTC) instead of the BDC linker in UiO-66[1,152]. Each  $Zr_6$  cluster is bonded to 6 BTC linkers, however the  $Zr_6$  cluster is theoretically saturated with 12 carboxylic acid ligands (as is the case in UiO-66). As a result, 6 equatorial sites on the  $Zr_6$  cluster are available to coordinate other ligands. These ligands can be solvent, modulator or other species present in the synthesis medium[107]. The MOF has an spn topology consisting of tetrahedral cages with an internal pore diameter of 4.8 Å. In these cages, the BTC linkers are situated at the faces of the tetrahedron. The cages share the oxo-clusters situated in the vertices, resulting in an adamantane cage with an internal pore diameter of 18.4 Å[152,153]. The structure of MOF-808 and the MOF-808 node are shown in Figure 23c and d. Similar as for UiO-66, water based ‘green’ synthesis recipes have been reported for MOF-808 [107,149].

Different methods were developed to functionalize MOF-808. Since up to 6 modulator molecules can theoretically coordinate to the  $Zr_6$  cluster, using a different modulator will result in MOF-808 ligands with a different chemistry[154]. This property of MOF-808 allows tuning of the MOF properties by modifying the cage entrances. For example, Thür *et al.* used a series of perfluorinated and non-fluorinated alkyl carboxylic acids (e.g. TFA and acetic acid) as a modulator to increase the  $CO_2$  permeability and selectivity of MOF-808/Matrimid mixed matrix membranes in  $CO_2/CH_4$  gas separations[107]. The modulator ligands, present after each MOF-808 synthesis on the  $Zr_6$  cluster can also be exchanged for other charge balancing ions post-synthetically. Different examples of this technique have been reported to increase the performance of MOF-808 in a range of applications. Jiang *et al.* succeeded in forming a superacid sulfated MOF-808 by exchanging the formate ions for  $SO_4^{2-}$  ions[155]. Peng *et al.* post-synthetically formed a MOF-808 with EDTA ligands, resulting in an heavy metal ion capture trap[156]. Furthermore, Baek *et al.* succeeded in creating a highly selective methane to methanol oxidation catalyst by exchanging the formate ligands of MOF-808 for 5-benzimidazolecarboxylic acid, which were subsequently metalated with copper. In the same report, MOF-808 was effectively functionalized with histidine using the same procedure[154].

### Hexafluorosilicate (SIFSIX) MOFs

The SIFSIX family of MOFs, built out of  $M^{2+}$  (Cu or Zn) hexafluorosilicate ( $SiF_6^{2-}$ ) salt nodes connected by N-heterocycle containing linkers, have recently attracted attention as interesting materials for  $CO_2$  capture[157]. This family of MOFs all have a cubic topology formed by a bidentate linker coordinating to the  $M^{2+}$  cation. The  $SiF_6^{2-}$  anion is coordinated to the  $M^{2+}$  cation

in an axial position and connects the 2D structures formed between the cation and linker, resulting in a 3D framework[158]. Selection of various linkers allows to easily tune the pore size of the MOFs in the SIFSIX family[158].

Physical properties such as pore size, BET surface area and isosteric heat of CO<sub>2</sub> adsorption are shown in Table 6, together with the CO<sub>2</sub> uptake at 1 bar and the theoretical CO<sub>2</sub>/N<sub>2</sub> selectivity of the pure MOFs for 3 frameworks of the SIFSIX family: SIFSIX-2-Cu-i and SIFSIX-3-Zn and SIFSIX-3-Cu. Their crystal structure as well as linker chemical composition can be found in Figure 24. These frameworks have a 4-4'-dipyridylacetylene (dpa) and pyrazine linker respectively (for both the Zn and Cu form of SIFSIX-3). Clearly, pyrazine is the smaller molecule of the two resulting in the smaller pore size of the SIFSIX-3-Zn and SIFSIX-3-Cu frameworks[159]. The smaller pore size of SIFSIX-3-Cu compared to SIFSIX-2-Zn is suggested to be a result of the 3d<sup>9</sup> valence electron configuration of Cu (3d<sup>10</sup> in the case of Zn) which gives rise to a distorted octahedral coordination of Cu with elongated Cu-F bond length and shortened Cu-N bond lengths. The reduction in linker size also resulted in a reduced BET surface area of the frameworks[159].

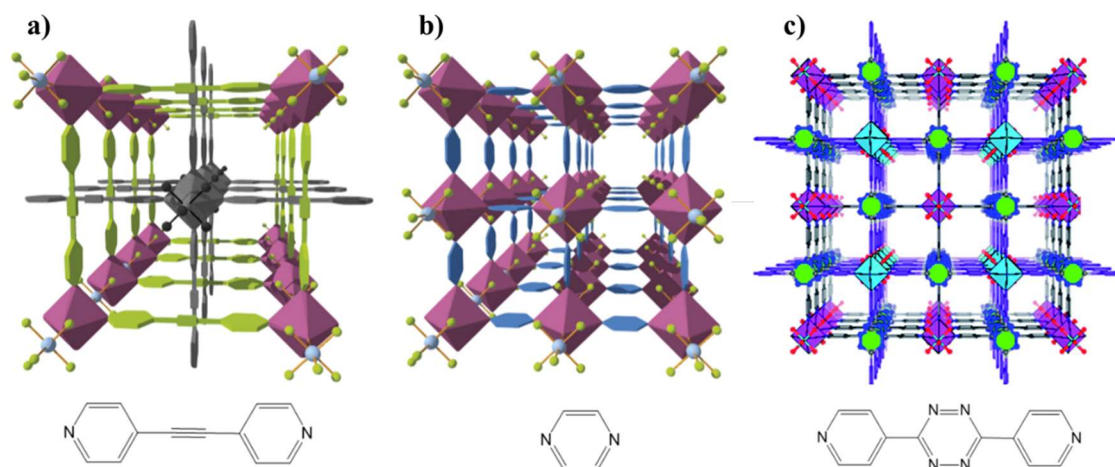


Figure 24: Crystal structure of a) SIFSIX-Cu-i, b) SIFSIX-Cu(Zn)-3 and c) UTSA-120a. In all figures the octahedra present Cu clusters, the structure attached to this cluster represents the SiF<sub>6</sub><sup>2-</sup> group and the other species the linker of the framework. The chemical structure of the framework linker is shown below (dpa, pyrazine and dpt respectively) Copied from refs. [157,159].

All of these MOFs show good CO<sub>2</sub> selectivities when used as adsorbent due to the strong interaction between the SiF<sub>6</sub><sup>2-</sup> anion and CO<sub>2</sub>, resulting in a high CO<sub>2</sub>-philicity of the MOF[158]. There are however large differences in their isosteric heat of CO<sub>2</sub> adsorption Q<sub>st</sub> of the various members of the SIFSIX family, with SIFSIX-2-Cu-i showing the lowest Q<sub>st</sub> values and SIFSIX-3-Cu the highest. This increase in Q<sub>st</sub> with decreasing linker size was attributed to an increase in the amount of fluorine atoms interacting with a CO<sub>2</sub> molecule within

the MOF pore, which is higher for the MOFs with a smaller pore size[158,159]. CO<sub>2</sub> uptake values at 1 bar are higher for the larger linker MOF and clearly linked to its larger BET surface area[158,159]. Finally, the calculated CO<sub>2</sub>/N<sub>2</sub> selectivity of the MOF shown with SIFSIX-3-Cu having clearly the highest selectivity.

Most of these SIFSIX MOFs have also been tested as filler material in MMM. SIFSIX-2-Cu-i incorporated in a polyphosphazene showed an increase in both CO<sub>2</sub>/N<sub>2</sub> ideal selectivity and permeability compared to the pure polymer[160]. Similarly, MMM of 6FDA-DAM combined with SIFSIX-3-Zn had an increased mixed gas separation factor and permeability in 50/50 CO<sub>2</sub>/CH<sub>4</sub> gas separation measurements[161]. Remarkably, 6FDA-DAM membranes containing SIFSIX-3-Cu displayed a slight decrease in separation factor compared to the pure polymer, together with a significant increase in permeability[162]. These results position the SIFSIX family as highly interesting filler materials for MMM development.

Recently Wen *et al.* succeeded in synthesizing a new member of the SIFSIX family called UTSA-120a. This framework also consists of CuSiF<sub>6</sub> nodes, but uses a 3,6-di(4-pyridyl)-1,2,4,5-tetrazine (dpt) linker. The introduction of the tetrazine functionalized linker in the MOF framework effectively reduces the pore size of the MOF to 4.4 Å (Figure 24)[157]. The tetrazine functionality was hypothesized to interact with CO<sub>2</sub> as well resulting, together with the reduced pore size, in a higher CO<sub>2</sub>/N<sub>2</sub> selectivity compared to SIFSIX-2-Cu-i (Table 6). Furthermore, the CO<sub>2</sub> uptake capacity and BET surface area of UTSA-120a suffer only a relatively small reduction[157].

Table 6: Physical properties together with MOF gas uptake and selectivity of various members of the SIFSIX family, including UTSA-120a. Data were taken from ref [157] and [163].

	SIFSIX-2-Cu-i	SIFSIX-3-Zn	SIFSIX-3-Cu	UTSA-120a
Pore size (Å)	5.15	3.84	3.54	4.4
BET surface area (m <sup>2</sup> /g)	734	250	300	638
Q <sub>st,max</sub> (Kj/mol)	32	45	54	27-31
CO <sub>2</sub> uptake (mmol/g) (1bar, 25°C)	5.41	2.54	2.55	5
CO <sub>2</sub> /N <sub>2</sub> selectivity (IAST, ratio 10/90, 25°C)	140	1700	>2000	600

### 3 Materials and methods

#### 3.1 Materials

Zirconyl chloride octahydrate ( $\text{ZrOCl}_2 \cdot 8\text{H}_2\text{O}$  Aber GmbH), 1,3,5-benzenetricarboxylic acid (BTC, J&K Chemicals), 1,4-benzenedicarboxylic acid (BDC, 98%, Sigma Aldrich), formic acid (FA, Sigma Aldrich), glycine (Sigma Aldrich), proline (Sigma Aldrich), hydrochloric acid (HCl, 37wt% in water, Fischer), N,N-dimethylformamide (DMF, >99%, Acros), serine (Ser, Sigma Aldrich), histidine (His, Sigma Aldrich), trifluoroacetic acid (TFA, Merck Schuchardt), glycolic acid (GA, 70 wt% in water, Acros), benzoic acid (BA, >99.5%, Sigma Aldrich), sulfuric acid ( $\text{SO}_4$ , 99.99%, Acros), lithium sulfate monohydrate ( $\text{Li}_2\text{SO}_4$ , >98.5%, Sigma Aldrich), chloroform (>99%, Acros), 4-trifluoromethylbenzoic acid (TFBA, 98%, Sigma Aldrich), 3,6-di(4-pyridyl)-1,2,4,5-tetrazine (dpt, >98%, TCI), copper hexafluorosilicate ( $\text{CuSiF}_6$ , Fluorochem), acetone (technical grade, Acros), ethanol (EtOH, Fischer), water ( $\text{H}_2\text{O}$ ), dimethylsulfoxide (DMSO, Acros), methanol (MeOH, VWR chemicals), tetrahydrofuran (THF, >99%, Acros), Matrimid® 5218 (Matrimid, Huntsman), 6FDA-DAM (Fujifilm), carbon dioxide ( $\text{CO}_2$ , Air Liquide), methane ( $\text{CH}_4$ , Air Liquide), nitrogen ( $\text{N}_2$ , Air Liquide).

#### 3.2 MOF-808-FA synthesis

Two recipes were used to synthesize MOF-808, both using FA as a modulator. The first recipe was developed by Thür *et al.* and the MOF formed using this recipe is referred to as MOF-FA[107,149]. First, 0.585 g of  $\text{ZrOCl}_2 \cdot 8\text{H}_2\text{O}$  (1.82 mmol) and 0.127 g of BTC (0.61 mmol) were dissolved in 4.55 mL water in a 10 mL crimp cap glass vial. After dissolving the MOF-808 precursors, 0.819 g (17.8 mmol) of FA was added to the reaction mixture. Subsequently, the vial was sealed and heated to 100 °C under constant stirring for 24 h. The next day, a white suspension was formed. The reaction mixture was transferred to a falcon tube and centrifuged for 30 min at 4500 rpm to separate the formed MOF. The product was then washed 3 times with  $\text{H}_2\text{O}$  and 3 times with EtOH, centrifuging again after each washing step. Finally the MOF was dried overnight in an oven at 70 °C, grinded and stored for further use.

An upscaled version of the synthesis recipe was developed as well. The MOF obtained through this upscaled recipe is referred to as MOF-FA-u. In this recipe 5.080 g BTC (24.20 mmol) and 23.400 g  $\text{ZrOCl}_2 \cdot 8\text{H}_2\text{O}$  (72.80 mmol) are dissolved in  $\text{H}_2\text{O}$  (182 mL) in a 500 mL round-bottom flask and subsequently 32.744 g FA (712.00 mmol) is added. Next, the reaction mixture is heated to 100 °C under reflux for 5 h. Again, a white suspension was obtained. Washing, drying and grinding of the MOF was done in the same way for both synthesis procedures.

### 3.3 MOF-808 functionalization strategies

#### 3.3.1 In-situ functionalization

Amino acid modulation of MOF-808 was investigated starting from the MOF-808 synthesis recipe reported by Thür *et al.*[107,149]. This is a water-based synthesis recipe offering two distinct advantages: it excludes the use of toxic solvents such as DMF and circumvents solubility issues of the amino acids in DMF, since these are highly soluble in H<sub>2</sub>O[132,164]. HCl was added to the reaction mixture based on results obtained by Marshall *et al.*, who reported HCl to assist in MOF synthesis for amino acid modulated Zr-MOFs[165]. All of the synthesis conditions are shown in Table 7. Recipes 17-20 were analogous to the ones used by Marshall *et al.*. Similar to the synthesis of MOF-FA the reaction product was recovered using centrifugation and washed 3 times with the solvent used during synthesis and 3 times with EtOH. Finally, the samples were dried in an oven at 70 °C overnight grinded and stored.

Table 7: Synthesis conditions explored in in-situ MOF functionalization. (a) Water (or DMF) was added until the total volume of the reaction mixture was 5 mL. (b) in this recipe UiO-66 was synthesized and thus a BDC linker was used instead of BTC. (c) For these recipes DMF was used instead of H<sub>2</sub>O.

Recipe	ZrOCl <sub>2</sub> ·8H <sub>2</sub> O (mmol)	BTC (mmol)	Proline (mmol)	Glycine (mmol)	HCl (mmol)	H <sub>2</sub> O (a) (mL)	T(°C)	Time (h)	Ref.
1	1.82	0.61	1.82	-	1.82	5	100	24	[107]
2	1.82	0.61	2.72	-	2.72	5	100	24	[107]
3	1.82	0.61	3.63	-	3.63	5	100	24	[107]
4	1.82	0.61	1.82	-	2.72	5	100	24	[107]
5	1.82	0.61	1.82	-	3.63	5	100	24	[107]
6	1.82	0.61	2.72	-	0.00	5	100	24	[107]
7	1.82	0.61	3.63	-	0.00	5	100	24	[107]
8	1.82	0.61	3.63	-	3.63	5	100	24	[107]
9	1.82	0.61	-	1.82	1.82	5	100	24	[107]
10	1.82	0.61	-	2.72	2.72	5	100	24	[107]
11	1.82	0.61	-	3.63	3.63	5	100	72	[107]
12	1.82	0.61	-	1.82	2.72	5	100	24	[107]
13	1.82	0.61	-	1.82	3.63	5	100	72	[107]
14	1.82	0.61	-	2.72	0.00	5	100	24	[107]
15	1.82	0.61	-	3.63	0.00	5	100	24	[107]
16	1.82	0.61	-	3.63	3.63	5	100	72	[107]
17	0.45	0.45	2.25	-	0.45	5 (c)	120	24	[165]
18	0.45	0.45	-	2.25	0.45	5 (c)	120	24	[165]
19	0.45	0.45 (b)	2.25	-	0.45	5 (c)	120	24	[165]
20	0.45	0.45 (b)	-	2.25	0.45	5 (c)	120	24	[165]

#### 3.3.2 Post-synthetic functionalization

##### 3.3.2.1 Method 1

Method 1 is based on a method developed by Baek *et al.* to functionalize MOF-808 with various N-heterocycle functionalized carboxylic acids[154]. 0.250 g of MOF-FA(-u) is suspended in a 50 mL DMSO solution containing 9.30 mmol functionalizing agent. Next, the suspension is transferred to a bottle, which was sealed and heated in an oil bath at 100 °C under constant stirring. After 24 h the MOF suspension was transferred to a falcon tube and centrifuged for 30 min at a rotation speed of 4500 rpm. Subsequently the precipitated MOF is washed 3 times with

DMSO and 3 times with acetone. After each washing step centrifugation was used to recover the MOF. Finally, the MOF was dried in an oven at 70 °C overnight, grinded and stored for further use. This functionalization strategy was used to synthesize the Ser, BA and TFBA functionalized MOFs, respectively referred to as MOF-Ser, MOF-BA and MOF-TFBA.

### 3.3.2.2 Method 2

A second functionalization strategy was used for the synthesis of the His, TFA, GA and SO<sub>4</sub> functionalized MOFs, respectively referred to as MOF-His, MOF-TFA, MOF-GA and MOF-SO<sub>4</sub>. This recipe was first used by Jiang *et al.* to functionalize MOF-808 with sulfuric acid[155]. A 50 mL aqueous solution of 5.00 mmol functionalizing agent (0.1 M) is used to suspend 0.500 g of MOF-FA-u. This reaction mixture is then transferred to a sealed bottle and left to stir for 24 h at room temperature. Upon completing the reaction, a similar washing procedure as described for method 1 is used. However, in this case the functionalized MOF is washed 3 times with H<sub>2</sub>O and 3 times with acetone. MOF-SO<sub>4</sub> was additionally washed 3 times with chloroform, in analogy with the procedure described by Jiang *et al.*[155]. Finally, the MOFs were dried in an oven at 70 °C overnight, grinded and stored for further use.

### 3.3.2.3 Method 3

A third functionalization strategy was developed to functionalize MOF-808 with Li<sub>2</sub>SO<sub>4</sub>. 0.250 g of MOF-SO<sub>4</sub> was suspended in a 50 mL aqueous solution containing 5.00 mmol of Li<sub>2</sub>SO<sub>4</sub>. The suspension was transferred to a closed bottle and left to stir at room temperature for 24 h. Subsequently, the same washing (using water and acetone), drying and storage procedure as described in method 2 was applied.

## 3.4 UTSA-120a synthesis

UTSA-120a was prepared using the synthesis recipe of Wen *et al.*[157]. Under mild stirring, a 2 mL solution containing 0.110 g (0.49 mmol) CuSiF<sub>6</sub> in water was added dropwise to a 30 mL MeOH solution containing 0.120 g (0.51 mmol) of dpt at room temperature. Upon addition of the first droplets, the previously transparent pink solution immediately became turbid. After 24 h the synthesis was stopped and the formed UTSA-120a was washed 3 times a day with MeOH over a 2 day period, centrifuging for 45 min at 4500 rpm each washing step. Finally, the MOF was dried overnight in an oven at 50 °C, grinded and stored for further use.

## 3.5 Membrane synthesis

MMM were synthesized by suspending 0.048 g of MOF in 5.580 g of THF. After sonicating, for 2 min 0.140 g of polymer (Matrimid or 6FDA-DAM) was added to the mixture and left to

stir for 2 h. Two more times 0.140 g of polymer was added to the solution, each time first sonicating the mixture for 2 min. Between the addition steps was a 2 h waiting period, during which the mixture was continuously stirred. This stepwise addition of polymer (priming) was used to ensure optimal interactions between the polymer and MOF filler. Next, the formed polymer/MOF dispersions were sonicated 2 min for a final time and subsequently cast in a Teflon petri dish with a cross section of 6 cm under a N<sub>2</sub> atmosphere at room temperature. The cast membranes were left in this N<sub>2</sub> atmosphere for 24 h, allowing THF to evaporate. Afterwards, the MMM were cut in 20 mm coupons and annealed for 2 h at 110°C and 6 h at 180 °C in an oven using a heating rate of 5 °C/min in case of the Matrimid based membranes and for 48h in an oven at 100°C in case of the 6FDA-DAM based membranes. Pure polymer membranes were synthesized by dissolving 0.420 g of polymer in 5.580 g of THF. The obtained polymer solution was left to stir for a 6 h period. The casting, cutting and subsequent annealing of the membranes is completely analogous to the respective MMM synthesis procedures. This recipe was optimized by Thür *et al.* to obtain MMM with a 10 wt% MOF loading[107].

### **3.6 X-ray diffraction (XRD)**

Powder XRD diffractograms of all of the MOFs were measured to confirm crystallinity of the synthesized and functionalized MOFs. The measurements were conducted on a Malvern PANalytical Empyrean diffractometer in transmission mode, equipped with a PIXcel3D solid-state detector. Angles ( $2\theta$ ) ranging from 1.3-45° were scanned and a Cu anode was used (Cu K $\alpha$ 1: 1.5406 Å; Cu K $\alpha$ 2: 1.5444 Å)[107].

### **3.7 Nuclear magnetic resonance (NMR)**

Proton (<sup>1</sup>H) NMR measurements were conducted on a Bruker AMX-300 spectrometer (300 MHz) in order to determine the loading of functionalizing agent for the post-synthetically modified MOFs. The MOF sample (0.003 g) was dissolved in 600  $\mu$ L deuterated DMSO using 40  $\mu$ L of hydrofluoric acid (40 wt% aqueous solution). Each sample was scanned 16 times with a recycle delay time of 30s. Spectra were analyzed with the SpinWorks 4.2 software[107].

### **3.8 Attenuated total reflection Fourier transform infrared spectroscopy (ATR-FTIR)**

ATR-FTIR spectra were recorded on a Varian 670 FTIR imaging microscope to evaluate the chemical changes in the MOF upon functionalization and upon incorporation in a MMM. The apparatus used a single point MCT detector and diamond ATR crystal. Spectra were measured with a resolution of 2 cm<sup>-1</sup>. 64 scans per sample were conducted, respectively 32 scans to measure a background and 32 to measure the infrared (IR) transmission of the sample[107].

### 3.9 Scanning electron microscopy (SEM) and energy dispersive X-ray analysis (EDX)

SEM was used to determine the particle sizes of the different MOFs. SEM measurements were conducted on a Philips XL30 FEG SEM. Powder samples were immobilized on carbon tape and subsequently coated with a gold/palladium coating to increase the sample conductivity. The Philips SEM was also used to measure EDX spectra of MOF-Li<sub>2</sub>SO<sub>4</sub> to get a measure of functionalizing agent loading in the MOF[107].

### 3.10 CO<sub>2</sub> adsorption measurements

CO<sub>2</sub> adsorption measurements were used to obtain adsorption isotherms of the functionalized MOFs at various temperatures. These isotherms provide the CO<sub>2</sub> uptake of the MOF for a pressure up to 1 bar and, through a Clausius-Clapeyron analysis, the isosteric heat of CO<sub>2</sub> adsorption ( $Q_{st}$ ). CO<sub>2</sub> adsorption isotherms were measured at a temperature of 0, 20 and 40 °C. Each of the isotherms was fitted with the dual-site Langmuir equation (equation 16)[125,134,166–169].

$$N = \frac{N_{m,1}b_1p}{1 + b_1p} + \frac{N_{m,2}b_2p}{1 + b_2p} \quad (16)$$

In this model  $N$  (mmol/g) and  $N_{m,1}$  (mmol/g) and  $N_{m,2}$  (mmol/g) are the amount of adsorbed gas and amount of adsorbed gas at saturation for both sites respectively,  $b_1$  (Pa<sup>-1</sup>) and  $b_2$  (Pa<sup>-1</sup>) are Langmuir constants. This equation was chosen based on the success of this method for determination of  $Q_{st}$  for other MOFs reported in literature[125,134,166–169]. The fits were used to determine, through interpolation, the pressure associated with a certain MOF CO<sub>2</sub> coverage for each of the measured temperatures. Subsequently for each of these coverages a plot of  $\ln p$  vs  $1/T$  was made. The slope of these plots can be used to calculate  $Q_{st}$  (kJ/mol), as described by the Clausius-Clapeyron equation[125,134,166–169]:

$$\frac{\partial(\ln p)}{\partial\left(\frac{1}{T}\right)} = -\frac{Q_{st}}{R} \quad (17)$$

With  $p$  (Pa) the pressure,  $T$  (K) the temperature and  $R$  (J/mol.K) the gas constant.

Measurements were conducted on a Micrometrics 3Flex surface analyzer. Before each measurement the MOF samples were activated by heating them to 100 °C under vacuum for 16 h[107].

### 3.11 High-throughput gas separation measurements (HTGS)

Gas separation performance of the MMM and pure polymer membranes was measured on a custom made HTGS setup, which allows the testing of 16 membrane coupons simultaneously. Mixed-gas separation factors were obtained by separating the permeate over a Porabond Q column installed in a compact gas chromatograph developed by Interscience, Belgium. The column is connected to a thermal conductivity detector[170]. By comparing the feed and permeate mole fractions of the gasses in the mixture, the separation factor ( $\alpha^*_{i/j}$ ) can be determined using the formula:

$$\alpha^*_{i/j} = \frac{y_i/y_j}{x_i/x_j} \quad (18)$$

With  $y_{i,j}$  the permeate and  $x_{i,j}$  the feed mole fraction of the gasses i and j in the gas mixture[170]. Gas permeability was measured using a constant-volume-varying-pressure method. The permeate is collected in an auxiliary cylinder with a known volume of 75 cm<sup>3</sup>. Simultaneously, the pressure increase due to permeate accumulation is measured with a pressure transducer developed by MKS instruments (upper limit of 10 mbar)[170]. The transducer measures the change in pressure per unit of time (dp/dt (Torr/s)), which can be used to calculate the gas permeability of a component of a gas mixture using the following formula[107,170]:

$$P_{i,mixed}(Barrer) = 10^{10} \frac{y_i \times V \times L}{x_i \times p_{up} \times A \times R \times T} \frac{dp}{dt} \quad (19)$$

Where  $P_{i,mixed}$  represents the CO<sub>2</sub> permeability through the membrane in Barrer, V the downstream volume (cm<sup>3</sup>), L the membrane thickness (cm), A the membrane permeation area (1.91 cm<sup>2</sup>), T the operating temperature (K),  $p_{up}$  the upstream pressure (Torr) and R the gas constant. The pure gas permeability was calculated using equation 20[107,170]:

$$P_{i,pure}(Barrer) = 10^{10} \frac{V \times L}{P_{up} \times A \times R \times T} \frac{dp}{dt} \quad (20)$$

All measurements were conducted at an upstream pressure of 5 bar and at a temperature of 35 °C. Membrane performance was measured for membranes in steady state. This steady-state condition was evaluated by permeability measurements with a 30 min time interval. When permeability changes were smaller than 1% for 3 subsequent measurements, the membranes were assumed to have reached their steady state behavior.

## 4 Results and discussion

### 4.1 Introduction

Previous results of Thür *et al.* demonstrated modulation-mediated functionalization of MOF-808 with fluorinated carboxylic acids is an efficient strategy to increase gas separation performance of MMM[107]. This work intends to extend MOF-808 functionalization to other functionalizing agents, such as amino acids, other organic acids and alkali salts. First, amino acids were investigated as potential modulator for an in-situ, green functionalization of MOF-808. In a second part, post-synthetic functionalization of MOF-808 with a broad range of ligands was conducted in an attempt to correlate important MOF parameters (e.g. CO<sub>2</sub> uptake and isosteric heat of adsorption) with the CO<sub>2</sub> permeation behavior of the MMM. In a final section, the potential of another MOF, UTSA-120a, as filler material for MMM was evaluated.

### 4.2 Amino acid functionalization of MOF-808

Amino acids are interesting candidates for MOF-808 functionalization because (1) they bear functional groups which have been reported to increase the CO<sub>2</sub> affinity of MOFs and the gas separation performance of the corresponding MMM[125,132,137,171], (2) they have a carboxylic acid group, necessary for coordination with the Zr<sub>6</sub> cluster of MOF-808 and (3) they are relatively cheap and have a low toxicity[107,172]. Therefore, amino acid functionalization of MOF-808 for the development of MMM is evaluated in this section.

#### 4.2.1 In-situ functionalization of MOF-808 with amino acids

Thür *et al.* developed an in-situ functionalization procedure to synthesize their functionalized MOF-808. In this procedure, the desired functionalizing agent fulfills two roles: it acts as a modulator, controlling the growth of the MOF and it coordinates with the MOF-808 Zr<sub>6</sub> cluster, functionalizing the MOF[107,173,174]. Amino acids have previously been used as a modulator in the synthesis of Zr-MOFs[132,165]. Possibly, amino acids could also be used as modulator for the synthesis of MOF-808 and as a result be incorporated in the MOF-808 structure through a similar in-situ functionalization procedure. In this work amino acids were applied as modulator for MOF-808 to investigate this hypothesis. Initially, glycine and proline were selected as modulator. Glycine was chosen because of its comparable structure and size to FA whereas proline was selected based on its good performance as modulator in the synthesis of other Zr-MOFs[132,165]. The chemical structures of glycine, proline and FA are shown in Figure 25. The synthesis of MOF-808 using these modulators will be used as a proof-of-concept, to later extend the approach to more promising amino acids for interaction with CO<sub>2</sub>.

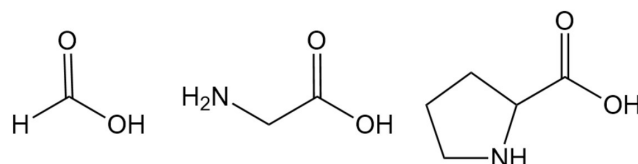


Figure 25: Chemical structure of formic acid (left), glycine (middle) and proline (right).

In an attempt to achieve crystalline MOF-808, two synthesis parameters were varied: the molar ratio of modulator/ $Zr_6$  cluster and the molar ratio of HCl/modulator. For both proline and glycine, synthesis mixtures with a ratio of 1, 1.5 and 2 equivalents modulator/cluster and 0, 1, 1.5 and 2 equivalents HCl/modulator were prepared. By increasing the synthesis time from 24 h to 72 h, the effect of synthesis time was investigated as well for some of the glycine modulated recipes. An overview of the evaluated parameters can be found in Table 8.

Table 8: Parameters evaluated for in-situ amino acid modulation of MOF-808.

MOF	Modulator	Amino acid modulation		Temperature (°C)	Synthesis time (h)	Solvent
		Ratio modulator/cluster	Ratio HCl/modulator			
MOF-808	Proline	1 - 2	0 - 2	100	24	H <sub>2</sub> O
	Glycine	1 - 2	0 - 2	100	24	H <sub>2</sub> O
	Glycine	1.5	0 - 2	100	72	H <sub>2</sub> O
	Proline	5	0.2	120	24	DMF
UiO-66	Glycine	5	0.2	120	24	DMF
	Proline	5	0.2	120	24	DMF
	Glycine	5	0.2	120	24	DMF
	Glycine	5	0.2	120	24	DMF

After synthesis, all obtained products consisted of a grey, opaque, gel-like mixture, regardless of the selected synthesis conditions. Contrarily, MOF-808 modulated with either FA or TFA yields a clear, white MOF suspension[107]. XRD diffractograms of the formed materials were measured to determine if the product was crystalline. All of the measured diffractograms showed broad, badly resolved peaks, indicating no crystalline material was formed. The XRD diffractogram of the synthesis mixture for proline modulated MOF-808 with a ratio of modulator/cluster of 1 and a ratio of HCl/modulator of 1 is given as example in Figure 26.

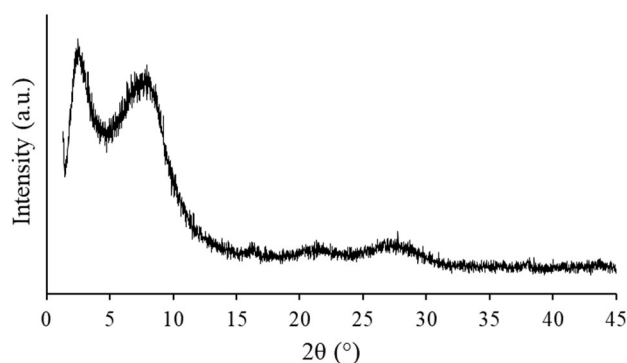


Figure 26: XRD diffractogram of the obtained material for the MOF-808 amino acid modulation synthesis mixture with a modulator/cluster ratio of 1 and a HCl/modulator ratio of 1.

Marshall *et al.* defined an optimum molar ratio of modulator/cluster of 5 and HCl/Zr-source molar ratio of 1 for amino acid modulation of other Zr-MOFs (molar ratio of HCl/modulator of 0.2). Furthermore, they heated their synthesis mixture to 120 °C and used DMF as a solvent instead of H<sub>2</sub>O, a solvent which has also been used for MOF-808 synthesis[152,165]. Therefore, a MOF-808 synthesis recipe using the same synthesis conditions as described by Marshall *et al.* was evaluated. Simultaneously, UiO-66 modulated with glycine and proline was synthesized. The XRD diffractograms measured for UiO-66 modulated with glycine and proline respectively are shown in Figure 27a and c. The XRD diffractograms of MOF-808 modulated with proline and glycine are shown in Figure 27b and d.

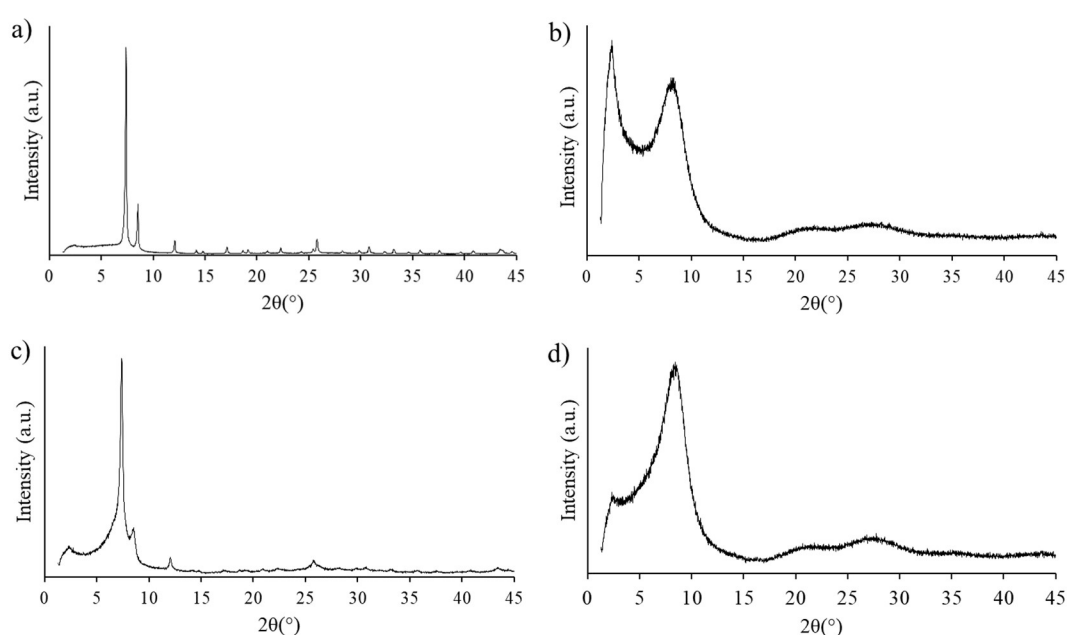


Figure 27: UiO-66 and MOF-808 synthesized using the recipe described by Marshall *et al.* for amino acid modulated UiO-66 synthesis. a) UiO-66-proline, b) MOF-808-proline, c) UiO-66-glycine, d) MOF-808-glycine.

The amino acid modulation of UiO-66 clearly results in a crystalline material with peaks being observed at an angle of 7.4°, 8.5° and 12.7°. The diffractogram corresponds well to diffractograms for UiO-66 reported in literature[165]. Both UiO-66 modulated with proline and glycine are crystalline. However, the glycine modulated MOFs diffractogram is less resolved, which indicates a lower degree of crystallinity[131,175,176]. Unfortunately, both the glycine and proline modulated MOF-808 sample resulted in a gel-like product, with the XRD diffractogram once more indicating no crystalline material was formed.

It is unclear what lays at the base of the failed MOF-808 synthesis. In general, it seems likely the amine functionality of the amino acid plays a central role. It could be hypothesized that the amine group negatively affects the pH of the MOF mixture[173,177,178]. A second theory would be that the zwitterionic nature of the amino acid causes electrostatic repulsion between

positively charged  $Zr_6$ -clusters or disrupts in general the electrostatic balance between reagents during synthesis ( $pK_{a_{\text{glycine-amine}}} = 9.60$ ,  $pK_{a_{\text{proline-amine}}} = 10.60$ )[179]. However, no direct evidence could be provided for both of these theories. Gutov *et al.* also evaluated the modulating properties of N-formylproline, proline methyl ester and pipercolinic acid (N-containing 6 ring instead of 5-ring in the case of proline) in the synthesis of UiO-67. These modulators resulted in MOF samples with poorer crystallinity, indicating that both the  $NH_2^+$  and  $CO_2H$  functional groups as well as the ring structure of proline played an important role in the modulation[132].

#### 4.2.2 Post-synthetic functionalization of MOF-808 with serine

Based on the previous experiments it was concluded that, starting from the known synthesis recipes, no straightforward in-situ amino acid functionalization strategy for MOF-808 could be derived. To circumvent this problem and still combine the advantages of amino acids with MOF-808, a post-synthetic functionalization strategy was applied. In this approach, MOF-808 is first synthesized using a well-known synthesis procedure. After synthesis, the MOF is re-suspended in a solution containing the desired amino acid, which is subsequently exchanged with the species occupying the cluster of the as-synthesized MOF. Since in this case the MOF is already formed, the amino acids cannot interfere with the MOF formation. Post-synthetic amino acid functionalization of MOF-808 has already been performed by Baek *et al.*. They successfully functionalized MOF-808 with histidine by the synthesis method described in this work as method 1[154]. More specifically, serine (structure shown below) could be of particular interest for  $CO_2$  separations due to its highly similar chemical structure compared to monoethanolamine (MEA, Figure 28), one of the most prevalent amine absorption reagents for  $CO_2$  removal in various applications[125,180]. Therefore, serine functionalized MOF-808 (MOF-Ser) was characterized and evaluated as a filler in Matrimid MMM in the next paragraph.

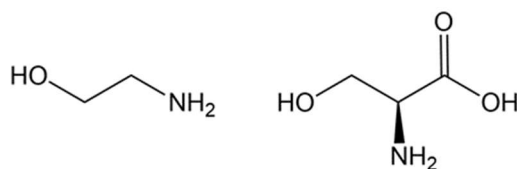


Figure 28: Chemical structure of MEA (left) and Serine (right).

##### 4.2.2.1 Characterization of MOF-Ser

MOF-Ser was synthesized using functionalization method 1, described in the materials and methods section. XRD diffractograms of MOF-FA and MOF-Ser were taken to confirm the crystallinity of the synthesized MOFs (Figure 29). Well-resolved peaks in the diffractogram occur around an angle of  $4.3^\circ$ ,  $8.3^\circ$ ,  $8.7^\circ$ ,  $10.0^\circ$  and  $10.9^\circ$  for both MOFs. The observed XRD

pattern of MOF-Ser correspond well with the diffractogram of the ‘unfunctionalized’ MOF-FA, the calculated MOF-808 diffractogram and diffractograms of MOF-808 in literature, indicating the crystal structure of the MOF remains unaffected by functionalization[152,181]. There is a clear difference in relative intensity of the peaks at  $4.3^\circ$  and the doublet at  $8.3^\circ$  and  $8.7^\circ$  between MOF-FA and MOF-Ser. Such a difference was also observed by Baek *et al.* for their histidine functionalized MOF-808. A possible explanation is the different pore contents of the framework. Differences in pore content have previously been hypothesized to alter the relative intensity of peaks in diffractograms of MOF-5[176,182,183].

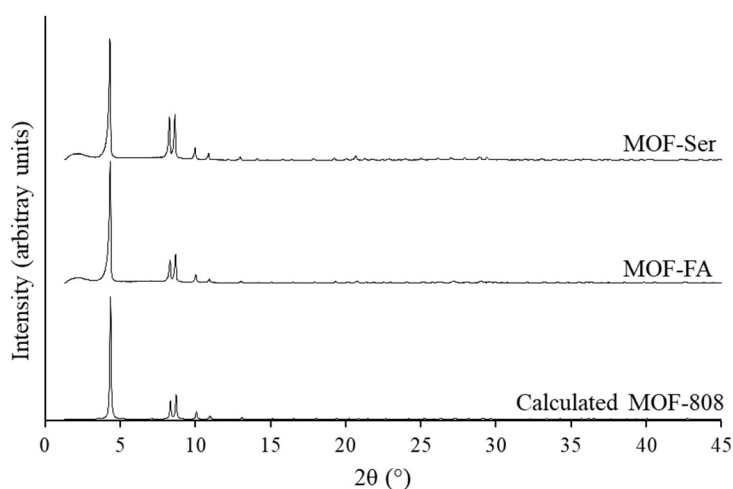


Figure 29: XRD diffractogram of MOF-FA and MOF-Ser, scaled to the peak situated at a  $2\theta$  value of  $4.3^\circ$ .

The framework of MOF-808 consists of a  $Zr_6$  cluster with 12 positive charges that have to be compensated. The BTC linker carboxylic acid functionalities compensate 6 charges, while the 6 planar binding sites are occupied by other charge compensating species[152,184]. As a result theoretically up to 6 molecules of Ser can be present per  $Zr_6$  cluster. To verify whether functionalization was successful, this Ser/cluster ratio is determined using  $^1H$  NMR. On average 2.5 FA molecules are present per  $Zr_6$  cluster in MOF-FA and 3.2 Ser molecules per  $Zr_6$  cluster in MOF-Ser, indicating a successful functionalization (Table 9). The other sites of the cluster are expected to be occupied by hydroxyl groups ( $OH^-$ ) and water molecules, since synthesis of MOF-FA is carried out in an aqueous environment, or by chloride ( $Cl^-$ ) originating from the  $ZrOCl_2 \cdot 8H_2O$  precursor[155,184–186]. Remarkably, all FA molecules were removed from the  $Zr_6$  cluster in MOF-Ser after functionalization.

Table 9: Cluster composition of MOF-FA and MOF-Ser as determined by  $^1H$  NMR.

	Cluster composition			
	BTC	FA	Serine	hydroxyl/chloride
MOF-FA	2.0	2.5	0.0	3.5
MOF-Ser	2.0	0.0	3.2	2.8

Next, CO<sub>2</sub> adsorption isotherms of MOF-FA and MOF-Ser were measured. The adsorption isotherms of both MOFs are shown in Figure 30. MOF-Ser had a higher CO<sub>2</sub> uptake over the entire investigated pressure ranges. At 1000 mbar, a CO<sub>2</sub> uptake capacity of 2.79 mmol/g is observed, which is 62% higher than the CO<sub>2</sub> uptake of MOF-FA (1.72 mmol/g) at the same pressure. For the investigated pressure range, CO<sub>2</sub> adsorption is expected to correlate primarily with the strength of CO<sub>2</sub> binding to the MOF instead of the available surface area[125,187,188]. Therefore, the higher CO<sub>2</sub> uptake capacity of MOF-Ser suggests the increase in CO<sub>2</sub> affinity of the MOF can be attributed to incorporation of CO<sub>2</sub>-philic groups. However, contributions of changes in MOF structural parameters such as pore volume, pore diameter, BET surface area and number of defects upon functionalization with serine cannot be excluded. It was demonstrated in previous work that changes in functionalizing agent size can severely influence pore volume, pore diameter and BET surface area[88,107]. Unfortunately, N<sub>2</sub> physisorption experiments could not be conducted. Determination of pore volume, the pore size distribution and BET surface area is therefore required.

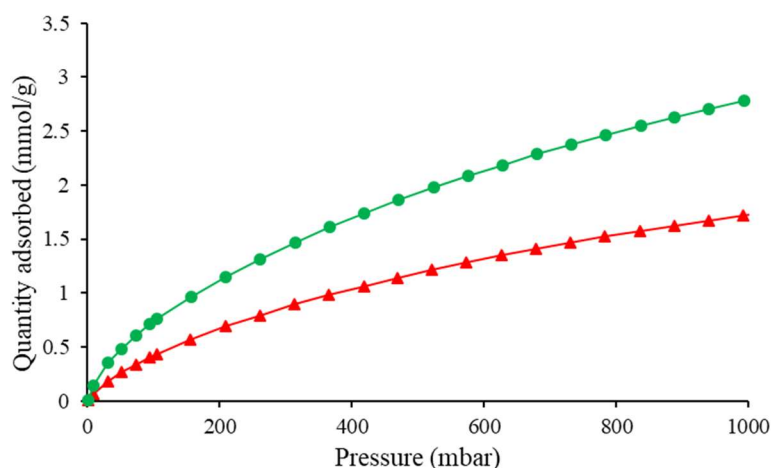


Figure 30: CO<sub>2</sub> adsorption isotherms of MOF-FA (red triangles) and MOF-Ser (green circles) measured at 0 °C for a pressure range of 0-1000 mbar.

#### 4.2.2.2 Gas separation performance of MOF-Ser

MMM of MOF-Ser and MOF-FA combined with Matrimid were prepared and tested for their CO<sub>2</sub>/N<sub>2</sub> gas separation performance for a 50/50 CO<sub>2</sub>/N<sub>2</sub> gas mixture (Figure 31). Inclusion of the MOF in Matrimid enhanced the gas separation performance in terms of mixed-gas separation factor as well as CO<sub>2</sub> permeability. The increase in CO<sub>2</sub> permeability can be the result of an increase in free volume as a result of incorporation of the porous MOF and/or of an increase in free volume due to disruption of the polymer packing[89,138]. The higher mixed-gas separation factor is most likely caused by interaction of CO<sub>2</sub> with the MOF filler, increasing the gas solubility of CO<sub>2</sub> in the MMM[89,138]. Another parameter which could influence the

separation factor is polymer rigidification upon MOF inclusion, which might enhance size (diffusivity) selectivity[107]. The difference in gas separation performance of the MMM based on unfunctionalized MOF-FA and MOF-Ser is very small, with MOF-FA showing a 7% higher permeability and a 4% lower separation factor compared to MOF-Ser. The lower permeability of MOF-Ser MMM compared to MOF-FA MMM might be a result of differences in the MOF/polymer interface caused by the functionalization procedure. These could possibly result in more pronounced polymer rigidification and thus a decrease in permeability[107,189]. The slightly higher separation factor might be a result of the higher CO<sub>2</sub> affinity of MOF-Ser or enhanced size selectivity as a result of polymer rigidification [89,138,190]. However, this difference in gas separation performance of only 4% is smaller than might be expected based on the 62% higher CO<sub>2</sub> uptake of MOF-Ser compared to MOF-FA.

This observation gives rise to the question if CO<sub>2</sub> uptake is useful to predict MMM gas separation performance, and in general, which MOF parameters can be used to predict MMM gas separation performance. Various additional measurements, such as N<sub>2</sub> physisorption (to determine the pore size distribution and thus the possibility of size selectivity), membrane gas solubility measurements for N<sub>2</sub> and CO<sub>2</sub> (to determine if CO<sub>2</sub> sorption in the membrane is enhanced) and differential scanning calorimetry (DSC, to determine T<sub>g</sub>, which might indicate rigidification) are required to better comprehend the MOF-Ser/Matrimid system[89,138].

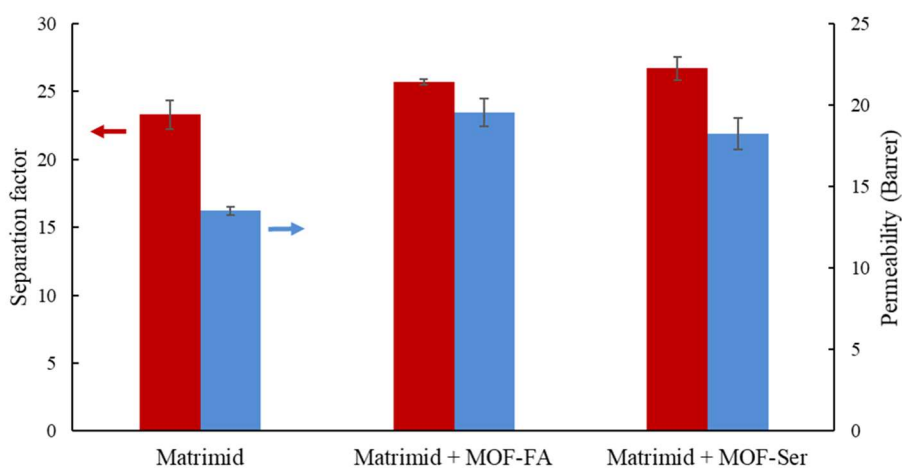


Figure 31: a) CO<sub>2</sub>/N<sub>2</sub> mixed gas separation performance of Matrimid, Matrimid + MOF-FA and Matrimid + MOF-Ser MMM for a 50/50 CO<sub>2</sub>/N<sub>2</sub> gas mixture measured at 5 bar and 35°C.

### 4.3 Platform MOF-808: correlation of MOF parameters with MMM gas separation performance

The unique structure of MOF-808, with 6 vacant positions on the cluster that can be functionalized, allows a thorough and more fundamental study on the effects of (functionalized) MOF-808 parameters on CO<sub>2</sub> permeation in the corresponding MMM[152,184]. In this section,

a series of 5 differently functionalized MOFs are characterized, all synthesized through post-synthetic functionalization of MOF-808 developed with the upscaled, FA-modulated MOF-808 synthesis recipe (denoted as MOF-FA-u). Upscaled MOF-FA was used to ensure the same starting material for all functionalizations, minimizing effects of batch variations. Histidine (MOF-His), trifluoroacetic acid (MOF-TFA), glycolic acid (MOF-GA), benzoic acid (MOF-BA) and lithium sulfate (MOF-Li<sub>2</sub>SO<sub>4</sub>) were selected as functionalizing agent. For these functionalized materials the ‘-u’ denotation was dropped. They were selected based on their hypothesized potential to increase the MOF CO<sub>2</sub> affinity through either an increase in pore polarization through heteroatom incorporation, H-bonding interactions with CO<sub>2</sub>,  $\pi$ - $\pi$  stacking interaction between CO<sub>2</sub> and aromatic rings or a combination of these mechanisms [125,171,191]. Furthermore, various literature reports showed enhanced CO<sub>2</sub> uptake for MOFs containing similar functionalities[89,107,125,192,193].

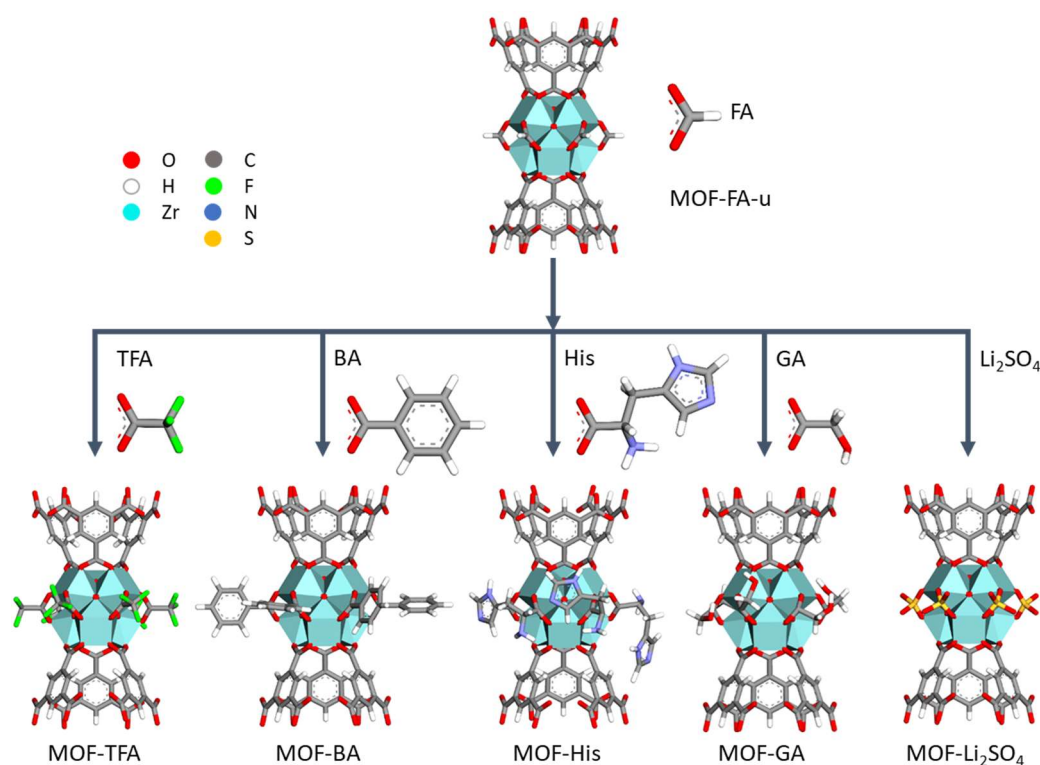


Figure 32: Hypothesized coordination of the functionalizing agents to the MOF cluster. The hypothesized coordination is based on results obtained by Furukawa et al. and Baek et al. [148,164]. The coordination of Li<sup>+</sup> is not shown on the figure.

Figure 32 gives a schematic overview of the hypothesized coordination of the functionalizing agents to the MOF cluster, based on literature single crystal XRD (SCXRD) studies of functionalized MOF-808[139,154]. The functionalizing agents coordinate to the MOF cluster with their carboxylic acid groups (except for MOF-Li<sub>2</sub>SO<sub>4</sub>, which has no carboxylic acid group), effectively pointing their functional groups towards the MOF pore and thus supposedly altering interactions of CO<sub>2</sub> in this pore[154]. Functionalization of MOF-Li<sub>2</sub>SO<sub>4</sub> is

hypothesized to occur through an exchange of a sulfate bonded proton from MOF-SO<sub>4</sub> with Li<sup>+</sup> from Li<sub>2</sub>SO<sub>4</sub>. This is a new functionalization strategy, therefore no SCXRD data are available to make assumptions on the position of the Li<sup>+</sup> cations. As a result, only the sulfate groups are shown for MOF-Li<sub>2</sub>SO<sub>4</sub>[155].

The aim of this section is to gain insight in (1) the potential of MOF-808 functionalization through post-synthetic functionalization, (2) the influence of the different functionalizations on the CO<sub>2</sub> affinity of MOF-808, (3) the effect of MOF-808 functionalization on MMM gas separation performance and (4) a possible correlation between the MOF properties CO<sub>2</sub> uptake and isosteric heat of CO<sub>2</sub> adsorption and MMM performance.

### 4.3.1 XRD

Figure 33 shows the stacked XRD diffractograms of each of the MOFs, together with a calculated spectrum of MOF-808, scaled to the peak situated at a 2θ of 4.3°. All of the functionalized MOFs, the unfunctionalized MOF-FA-u and the calculated MOF-808 diffractogram, show major peaks occurring at an angle of 4.3°, 8.3°, 8.7°, 10.0° and 10.9°. Additionally, the observed XRD diffractograms correspond well with previously reported results for MOF-808 in literature[152,181]. Similar to MOF-Ser, the differences in relative intensities of the peak at 4.3° and the doublet at 2θ values of 8.3° and 8.7° might be caused due to differences in pore content[176,182,183]. The individual XRD diffractograms for each of the MOFs are available in the appendix (Figure A 1 to Figure A 6).

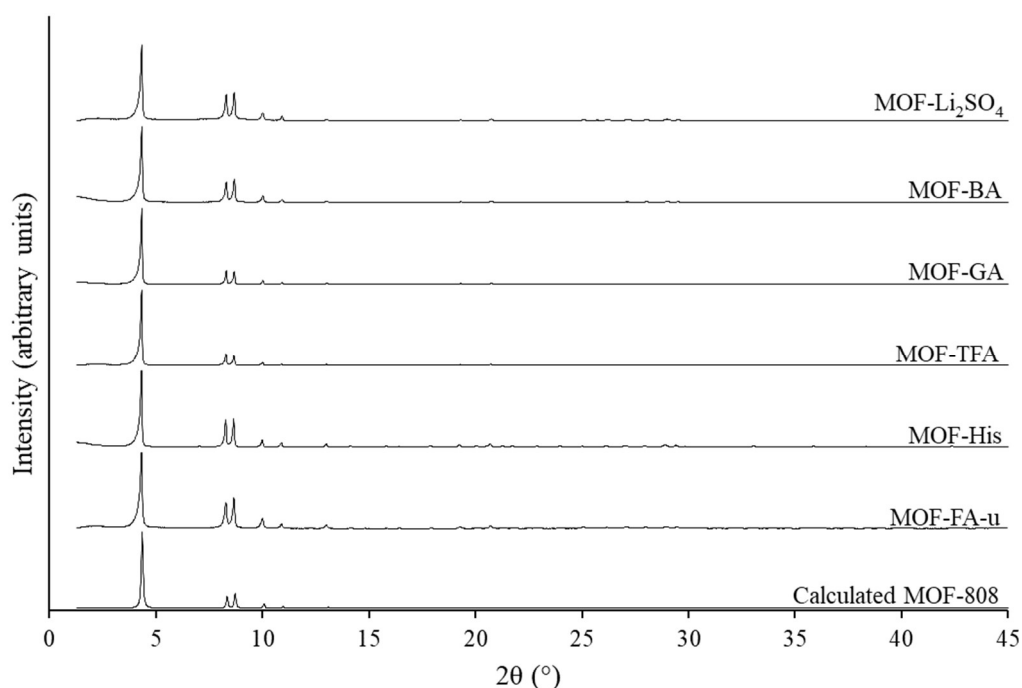


Figure 33: XRD diffractograms of the various functionalized MOFs together with the calculated XRD pattern of MOF-808, stacked and scaled to the peak situated around 4.3°.

### 4.3.2 SEM

SEM images with a magnification (x20000) were taken for each of the MOF samples to evaluate the effect of the different functionalization strategies on particle size and morphology (Figure 34). The SEM images indicate no significant changes in particle morphology upon functionalization. All of the MOFs have particles with an overall truncated octahedron like shape, with most of the particles showing distinct edges. A larger magnification (x50000) showed a similar morphology (Figure A 7).

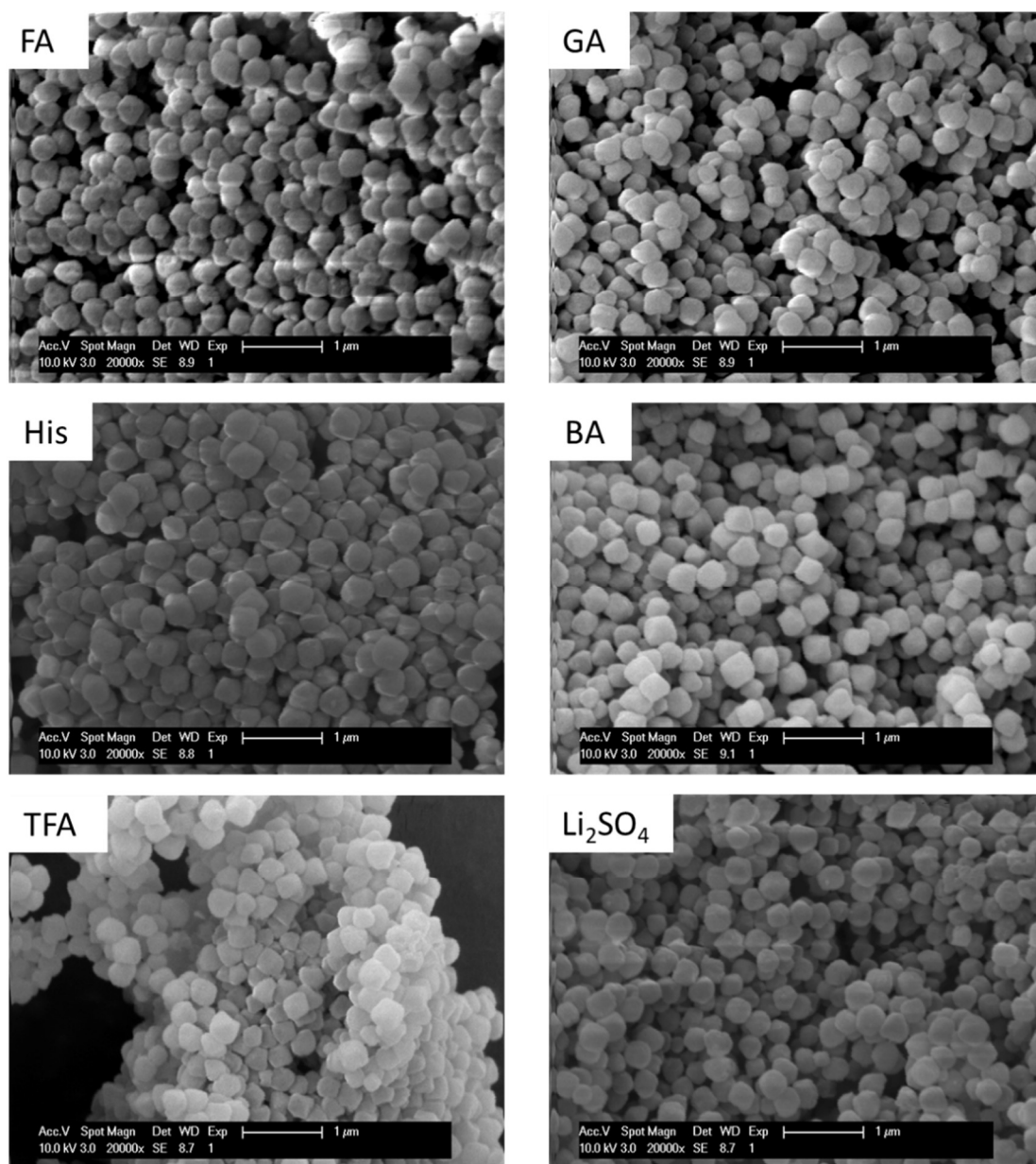


Figure 34: SEM pictures of the functionalize MOFs. Images are taken at a magnification (x20000), a scale bar is represented at the bottom of each figure.

SEM images were used as well to derive a particle size distribution. For each of the SEM pictures the size of 20 particles was measured to obtain a distribution of particle sizes. All MOF

particles have a submicron size in the 300-400 nm range. The average particle size, together with its standard deviation, is reported in Table 10. A one-way analysis of variance (ANOVA) was used to determine if the differences observed in particle size, given the standard deviation of the measurement, were statistically significant. The test resulted in a p-value of 0.1843 for a test with a 95% confidence interval. This p-value indicates that, based on these SEM measurements, there is no difference in particle size between the functionalized MOFs and the parent MOF-FA-u. Therefore, functionalization does not seem to alter the MOF particle size.

Table 10: Particle size distribution with standard deviation for each of the functionalized MOF frameworks.

	Average particle size (nm)		
MOF-FA-u	330	±	30
MOF-His	350	±	30
MOF-TFA	350	±	30
MOF-GA	340	±	20
MOF-BA	350	±	30
MOF-Li <sub>2</sub> SO <sub>4</sub>	340	±	30

### 4.3.3 NMR

<sup>1</sup>H NMR was used to confirm if functionalization was successful and to determine the average loading of functionalizing agent molecules per Zr<sub>6</sub> cluster. Both MOF-TFA and MOF-Li<sub>2</sub>SO<sub>4</sub> lack protons in their chemical structure required for this measurement. To determine the amount of functionalizing agent for MOF-TFA and -Li<sub>2</sub>SO<sub>4</sub>, <sup>19</sup>F NMR and ICP-OES (inductive coupled plasma – optical emission spectroscopy) measurements should be conducted[107,194]. Results for the cluster compositions determined with <sup>1</sup>H NMR are shown in Table 11. For each of the functionalized MOFs, the respective functionalizing agent was present in the framework, suggesting a successful functionalization.

Clearly, MOF-His had the highest loading with 4.7 molecules of histidine present per Zr<sub>6</sub> cluster. The second highest loading was observed for MOF-BA (3.2), followed by MOF-GA and MOF-FA. The difference in loading between these last two MOFs is small (2.3 and 2.2 molecules/Zr<sub>6</sub>-cluster, respectively). The variation in functionalizing agent loading seems to increase with decreasing pKa of the carboxylic acid functional group in the series MOF-His (pKa = 1.78), MOF-GA (pKa = 3.83) and MOF-FA (pKa = 3.75)[179,195]. A lower pKa results in a larger concentration of deprotonated functionalizing agent at similar pH. Since coordination of the functionalizing agent to the cluster is expected to occur with its carboxylate group, it seems probable that a higher availability of the deprotonated functionalizing agent might lead

to higher loadings[154]. MOF-BA deviates from this trend with its pKa of 4.20 and loading of 3.2 molecules/ $Zr_6$  cluster[195]. However, MOF-BA was synthesized using method 1, which uses DMSO as a solvent, whereas the other frameworks were synthesized using the water based method 2, making a comparison difficult. The choice of solvent proved to be a crucial parameter for adsorption of the organic molecule rhodamine B in an Eu-MOF[196]. Similarly, solvent effects might also play a crucial role in functionalizing agent availability in MOF-808 functionalization. None of the frameworks had a functionalizing agent loading equal to the theoretical maximum of 6 molecules/ $Zr_6$  cluster. Therefore, similar as for MOF-Ser, charge neutrality suggest other coordinating species, such as  $OH^-$  or  $Cl^-$ , are associated with the  $Zr_6$  cluster (Table 11)[153,155,184–186].

The loading of MOF-FA (2.5) and MOF-FA-u varied slightly, indicating a small effect of the synthesis procedure (normal and upscaled respectively) on the FA loading of the MOF. A similar variation in FA/ $Zr_6$  cluster was observed for other, different FA modulated MOF-808 synthesis recipes[155]. Finally, all FA groups are removed upon functionalization, independent of the used functionalizing agent (similar as for MOF-Ser). The fact that FA is easily removed together with its low loading on the cluster after MOF-FA-u synthesis indicate FA has a rather low affinity for the MOF cluster[186]. Similarly, FA was readily removed from the MOF-808 cluster by treatment with MeOH at 80°C as reported by Jia *et al.*[153].

Table 11: Cluster composition of functionalized MOF-808 determined by  $^1H$  NMR.

	Cluster composition			
	MOF-FA-u	MOF-His	MOF-GA	MOF-BA
BTC	2.0	2.0	2.0	2.0
FA	2.2	0.0	0.0	0.0
Functionalizing agent	0.0	4.7	2.3	3.2
hydroxyl/ chloride	3.8	1.3	3.7	2.8

#### 4.3.4 EDX

The EDX spectrum of MOF- $Li_2SO_4$  (Figure A 8) shows well-resolved peaks, which can be associated with the Zr content of the MOF. Additional peaks associated with sulfur (S) and chlorine (Cl) are observed as well and thus allow to conclude that S was incorporated in the MOF after functionalization. Based on the EDX spectrum, an average elemental composition of the MOF was calculated, which is shown in Table 12. The atomic composition, expressed as a percentage, indicates a MOF consisting out of 45% S and only 37% Zr. These results are unanticipated, because each cluster in the MOF consists of 6 Zr atoms and has 6 charges to be

compensated. Assuming that the sulfate groups bind in a similar fashion as carboxylic acids and thus compensate only one charge, the maximum theoretical loading of S atoms per  $Zr_6$  cluster would be 6 and the maximum theoretical ratio of S to Zr equal to 1. A higher S percentage might be caused by  $Li_2SO_4$  deposition within the MOF pore. In this case, the  $SO_4$  present in the MOF pore is not solely associated with the MOF cluster but also present as ‘unbound’ material, effectively reducing the MOF pore volume. Another possible explanation for the high S-content is the measurement error of the atomic S percentage (32%). EDX is less suited for analysis of lighter elements because ionization of elements becomes increasingly difficult with decreasing atomic numbers. Furthermore, these elements produce longer wavelength X-rays which are more easily absorbed in the sample. Combined, this results in lower intensity signals for these lighter elements and as a result large errors in the measurements[197]. This is also the reason why no Li signal is observed in the EDX spectrum. Due to the error of 32% on the atomic percentage of sulfur, it is difficult to decisively conclude  $Li_2SO_4$  is deposited in the MOF pores and other measurements such as  $N_2$  physisorption and ICP-OES are required. Finally, the spectrum indicates the presence of Cl which might be present as a residual of the  $ZrOCl_2 \cdot 8H_2O$  precursor used in the MOF-808 synthesis, however this measurement also shows a very high error.

Table 12: Elemental composition of MOF- $Li_2SO_4$ , determined using EDX.

Elemental composition		
Element	Atomic composition (%)	Error (%)
Zr	37	8
S	45	32
Cl	18	76

#### 4.3.5 ATR-FTIR

ATR-FTIR measurements of the MOF are used to confirm that the functionalized MOFs share a similar chemical structure and simultaneously provide information on MOF functionalization. FTIR spectra ranging from a wavenumber of  $400\text{ cm}^{-1}$  to  $1800\text{ cm}^{-1}$  are shown in Figure 35. Peaks located at  $453\text{ cm}^{-1}$  ( $Zr-\mu_3\text{-OH}$  vibration)  $660\text{ cm}^{-1}$  and  $714\text{ cm}^{-1}$  are all associated with the  $Zr_6$  cluster of the MOF and therefore present in each spectrum[89,198]. Likewise, each spectrum shows clearly distinguishable peaks at  $760\text{ cm}^{-1}$ ,  $1385\text{ cm}^{-1}$ ,  $1572\text{ cm}^{-1}$  and  $1620\text{ cm}^{-1}$  corresponding to vibrations of the BTC linker[198]. None of the MOFs showed an absorption band at  $1715\text{ cm}^{-1}$ . This band is normally associated with the vibration of uncoordinated COOH. Therefore its absence suggests no excess BTC or functionalizing agent is present in the MOF pores[198]. Finally, all MOFs showed a broad absorption band around  $3300\text{ cm}^{-1}$  associated

with, amongst others, -OH vibrations of adsorbed solvents (EtOH, H<sub>2</sub>O) [199]. The full 400 cm<sup>-1</sup> to 4000 cm<sup>-1</sup> spectra of the MOFs can be found in Figure A 9 to Figure A 14.

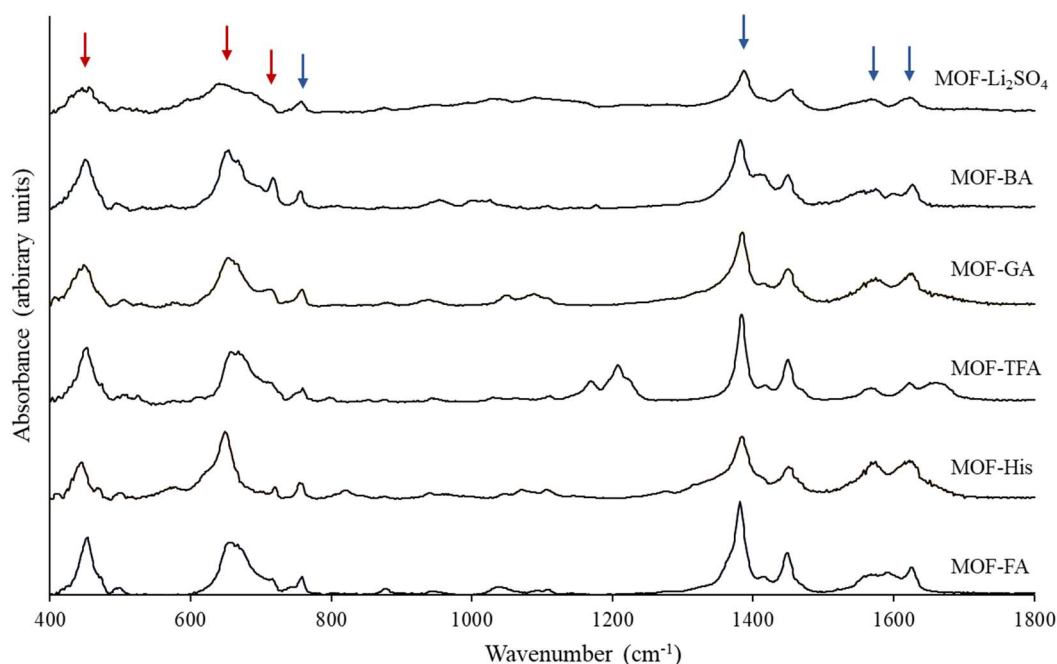


Figure 35: ATR-FTIR spectra of the functionalized MOFs. Wavenumbers associated with the MOF cluster and BTC linker are respectively marked with red and blue arrows.

The absorbance FTIR spectrum of MOF-His is shown in more detail in Figure 36a. Additional peaks for MOF-His compared to MOF-FA-u are visible at 822 cm<sup>-1</sup> and 1067 cm<sup>-1</sup>. They are both associated with mixed NH<sub>3</sub><sup>+</sup> and CH bend vibrations[200]. Additionally, the increase in absorption of the peak situated at 1574 cm<sup>-1</sup> can be attributed as well to NH<sub>3</sub><sup>+</sup> deformation. These NH<sub>3</sub><sup>+</sup> associated peaks suggest the histidine amine group is present in a (partially) protonated form in the MOF pore. Both MOF-FA-u and MOF-His have a clear absorption band at 1380 cm<sup>-1</sup>, which broadens in the case of MOF-His, possibly due to peak overlap with peaks at 1414 cm<sup>-1</sup> and 1416 cm<sup>-1</sup> associated with the C-N stretch of the amine and imidazole functionality[200]. The increase in absorbance at 1622 cm<sup>-1</sup> compared to MOF-FA-u can be attributed to the COO<sup>-</sup> asymmetric stretch and NH bend of histidine[200]. Finally, an increase in absorbance in the band around 3300 cm<sup>-1</sup> can be associated with the N-H stretching of the amine group of histidine, or an increase in OH vibrations (possibly due to an increase of H<sub>2</sub>O or EtOH entrapped in the pore)[136,148]. The full absorbance spectrum can be found in Figure A 10 in the appendix.

The FTIR spectrum of MOF-TFA together with the spectrum of MOF-FA-u can be found in Figure 36b. Two absorption peaks observed at 1170 cm<sup>-1</sup> and 1208 cm<sup>-1</sup> can be attributed to the

C-F symmetrical and anti-symmetrical stretch respectively, indicating a successful TFA functionalization[107]. Signals of a successful functionalization are less pronounced in the FTIR spectra of MOF-GA and MOF-BA (Figure 36c and d). For MOF-GA, a band can be observed in the 1000-1075  $\text{cm}^{-1}$  range, which can be associated with the -OH stretch of the alcohol group of GA[201]. Additionally, a broad signal around 3300  $\text{cm}^{-1}$  can be attributed to the O-H stretching of the alcohol or again by differences in solvent content (Figure A 12)[201,202]. In the case of MOF-BA, a clear increase in absorbance is observed at 718  $\text{cm}^{-1}$ , associated with the C-H out of plane stretch of the benzene ring. Other absorbance peaks at 1026  $\text{cm}^{-1}$  and 1178  $\text{cm}^{-1}$  correspond to the C-H out of plane stretch, ring bend and C-H bend of the benzene ring respectively[203].

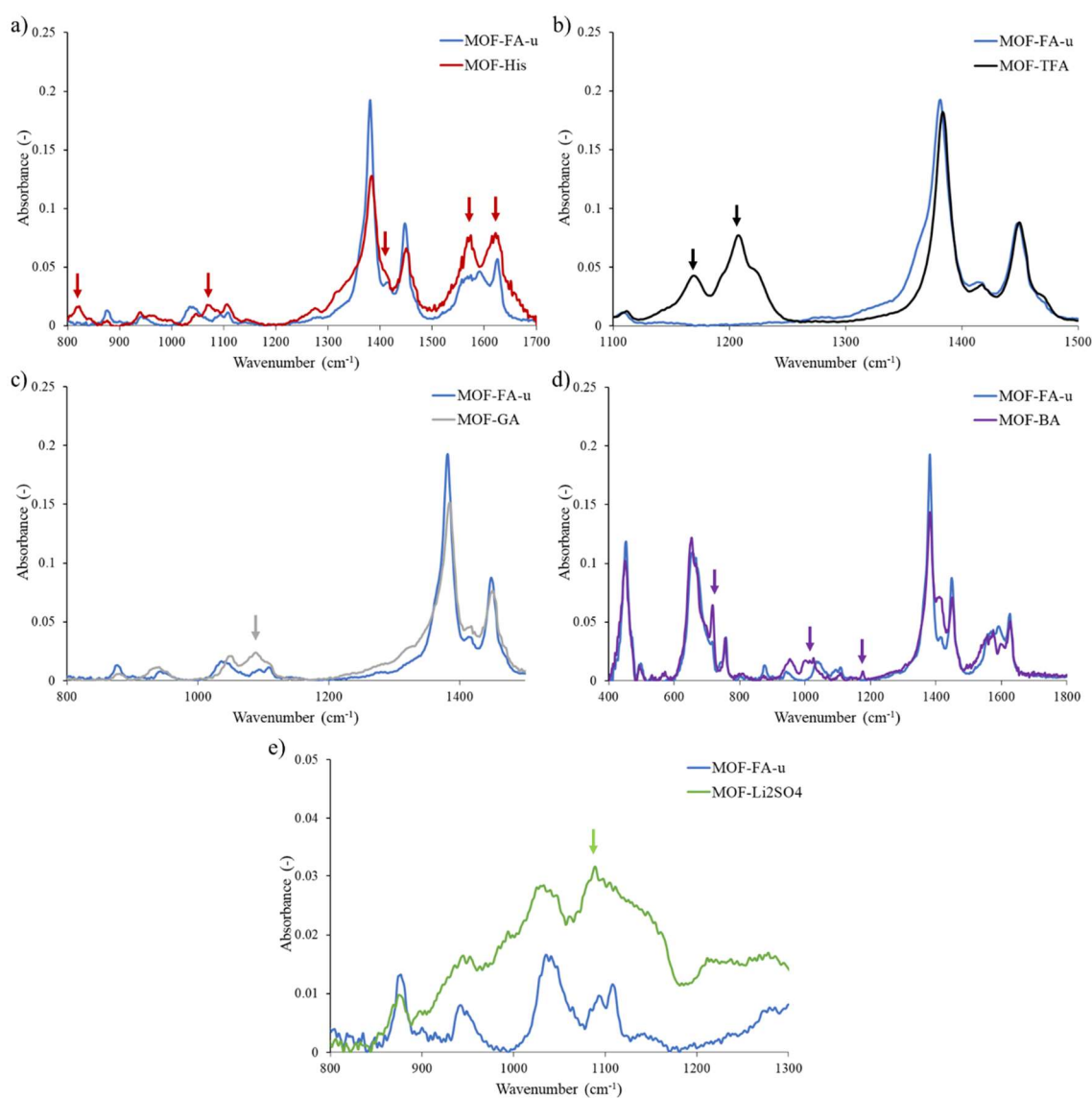


Figure 36: Specific sections out of the ATR-FTIR spectra of each of the functionalized MOFs compared to the spectrum of MOF-FA-u. Characteristic functionalizing agent wavenumbers are indicated with arrows. a) MOF-His, b) MOF-TFA, c) MOF-GA, d) MOF-BA and e) MOF-Li<sub>2</sub>SO<sub>4</sub>.

The ATR-FTIR measurement of MOF-Li<sub>2</sub>SO<sub>4</sub> deviated from the other MOFs, showing a significantly lower intensity and less resolved spectrum. Several consecutive measurements all resulted in the same low intensity spectrum, shown in Figure 36e (full in Figure A 14). A similar trend was observed for the MMM comprised of Matrimid and this MOF (Figure A 19). Nonetheless, signals located at 1095 cm<sup>-1</sup> can be observed, which correspond to the S-O stretching vibration of the sulfate group[204]. Additionally, the overall increase in signal intensity in the 900-1200 cm<sup>-1</sup> region has previously been associated with SO<sub>4</sub> functionalization of MOF-808[155].

During the annealing procedure of the MMM, covalent bonds between the MOF filler and polymer can be formed. This has previously been observed for UiO-66-NH<sub>2</sub> fillers in a Matrimid matrix, where the -NH<sub>2</sub> group of UiO-66-NH<sub>2</sub> reacted with the imine group of Matrimid resulting in an amide[147]. Since histidine has an amine functionality as well, histidine molecules on the surface of MOF-His could possibly react in a similar fashion. This interaction can alter the interfacial morphology of the filler-polymer system, which in turn influences the gas separation performance of the MMM[113]. The formed amide in the UiO-66-NH<sub>2</sub>/Matrimid MMM showed characteristic FTIR absorption peaks associated with the amide functionality at 1534 cm<sup>-1</sup> (C-N stretch and/or N-H bend) and 1648 cm<sup>-1</sup> (C=O stretch)[147]. For each of the functionalized MOFs, MMM ATR-FTIR spectra were measured and compared to the pure Matrimid and functionalized MOF spectrum. The MOF, Matrimid and MMM absorption spectrum of MOF-His are shown in Figure 37. The other spectra can be found in Figure A 15 to Figure A 19.

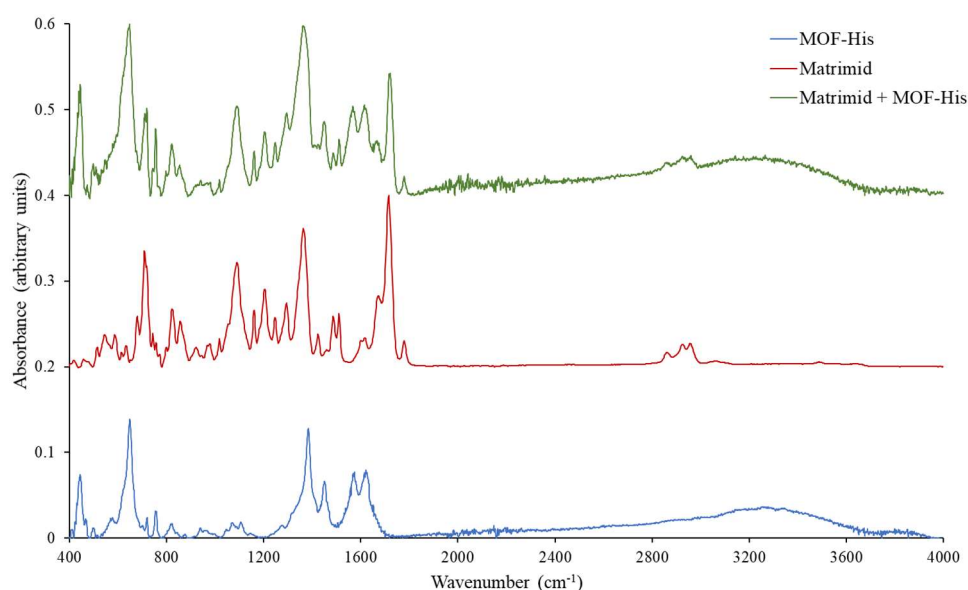


Figure 37: ATR-FTIR adsorption spectrum of MOF-His, Matrimid and Matrimid + MOF-His MMM. Spectra were scaled to an identical intensity for the most intense absorption peak for clarity.

The ATR-FTIR spectra of Matrimid shows various well-resolved absorption peaks associated with the different functionalities of the polymer. Peaks at 2957  $\text{cm}^{-1}$  and 2862  $\text{cm}^{-1}$  are associated with the C-H aliphatic stretch vibration and peaks at 1777  $\text{cm}^{-1}$  and 1717  $\text{cm}^{-1}$  are a result of the C=O asymmetric and symmetric stretch vibrations[89]. Other characteristic vibrations are the benzophenone stretch at 1672  $\text{cm}^{-1}$ , the C=C symmetric stretch at 1618  $\text{cm}^{-1}$ , the aromatic stretching of the para disubstituted phenyl group at 1510  $\text{cm}^{-1}$  and 1488  $\text{cm}^{-1}$ , the C-N stretch at 1363  $\text{cm}^{-1}$  and the C-N-C stretch at 1089  $\text{cm}^{-1}$ [89,205]. The MMM have a filler loading of 10 wt%, therefore the Matrimid signal is predominantly visible in the MMM spectrum. Peaks associated with the MOF can also be found but tend to coincide with the peaks of the Matrimid spectrum, altering their relative intensities. The MOF-His MMM show no distinct new absorption peaks suggesting there were no covalent bonds formed between the polymer and filler. Possibly, the signal of these bonds might be lost in the more pronounced Matrimid absorption peaks. The MMM based on the other MOFs showed similar results with both polymer and MOF functionalities present in the spectrum. None of them showed new absorption maxima.

#### **4.3.6 CO<sub>2</sub> physisorption**

The functionalizing agents used in this work were each selected based on their hypothesized potential to increase the CO<sub>2</sub> affinity of the MOF. In this section, CO<sub>2</sub> adsorption isotherms were measured for the functionalized MOFs. Two parameters associated with CO<sub>2</sub> affinity of the MOF are discussed: CO<sub>2</sub> uptake and the isosteric heat of CO<sub>2</sub> adsorption.

##### *4.3.6.1 CO<sub>2</sub> uptake*

The adsorption isotherms of the MOFs measured at a temperature of 0 °C, 20 °C and 40 °C are shown in Figure 38a-c. The initial region of the adsorption isotherms (0-150 mbar) is shown in more detail for all temperatures in Figure 38d-f. The overall trend observed for CO<sub>2</sub> uptake differs depending on the investigated pressure region, with MOF-TFA showing the highest uptakes up to around 150 mbar for all temperatures. In this low pressure region, CO<sub>2</sub> uptake decreases in the order MOF-TFA > MOF-His > MOF-FA-u > MOF-GA > MOF-Li<sub>2</sub>SO<sub>4</sub> > MOF-BA. Above 150 mbar, MOF-His and MOF-FA shows a stronger increase in CO<sub>2</sub> uptake than MOF-TFA. Initially, MOF-His shows the highest CO<sub>2</sub> uptake, but at even higher pressures it is surpassed by MOF-FA. Finally, at 1000 mbar the CO<sub>2</sub> uptake follows the same general trend for all temperatures, with CO<sub>2</sub> uptake decreasing in the order MOF-FA-u > MOF-His > MOF-TFA > MOF-GA > MOF-BA > MOF-Li<sub>2</sub>SO<sub>4</sub>.

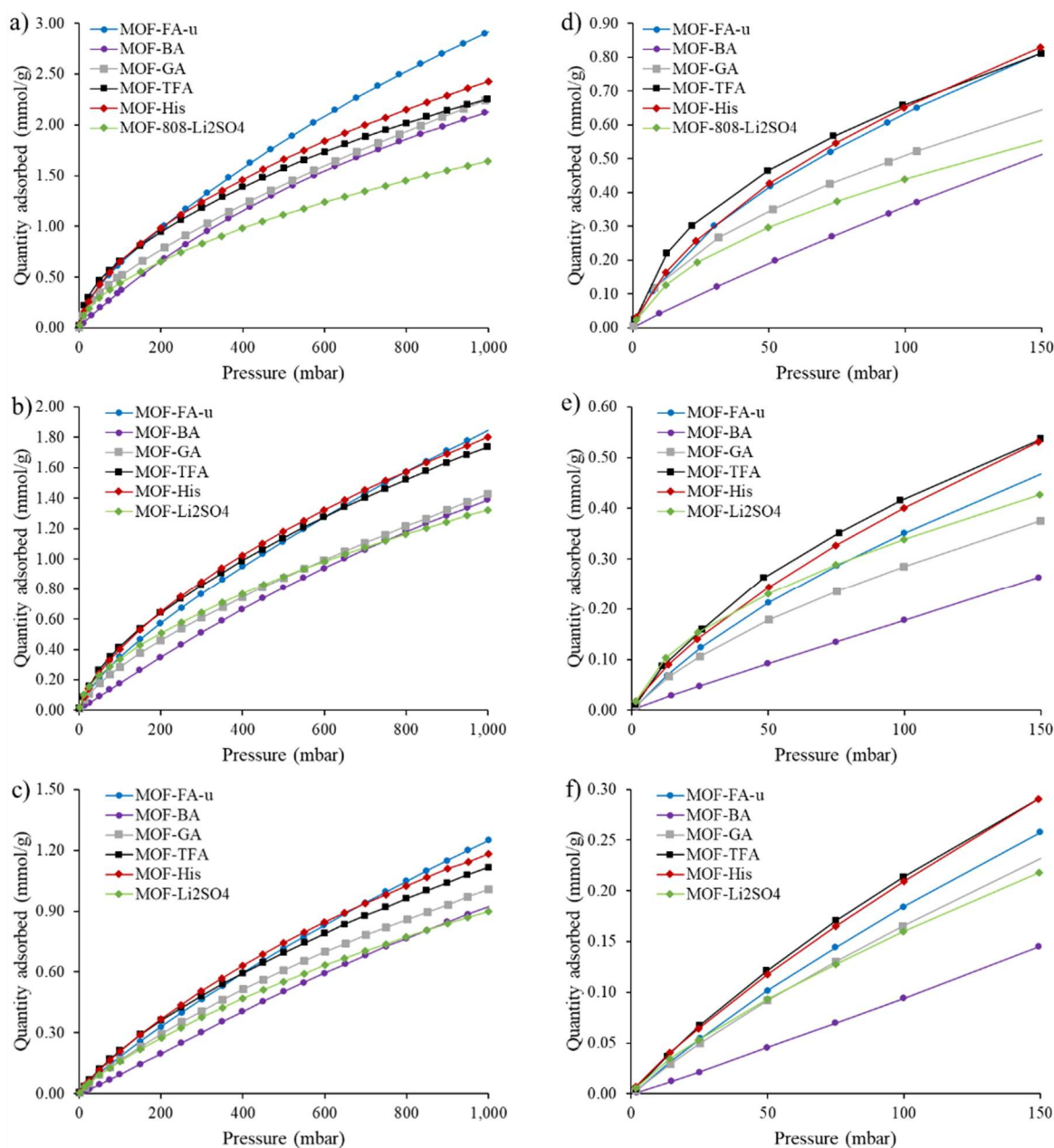


Figure 38: Comparison of the CO<sub>2</sub> adsorption isotherms for each of the functionalized MOFs for the entire pressure range up to 1000 mbar at a temperature of a) 0°C, b) 20°C and c) 40°C. The initial uptake in the low pressure region is also shown for a temperature of d) 0°C, e) 20°C and f) 40°C.

The CO<sub>2</sub> uptake values measured at 50 mbar and 1000 mbar can be found in Table 13. The steeper initial increase in CO<sub>2</sub> uptake of MOF-TFA compared to the other MOFs indicate stronger interaction between CO<sub>2</sub> and this MOF[167,206–208]. Similarly the lower initial uptakes of MOF-GA, MOF-Li<sub>2</sub>SO<sub>4</sub> and MOF-BA suggests these functionalizations resulted in a framework with weaker interaction with CO<sub>2</sub> compared to MOF-FA-u. MOF-BA shows a significantly lower initial CO<sub>2</sub> uptake with the adsorption isotherm showing almost linear behavior in the low pressure region. This behavior has in other work been associated with a lack of high affinity CO<sub>2</sub> binding sites in the MOF[206,209]. At higher pressure, the difference

total in total CO<sub>2</sub> uptake between MOF-BA and the other MOFs is less pronounced, with an almost similar uptake as MOF-GA at 1000 mbar. Another important observation is the relatively lower CO<sub>2</sub> uptake at 1000 mbar of MOF-Li<sub>2</sub>SO<sub>4</sub> compared to the other functionalized MOFs at a temperature of 0°C, which further adds to the hypothesis of Li<sub>2</sub>SO<sub>4</sub> deposition in the MOF pore (in agreement with EDX), possibly resulting in a decrease in available surface area for interaction with CO<sub>2</sub>. A similar trend was observed for open metal site MOFs with solvent molecules blocking access to the metal sites[210]. However, N<sub>2</sub> physisorption measurements are necessary to confirm this. At higher temperatures MOF-Li<sub>2</sub>SO<sub>4</sub> also has the lowest CO<sub>2</sub> uptake at 1000 mbar, but the difference in CO<sub>2</sub> uptake is less pronounced. Upon increasing the temperature, the CO<sub>2</sub> uptake of the MOFs decreases, as can be seen in both Table 13 and Figure 38. This is a result of the higher thermal energy of the CO<sub>2</sub> molecules at higher temperatures[206].

Table 13: CO<sub>2</sub> uptake of the MOFs at 50 mbar and 1000 mbar for a temperature of 0 °C, 20°C and 40°C.

Temperature	CO <sub>2</sub> uptake 50 mbar (mmol/g)			CO <sub>2</sub> uptake 1000 mbar (mmol/g)		
	0 °C	20 °C	40 °C	0 °C	20 °C	40 °C
MOF-FA-u	0.42	0.21	0.10	2.90	1.84	1.25
MOF-His	0.43	0.24	0.12	2.43	1.80	1.18
MOF-TFA	0.46	0.26	0.12	2.25	1.74	1.12
MOF-GA	0.35	0.18	0.09	2.24	1.43	1.01
MOF-BA	0.20	0.09	0.05	2.12	1.39	0.92
MOF-Li <sub>2</sub> SO <sub>4</sub>	0.30	0.23	0.09	1.64	1.32	0.90

#### 4.3.6.2 Comparison of MOF-FA and MOF-FA-u

MOF-FA, synthesized with the normal synthesis recipe, and MOF-FA-u, synthesized with the upscaled recipe, show a significant difference in CO<sub>2</sub> uptake at 0°C. The CO<sub>2</sub> uptake of MOF-FA-u is 69% higher compared to MOF-FA (Figure 30, p51). It seems probable this difference is a result of the used synthesis recipe. Similar differences in CO<sub>2</sub> uptake were observed by Stawowy *et al.* for UiO-66 frameworks built from cerium-oxide nodes, with CO<sub>2</sub> uptake at 1000 mbar varying from 1.34 mmol/g to 1.90 mmol/g (42% difference) by only varying the linker to metal precursor ratio during synthesis. They attributed the difference in adsorption properties of the MOFs to differences in the amount of framework missing linker defects, which might interact preferably with CO<sub>2</sub>[211]. A similar increase in CO<sub>2</sub> uptake was observed by Wu *et al.* for UiO-66 MOFs specifically synthesized with missing linker defects[144]. Missing linker defects in UiO-66 result in a coordinatively unsaturated Zr<sub>6</sub> cluster. Similarly, removal of formate ions from MOF-808 has been used to increase the coordinative unsaturation of the MOF-808 Zr<sub>6</sub> cluster (missing ligand defects)[153,212]. Analogous to UiO-66, CO<sub>2</sub> adsorption

in MOF-808 might be influenced by coordinative unsaturation of the  $Zr_6$  cluster in MOF-808. The average FA loading of MOF-FA-u is 0.3 molecules/ $Zr_6$  cluster lower than for MOF-FA, and thus has a higher amount of missing ligand defects, which might explain the observed difference in  $CO_2$  uptake. In order to investigate this hypothesis,  $CO_2$  adsorption isotherms for MOF-808 with different concentrations of missing ligand defects should be measured.

#### 4.3.6.3 Isothermic heat of $CO_2$ adsorption

Finally, the isothermic heat of  $CO_2$  adsorption ( $Q_{st}$ ) was calculated for the functionalized MOFs, using the Clausius-Clapeyron method. For this calculation, each isotherm was fit with a dual-site Langmuir equation, this fit was subsequently used in the calculation of  $Q_{st}$ [125,166,169,210]. The fit parameters are shown in Table A 1.

Figure 39 shows the results of this analysis for a coverage ranging from 0.1 mmol/g up to 1 mmol/g. In the low coverage region (0.1 mmol/g), a difference of up to 11.6 kJ/mol in  $Q_{st}$  is observed between the MOF with the highest affinity for  $CO_2$  and the lowest affinity for  $CO_2$ , MOF-TFA ( $Q_{st} = 38.6$  kJ/mol at 0.1 mmol/g) and MOF-BA ( $Q_{st} = 27$  kJ/mol at 0.1 mmol/g) respectively. The large differences in  $Q_{st}$  are assumed to be the result of the applied functionalization[134,168,169]. MOF-TFA has the highest  $Q_{st}$  value over the entire measured pressure range. The higher  $Q_{st}$  value of MOF-TFA over MOF-FA-u indicates TFA functionalization effectively succeeded in enhancing the  $CO_2$  affinity of the MOF. This increase in affinity is presumably the result of incorporation of the polar -F groups in the MOF. Deria *et al.* obtained similar results for TFA functionalized NU-1000 (SALI-1) MOFs. They suggested the higher affinity of  $CO_2$  for the MOF was a result of synergistic effects of the  $Zr_6$  cluster and the C-F groups[134].

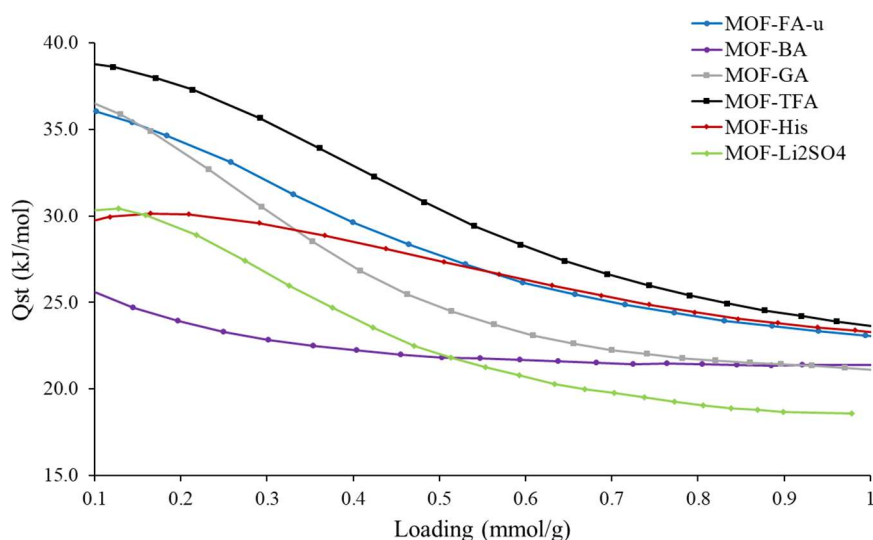


Figure 39:  $Q_{st}$  values of the functionalized MOFs calculated using the Clausius-Clapeyron method.

Remarkably, next to MOF-TFA, MOF-FA-u shows the second highest  $Q_{st}$  value over a large portion of the evaluated coverage range. Only MOF-GA has a slightly higher  $Q_{st}$  (difference of 0.7 kJ/mol at 0.1 mmol/g) up to a coverage of 0.2 mmol/g. Finally, starting from a coverage of roughly 0.6 mmol/g, the  $Q_{st}$  of MOF-His surpasses MOF-FA-u. Again the difference in  $Q_{st}$  is small for these MOFs, with a respective value of 23.2 kJ/mol and 22.9 kJ/mol at a coverage of 1 mmol/g. The high  $Q_{st}$  values at low coverages of MOF-FA-u (and MOF-GA) compared to some of the other functionalized MOFs suggest this framework has a high affinity for CO<sub>2</sub> as well[166,167]. MOF-BA and MOF-His on the other hand showed relatively small changes in  $Q_{st}$  with increasing CO<sub>2</sub> loading, indicating a larger binding site homogeneity[135].

Functionalization altered  $Q_{st}$  both at high and low CO<sub>2</sub> coverages. MOF-TFA, MOF-FA-u, MOF-GA and MOF-Li<sub>2</sub>SO<sub>4</sub> all show a significant decrease in  $Q_{st}$  with increasing coverage. This decrease is the more pronounced in the low coverage region whereas for higher coverages their  $Q_{st}$  appears to approach a pseudo-constant value. This stronger initial decrease has previously been associated with saturation of high affinity binding sites[133,134,167]. For MOF-His and MOF-BA this initial decrease is significantly lower. Both observations suggest functionalization influences the CO<sub>2</sub> binding strength at low coverages. The pseudo-plateau in  $Q_{st}$  observed for all MOFs at higher coverages has been suggested to be a result of pore filling of the MOF based on measurements for isostructural MOFs[133,167,168,213]. Since all of the functionalized MOFs share the MOF-808 general pore architecture this might explain the similar  $Q_{st}$  values at 1 mmol/g for MOF-TFA, MOF-FA-u and MOF-his (23-24 kJ/mol)[133,167]. However, MOF-BA and MOF-GA have a similar but lower pseudo-constant  $Q_{st}$  at 1 mmol/g (22.4 kJ/mol), and the pseudo constant  $Q_{st}$  for MOF-Li<sub>2</sub>SO<sub>4</sub> is even lower (18.6 kJ/mol). These differences are similar to literature differences in  $Q_{st}$  at the pseudo-plateau for functionalized NU-1000[134]. Thus, functionalization also seems to influence  $Q_{st}$  at higher coverages, possibly as a result of the functionalizing agent modifying pore chemistry and physical parameters such as pore volume[127,167,168,214,215].

#### **4.3.7 Gas separation performance**

MMM consisting of the functionalized MOFs in Matrimid were synthesized and tested for their CO<sub>2</sub>/N<sub>2</sub> gas separation performance. Mixed-gas separation factors and permeabilities were measured for gas mixtures consisting of 15/85 and 50/50 CO<sub>2</sub>/N<sub>2</sub>, together with the permeability of the pure gasses. These pure gas permeabilities were used to calculate the CO<sub>2</sub>/N<sub>2</sub> ideal selectivities of the MMM.

#### 4.3.7.1 CO<sub>2</sub> permeability

The CO<sub>2</sub> permeability of the MMM based on the functionalized MOFs is shown in Figure 40 for different CO<sub>2</sub>/N<sub>2</sub> feed gas mixtures. Similar as for the MOF-Ser MMM (section 4.2.2.2), incorporation of the MOF in the polymer matrix results in an increase in permeability. This is attributed to either the increase in free volume of the MMM compared to the pure polymer membrane upon MOF incorporation or an increase in free volume due to disruption of polymer packing[89,138].

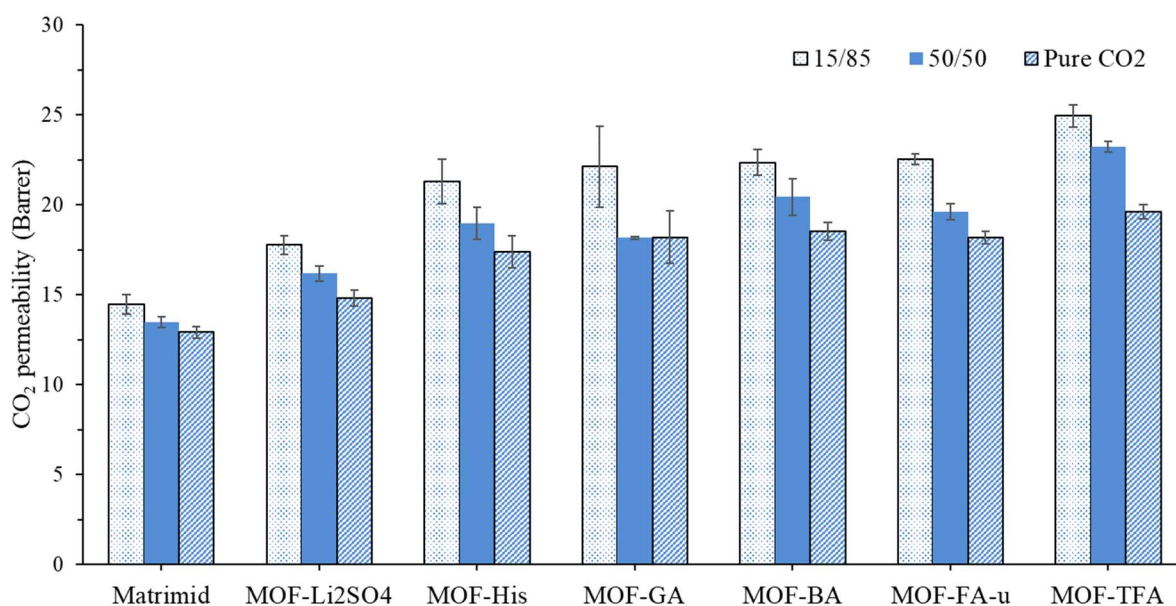


Figure 40: CO<sub>2</sub> permeability of the functionalized MOFs in Matrimid MMM for a 15/85 and 50/50 gas mixture and pure CO<sub>2</sub> gas. All measurements were conducted at a pressure of 5 bar and temperature of 35 °C. The shown permeability values are an average value calculated from data of 3 membrane coupons, except for MOF-GA where only 2 coupons were measured.

For the MMM, a general trend in permeability is observed for the mixed-gas and pure gas permeation experiments: MOF-Li<sub>2</sub>SO<sub>4</sub> < MOF-His ~ MOF-GA ~ MOF-BA ~ MOF-FA < MOF-TFA. MOF-TFA clearly shows the highest permeability for each experiment, with a permeability of 24.9 Barrer, 23.2 Barrer and 19.6 Barrer for the 15/85 CO<sub>2</sub>/N<sub>2</sub>, 50/50 CO<sub>2</sub>/N<sub>2</sub> and pure CO<sub>2</sub> feed. This corresponds to a 72% increase for the mixed gas measurements and a 52% increase for the pure gas respectively compared to the pristine Matrimid membrane.

MOF-TFA also had the highest Q<sub>st</sub> value over the entire evaluated CO<sub>2</sub> coverage range (Figure 39), suggesting the higher permeability could be a result of the stronger interaction of the MOF with CO<sub>2</sub>. The other MMM, except for the ones based on MOF-Li<sub>2</sub>SO<sub>4</sub>, had similar CO<sub>2</sub> permeabilities (overlapping error bars). MOF-Li<sub>2</sub>SO<sub>4</sub> based MMM showed a lower permeability for all feed compositions, suggesting a fundamental difference in the properties of this MOF compared to the others. Based on the EDX and gas uptake measurements this might

be a result of the hypothesized  $\text{Li}_2\text{SO}_4$  deposition in the MOF pores influencing permeability. Again,  $\text{N}_2$  physisorption measurements are required to get a more comprehensive understanding of this observation. Next to the properties of the MOF, functionalization might affect the interactions in the MOF/polymer system, possibly causing differences in (1) polymer packing disruption, resulting in an increase in free volume and thus higher permeabilities and (2) polymer rigidification, resulting in lower permeabilities [89,136,138,216]. Differential scanning calorimetry (DSC) measurements and positronium annihilation lifetime spectroscopy (PALS) could provide more insight in the mechanism causing the permeability increase, respectively giving insight in  $T_g$  changes (and thus polymer rigidification) and changes in free volume.

Finally, all membranes (including Matrimid) showed a decrease in permeability with increasing  $\text{CO}_2$  partial pressure. The  $\text{CO}_2$  partial pressure increases for the various feed compositions in the order 15/85  $\text{CO}_2/\text{N}_2$  feed (0.75 bar) < 50/50  $\text{CO}_2/\text{N}_2$  (2.5 bar) < pure  $\text{CO}_2$  (5 bar). A similar trend was observed for UiO-66- $\text{NH}_2$  in 6FDA-DAM and imide functionalized UiO-66- $\text{NH}_2$  in 6FDA-Durene [138,217,218]. In both cases, the behavior was associated with the dual-sorption model (equation 12) used to describe gas solubility in glassy polymers. The excess free volume elements of Matrimid adsorb  $\text{CO}_2$ , thus contributing to the gas solubility and permeability ( $P = S \times D$ ). Upon increasing the pressure these Langmuir sorption sites are saturated and gas adsorption in the polymer is dominated by the Henry adsorption part of the dual-sorption equation. Absolute values of gas adsorbed in Matrimid keep on increasing with increasing pressure, but solubility is defined as the pressure normalized adsorption and thus solubility and permeability will decrease with increasing pressure. A similar trend was observed for pure Matrimid membranes in this work and in literature [219].

#### 4.3.7.2 $\text{CO}_2/\text{N}_2$ selectivity and separation factor

Figure 41 shows both the mixed-gas separation factor and ideal selectivity for Matrimid and the MMM. Differences in separation factor are rather small for the 15/85  $\text{CO}_2/\text{N}_2$  gas mixture. In general, incorporation of the MOF increases the separation factor slightly compared to Matrimid. The highest increases are observed for MMM of MOF-BA and MOF-TFA. These MMM respectively showed an increase in separation factor of 15% (34.0) and 12% (33.0) compared to Matrimid. For the 50/50  $\text{CO}_2/\text{N}_2$  gas mixture, differences in separation factor were more pronounced. Again the highest increases compared to Matrimid were observed for MOF-TFA and MOF-BA with an increase of 32% (34.1) for the former and 26% (32.7) for the latter. Remarkably, MMM based on MOF- $\text{Li}_2\text{SO}_4$  and MOF-FA showed no increase in separation factor for the 50/50  $\text{CO}_2/\text{N}_2$  feed mixture compared to pure Matrimid membranes.

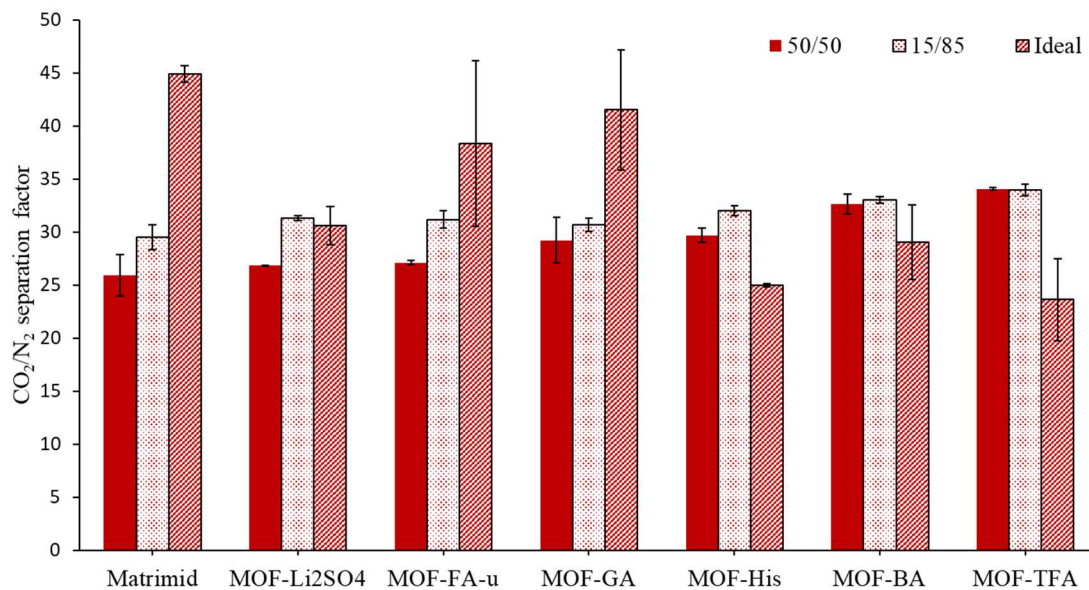


Figure 41:  $\text{CO}_2/\text{N}_2$  separation factor of the functionalized MOFs in Matrimid MMM for a 15/85 and 50/50 gas mixture together with the ideal  $\text{CO}_2/\text{N}_2$  selectivity. All measurements were conducted at a pressure of 5 bar and temperature of 35 °C. The shown selectivity and separation factor values are an average value calculated from data of 3 membrane coupons, except for MOF-GA where only 2 coupons were measured.

MOF-TFA MMM showed the highest separation factor for both experiments. Similar as for the permeability, this seems to correspond with the stronger interaction between  $\text{CO}_2$  and the MOF, as evidenced by its higher  $Q_{\text{st}}$  value. However, the second best separation factor was measured for MOF-BA MMM for both gas mixtures and this MOF had a lower  $Q_{\text{st}}$  value than most of the others MOFs over the entire  $\text{CO}_2$  loading range (Figure 39). This suggest differences in  $Q_{\text{st}}$  have no straightforward relationship with mixed-gas separation performance.

Other factors might be influencing the separation factor of the MMM as well. Polymer rigidification could result in an enhanced separation factor/selectivity through an increase in size selectivity[89,136,138,216]. This seems to be contradicted by the observed increase in permeability. However, at low MOF loadings polymer rigidification effects on permeability might be moderate and compensated by the increase in volume by incorporation of the porous MOF[216]. MOF/polymer interaction could also occur in the form of polymer infiltration in the MOF pore. This type of interaction could possibly result in an increase in selectivity (through enhanced size selectivity of the infiltrated MOF pores), but also reduces the  $\text{CO}_2$  permeability[190]. Moreover, functionalization is expected to alter the surface chemistry of the MOFs. This concept was used to enhance gas separation performance of Matrimid membranes containing UiO-66- $\text{NH}_2$  post synthetically modified with various organic functionalizing agents. The resulting MOFs showed an increase in selectivity which was ascribed to the better interfacial compatibility of the MOF/polymer system. Interestingly the best performance was

associated with a phenyl acetyl group modified MOF. The hypothesized increase in compatibility was partially attributed to  $\pi$ - $\pi$  interaction of the phenyl group and Matrimid. A similar interaction might explain the good performance of MOF-BA[189].

Similar as for the permeability data, a decrease in  $\text{CO}_2/\text{N}_2$  separation factor is observed for the 50/50  $\text{CO}_2/\text{N}_2$  gas mixture compared to the 15/85 gas mixture. Again the dual-sorption model can be used to rationalize this decrease. The decrease in permeability for increased  $\text{CO}_2$  partial pressure discussed in the previous section is a result of saturation of the excess free volume present in the polymer, thus lowering the  $\text{CO}_2$  solubility[41]. Similarly a decrease in  $\text{N}_2$  partial pressure will cause the  $\text{N}_2$  solubility to increase. However, this increase will be less pronounced for  $\text{N}_2$  than it would be for  $\text{CO}_2$ , since  $\text{N}_2$  generally shows a lower affinity for the polymer matrix[41]. The decrease in  $\text{CO}_2$  solubility and increase in  $\text{N}_2$  solubility will result in an overall decrease in solubility selectivity and thus in a decrease in separation factor. A similar trend, although measured at higher pressures, was observed by Ahmad *et al.* for various functionalized UiO-66/6FDA-DAM MMM[217,220]. They used the dual-sorption model in a similar way as described in this paragraph to explain their results. The fact that some MOFs show a less pronounced, to no decrease upon changing the feed gas mixture might be a result of different effects of MOF functionalization on the MMM gas sorption behavior of  $\text{CO}_2$ .  $\text{CO}_2$  adsorption measurements of the MMM are required to further investigate this observation.

Finally, Matrimid and some of the MMM had a significantly higher ideal selectivity compared to their separation factor[221]. In literature this phenomenon has often been ascribed to competitive sorption of the less permeable component. The presence of this component in the feed gas mixture causes it to adsorb in free volume elements which normally would be available for  $\text{CO}_2$  adsorption. This decrease in adsorption and thus solubility causes a decline in  $\text{CO}_2$  permeability and separation factor. A similar trend has been observed for other MMM[221,222]. On the other hand, MMM based on MOF-His, MOF-BA and MOF-TFA showed a higher separation factor compared to their ideal selectivity. This behavior has also been reported in literature and is rationalized by stating  $\text{CO}_2$  blocks adsorption sites which would otherwise be available to the minor gas component, resulting in an increase in separation factor compared to ideal selectivity[220]. In this work both trends were observed and the differences in ideal selectivity between the MMM were very pronounced, suggesting the type of functionalization influences this behavior strongly. However, the high error bars on the ideal selectivity measurements make it difficult to couple this behavior to any MOF or MOF/polymer system properties, thus leaving this trend largely unexplained.

### 4.3.8 Correlation of MOF parameters with MMM performance

The premise of this section was to examine which MOF parameters could be related to the MMM gas separation performance. Two parameters were evaluated: the CO<sub>2</sub> uptake of the MOF (at various temperatures and pressures) and the Q<sub>st</sub> at various coverages. To quantify the relationship between these parameters and MMM performance parameters, a correlation coefficient was calculated. It is important to note that this correlation coefficient only gives the degree of linearity of the relationship between parameters, and as a result does not say anything about other possible relationships (e.g. exponential). In addition, correlation does not mean causality[223]. The calculated correlation coefficients are shown in Table 14. The guidelines stated by Sheldon *et al.* were followed to interpret the results. A correlation above 0.80 was interpreted as strong and a correlation coefficient of 0.30 or less as weak. Correlation values between 0.30 and 0.80 were considered moderate[223].

Table 14: Calculated correlation coefficients for MOF parameters and MMM gas separation performance ( $\alpha$  = selectivity,  $a^*$  = separation factor,  $P$  = CO<sub>2</sub> permeability).

	CO <sub>2</sub> uptake 50 mbar			CO <sub>2</sub> uptake 1000 mbar			Q <sub>st</sub> , 0.1 mmol/g	Q <sub>st</sub> , 0.5 mmol/g	Q <sub>st</sub> , 1 mmol/g
	0 °C	20 °C	40 °C	0 °C	20 °C	40 °C			
$\alpha^*_{15/85}$	0.06	0.08	0.01	-0.08	0.25	0.04	-0.20	0.34	0.38
$\alpha^*_{50/50}$	-0.04	-0.27	-0.17	-0.05	-0.01	-0.13	0.05	0.30	0.48
$\alpha_{ideal}$	-0.14	-0.30	-0.22	0.27	-0.20	0.00	0.30	-0.31	-0.28
$P_{15/85}$	0.43	-0.01	0.17	0.58	0.54	0.48	0.50	0.71	0.86
$P_{50/50}$	0.37	0.05	0.15	0.40	0.50	0.38	0.34	0.70	0.81
$P_{ideal}$	0.31	-0.16	0.03	0.57	0.45	0.41	0.41	0.60	0.81

The CO<sub>2</sub> uptake of the MOF in general showed a poor correlation with the 15/85 and 50/50 CO<sub>2</sub>/N<sub>2</sub> separation factors and CO<sub>2</sub>/N<sub>2</sub> ideal selectivity of the MMM, with all calculated correlation coefficients being classified as weak. The correlation between CO<sub>2</sub> uptake and MMM CO<sub>2</sub> permeability is somewhat better with the CO<sub>2</sub> uptake at 1000 mbar showing stronger correlations than CO<sub>2</sub> uptake at 50 mbar. Although the correlation of CO<sub>2</sub> uptake with CO<sub>2</sub> permeability was stronger than with the separation factor, the correlation coefficients for this relationship were still considered weak. Therefore, it can be concluded that CO<sub>2</sub> uptake shows no linear relationship with MMM performance for the system studied in this thesis.

Likewise, Q<sub>st</sub> at low coverage values shows a weak linear relationship with the separation factor. At a coverage of 1 mmol/g Q<sub>st</sub> correlations with the separation factor were slightly better than for the CO<sub>2</sub> uptake. Additionally, at this coverage correlations with the separation factor were clearly stronger than these observed for the lower coverage Q<sub>st</sub> values. However, once more the correlation remains rather weak with no values higher than 0.5 being observed for the

correlation coefficient. As a result, there seems to be no linear relationship between  $Q_{st}$  and separation factor as well. These results correspond well with the experimental observations for MOF-TFA and MOF-BA. MMM based on these MOFs showed respectively the highest and second highest separation factor, but the MOFs themselves differed strongly in their relative  $Q_{st}$  compared to the other MOFs. MOF-TFA had the highest  $Q_{st}$  of all MOFs over the entire  $CO_2$  coverage range, whereas MOF-BA had a low  $Q_{st}$  compared to most other functionalized MOFs.  $Q_{st}$  at various coverages correlated better with  $CO_2$  permeability, both for the mixed and pure gas experiments. Furthermore, the correlation became stronger with increasing  $CO_2$  coverage. The strongest correlations with  $CO_2$  permeability were observed for  $Q_{st}$  at a coverage of 1 mmol/g, which was the only parameter having correlation coefficients classified as strong. Therefore, there seems to be an adequate linear relationship between  $Q_{st}$  and  $CO_2$  permeability. In strong contradiction to literature, where  $CO_2$  uptake is often used to explain enhancement of MMM separation performance, in this work no such relationship was observed[89,138]. Other MOF parameters such as BET area, pore volume and pore size might be interesting to correlate with MMM parameters as well. As a final note, it is important to consider that these observations are specific for the functionalized MOF-808/Matrimid system herein described. Other MOF/polymer combinations might result in different observations. Extending this strategy to other polymer/MOF combinations might help generalize some of these observations.

#### **4.4 MMM based on UTSA-120a**

MOFs from the SIFSIX family have shown exceptional performance as filler in MMM[160,161]. Recently, a new member of this family was developed, the  $CuSiF_6$  based MOF UTSA-120a. This MOF showed an exceptional  $CO_2/N_2$  selectivity as adsorbent, making it a promising material for  $CO_2$  capture. The good gas separation performance of MMM based on MOFs from the SIFSIX family, together with the exceptional adsorbent properties of UTSA-120a, make this MOF a potentially interesting filler for MMM. UTSA-120a was synthesized, characterized and subsequently incorporated in a 6FDA-DAM polymer matrix. Finally, these MMM were evaluated for their mixed gas  $CO_2/N_2$  and  $CO_2/CH_4$  gas separation performance.

##### **4.4.1 XRD**

XRD measurements of the synthesized MOF particles were conducted to simultaneously confirm whether a crystalline material was formed and whether this material had the crystal structure of UTSA-120a. The measured XRD diffractogram is shown in Figure 42. High intensity peaks are observed at a  $2\theta$  value of  $8.28^\circ$ ,  $11.76^\circ$  and  $12.26^\circ$ . Some peaks with a lower

intensity were found at  $16.65^\circ$ ,  $17.01^\circ$  and  $18.64^\circ$ . Finally, there are well-resolved high intensity peaks at  $20.75^\circ$ ,  $21.63^\circ$ ,  $23.66^\circ$  and  $24.69^\circ$  as well. The measured diffractogram strongly resembles literature results for UTSA-120a in terms of peak position as well as relative intensity[157]. Based on this diffractogram it can be concluded that a crystalline material with the UTSA-120a crystal structure is obtained after synthesis.

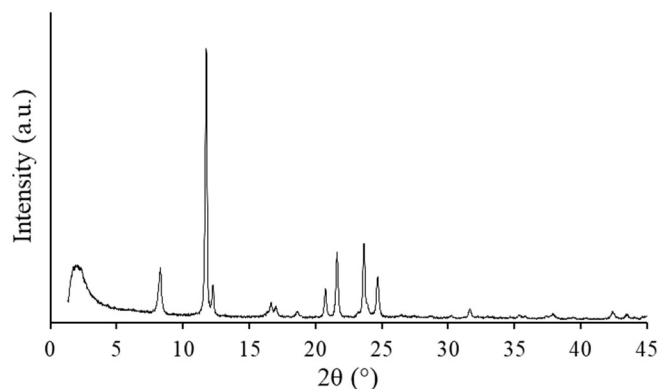


Figure 42: XRD diffractogram of UTSA-120a.

#### 4.4.2 ATR-FTIR

ATR-FTIR measurements of UTSA-120a showed characteristic absorption at wavenumbers associated with both the nodes and linkers of the MOF (Figure 43). Both signals observed at  $479\text{ cm}^{-1}$  and  $733\text{ cm}^{-1}$  are associated with the Si-F asymmetric stretch of the hexafluorosilicate anion[224,225]. The tetrazine group of the linker is responsible for the strong absorption peaks at  $1401\text{ cm}^{-1}$  and  $1425\text{ cm}^{-1}$ , which are attributed to the ring stretch of the tetrazine ring. The band observed at  $880\text{ cm}^{-1}$  to  $970\text{ cm}^{-1}$  is a result of the in plane ring bend vibration of the tetrazine functionality[201,226]. The vibration observed at  $1517\text{ cm}^{-1}$  and  $1568\text{ cm}^{-1}$  are assigned to the pyridine rings in the dpt linker. Similarly, the strong absorption peak at  $1623\text{ cm}^{-1}$  might be due to the pyridine ring vibrations[201]. However, this vibration slightly deviates from the expected value of  $1610\text{ cm}^{-1}$  for a 4-substituted pyridine ring. Possibly, this deviation is a result of the interaction between the pyridine ring and the  $\text{Cu}^{2+}$  of the copper hexafluorosilicate nodes[201]. The absorption band ranging from  $810\text{ cm}^{-1}$  to  $850\text{ cm}^{-1}$  is a result of the out of plane vibration of 2 adjacent protons on the pyridine ring[201]. Finally, the vibration at  $3090\text{ cm}^{-1}$  and  $3120\text{ cm}^{-1}$  are associated with the C-H stretch vibration of the aromatic ring protons[226]. The strong band observed in the higher wavenumber region, especially around  $3200\text{-}3700\text{ cm}^{-1}$ , is possibly a result of leftover methanol from the washing procedure present in the pore structure, since no MOF activation step was conducted[201,202]. Absorption peaks associated with all of the expected framework species can be found in the spectrum, indicating the synthesized particles have the desired chemical structure.

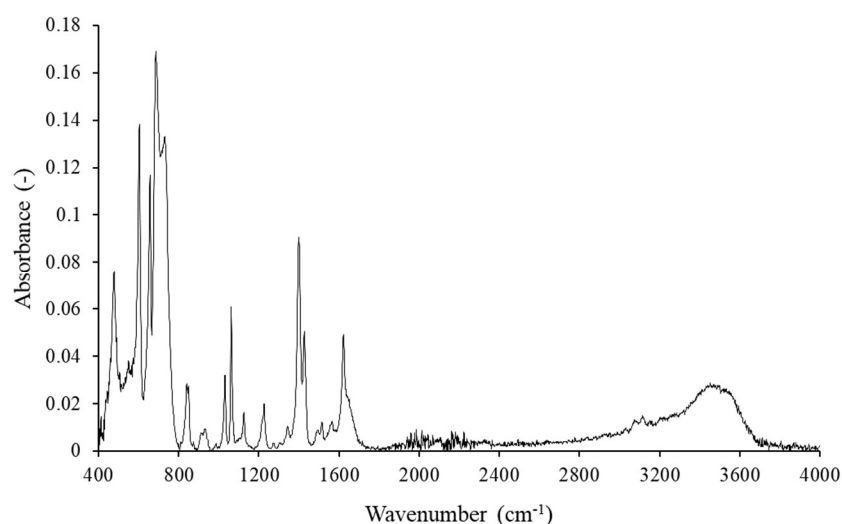


Figure 43: ATR-FTIR spectrum of UTSA-120a.

#### 4.4.3 Gas separation performance

Finally, MMM of 6FDA-DAM containing UTSA-120a as filler material were synthesized and tested for their mixed-gas separation performance. The results for a feed gas composition of 15/85 CO<sub>2</sub>/N<sub>2</sub> and a 50/50 CO<sub>2</sub>/CH<sub>4</sub> are shown in Figure 44. The MMM show a small decrease in separation factor for the CO<sub>2</sub>/N<sub>2</sub> gas mixture of 4.4%. However, the opposite trend is observed for the CO<sub>2</sub>/CH<sub>4</sub> gas separation experiment, where inclusion of UTSA-120a increases the separation factor to 23.4 (7.2% increase). Furthermore, a ~32% decrease in permeability for the MMM is observed for both experiments.

Enhancements in CO<sub>2</sub> solubility will influence the CO<sub>2</sub>/N<sub>2</sub> selectivity more strongly than CO<sub>2</sub>/CH<sub>4</sub> selectivity, since condensation temperature is often used as a measure for solubility and it decreases in the order CO<sub>2</sub> > CH<sub>4</sub> > N<sub>2</sub>[21]. Differences in diffusivity will be more pronounced in CO<sub>2</sub>/CH<sub>4</sub> separations as a result of the relatively larger kinematic diameter of CH<sub>4</sub> compared to N<sub>2</sub> and CO<sub>2</sub>[227]. In this case, the difference in CO<sub>2</sub>/CH<sub>4</sub> separation factor is increased and the CO<sub>2</sub>/N<sub>2</sub> separation factor is not. This suggests the increase is the result of a parameter influencing diffusivity selectivity. Enhanced diffusivity selectivity could be the result of (1) size selective separation between the molecules by the MOF, (2) a densification of the polymer matrix surrounding the MOF particles, (3) size selective interfacial defects occurring at the MOF/polymer interface or (4) polymer intrusion resulting in size selective MOF pores[21,98,137,162,228]. The decrease in permeability makes explanation (3) less likely. Polymer rigidification seems to be able to explain both the observed decrease in permeability and increase in separation factor[104,136,227]. This however does not exclude the possibility of pore infiltration or even possible pore blocking of the MOF[227,228]. Further

characterization (DSC, membrane gas sorption, PALS) and gas permeation experiments (pure gas, varying pressure and feed conditions) are needed to elucidate the exact mechanism at play.

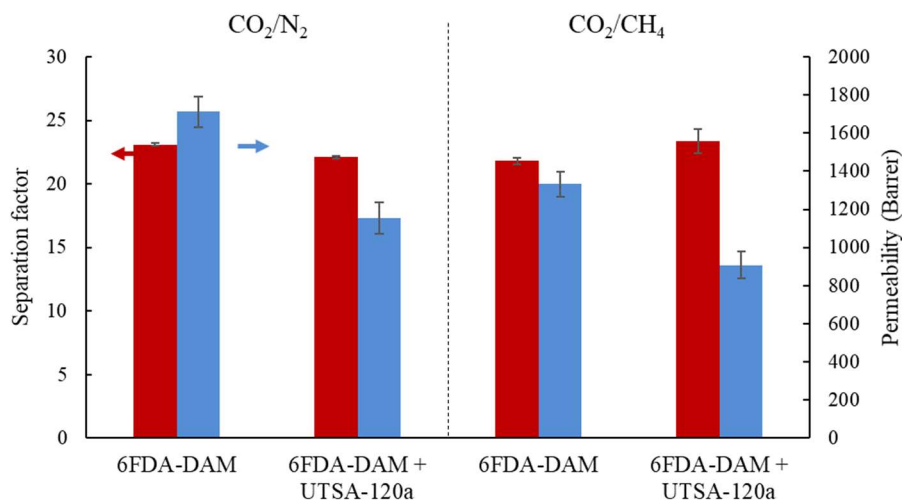


Figure 44: Gas separation performance of 6FDA-DAM pure polymer and 6FDA-DAM + UTSA-120a for a 15/85 CO<sub>2</sub>/N<sub>2</sub> gas mixture and a 50/50 CO<sub>2</sub>/CH<sub>4</sub> gas mixture, measured at an upstream pressure of 5 bar and temperature of 35 °C.

#### 4.5 Comparison of MMM with the Robeson upper bound

In this final section, a comparison of the membranes developed in this thesis with the Robeson upper bound for the evaluated gas mixtures is provided. This theoretical line represents the gas separation performance of state of the membranes reported in 2008. Figure 45 shows the CO<sub>2</sub>/N<sub>2</sub> gas separation performance of Matrimid MMM of the modified MOF-808 synthesized in this thesis. Although a movement towards the upper bound is observed, the final performance is still far removed from crossing it. These results are not surprising, since the polymer material dictates the baseline for MMM performance and Matrimid is known to be a moderately performing polymer[107]. UTSA-120a MMM showed for both CO<sub>2</sub>/N<sub>2</sub> and CO<sub>2</sub>/CH<sub>4</sub> separations a movement away from the upper bound, as a result of the decrease in permeability compared to pure 6FDA-DAM(Figure A 20 and Figure A 21).

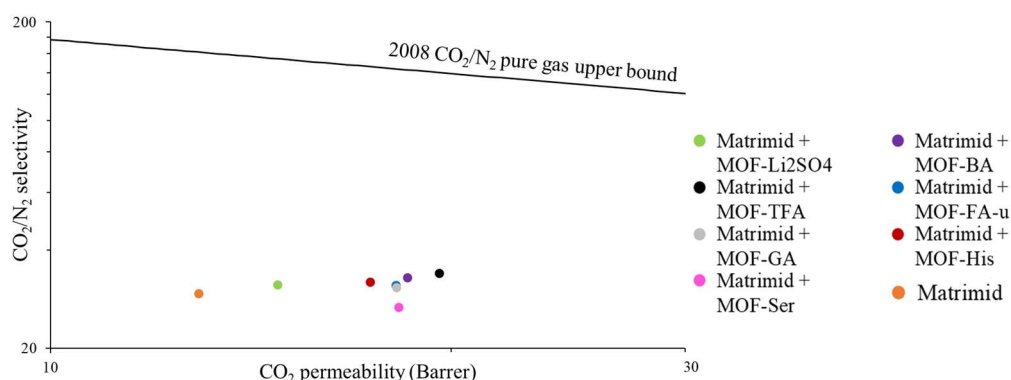


Figure 45: CO<sub>2</sub>/N<sub>2</sub> Robeson upper bound plot for MMM of Matrimid/functionalized MOF-808[69]. Data for the 15/85 CO<sub>2</sub>/N<sub>2</sub> mixture are shown for all MMM and Matrimid, except for MOF-Ser MMM where data for the 50/50 CO<sub>2</sub>/N<sub>2</sub> mixture is shown.

## 5 General conclusion and Future work

### 5.1 Amino acid functionalization of MOF-808

In the first part of this work, the potential of amino acid functionalized MOF-808 as filler in MMM for enhanced CO<sub>2</sub>/N<sub>2</sub> gas separation was investigated. Initially, attempts were made to develop an in-situ functionalization strategy through amino acid modulated MOF-808 synthesis. Various synthesis parameters, such as the HCl/modulator molar ratio, the modulator/Zr<sub>6</sub> cluster molar ratio and synthesis time were varied. Unfortunately, none of the synthesis recipes resulted in a crystalline material, as confirmed by XRD. Therefore, a post-synthetic functionalization strategy was developed, which modified a pre-formed MOF-808 with amino acids. The method was used successfully to develop a serine functionalized MOF, with <sup>1</sup>H NMR confirming serine was incorporated in the MOF. MOF-Ser showed a strong increase (62%) in CO<sub>2</sub> uptake at 1 bar compared to the pristine MOF-FA. Remarkably, the MMM of MOF-Ser in Matrimid performed only marginally better in terms of CO<sub>2</sub>/N<sub>2</sub> gas separation performance compared to MOF-FA based MMM. They showed a slightly higher separation factor, but a lower permeability for a 50/50 CO<sub>2</sub>/N<sub>2</sub> feed mixture being observed. The discrepancy between the strong increase in MOF CO<sub>2</sub> uptake and marginally better MMM performance gave rise to the question which MOF parameters correlate with the MMM gas separation performance.

### 5.2 Platform MOF-808: correlation of MOF parameters with MMM gas separation performance

In the second section, an attempt was made to correlate MOF parameters, specifically CO<sub>2</sub> uptake and isosteric heat of CO<sub>2</sub> adsorption, to the gas separation performance of the corresponding MMM. For this purpose, MOF-FA-u was functionalized with a series of functionalizing agents (i.e. His, TFA, GA, BA and Li<sub>2</sub>SO<sub>4</sub>), through a post-synthetic functionalization procedure. XRD, <sup>1</sup>H NMR and ATR-FTIR confirmed a successful functionalization. In the case of MOF-Li<sub>2</sub>SO<sub>4</sub>, EDX and ATR-FTIR indicated the presence of SO<sub>4</sub><sup>2-</sup> in the MOF pore, but no evidence for the presence of Li was obtained. Furthermore, EDX, CO<sub>2</sub> sorption and gas permeation measurements suggested Li<sub>2</sub>SO<sub>4</sub> might be deposited in the pores of this MOF. Additionally, XRD and SEM measurements showed functionalization did not significantly alter the MOF particle size or crystal structure.

Next, CO<sub>2</sub> adsorption isotherms were measured and the isosteric heat of CO<sub>2</sub> adsorption ( $Q_{st}$ ) was determined. MOF functionalization was found to alter both CO<sub>2</sub> uptake and  $Q_{st}$ . The CO<sub>2</sub>

uptake at 1000 mbar of the functionalized MOFs was reduced compared to the MOF-FA-u parent material. Contrarily,  $Q_{st}$  increased for MOF-TFA compared to MOF-FA, possibly a result of the incorporation of the highly polar C-F groups. Furthermore, strong deviations in  $Q_{st}$  were observed amongst the differently functionalized MOFs, suggesting functionalization significantly alters the CO<sub>2</sub> affinity of the MOF. Finally, Matrimid MMM of the functionalized MOFs were synthesized and their CO<sub>2</sub>/N<sub>2</sub> gas separation behavior was characterized under varying feed conditions (15/85 CO<sub>2</sub>/N<sub>2</sub>, 50/50 CO<sub>2</sub>/N<sub>2</sub> and pure CO<sub>2</sub>). MMM of MOF-TFA and MOF-BA showed a significant increase in gas separation performance compared to the MMM with MOF-FA. The most pronounced increase was observed for the 50/50 CO<sub>2</sub>/N<sub>2</sub> gas mixture where MMM based on these MOFs respectively showed a 72% and 52% increase in permeability and a 32% and 26% increase in separation factor compared to Matrimid membranes.

Lastly, the MMM gas separation performance was correlated with the aforementioned MOF parameters. The results showed a poor linear relationship between MOF CO<sub>2</sub> uptake and MMM CO<sub>2</sub>/N<sub>2</sub> separation factor, CO<sub>2</sub>/N<sub>2</sub> selectivity and CO<sub>2</sub> permeability. This observation is contradictory to MMM literature where an increase in CO<sub>2</sub> uptake is often associated with better MMM performance.  $Q_{st}$  showed no significant linear relationship with separation factor neither. However, the correlation between CO<sub>2</sub> permeability and  $Q_{st}$  was high for each of the studied feed composition, suggesting  $Q_{st}$  might be an interesting parameter to predict MMM CO<sub>2</sub> permeability for the functionalized MOF-808/Matrimid system.

### **5.3 MMM based on UTSA-120a**

In a final section, the potential of UTSA-120a as filler material for MMM was evaluated. UTSA-120a particles were successfully synthesized, as confirmed by XRD and ATR-FTIR measurements. The MMM based on UTSA-120a and 6FDA-DAM were subsequently evaluated for their CO<sub>2</sub>/N<sub>2</sub> and CO<sub>2</sub>/CH<sub>4</sub> mixed-gas separation performance. The MMM showed an increase in separation factor of 7.2 % compared to the pure 6FDA-DAM for the CO<sub>2</sub>/CH<sub>4</sub> separation. However, no increase in separation factor was observed for the CO<sub>2</sub>/N<sub>2</sub> mixture. Furthermore, permeability decreased significantly for both gas mixtures upon incorporation of UTSA-120A in the polymer matrix (~32% decrease). These observations suggest the differences in performance between the pure polymer and UTSA-120a MMM are a result of interactions occurring at the MOF/polymer interface. Extensive further research is required to characterize and optimize this MMM system.

## 5.4 Future work

### 5.4.1 Additional characterization

Additional characterization could expand insight in the influence of post-synthetic functionalization of MOF-808 on the physical properties of the MOF as well as on the gas separation performance of MMM based on the functionalized MOF:

- $^{19}\text{F}$  NMR measurements to obtain the functionalizing agent loading of MOF-TFA.
- ICP-OES measurements to obtain the functionalizing agent loading and investigate potential pore blocking of MOF- $\text{Li}_2\text{SO}_4$ .
- $\text{N}_2$  or Ar physisorption measurements for MOF-FA, MOF-FA-u and all of the functionalized MOFs to determine:
  - o The influence of the synthesis procedure (normal vs upscaled) on MOF-808 physical properties such as BET area, pore volume and pore size.
  - o The influence of functionalization on these MOF properties.
  - o The influence of these MOF properties on MMM gas separation performance.
- DSC measurement to determine the  $T_g$  of the MMM and hopefully gain insight in the impact of functionalization on polymer rigidification.
- PALS or density measurements to determine the effect of MOF incorporation on the amount of free volume and the free volume distribution in MMM.
- Membrane  $\text{CO}_2$  and  $\text{N}_2$  adsorption measurements to evaluate the effect of MOF incorporation on solubility of these gasses in the membrane and simultaneously the contribution of solubility selectivity to MMM selectivity.
- Gas separation measurements
  - o  $\text{CO}_2/\text{N}_2$  gas separation measurements at various pressures and for various feed compositions.
  - o  $\text{CO}_2/\text{CH}_4$  gas separation measurements.
  - o Measurements for 20 wt% MOF MMM, where differences in gas separation behavior might be more pronounced[114].

For UTSA-120a extensive characterization is required of the MOF itself (SEM,  $\text{N}_2$  physisorption,  $\text{CO}_2$  physisorption, thermogravimetric analysis) as well as the MMM (SEM, DSC, membrane  $\text{N}_2$  and  $\text{CO}_2$  adsorption measurements, ideal gas permeability measurements, effect of feed gas composition and feed pressure).

## 5.4.2 Additional experiments

Next to further characterization required to further understand MOF-808 functionalization, this work also reveals a few interesting research opportunities:

- The upscaled MOF-808 synthesis recipe could be applied to other modulators, such as TFA, revealing the potential of this recipe for large scale MOF-808 production.
- MOF-Ser showed a 62% increase in CO<sub>2</sub> uptake when it was synthesized from MOF-FA. The upscaled MOF, MOF-FA-u, showed a 69% higher CO<sub>2</sub> uptake than MOF-FA. Therefore it might be interesting to functionalize MOF-FA-u with serine to obtain a MOF-with a high CO<sub>2</sub> storage capacity.
- The amount of available missing ligand defects in MOF-808 can be easily tuned as evidenced by the De Vos group[153]. The effect of the amount of ligand defects on CO<sub>2</sub> uptake, Q<sub>st</sub> and MMM performance might reveal the importance of these defects for interaction with CO<sub>2</sub>.
- In this work, no attempt was made to vary the loading of functionalizing agent per Zr<sub>6</sub> cluster of the MOF. Optimizing this loading for CO<sub>2</sub> uptake or MMM fabrication might yield interesting result.
- MOF-TFA and MOF-BA respectively showed the best and second best MMM gas separation performance. Therefore functionalization of MOF-808 with 4(-trifluormethyl) benzoic acid might result in an interesting filler for MMM.
- The applied analysis could be extended to other MOF/polymer systems. This might result in a more fundamental understanding of gas transport through MMM.
- UTSA-120a might give interesting gas separation results when incorporated in another polymer matrix (e.g. Matrimid).

## References

- [1] M. Galizia, W.S. Chi, Z.P. Smith, T.C. Merkel, R.W. Baker, B.D. Freeman, 50th Anniversary Perspective: Polymers and Mixed Matrix Membranes for Gas and Vapor Separation: A Review and Prospective Opportunities, *Macromolecules*. 50 (2017) 7809–7843. doi:10.1021/acs.macromol.7b01718.
- [2] S. Nakao, K. Yogo, K. Goto, T. Kai, H. Yamada, *Advanced CO2 Capture Technologies*, Springer International Publishing, 2019. doi:10.1007/978-3-030-18858-0.
- [3] Moonshot: Vlaanderen CO2-arm in 2050 | Agentschap Innoveren en Ondernemen, (n.d.). <https://www.vlaio.be/nl/nieuws/moonshot-vlaanderen-co2-arm-2050> (accessed March 1, 2020).
- [4] EU Emissions Trading System (EU ETS) | Climate Action, (n.d.). [https://ec.europa.eu/clima/policies/ets\\_en](https://ec.europa.eu/clima/policies/ets_en) (accessed April 23, 2020).
- [5] Een Europese Green Deal | Europese Commissie, (n.d.). [https://ec.europa.eu/info/strategy/priorities-2019-2024/european-green-deal\\_nl](https://ec.europa.eu/info/strategy/priorities-2019-2024/european-green-deal_nl) (accessed March 1, 2020).
- [6] D.F. Sanders, Z.P. Smith, R. Guo, L.M. Robeson, J.E. McGrath, D.R. Paul, B.D. Freeman, Energy-efficient polymeric gas separation membranes for a sustainable future: A review, *Polymer (Guildf)*. 54 (2013) 4729–4761. doi:10.1016/j.polymer.2013.05.075.
- [7] M.A. Mac Kinnon, J. Brouwer, S. Samuelsen, The role of natural gas and its infrastructure in mitigating greenhouse gas emissions, improving regional air quality, and renewable resource integration, *Prog. Energy Combust. Sci.* 64 (2018) 62–92. doi:10.1016/j.pecs.2017.10.002.
- [8] M. Garside, • Global natural gas consumption 2018 | Statista, (n.d.). <https://www.statista.com/statistics/282717/global-natural-gas-consumption/> (accessed September 4, 2019).
- [9] M.A. Mac Kinnon, J. Brouwer, S. Samuelsen, The role of natural gas and its infrastructure in mitigating greenhouse gas emissions, improving regional air quality, and renewable resource integration, *Prog. Energy Combust. Sci.* (2018). doi:10.1016/j.pecs.2017.10.002.
- [10] S. Roussanaly, R. Anantharaman, K. Lindqvist, Multi-criteria analyses of two solvent and one low-temperature concepts for acid gas removal from natural gas, *J. Nat. Gas Sci. Eng.* 20 (2014) 38–49. doi:10.1016/j.jngse.2014.05.027.
- [11] S. Faramawy, T. Zaki, A.A.E. Sakr, Natural gas origin, composition, and processing: A review, *J. Nat. Gas Sci. Eng.* 34 (2016) 34–54. doi:10.1016/j.jngse.2016.06.030.
- [12] X.Y. Chen, H. Vinh-Thang, A.A. Ramirez, D. Rodrigue, S. Kaliaguine, Membrane gas separation technologies for biogas upgrading, *RSC Adv.* 5 (2015) 24399–24448.

doi:10.1039/c5ra00666j.

- [13] R.W. Baker, K. Lokhandwala, Natural gas processing with membranes: An overview, *Ind. Eng. Chem. Res.* 47 (2008) 2109–2121. doi:10.1021/ie071083w.
- [14] European environmental agency, CO2 emission intensity, (2016).  
[https://www.eea.europa.eu/data-and-maps/daviz/co2-emission-intensity-5#tab-googlechartid\\_chart\\_11\\_filters=%7B%22rowFilters%22%3A%7B%7D%3B%22columnFilters%22%3A%7B%22pre\\_config\\_ugeo%22%3A%5B%22European Union \(current composition\)%22%5D%7D%7D](https://www.eea.europa.eu/data-and-maps/daviz/co2-emission-intensity-5#tab-googlechartid_chart_11_filters=%7B%22rowFilters%22%3A%7B%7D%3B%22columnFilters%22%3A%7B%22pre_config_ugeo%22%3A%5B%22European Union (current composition)%22%5D%7D%7D) (accessed October 11, 2019).
- [15] CO2 Emissions from Fuel Combustion 2019: Overview – Analysis - IEA, (n.d.).  
<https://www.iea.org/reports/co2-emissions-from-fuel-combustion-2019-2> (accessed December 19, 2019).
- [16] R. Khalilpour, K. Mumford, H. Zhai, A. Abbas, G. Stevens, E.S. Rubin, Membrane-based carbon capture from flue gas: A review, *J. Clean. Prod.* 103 (2015) 286–300.  
doi:10.1016/j.jclepro.2014.10.050.
- [17] O. de Q.F. Araújo, J.L. de Medeiros, Carbon capture and storage technologies: present scenario and drivers of innovation, *Curr. Opin. Chem. Eng.* 17 (2017) 22–34.  
doi:10.1016/j.coche.2017.05.004.
- [18] The Future of Hydrogen – Analysis - IEA, (n.d.). <https://www.iea.org/reports/the-future-of-hydrogen> (accessed December 19, 2019).
- [19] T.L. Levalley, A.R. Richard, M. Fan, The progress in water gas shift and steam reforming hydrogen production technologies - A review, *Int. J. Hydrogen Energy.* 39 (2014) 16983–17000. doi:10.1016/j.ijhydene.2014.08.041.
- [20] H. Lin, Z. He, Z. Sun, J. Vu, A. Ng, M. Mohammed, J. Kniep, T.C. Merkel, T. Wu, R.C. Lambrecht, CO2-selective membranes for hydrogen production and CO2 capture - Part I: Membrane development, *J. Memb. Sci.* 457 (2014) 149–161.  
doi:10.1016/j.memsci.2014.01.020.
- [21] R.W. Baker, *Membrane Technology and Applications*, John Wiley & Sons, Ltd, Chichester, UK, 2004. doi:10.1002/0470020393.
- [22] V. Stannett, The transport of gases in synthetic polymeric membranes - an historic perspective, *J. Memb. Sci.* 3 (1978) 97–115. doi:10.1016/S0376-7388(00)83016-1.
- [23] R.W. Baker, Future directions of membrane gas separation technology, *Ind. Eng. Chem. Res.* 41 (2002) 1393–1411. doi:10.1021/ie0108088.
- [24] M. Mulder, *Basic principles of membrane technology*, 2nd ed., Kluwer Academic, 1996.

doi:10.1007/978-94-009-1766-8.

- [25] E. V. Perez, C. Karunaweera, I.H. Musselman, K.J. Balkus, J.P. Ferraris, Origins and evolution of inorganic-based and MOF-based mixed-matrix membranes for gas separations, *Processes*. 4 (2016). doi:10.3390/pr4030032.
- [26] S. Matteucci, Y. Yampolskii, B.D. Freeman, I. Pinnau, Transport of Gases and Vapors in Glassy and Rubbery Polymers, in: *Mater. Sci. Membr. Gas Vap. Sep.*, John Wiley & Sons, Ltd, 2006: pp. 1–47. doi:10.1002/047002903X.ch1.
- [27] R.W. Baker, B.T. Low, Gas separation membrane materials: A perspective, *Macromolecules*. 47 (2014) 6999–7013. doi:10.1021/ma501488s.
- [28] C.A. Scholes, G.W. Stevens, S.E. Kentish, Membrane gas separation applications in natural gas processing, *Fuel*. 96 (2012) 15–28. doi:10.1016/j.fuel.2011.12.074.
- [29] P. Bernardo, E. Drioli, G. Golemme, Membrane gas separation: A review/state of the art, *Ind. Eng. Chem. Res.* 48 (2009) 4638–4663. doi:10.1021/ie8019032.
- [30] S.E. Kentish, C.A. Scholes, G.W. Stevens, Carbon Dioxide Separation through Polymeric Membrane Systems for Flue Gas Applications, *Recent Patents Chem. Eng.* 1 (2010) 52–66. doi:10.2174/1874478810801010052.
- [31] Cellulose Acetate, (n.d.). [http://www.polymerdatabase.com/polymers/Cellulose Acetate.html](http://www.polymerdatabase.com/polymers/Cellulose%20Acetate.html) (accessed October 1, 2019).
- [32] Y.W. Jeon, D.H. Lee, Gas membranes for CO<sub>2</sub>/CH<sub>4</sub> (biogas) separation: A review, *Environ. Eng. Sci.* 32 (2015) 71–85. doi:10.1089/ees.2014.0413.
- [33] A. Bos, I.G.M. Pünt, M. Wessling, H. Strathmann, CO<sub>2</sub>-induced plasticization phenomena in glassy polymers, *J. Memb. Sci.* 155 (1999) 67–78. doi:10.1016/S0376-7388(98)00299-3.
- [34] E.P. Favvas, F.K. Katsaros, S.K. Papageorgiou, A.A. Sapalidis, A.C. Mitropoulos, A review of the latest development of polyimide based membranes for CO<sub>2</sub> separations, *React. Funct. Polym.* 120 (2017) 104–130. doi:10.1016/j.reactfunctpolym.2017.09.002.
- [35] S. Sridhar, R.S. Veerapur, M.B. Patil, K.B. Gudasi, T.M. Aminabhavi, Matrimid polyimide membranes for the separation of carbon dioxide from methane, *J. Appl. Polym. Sci.* 106 (2007) 1585–1594. doi:10.1002/app.26306.
- [36] I. Ugo Moretti, CHAPTER 9. Polymeric Membrane-based Plants for Biogas Upgrading, in: 2017: pp. 242–255. doi:10.1039/9781788010436-00242.
- [37] S.A. Stern, Y. Mi, H. Yamamoto, A.K. St. Clair, Structure/permeability relationships of polyimide membranes. Applications to the separation of gas mixtures, *J. Polym. Sci. Part B Polym. Phys.* 27 (1989) 1887–1909. doi:10.1002/polb.1989.090270908.

- [38] C. Staudt-Bickel, W. J. Koros, Improvement of CO<sub>2</sub>/CH<sub>4</sub> separation characteristics of polyimides by chemical crosslinking, *J. Memb. Sci.* 155 (1999) 145–154. doi:10.1016/S0376-7388(98)00306-8.
- [39] W. Qiu, L. Xu, C.C. Chen, D.R. Paul, W.J. Koros, Gas separation performance of 6FDA-based polyimides with different chemical structures, *Polymer (Guildf)*. 54 (2013) 6226–6235. doi:10.1016/j.polymer.2013.09.007.
- [40] A.M. Kratochvil, W.J. Koros, Decarboxylation-induced cross-linking of a polyimide for enhanced CO<sub>2</sub> plasticization resistance, *Macromolecules*. 41 (2008) 7920–7927. doi:10.1021/ma801586f.
- [41] C.A. Scholes, W.X. Tao, G.W. Stevens, S.E. Kentish, Sorption of methane, nitrogen, carbon dioxide, and water in Matrimid 5218, *J. Appl. Polym. Sci.* 117 (2010) 2284–2289. doi:10.1002/app.32148.
- [42] H. Julian, I.G. Wenten, Polysulfone membranes for CO<sub>2</sub>/CH<sub>4</sub> separation: State of the art, *IOSR J. Eng.* 2 (2012) 484–495. doi:10.9790/3021-0203484495.
- [43] J.S. McHattie, W.J. Koros, D.R. Paul, Gas transport properties of polysulphones: 1. Role of symmetry of methyl group placement on bisphenol rings, *Polymer (Guildf)*. 32 (1991) 840–850. doi:10.1016/0032-3861(91)90508-G.
- [44] H. Vogel, C.S. Marvel, Polybenzimidazoles, new thermally stable polymeres, *J. Polym. Sci. Part A Polym. Chem.* 34 (1996) 1125–1153. doi:10.1002/pola.1996.826.
- [45] X. Li, R.P. Singh, K.W. Dudeck, K.A. Berchtold, B.C. Benicewicz, Influence of polybenzimidazole main chain structure on H<sub>2</sub>/CO<sub>2</sub> separation at elevated temperatures, *J. Memb. Sci.* 461 (2014) 59–68. doi:10.1016/j.memsci.2014.03.008.
- [46] K.A. Stevens, J.D. Moon, H. Borjigin, R. Liu, R.M. Joseph, J.S. Riffle, B.D. Freeman, Influence of temperature on gas transport properties of tetraaminodiphenylsulfone (TADPS) based polybenzimidazoles, *J. Memb. Sci.* 593 (2020) 117427. doi:10.1016/j.memsci.2019.117427.
- [47] R.P. Singh, G.J. Dahe, K.W. Dudeck, C.F. Welch, K.A. Berchtold, High temperature polybenzimidazole hollow fiber membranes for hydrogen separation and carbon dioxide capture from synthesis gas, in: *Energy Procedia*, Elsevier Ltd, 2014: pp. 153–159. doi:10.1016/j.egypro.2014.11.015.
- [48] P.M. Budd, K.J. Msayib, C.E. Tattershall, B.S. Ghanem, K.J. Reynolds, N.B. McKeown, D. Fritsch, Gas separation membranes from polymers of intrinsic microporosity, *J. Memb. Sci.* 251 (2005) 263–269. doi:10.1016/j.memsci.2005.01.009.

- [49] C. Ma, J.J. Urban, Polymers of Intrinsic Microporosity (PIMs) Gas Separation Membranes: A mini Review, *Proc. Nat. Res. Soc.* 2 (2018). doi:10.11605/j.pnrs.201802002.
- [50] R. Swaidan, B. Ghanem, E. Litwiller, I. Pinnau, Physical Aging, Plasticization and Their Effects on Gas Permeation in “rigid” Polymers of Intrinsic Microporosity, *Macromolecules.* 48 (2015) 6553–6561. doi:10.1021/acs.macromol.5b01581.
- [51] N.B. McKeown, P.M. Budd, Polymers of intrinsic microporosity (PIMs): Organic materials for membrane separations, heterogeneous catalysis and hydrogen storage, *Chem. Soc. Rev.* 35 (2006) 675–683. doi:10.1039/b600349d.
- [52] H.B. Park, C.H. Jung, Y.M. Lee, A.J. Hill, S.J. Pas, S.T. Mudie, E. Van Wagner, B.D. Freeman, D.J. Cookson, Polymers with cavities tuned for fast selective transport of small molecules and ions, *Science* (80-. ). 318 (2007) 254–258. doi:10.1126/science.1146744.
- [53] Z.P. Smith, D.F. Sanders, C.P. Ribeiro, R. Guo, B.D. Freeman, D.R. Paul, J.E. McGrath, S. Swinnea, Gas sorption and characterization of thermally rearranged polyimides based on 3,3'-dihydroxy-4,4'-diamino-biphenyl (HAB) and 2,2'-bis-(3,4-dicarboxyphenyl) hexafluoropropane dianhydride (6FDA), *J. Memb. Sci.* 415–416 (2012) 558–567. doi:10.1016/j.memsci.2012.05.050.
- [54] M.G. Buonomenna, W. Yave, G. Golemme, Some approaches for high performance polymer based membranes for gas separation: block copolymers, carbon molecular sieves and mixed matrix membranes, *RSC Adv.* 2 (2012) 10745. doi:10.1039/c2ra20748f.
- [55] M. Malankowska, L. Martínez-Izquierdo, J. Sánchez-Láinez, C. Téllez, J. Coronas, Poly(ether-block-amide) copolymer membrane for CO<sub>2</sub>/N<sub>2</sub> separation: the influence of the casting solution concentration on its morphology, thermal properties and gas separation performance, (2019). doi:10.1098/rsos.190866.
- [56] V.I. Bondar, B.D. Freeman, I. Pinnau, Gas transport properties of poly(ether-b-amide) segmented block copolymers, *J. Polym. Sci. Part B Polym. Phys.* 38 (2000) 2051–2062. doi:10.1002/1099-0488(20000801)38:15<2051::AID-POLB100>3.0.CO;2-D.
- [57] P. Klingberg, K. Wilkner, M. Schlüter, J. Grünauer, S. Shishatskiy, Separation of Carbon Dioxide from Real Power Plant Flue Gases by Gas Permeation Using a Supported Ionic Liquid Membrane: An Investigation of Membrane Stability, *Membranes (Basel).* 9 (2019) 35. doi:10.3390/membranes9030035.
- [58] X. He, The Latest Development on Membrane Materials and Processes for Post-combustion CO<sub>2</sub> Capture: A Review, *Sci. Publ. LLC., |. SF J Mater. Chem Eng.* 1 (2018) 1009. <https://scienceforecastoa.com/> (accessed November 22, 2019).
- [59] K. Xie, Q. Fu, J. Kim, H. Lu, Y. He, Q. Zhao, J. Scofield, P.A. Webley, G.G. Qiao, Increasing

- both selectivity and permeability of mixed-matrix membranes: Sealing the external surface of porous MOF nanoparticles, *J. Memb. Sci.* 535 (2017) 350–356.  
doi:10.1016/j.memsci.2017.04.022.
- [60] T. Khosravi, M. Omidkhah, Preparation of CO<sub>2</sub> selective composite membranes using Pebax/CuBTC/PEG-ran-PPG ternary system, *J. Energy Chem.* 26 (2017) 530–539.  
doi:10.1016/j.jechem.2016.10.013.
- [61] X.Y. Chen, H. Vinh-Thang, A. Avalos Ramirez, D. Rodrigue, S. Kaliaguine, Membrane gas separation technologies for biogas upgrading, (2015). doi:10.1039/c5ra00666j.
- [62] S. Meshkat, S. Kaliaguine, D. Rodrigue, Enhancing CO<sub>2</sub> separation performance of Pebax® MH-1657 with aromatic carboxylic acids, (2018). doi:10.1016/j.seppur.2018.12.008.
- [63] K. Tanaka, H. Kita, M. Okano, K. ichi Okamoto, Permeability and permselectivity of gases in fluorinated and non-fluorinated polyimides, *Polymer (Guildf)*. 33 (1992) 585–592.  
doi:10.1016/0032-3861(92)90736-G.
- [64] L.M. Robeson, Q. Liu, B.D. Freeman, D.R. Paul, Comparison of transport properties of rubbery and glassy polymers and the relevance to the upper bound relationship, *J. Memb. Sci.* 476 (2015) 421–431. doi:10.1016/j.memsci.2014.11.058.
- [65] C.A. Scholes, W.X. Tao, G.W. Stevens, S.E. Kentish, Sorption of methane, nitrogen, carbon dioxide, and water in Matrimid 5218, *J. Appl. Polym. Sci.* 117 (2010) 2284–2289.  
doi:10.1002/app.32148.
- [66] E. Smit, M.H.V. Mulder, C.A. Smolders, H. Karrenbeld, J. van Eerden, D. Feil, Modelling of the diffusion of carbon dioxide in polyimide matrices by computer simulation, *J. Memb. Sci.* 73 (1992) 247–257. doi:10.1016/0376-7388(92)80133-5.
- [67] M.I. Artsis, A.E. Chalykh, N.A. Khalturinskii, Y. V. Moiseev, G.E. Zaikov, Diffusion of organic diluents into ethyl cellulose, *Eur. Polym. J.* 8 (1972) 613–626. doi:10.1016/0014-3057(72)90137-1.
- [68] L.M. Robeson, Polymer membranes for gas separation, *Curr. Opin. Solid State Mater. Sci.* 4 (1999) 549–552. doi:10.1016/S1359-0286(00)00014-0.
- [69] L.M. Robeson, The upper bound revisited, *J. Memb. Sci.* 320 (2008) 390–400.  
doi:10.1016/j.memsci.2008.04.030.
- [70] H.B. Park, J. Kamcev, L.M. Robeson, M. Elimelech, B.D. Freeman, Maximizing the right stuff: The trade-off between membrane permeability and selectivity, *Science (80-. )*. 356 (2017) 1138–1148. doi:10.1126/science.aab0530.
- [71] M.S. Suleman, K.K. Lau, Y.F. Yeong, Plasticization and Swelling in Polymeric Membranes in

- CO<sub>2</sub> Removal from Natural Gas, *Chem. Eng. Technol.* 39 (2016) 1604–1616.  
doi:10.1002/ceat.201500495.
- [72] J. Adewole, A. Ahmad, S. Ismail, C. Leo, N. Tebal, S. Prai Selatan, P. Pinang, Current challenges in membrane separation of CO<sub>2</sub> from natural gas: A review, *Int. J. Greenh. Gas Control.* 17 (2013) 46–65. doi:10.1016/j.ijggc.2013.04.012.
- [73] A.F. Ismail, W. Lorna, Penetrant-induced plasticization phenomenon in glassy polymers for gas separation membrane, *Sep. Purif. Technol.* 27 (2002) 173–194. doi:10.1016/S1383-5866(01)00211-8.
- [74] M. Wessling, M. Lidon Lopez, H. Strathmann, Accelerated plasticization of thin-film composite membranes used in gas separation, *Sep. Purif. Technol.* 24 (2001) 223–233. doi:10.1016/S1383-5866(01)00127-7.
- [75] J. Xia, T.S. Chung, P. Li, N.R. Horn, D.R. Paul, Aging and carbon dioxide plasticization of thin polyetherimide films, *Polymer (Guildf).* 53 (2012) 2099–2108. doi:10.1016/j.polymer.2012.03.009.
- [76] N. Schmeling, R. Konietzny, D. Sieffert, P. Rölling, C. Staudt, Functionalized copolyimide membranes for the separation of gaseous and liquid mixtures, *Beilstein J. Org. Chem.* 6 (2010) 789–800. doi:10.3762/bjoc.6.86.
- [77] B.W. Rowe, B.D. Freeman, D.R. Paul, Influence of previous history on physical aging in thin glassy polymer films as gas separation membranes, *Polymer (Guildf).* 51 (2010) 3784–3792. doi:10.1016/j.polymer.2010.06.004.
- [78] Y. Xiao, B.T. Low, S.S. Hosseini, T.S. Chung, D.R. Paul, The strategies of molecular architecture and modification of polyimide-based membranes for CO<sub>2</sub> removal from natural gas-A review, *Prog. Polym. Sci.* 34 (2009) 561–580. doi:10.1016/j.progpolymsci.2008.12.004.
- [79] Y. Huang, D.R. Paul, Effect of Temperature on Physical Aging of Thin Glassy Polymer Films, (2005). doi:10.1021/ma051284g.
- [80] Z.-X. Low, P.M. Budd, N.B. McKeown, D.A. Patterson, Gas Permeation Properties, Physical Aging, and Its Mitigation in High Free Volume Glassy Polymers, *Chem. Rev.* 118 (2018) 5871–5911. doi:10.1021/acs.chemrev.7b00629.
- [81] A. Singh, W.J. Koros, Significance of Entropic Selectivity for Advanced Gas Separation Membranes, *Ind. Eng. Chem. Res.* 35 (1996) 1231–1234. doi:10.1021/ie950559l.
- [82] C.M. Zimmerman, A. Singh, W.J. Koros, Tailoring mixed matrix composite membranes for gas separations, *J. Memb. Sci.* 137 (1997) 145–154. doi:10.1016/S0376-7388(97)00194-4.
- [83] P.S. Goh, A.F. Ismail, S.M. Sanip, B.C. Ng, M. Aziz, Recent advances of inorganic fillers in

- mixed matrix membrane for gas separation, (2011). doi:10.1016/j.seppur.2011.07.042.
- [84] F.F. Krull, C. Fritzmann, T. Melin, Liquid membranes for gas/vapor separations, *J. Memb. Sci.* 325 (2008) 509–519. doi:10.1016/j.memsci.2008.09.018.
- [85] M. Pera-Titus, Porous inorganic membranes for CO<sub>2</sub> capture: Present and prospects, *Chem. Rev.* 114 (2014) 1413–1492. doi:10.1021/cr400237k.
- [86] T.S. Chung, L.Y. Jiang, Y. Li, S. Kulprathipanja, Mixed matrix membranes (MMMs) comprising organic polymers with dispersed inorganic fillers for gas separation, *Prog. Polym. Sci.* 32 (2007) 483–507. doi:10.1016/j.progpolymsci.2007.01.008.
- [87] A.F. Ismail, K.C. Khulbe, T. Matsuura, *Gas separation membranes: Polymeric and inorganic*, Springer International Publishing, 2015. doi:10.1007/978-3-319-01095-3.
- [88] W. Liang, H. Chevreau, F. Ragon, P.D. Southon, V.K. Peterson, D.M. D’Alessandro, Tuning pore size in a zirconium-tricarboxylate metal-organic framework, *CrystEngComm.* 16 (2014) 6530–6533. doi:10.1039/c4ce01031k.
- [89] R. Thür, N. Van Velthoven, S. Sloodmaekers, J. Didden, R. Verbeke, S. Smolders, M. Dickmann, W. Egger, D. De Vos, I.F.J. Vankelecom, Bipyridine-based UiO-67 as novel filler in mixed-matrix membranes for CO<sub>2</sub>-selective gas separation, *J. Memb. Sci.* (2019) 78–87. doi:10.1016/j.memsci.2019.01.016.
- [90] G. Liu, V. Chernikova, Y. Liu, K. Zhang, Y. Belmabkhout, O. Shekhah, C. Zhang, S. Yi, M. Eddaoudi, W.J. Koros, Mixed matrix formulations with MOF molecular sieving for key energy-intensive separations, *Nat. Mater.* 17 (2018) 283–289. doi:10.1038/s41563-017-0013-1.
- [91] D.R. Paul, D.R. Kemp, DIFFUSION TIME LAG IN POLYMER MEMBRANES CONTAINING ADSORPTIVE FILLERS., *J Polym Sci, Part C, Polym Symp.* (1973) 79–93. doi:10.1002/polc.5070410109.
- [92] M. Vinoba, M. Bhagiyalakshmi, Y. Alqaheem, A.A. Alomair, A. Pérez, M.S. Rana, Recent progress of fillers in mixed matrix membranes for CO<sub>2</sub> separation: A review, *Sep. Purif. Technol.* 188 (2017) 431–450. doi:10.1016/j.seppur.2017.07.051.
- [93] H. Vinh-Thang, S. Kaliaguine, Predictive models for mixed-matrix membrane performance: A review, *Chem. Rev.* 113 (2013) 4980–5028. doi:10.1021/cr3003888.
- [94] A.A. Gray-Weale, R.H. Henchman, R.G. Gilbert, M.L. Greenfield, D.N. Theodorou, Transition-state theory model for the diffusion coefficients of small penetrants in glassy polymers, *Macromolecules.* 30 (1997) 7296–7306. doi:10.1021/ma970349f.
- [95] W.J. Koros, C. Zhang, Materials for next-generation molecularly selective synthetic membranes, *Nat. Mater.* 16 (2017) 289–297. doi:10.1038/nmat4805.

- [96] R.H.B. Bouma, A. Checchetti, G. Chidichimo, E. Drioli, Permeation through a heterogeneous membrane: The effect of the dispersed phase, *J. Memb. Sci.* 128 (1997) 141–149. doi:10.1016/S0376-7388(96)00303-1.
- [97] M.A. Aroon, A.F. Ismail, T. Matsuura, M.M. Montazer-Rahmati, Performance studies of mixed matrix membranes for gas separation: A review, *Sep. Purif. Technol.* 75 (2010) 229–242. doi:10.1016/j.seppur.2010.08.023.
- [98] T.T. Moore, W.J. Koros, Non-ideal effects in organic-inorganic materials for gas separation membranes, *J. Mol. Struct.* 739 (2005) 87–98. doi:10.1016/j.molstruc.2004.05.043.
- [99] R. Mahajan, R. Burns, M. Schaeffer, W.J. Koros, Challenges in forming successful mixed matrix membranes with rigid polymeric materials, *J. Appl. Polym. Sci.* 86 (2002) 881–890. doi:10.1002/app.10998.
- [100] J.A. Manson, E.H. Chiu, PERMEATION OF LIQUID WATER IN A FILLED EPOXY RESIN., *J Polym Sci, Part C, Polym Symp.* (1973) 95–108. doi:10.1002/polc.5070410110.
- [101] T.T. Moore, R. Mahajan, D.Q. Vu, W.J. Koros, Hybrid Membrane Materials Comprising Organic Polymers with Rigid Dispersed Phases, *AIChE J.* 50 (2004) 311–321. doi:10.1002/aic.10029.
- [102] Y. Li, T.S. Chung, C. Cao, S. Kulprathipanja, The effects of polymer chain rigidification, zeolite pore size and pore blockage on polyethersulfone (PES)-zeolite A mixed matrix membranes, *J. Memb. Sci.* 260 (2005) 45–55. doi:10.1016/j.memsci.2005.03.019.
- [103] R. Lin, B. Villacorta Hernandez, L. Ge, Z. Zhu, Metal organic framework based mixed matrix membranes: An overview on filler/polymer interfaces, *J. Mater. Chem. A.* 6 (2018) 293–312. doi:10.1039/c7ta07294e.
- [104] B. Seoane, J. Coronas, I. Gascon, M.E. Benavides, O. Karvan, J. Caro, F. Kapteijn, J. Gascon, Metal-organic framework based mixed matrix membranes: A solution for highly efficient CO<sub>2</sub> capture?, *Chem. Soc. Rev.* 44 (2015) 2421–2454. doi:10.1039/c4cs00437j.
- [105] Y. Zhang, X. Feng, S. Yuan, J. Zhou, B. Wang, Challenges and recent advances in MOF-polymer composite membranes for gas separation, *Inorg. Chem. Front.* 3 (2016) 896–909. doi:10.1039/c6qi00042h.
- [106] J. Sánchez-Laínez, B. Zornoza, S. Friebe, J. Caro, S. Cao, A. Sabetghadam, B. Seoane, J. Gascon, F. Kapteijn, C. Le Guillouzer, G. Clet, M. Daturi, C. Téllez, J. Coronas, Influence of ZIF-8 particle size in the performance of polybenzimidazole mixed matrix membranes for pre-combustion CO<sub>2</sub> capture and its validation through interlaboratory test, *J. Memb. Sci.* 515 (2016) 45–53. doi:10.1016/j.memsci.2016.05.039.

- [107] R. Thür, N. Van Velthoven, V. Lemmens, M. Bastin, S. Smolders, D. De Vos, I.F.J. Vankelecom, Modulator-Mediated Functionalization of MOF-808 as a Platform Tool to Create High-Performance Mixed-Matrix Membranes, (2019). doi:10.1021/acsami.9b19774.
- [108] R. Mahajan, W.J. Koros, Factors controlling successful formation of mixed-matrix gas separation materials, *Ind. Eng. Chem. Res.* 39 (2000) 2692–2696. doi:10.1021/ie990799r.
- [109] Q. Song, S.K. Nataraj, M. V. Roussenova, J.C. Tan, D.J. Hughes, W. Li, P. Bourgoïn, M.A. Alam, A.K. Cheetham, S.A. Al-Muhtaseb, E. Sivaniah, Zeolitic imidazolate framework (ZIF-8) based polymer nanocomposite membranes for gas separation, *Energy Environ. Sci.* 5 (2012) 8359–8369. doi:10.1039/c2ee21996d.
- [110] E.M. Mahdi, J.-C. Tan, Mixed-matrix membranes of zeolitic imidazolate framework (ZIF-8)/Matrimid nanocomposite: Thermo-mechanical stability and viscoelasticity underpinning membrane separation performance, *J. Memb. Sci.* 498 (2016) 276–290. doi:10.1016/j.memsci.2015.09.066.
- [111] I.S. Flyagina, E.M. Mahdi, K. Titov, J.-C. Tan, Thermo-mechanical properties of mixed-matrix membranes encompassing zeolitic imidazolate framework-90 and polyvinylidene difluoride: ZIF-90/PVDF nanocomposites, *APL Mater.* 5 (2017) 086104. doi:10.1063/1.4986565.
- [112] T. Rodenas, M. Van Dalen, P. Serra-Crespo, F. Kapteijn, J. Gascon, Mixed matrix membranes based on NH<sub>2</sub>-functionalized MIL-type MOFs: Influence of structural and operational parameters on the CO<sub>2</sub>/CH<sub>4</sub> separation performance, *Microporous Mesoporous Mater.* 192 (2014) 35–42. doi:10.1016/j.micromeso.2013.08.049.
- [113] G. Dong, H. Li, V. Chen, Challenges and opportunities for mixed-matrix membranes for gas separation, *J. Mater. Chem. A.* 1 (2013) 4610–4630. doi:10.1039/c3ta00927k.
- [114] S. Basu, A. Cano-Odena, I.F.J. Vankelecom, MOF-containing mixed-matrix membranes for CO<sub>2</sub>/CH<sub>4</sub> and CO<sub>2</sub>/N<sub>2</sub> binary gas mixture separations, *Sep. Purif. Technol.* 81 (2011) 31–40. doi:10.1016/j.seppur.2011.06.037.
- [115] C.A. Trickett, A. Helal, B.A. Al-Maythalony, Z.H. Yamani, K.E. Cordova, O.M. Yaghi, The chemistry of metal-organic frameworks for CO<sub>2</sub> capture, regeneration and conversion, *Nat. Rev. Mater.* 2 (2017). doi:10.1038/natrevmats.2017.45.
- [116] M. Safaei, M.M. Foroughi, N. Ebrahimipoor, S. Jahani, A. Omid, M. Khatami, A review on metal-organic frameworks: Synthesis and applications, *TrAC - Trends Anal. Chem.* 118 (2019) 401–425. doi:10.1016/j.trac.2019.06.007.
- [117] S. Yuan, L. Feng, K. Wang, J. Pang, M. Bosch, C. Lollar, Y. Sun, J. Qin, X. Yang, P. Zhang, Q. Wang, L. Zou, Y. Zhang, L. Zhang, Y. Fang, J. Li, H.C. Zhou, Stable Metal–Organic Frameworks: Design, Synthesis, and Applications, *Adv. Mater.* 30 (2018).

doi:10.1002/adma.201704303.

- [118] V.R. Remya, M. Kurian, Synthesis and catalytic applications of metal–organic frameworks: a review on recent literature, *Int. Nano Lett.* 9 (2019) 17–29. doi:10.1007/s40089-018-0255-1.
- [119] S. Li, F. Huo, Metal-organic framework composites: From fundamentals to applications, *Nanoscale.* 7 (2015) 7482–7501. doi:10.1039/c5nr00518c.
- [120] M. Eddaoudi, J. Kim, N. Rosi, D. Vodak, J. Wachter, M. O’Keeffe, O.M. Yaghi, Systematic design of pore size and functionality in isorecticular MOFs and their application in methane storage, *Science* (80-. ). 295 (2002) 469–472. doi:10.1126/science.1067208.
- [121] C. Wang, D. Liu, W. Lin, Metal-organic frameworks as a tunable platform for designing functional molecular materials, *J. Am. Chem. Soc.* 135 (2013) 13222–13234. doi:10.1021/ja308229p.
- [122] S. Saha, S. Chandra, B. Garai, R. Banerjee, Carbon dioxide capture by metal organic frameworks, *Indian J. Chem. - Sect. A Inorganic, Phys. Theor. Anal. Chem.* 51 (2012) 1223–1230. doi:10.1021/cr2003272.
- [123] D. Xue, P.M. Bhatt, A. Shkurenko, L. Wojtas, C. Zhijie, Y. Belmabkhout, K. Adil, fine tuning : ftw-MOF platform for energy-efficient, (2018) 6404–6407. doi:10.1039/c8cc03841d.
- [124] C. Zhang, Y. Dai, J.R. Johnson, O. Karvan, W.J. Koros, High performance ZIF-8/6FDA-DAM mixed matrix membrane for propylene/propane separations, *J. Memb. Sci.* 389 (2012) 34–42. doi:10.1016/j.memsci.2011.10.003.
- [125] K. Sumida, D.L. Rogow, J.A. Mason, T.M. McDonald, E.D. Bloch, Z.R. Herm, T.H. Bae, J.R. Long, Carbon dioxide capture in metal-organic frameworks, *Chem. Rev.* 112 (2012) 724–781. doi:10.1021/cr2003272.
- [126] S. Kazemi, V. Safarifard, Carbon dioxide capture in MOFs: The effect of ligand functionalization, *Polyhedron.* 154 (2018) 236–251. doi:10.1016/j.poly.2018.07.042.
- [127] G.E. Cmarik, M. Kim, S.M. Cohen, K.S. Walton, Tuning the Adsorption Properties of UiO-66 via Ligand Functionalization, (2012). doi:10.1021/la3035352.
- [128] S. Chaemchuen, N.A. Kabir, K. Zhou, F. Verpoort, Metal-organic frameworks for upgrading biogas via CO<sub>2</sub> adsorption to biogas green energy, *Chem. Soc. Rev.* 42 (2013) 9304–9332. doi:10.1039/c3cs60244c.
- [129] Y.S. Bae, O.K. Farha, A.M. Spokoyny, C.A. Mirkin, J.T. Hupp, R.Q. Snurr, Carborane-based metal-organic frameworks as highly selective sorbents for CO<sub>2</sub> over methane, *Chem. Commun.* (2008) 4135–4137. doi:10.1039/b805785k.
- [130] W.L. Queen, M.R. Hudson, E.D. Bloch, J.A. Mason, M.I. Gonzalez, J.S. Lee, D. Gygi, J.D.

- Howe, K. Lee, T.A. Darwish, M. James, V.K. Peterson, S.J. Teat, B. Smit, J.B. Neaton, J.R. Long, C.M. Brown, Comprehensive study of carbon dioxide adsorption in the metal-organic frameworks M<sub>2</sub>(dobdc) (M = Mg, Mn, Fe, Co, Ni, Cu, Zn), *Chem. Sci.* 5 (2014) 4569–4581. doi:10.1039/c4sc02064b.
- [131] W. Morris, S. Wang, D. Cho, E. Auyeung, P. Li, O.K. Farha, C.A. Mirkin, Role of modulators in controlling the colloidal stability and polydispersity of the UiO-66 metal-organic framework, *ACS Appl. Mater. Interfaces.* 9 (2017) 33413–33418. doi:10.1021/acsami.7b01040.
- [132] O. V. Gutov, S. Molina, E.C. Escudero-Adán, A. Shafir, Modulation by Amino Acids: Toward Superior Control in the Synthesis of Zirconium Metal–Organic Frameworks, *Chem. - A Eur. J.* 22 (2016) 13582–13587. doi:10.1002/chem.201600898.
- [133] A. Koutsianos, E. Kazimierska, A.R. Barron, M. Taddei, E. Andreoli, A new approach to enhancing the CO<sub>2</sub> capture performance of defective UiO-66: Via post-synthetic defect exchange, *Dalt. Trans.* 48 (2019) 3349–3359. doi:10.1039/c9dt00154a.
- [134] P. Deria, J.E. Mondloch, E. Tylianakis, P. Ghosh, W. Bury, R.Q. Snurr, J.T. Hupp, O.K. Farha, Perfluoroalkane functionalization of NU-1000 via solvent-assisted ligand incorporation: Synthesis and CO<sub>2</sub> adsorption studies, *J. Am. Chem. Soc.* 135 (2013) 16801–16804. doi:10.1021/ja408959g.
- [135] Y. Belmabkhout, V. Guillerm, M. Eddaoudi, Low concentration CO<sub>2</sub> capture using physical adsorbents: Are metal-organic frameworks becoming the new benchmark materials?, *Chem. Eng. J.* 296 (2016) 386–397. doi:10.1016/j.cej.2016.03.124.
- [136] O.G. Nik, X.Y. Chen, S. Kaliaguine, Functionalized metal organic framework-polyimide mixed matrix membranes for CO<sub>2</sub>/CH<sub>4</sub> separation, *J. Memb. Sci.* 413–414 (2012) 48–61. doi:10.1016/j.memsci.2012.04.003.
- [137] B. Ghalei, K. Sakurai, Y. Kinoshita, K. Wakimoto, A.P. Isfahani, Q. Song, K. Doitomi, S. Furukawa, H. Hirao, H. Kusuda, S. Kitagawa, E. Sivaniah, Enhanced selectivity in mixed matrix membranes for CO<sub>2</sub> capture through efficient dispersion of amine-functionalized MOF nanoparticles, *Nat. Energy.* 2 (2017) 1–9. doi:10.1038/nenergy.2017.86.
- [138] Q. Qian, A.X. Wu, W.S. Chi, P.A. Asinger, S. Lin, A. Hypsher, Z.P. Smith, Mixed-Matrix Membranes Formed from Imide-Functionalized UiO-66-NH<sub>2</sub> for Improved Interfacial Compatibility, *ACS Appl. Mater. Interfaces.* 11 (2019) 31257–31269. doi:10.1021/acsami.9b07500.
- [139] H. Furukawa, K.E. Cordova, M. O’Keeffe, O.M. Yaghi, The chemistry and applications of metal-organic frameworks, *Science (80-. )*. 341 (2013). doi:10.1126/science.1230444.
- [140] A.J. Howarth, Y. Liu, P. Li, Z. Li, T.C. Wang, J.T. Hupp, O.K. Farha, Chemical, thermal and

- mechanical stabilities of metal-organic frameworks, (2016) 15018.  
doi:10.1038/natrevmats.2015.18.
- [141] J.H. Cavka, S. Jakobsen, U. Olsbye, N. Guillou, C. Lamberti, S. Bordiga, K.P. Lillerud, A new zirconium inorganic building brick forming metal organic frameworks with exceptional stability, *J. Am. Chem. Soc.* 130 (2008) 13850–13851. doi:10.1021/ja8057953.
- [142] B. Bueken, N. Van Velthoven, A. Krajnc, S. Smolders, F. Taulelle, C. Mellot-Draznieks, G. Mali, T.D. Bennett, D. De Vos, Tackling the Defect Conundrum in UiO-66: A Mixed-Linker Approach to Engineering Missing Linker Defects, (2017).  
doi:10.1021/acs.chemmater.7b04128.
- [143] Y. Jiao, Y. Liu, G. Zhu, J.T. Hungerford, S. Bhattacharyya, R.P. Lively, D.S. Sholl, K.S. Walton, Heat-Treatment of Defective UiO-66 from Modulated Synthesis: Adsorption and Stability Studies, *J. Phys. Chem. C.* 121 (2017) 23471–23479. doi:10.1021/acs.jpcc.7b07772.
- [144] H. Wu, Y.S. Chua, V. Krungleviciute, M. Tyagi, P. Chen, T. Yildirim, W. Zhou, Unusual and highly tunable missing-linker defects in zirconium metal-organic framework UiO-66 and their important effects on gas adsorption, *J. Am. Chem. Soc.* 135 (2013) 10525–10532.  
doi:10.1021/ja404514r.
- [145] W. Liang, C.J. Coghlan, F. Ragon, M. Rubio-Martinez, D.M. D'Alessandro, R. Babarao, Defect engineering of UiO-66 for CO<sub>2</sub> and H<sub>2</sub>O uptake - A combined experimental and simulation study, *Dalt. Trans.* 45 (2016) 4496–4500. doi:10.1039/c6dt00189k.
- [146] M.J. Katz, Z.J. Brown, Y.J. Colón, P.W. Siu, K.A. Scheidt, R.Q. Snurr, J.T. Hupp, O.K. Farha, A facile synthesis of UiO-66, UiO-67 and their derivatives, *Chem. Commun.* 49 (2013) 9449–9451. doi:10.1039/c3cc46105j.
- [147] M.W. Anjum, F. Vermoortele, A.L. Khan, B. Bueken, D.E. De Vos, I.F.J. Vankelecom, Modulated UiO-66-Based Mixed-Matrix Membranes for CO<sub>2</sub> Separation, (2015).  
doi:10.1021/acsami.5b08964.
- [148] Y. Jiang, C. Liu, J. Caro, A. Huang, A new UiO-66-NH<sub>2</sub> based mixed-matrix membranes with high CO<sub>2</sub>/CH<sub>4</sub> separation performance, *Microporous Mesoporous Mater.* 274 (2019) 203–211.  
doi:10.1016/j.micromeso.2018.08.003.
- [149] H. Reinsch, B. Bueken, F. Vermoortele, I. Stassen, A. Lieb, K.P. Lillerud, D. De Vos, Green synthesis of zirconium-MOFs, *CrystEngComm.* 17 (2015) 4070–4074.  
doi:10.1039/c5ce00618j.
- [150] N.S. Bobbitt, M.L. Mendonca, A.J. Howarth, T. Islamoglu, J.T. Hupp, O.K. Farha, R.Q. Snurr, Metal-organic frameworks for the removal of toxic industrial chemicals and chemical warfare agents, *Chem. Soc. Rev.* 46 (2017) 3357–3385. doi:10.1039/c7cs00108h.

- [151] T. Islamoglu, D. Ray, P. Li, M.B. Majewski, I. Akpınar, X. Zhang, C.J. Cramer, L. Gagliardi, O.K. Farha, From Transition Metals to Lanthanides to Actinides: Metal-Mediated Tuning of Electronic Properties of Isostructural Metal–Organic Frameworks, *17* (2018) 27. doi:10.1021/acs.inorgchem.8b01748.
- [152] H. Furukawa, F. Gándara, Y.B. Zhang, J. Jiang, W.L. Queen, M.R. Hudson, O.M. Yaghi, Water adsorption in porous metal-organic frameworks and related materials, *J. Am. Chem. Soc.* **136** (2014) 4369–4381. doi:10.1021/ja500330a.
- [153] C. Jia, F.G. Cirujano, B. Bueken, B. Claes, D. Jonckheere, K.M. Van Geem, D. De Vos, Geminal Coordinatively Unsaturated Sites on MOF-808 for the Selective Uptake of Phenolics from a Real Bio-Oil Mixture, *ChemSusChem*. **12** (2019) 1256–1266. doi:10.1002/cssc.201802692.
- [154] J. Baek, B. Rungtaweevoranit, X. Pei, M. Park, S.C. Fakra, Y.S. Liu, R. Matheu, S.A. Alshimri, S. Alshehri, C.A. Trickett, G.A. Somorjai, O.M. Yaghi, Bioinspired Metal-Organic Framework Catalysts for Selective Methane Oxidation to Methanol, *J. Am. Chem. Soc.* **140** (2018) 18208–18216. doi:10.1021/jacs.8b11525.
- [155] J. Jiang, F.G. Gándara, Y.-B. Zhang, K. Na, O.M. Yaghi, W.G. Klemperer, Superacidity in Sulfated Metal–Organic Framework-808, *J. Am. Chem. Soc.* **136** (2014) 3. doi:10.1021/ja507119n.
- [156] Y. Peng, H. Huang, Y. Zhang, C. Kang, S. Chen, L. Song, D. Liu, C. Zhong, A versatile MOF-based trap for heavy metal ion capture and dispersion, *Nat. Commun.* **9** (2018). doi:10.1038/s41467-017-02600-2.
- [157] H.M. Wen, C. Liao, L. Li, A. Alsalme, Z. Alothman, R. Krishna, H. Wu, W. Zhou, J. Hu, B. Chen, A metal-organic framework with suitable pore size and dual functionalities for highly efficient post-combustion CO<sub>2</sub> capture, *J. Mater. Chem. A*. **7** (2019) 3128–3134. doi:10.1039/c8ta11596f.
- [158] K.A. Forrest, T. Pham, B. Space, Comparing the mechanism and energetics of CO<sub>2</sub> sorption in the SIFSIX series, *CrystEngComm*. **19** (2017) 3338–3347. doi:10.1039/c7ce00594f.
- [159] O. Shekhah, Y. Belmabkhout, Z. Chen, V. Guillerm, A. Cairns, K. Adil, M. Eddaoudi, Made-to-order metal-organic frameworks for trace carbon dioxide removal and air capture, *Nat. Commun.* **5** (2014) 1–7. doi:10.1038/ncomms5228.
- [160] S.R. Venna, A. Spore, Z. Tian, A.M. Marti, E.J. Albenze, H.B. Nulwala, N.L. Rosi, D.R. Luebke, D.P. Hopkinson, H.R. Allcock, Polyphosphazene polymer development for mixed matrix membranes using SIFSIX-Cu-2i as performance enhancement filler particles, *J. Memb. Sci.* **535** (2017) 103–112. doi:10.1016/j.memsci.2017.04.033.

- [161] H. Gong, C.Y. Chuah, Y. Yang, T.H. Bae, High performance composite membranes comprising Zn(pyrz)<sub>2</sub>(SiF<sub>6</sub>) nanocrystals for CO<sub>2</sub>/CH<sub>4</sub> separation, *J. Ind. Eng. Chem.* 60 (2018) 279–285. doi:10.1016/j.jiec.2017.11.014.
- [162] G. Liu, A. Cadiou, Y. Liu, K. Adil, V. Chernikova, I.-D. Carja, Y. Belmabkhout, M. Karunakaran, O. Shekhah, C. Zhang, A.K. Itta, S. Yi, M. Eddaoudi, W.J. Koros, Enabling Fluorinated MOF-Based Membranes for Simultaneous Removal of H<sub>2</sub>S and CO<sub>2</sub> from Natural Gas, *Angew. Chemie.* 130 (2018) 15027–15032. doi:10.1002/ange.201808991.
- [163] M. Oschatz, M. Antonietti, A search for selectivity to enable CO<sub>2</sub> capture with porous adsorbents, *Energy Environ. Sci.* 11 (2018) 57–70. doi:10.1039/c7ee02110k.
- [164] I. Stassen, D. De Vos, R. Ameloot, Vapor-Phase Deposition and Modification of Metal-Organic Frameworks: State-of-the-Art and Future Directions, *Chem. - A Eur. J.* 22 (2016) 14452–14460. doi:10.1002/chem.201601921.
- [165] R.J. Marshall, C.L. Hobday, C.F. Murphie, S.L. Griffin, C.A. Morrison, S.A. Moggach, R.S. Forgan, Amino acids as highly efficient modulators for single crystals of zirconium and hafnium metal-organic frameworks, *J. Mater. Chem. A.* 4 (2016) 6955–6963. doi:10.1039/c5ta10401g.
- [166] R. Luebke, J.F. Eubank, A.J. Cairns, Y. Belmabkhout, L. Wojtas, M. Eddaoudi, The unique rht-MOF platform, ideal for pinpointing the functionalization and CO<sub>2</sub> adsorption relationship, *Chem. Commun.* 48 (2012) 1455–1457. doi:10.1039/c1cc15962c.
- [167] D.X. Xue, A.J. Cairns, Y. Belmabkhout, L. Wojtas, Y. Liu, M.H. Alkordi, M. Eddaoudi, Tunable rare-earth fcu-MOFs: A platform for systematic enhancement of CO<sub>2</sub> adsorption energetics and uptake, *J. Am. Chem. Soc.* 135 (2013) 7660–7667. doi:10.1021/ja401429x.
- [168] P. Deria, S. Li, H. Zhang, R.Q. Snurr, J.T. Hupp, O.K. Farha, A MOF platform for incorporation of complementary organic motifs for CO<sub>2</sub> binding † *ChemComm, Chem. Commun.* 51 (1247) 12478. doi:10.1039/c5cc04808g.
- [169] H.J. Park, M.P. Suh, Enhanced isosteric heat, selectivity, and uptake capacity of CO<sub>2</sub> adsorption in a metal-organic framework by impregnated metal ions, *Chem. Sci.* 4 (2013) 685–690. doi:10.1039/c2sc21253f.
- [170] A.L. Khan, S. Basu, A. Cano-Odena, I.F.J. Vankelecom, Novel high throughput equipment for membrane-based gas separations, *J. Memb. Sci.* 354 (2010) 32–39. doi:10.1016/j.memsci.2010.02.069.
- [171] A. Torrisi, C. Mellot-Draznieks, R.G. Bell, Impact of ligands on CO<sub>2</sub> adsorption in metal-organic frameworks: First principles study of the interaction of CO<sub>2</sub> with functionalized benzenes. II. Effect of polar and acidic substituents, *J. Chem. Phys.* 132 (2010) 044705.

doi:10.1063/1.3276105.

- [172] L-Serine ReagentPlus®, ≥99% (HPLC) | Sigma-Aldrich, (n.d.).  
<https://www.sigmaaldrich.com/catalog/product/sigma/s4500?lang=en&region=BE> (accessed March 23, 2020).
- [173] Z. Hu, I. Castano, S. Wang, Y. Wang, Y. Peng, Y. Qian, C. Chi, X. Wang, D. Zhao, Modulator Effects on the Water-Based Synthesis of Zr/Hf Metal-Organic Frameworks: Quantitative Relationship Studies between Modulator, Synthetic Condition, and Performance, *Cryst. Growth Des.* 16 (2016) 2295–2301. doi:10.1021/acs.cgd.6b00076.
- [174] A. Schaate, P. Roy, A. Godt, J. Lippke, F. Waltz, M. Wiebcke, P. Behrens, Modulated Synthesis of Zr-Based Metal-Organic Frameworks: From Nano to Single Crystals, *Chem. - A Eur. J.* 17 (2011) 6643–6651. doi:10.1002/chem.201003211.
- [175] T. Ungár, Microstructural parameters from X-ray diffraction peak broadening, *Scr. Mater.* 51 (2004) 777–781. doi:10.1016/j.scriptamat.2004.05.007.
- [176] B. Chen, X. Wang, Q. Zhang, X. Xi, J. Cai, H. Qi, S. Shi, J. Wang, D. Yuan, M. Fang, Synthesis and characterization of the interpenetrated MOF-5, *J. Mater. Chem.* 20 (2010) 3758. doi:10.1039/b922528e.
- [177] R. Seetharaj, P. V. Vandana, P. Arya, S. Mathew, Dependence of solvents, pH, molar ratio and temperature in tuning metal organic framework architecture, *Arab. J. Chem.* 12 (2019) 295–315. doi:10.1016/j.arabjc.2016.01.003.
- [178] B. Shan, J.B. James, M.R. Armstrong, E.C. Close, P.A. Letham, K. Nikkhah, Y.S. Lin, B. Mu, Influences of Deprotonation and Modulation on Nucleation and Growth of UiO-66: Intergrowth and Orientation, (2018). doi:10.1021/acs.jpcc.7b11012.
- [179] G.L. Fan, Y.L. Liu, H. Wang, Identification of thermophilic proteins by incorporating evolutionary and acid dissociation information into Chou's general pseudo amino acid composition, *J. Theor. Biol.* 407 (2016) 138–142. doi:10.1016/j.jtbi.2016.07.010.
- [180] P. Luis, Use of monoethanolamine (MEA) for CO<sub>2</sub> capture in a global scenario: Consequences and alternatives, *Desalination.* 380 (2016) 93–99. doi:10.1016/j.desal.2015.08.004.
- [181] C. Ardila-Suárez, J. Rodríguez-Pereira, V.G. Baldovino-Medrano, G.E. Ramírez-Caballero, An analysis of the effect of zirconium precursors of MOF-808 on its thermal stability, and structural and surface properties, *CrystEngComm.* 21 (2019) 1407–1415. doi:10.1039/c8ce01722k.
- [182] J. Hafizovic, M. Bjørgen, U. Olsbye, P.D.C. Dietzel, S. Bordiga, C. Prestipino, C. Lamberti, K.P. Lillerud, The Inconsistency in Adsorption Properties and Powder XRD Data of MOF-5 Is

- Rationalized by Framework Interpenetration and the Presence of Organic and Inorganic Species in the Nanocavities, (2007). doi:10.1021/ja0675447.
- [183] S. Øien-Ødegaard, G.C. Shearer, D.S. Wragg, K.P. Lillerud, Pitfalls in metal-organic framework crystallography: Towards more accurate crystal structures, *Chem. Soc. Rev.* 46 (2017) 4867–4876. doi:10.1039/c6cs00533k.
- [184] W. Zhang, A. Bu, Q. Ji, L. Min, S. Zhao, Y. Wang, J. Chen, pK<sub>a</sub>-Directed Incorporation of Phosphonates into MOF-808 via Ligand Exchange: Stability and Adsorption Properties for Uranium, (2019). doi:10.1021/acsami.9b10920.
- [185] S.-Y. Moon, Y. Liu, J.T. Hupp, O.K. Farha, Instantaneous Hydrolysis of Nerve-Agent Simulants with a Six-Connected Zirconium-Based Metal-Organic Framework, *Angew. Chemie Int. Ed.* 54 (2015) 6795–6799. doi:10.1002/anie.201502155.
- [186] H.Q. Zheng, C.Y. Liu, X.Y. Zeng, J. Chen, J. Lü, R.G. Lin, R. Cao, Z.J. Lin, J.W. Su, MOF-808: A Metal-Organic Framework with Intrinsic Peroxidase-Like Catalytic Activity at Neutral pH for Colorimetric Biosensing, *Inorg. Chem.* 57 (2018) 9096–9104. doi:10.1021/acs.inorgchem.8b01097.
- [187] † Houston Frost, ‡ and Tina Düren, † Randall Q. Snurr\*, Effects of Surface Area, Free Volume, and Heat of Adsorption on Hydrogen Uptake in Metal–Organic Frameworks, (2006). doi:10.1021/JP060433+.
- [188] Y.S. Bae, O.K. Farha, J.T. Hupp, R.Q. Snurr, Enhancement of CO<sub>2</sub>/N<sub>2</sub> selectivity in a metal-organic framework by cavity modification, *J. Mater. Chem.* 19 (2009) 2131–2134. doi:10.1039/b900390h.
- [189] S.R. Venna, M. Lartey, T. Li, A. Spore, S. Kumar, H.B. Nulwala, D.R. Luebke, N.L. Rosi, E. Albenze, Fabrication of MMMs with improved gas separation properties using externally-functionalized MOF particles †, (2015). doi:10.1039/c4ta05225k.
- [190] H. Ren, J. Jin, J. Hu, H. Liu, Affinity between Metal–Organic Frameworks and Polyimides in Asymmetric Mixed Matrix Membranes for Gas Separations, (2012). doi:10.1021/ie300553k.
- [191] H.M. Lee, I.S. Youn, M. Saleh, J.W. Lee, K.S. Kim, Interactions of CO<sub>2</sub> with various functional molecules, *Phys. Chem. Chem. Phys.* 17 (2015) 10925–10933. doi:10.1039/c5cp00673b.
- [192] Z. Niu, Q. Guan, Y. Shi, Y. Chen, Q. Chen, Z. Kong, P. Ning, S. Tian, R. Miao, A lithium-modified zirconium-based metal organic framework (UiO-66) for efficient CO<sub>2</sub> adsorption, *New J. Chem.* 42 (2018) 19764–19770. doi:10.1039/c8nj04945a.
- [193] Y.S. Bae, B.G. Hauser, O.K. Farha, J.T. Hupp, R.Q. Snurr, Enhancement of CO<sub>2</sub>/CH<sub>4</sub>

- selectivity in metal-organic frameworks containing lithium cations, *Microporous Mesoporous Mater.* 141 (2011) 231–235. doi:10.1016/j.micromeso.2010.10.048.
- [194] J.P. Pancras, G.A. Norris, M.S. Landis, K.D. Kovalcik, J.K. McGee, A.S. Kamal, Application of ICP-OES for evaluating energy extraction and production wastewater discharge impacts on surface waters in Western Pennsylvania, *Sci. Total Environ.* 529 (2015) 21–29. doi:10.1016/j.scitotenv.2015.04.011.
- [195] D. Lide, *CRC Handbook of Chemistry and Physics*, 91th Edition, 91st ed., Taylor & Francis Group, 2010.
- [196] Q. Meng, X. Xin, L. Zhang, F. Dai, R. Wang, D. Sun, A multifunctional Eu MOF as a fluorescent pH sensor and exhibiting highly solvent-dependent adsorption and degradation of rhodamine B †, (2015). doi:10.1039/c5ta04989j.
- [197] J. Konopka, T.F. Scientific, Options for Quantitative Analysis of Light Elements by SEM/EDS, (n.d.). [http://tools.thermofisher.com/content/sfs/brochures/TN52523\\_E\\_0713M\\_LightElement\\_H.pdf](http://tools.thermofisher.com/content/sfs/brochures/TN52523_E_0713M_LightElement_H.pdf) (accessed March 28, 2020).
- [198] K. Xuan, Y. Pu, F. Li, J. Luo, N. Zhao, F. Xiao, Metal-organic frameworks MOF-808-X as highly efficient catalysts for direct synthesis of dimethyl carbonate from CO<sub>2</sub> and methanol, *Chinese J. Catal.* 40 (2019) 553–566. doi:10.1016/S1872-2067(19)63291-2.
- [199] C. Ardila-Suárez, A.M. Díaz-Lasprilla, L.A. Díaz-Vaca, P.B. Balbuena, V.G. Baldovino-Medrano, G.E. Ramírez-Caballero, Synthesis, characterization, and post-synthetic modification of a micro/mesoporous zirconium-tricarboxylate metal-organic framework: Towards the addition of acid active sites, *CrystEngComm.* 21 (2019) 3014–3030. doi:10.1039/c9ce00218a.
- [200] S. Kumar, A.K. Rai, S.B. Rai, D.K. Rai, Infrared and Raman spectra of Histidine: An ab initio DFT calculations of Histidine molecule and its different protonated forms, *Indian J. Phys.* 84 (2010) 563–573. doi:10.1007/s12648-010-0039-6.
- [201] *Introduction to Infrared and Raman Spectroscopy*, Elsevier, 1975. doi:10.1016/b978-0-12-182552-2.x5001-3.
- [202] IR Spectrum Table & Chart | Sigma-Aldrich, (n.d.). <https://www.sigmaaldrich.com/technical-documents/articles/biology/ir-spectrum-table.html> (accessed March 29, 2020).
- [203] S.G. Stepanian, I.D. Reva, E.D. Radchenko, G.G. Sheina, Infrared spectra of benzoic acid monomers and dimers in argon matrix, *Vib. Spectrosc.* 11 (1996) 123–133. doi:10.1016/0924-2031(95)00068-2.
- [204] F.A. Najar, G.B. Vakil, B. Want, Infrared, Raman, electrical and thermal analysis of lithium

- sulphate monohydrate single crystals, *J. Mater. Sci. Mater. Electron.* 28 (2017) 14170–14178. doi:10.1007/s10854-017-7271-1.
- [205] M.J.C. Ordoñez, K.J. Balkus, J.P. Ferraris, I.H. Musselman, Molecular sieving realized with ZIF-8/Matrimid® mixed-matrix membranes, *J. Memb. Sci.* 361 (2010) 28–37. doi:10.1016/j.memsci.2010.06.017.
- [206] J.A. Mason, K. Sumida, Z.R. Herm, R. Krishna, J.R. Long, Evaluating metal-organic frameworks for post-combustion carbon dioxide capture via temperature swing adsorption, *Energy Environ. Sci.* 4 (2011) 3030–3040. doi:10.1039/c1ee01720a.
- [207] B. Arstad, H. Fjellvåg, · Kjell, O. Kongshaug, O. Swang, R. Blom, H. Fjellvåg, · K O Kongshaug, Amine functionalised metal organic frameworks (MOFs) as adsorbents for carbon dioxide, *Adsorption.* 14 (2008) 755–762. doi:10.1007/s10450-008-9137-6.
- [208] H.Y. Cho, D.A. Yang, J. Kim, S.Y. Jeong, W.S. Ahn, CO<sub>2</sub> adsorption and catalytic application of Co-MOF-74 synthesized by microwave heating, in: *Catal. Today*, Elsevier, 2012: pp. 35–40. doi:10.1016/j.cattod.2011.08.019.
- [209] M.I. Hossain, J.D. Cunningham, T.M. Becker, B.E. Grabicka, K.S. Walton, B.D. Rabideau, T.G. Glover, Impact of MOF defects on the binary adsorption of CO<sub>2</sub> and water in UiO-66, *Chem. Eng. Sci.* 203 (2019) 346–357. doi:10.1016/j.ces.2019.03.053.
- [210] M. Asgari, S. Jawahery, E.D. Bloch, M.R. Hudson, R. Flacau, B. Vlasisavljevich, J.R. Long, C.M. Brown, W.L. Queen, An experimental and computational study of CO<sub>2</sub> adsorption in the sodalite-type M-BTT (M = Cr, Mn, Fe, Cu) metal-organic frameworks featuring open metal sites, *Chem. Sci.* 9 (2018) 4579–4588. doi:10.1039/c8sc00971f.
- [211] M. Stawowy, M. Rózewicz, E. Szczepańska, J. Silvestre-Albero, M. Zawadzki, M. Musioł, R. Łuzny, J. Kaczmarczyk, J. Trawczyński, A. Łamacz, The Impact of Synthesis Method on the Properties and CO<sub>2</sub> Sorption Capacity of UiO-66(Ce), *Catalysts.* 9 (2019) 309. doi:10.3390/catal9040309.
- [212] H.H. Mautschke, F. Drache, I. Senkovska, S. Kaskel, F.X.I. Llabrés Xamena, Catalytic properties of pristine and defect-engineered Zr-MOF-808 metal organic frameworks, *Catal. Sci. Technol.* 8 (2018) 3610–3616. doi:10.1039/c8cy00742j.
- [213] P.D.C. Dietzel, V. Besikiotis, R. Blom, Application of metal-organic frameworks with coordinatively unsaturated metal sites in storage and separation of methane and carbon dioxide, *J. Mater. Chem.* 19 (2009) 7362–7370. doi:10.1039/b911242a.
- [214] C. Song, Y. Ling, L. Jin, M. Zhang, D.-L. Chen, Y. He, CO<sub>2</sub> adsorption of three isostructural metal-organic frameworks depending on the incorporated highly polarized heterocyclic moieties, *Dalt. Trans.* 45 (2015) 190. doi:10.1039/c5dt02845k.

- [215] P. Xydias, I. Spanopoulos, E. Klontzas, G.E. Froudakis, P.N. Trikalitis, Drastic Enhancement of the CO<sub>2</sub> Adsorption Properties in Sulfone-Functionalized Zr-and Hf-UiO-67 MOFs with Hierarchical Mesopores, (2013). doi:10.1021/ic402430n.
- [216] B. Ghalei, K. Sakurai, Y. Kinoshita, K. Wakimoto, A. Pournaghshband Isfahani, Q. Song, K. Doitomi, S. Furukawa, H. Hirao, H. Kusuda, S. Kitagawa, E. Sivaniah, Enhanced selectivity in mixed matrix membranes for CO<sub>2</sub> capture through efficient dispersion of amine-functionalized MOF nanoparticles, (2017) 17086. doi:10.1038/nenergy.2017.86.
- [217] M.Z. Ahmad, T.A. Peters, N.M. Konnertz, T. Visser, C. Téllez, J. Coronas, V. Fila, W.M. de Vos, N.E. Benes, High-pressure CO<sub>2</sub>/CH<sub>4</sub> separation of Zr-MOFs based mixed matrix membranes, *Sep. Purif. Technol.* 230 (2020) 115858. doi:10.1016/j.seppur.2019.115858.
- [218] C. Ma, J.J. Urban, Enhanced CO<sub>2</sub> Capture and Hydrogen Purification by Hydroxy Metal–Organic Framework/Polyimide Mixed Matrix Membranes, *ChemSusChem*. 12 (2019) 4405–4411. doi:10.1002/cssc.201902248.
- [219] P.S. Tin, T.S. Chung, Y. Liu, R. Wang, S.L. Liu, K.P. Pramoda, Effects of cross-linking modification on gas separation performance of Matrimid membranes, *J. Memb. Sci.* 225 (2003) 77–90. doi:10.1016/j.memsci.2003.08.005.
- [220] M. Khdhayyer, A.F. Bushell, P.M. Budd, M.P. Atfield, D. Jiang, A.D. Burrows, E. Esposito, P. Bernardo, M. Monteleone, A. Fuoco, G. Clarizia, F. Bazzarelli, A. Gordano, J.C. Jansen, Mixed matrix membranes based on MIL-101 metal–organic frameworks in polymer of intrinsic microporosity PIM-1, *Sep. Purif. Technol.* 212 (2019) 545–554. doi:10.1016/j.seppur.2018.11.055.
- [221] A. Ebadi Amooghin, M. Omidkhah, A. Kargari, Enhanced CO<sub>2</sub> transport properties of membranes by embedding nano-porous zeolite particles into Matrimid®5218 matrix, *RSC Adv.* 5 (2015) 8552–8565. doi:10.1039/c4ra14903c.
- [222] Z. Hu, Z. Kang, Y. Qian, Y. Peng, X. Wang, C. Chi, D. Zhao, Mixed Matrix Membranes Containing UiO-66(Hf)-(OH)<sub>2</sub> Metal–Organic Framework Nanoparticles for Efficient H<sub>2</sub>/CO<sub>2</sub> Separation, (2016). doi:10.1021/acs.iecr.5b04568.
- [223] *Introduction to Probability and Statistics for Engineers and Scientists*, 5th ed., Elsevier, 2014. doi:10.1016/C2013-0-19397-X.
- [224] B.D. Conley, B.C. Yearwood, S. Parkin, D.A. Atwood, Ammonium hexafluorosilicate salts, *J. Fluor. Chem.* 115 (2002) 155–160. doi:10.1016/S0022-1139(02)00046-5.
- [225] A. Ouasri, A. Rhandour, M.C. Dhamelincourt, P. Dhamelincourt, A. Mazzah, The infrared and Raman spectra of ethylammonium hexafluorosilicate [C<sub>2</sub>H<sub>5</sub>NH<sub>3</sub>]<sub>2</sub>SiF<sub>6</sub>, *Spectrochim. Acta - Part A Mol. Biomol. Spectrosc.* 59 (2003) 357–362. doi:10.1016/S1386-1425(02)00165-8.

- [226] M.H. Zaghal, H.A. Qaseer, Complexes of 2-(2'-pyridyl)quinoline and 3,6-Di(4'-pyridyl)-S-tetrazine, *Inorganica Chim. Acta.* 163 (1989) 193–200. doi:10.1016/S0020-1693(00)83451-9.
- [227] A. Ehsani, M. Pakizeh, Synthesis, characterization and gas permeation study of ZIF-11/Pebax® 2533 mixed matrix membranes, *J. Taiwan Inst. Chem. Eng.* 66 (2016) 414–423. doi:10.1016/j.jtice.2016.07.005.
- [228] Y. Li, T.S. Chung, C. Cao, S. Kulprathipanja, The effects of polymer chain rigidification, zeolite pore size and pore blockage on polyethersulfone (PES)-zeolite A mixed matrix membranes, *J. Memb. Sci.* 260 (2005) 45–55. doi:10.1016/j.memsci.2005.03.019.
- [229] Y. Wang, X. Ma, B.S. Ghanem, F. Alghunaimi, I. Pinnau, Y. Han, Polymers of intrinsic microporosity for energy-intensive membrane-based gas separations, *Mater. Today Nano.* 3 (2018) 69–95. doi:10.1016/j.mtnano.2018.11.003.

## Appendix

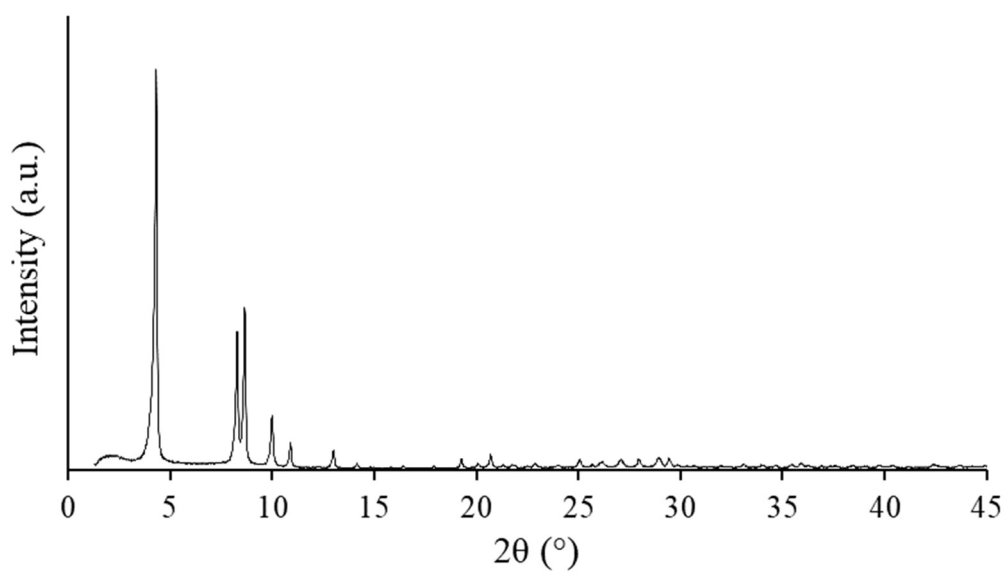


Figure A 1: XRD diffractogram of MOF-FA-u.

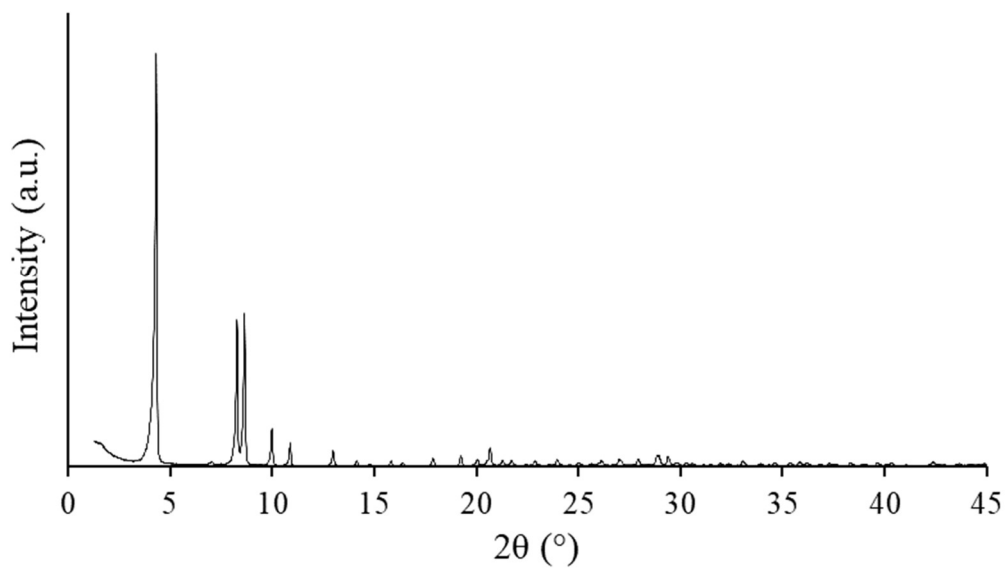


Figure A 2: XRD diffractogram of MOF-His.

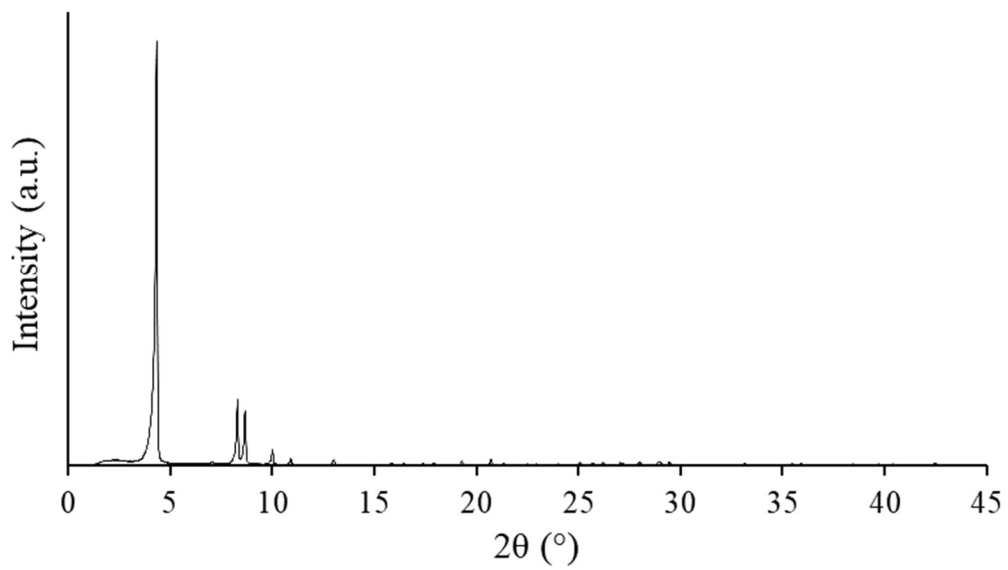


Figure A 3: XRD diffractogram of MOF-TFA.

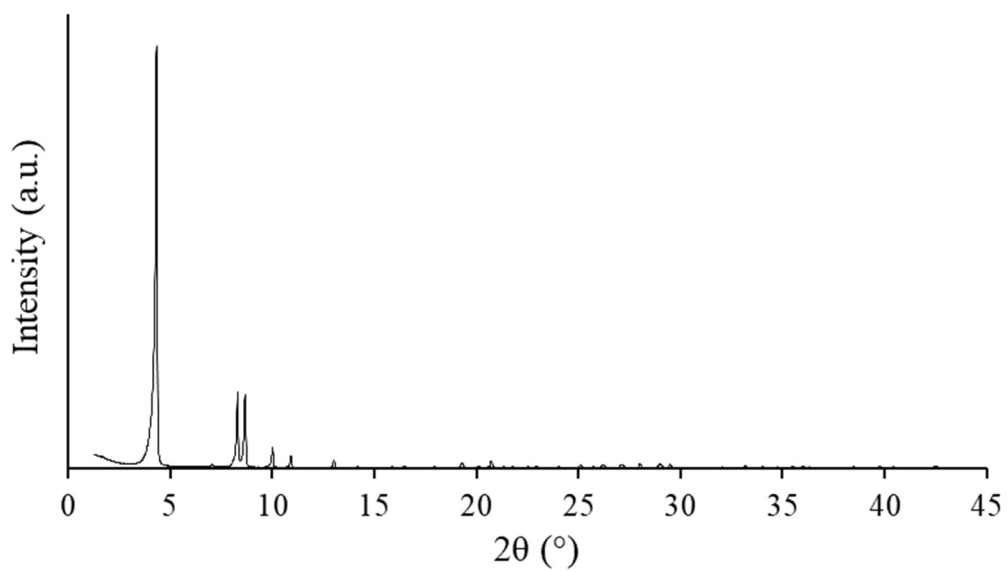


Figure A 4: XRD diffractogram of MOF-GA.

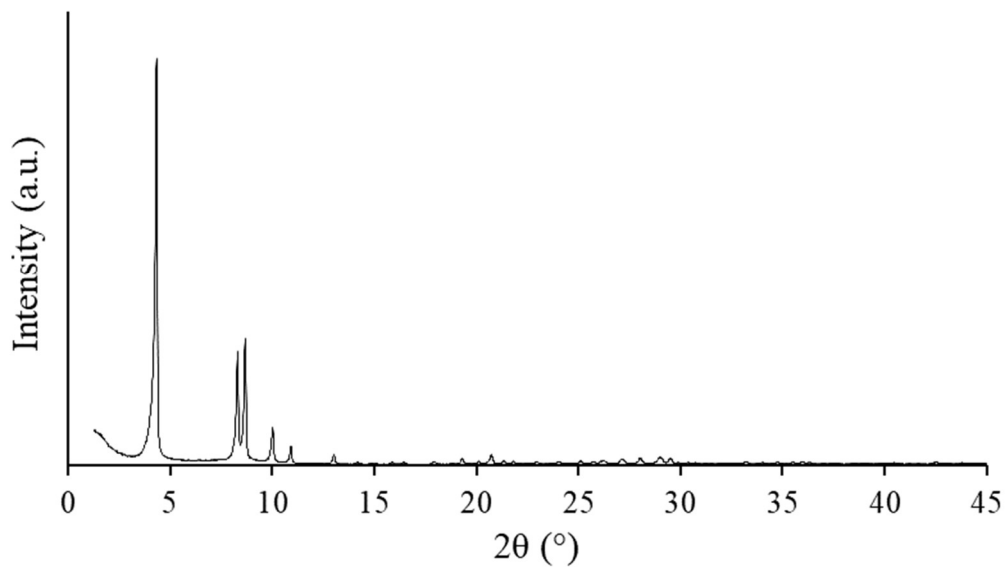


Figure A 5: XRD diffractogram of MOF-BA.

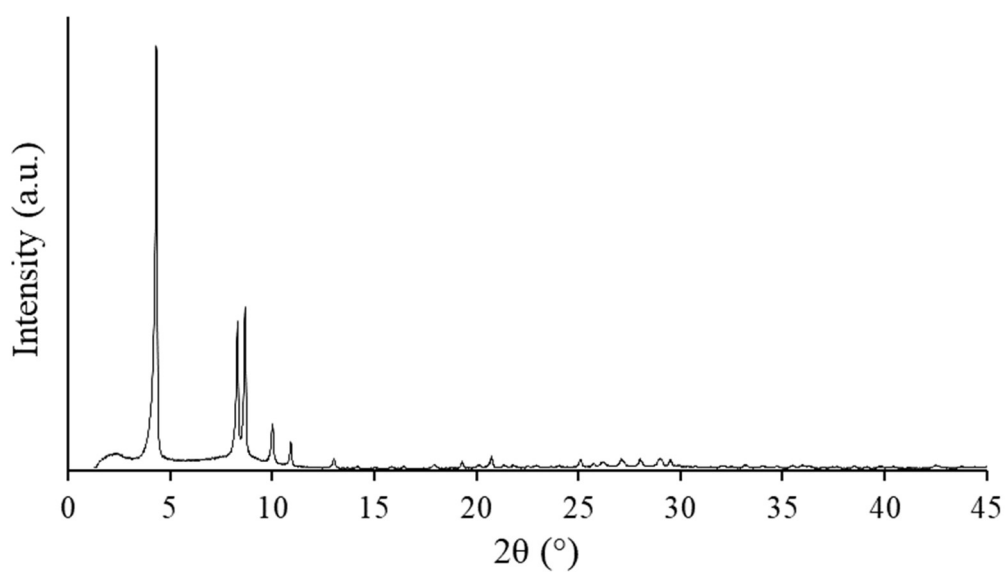


Figure A 6: XRD diffractogram of MOF-Li<sub>2</sub>SO<sub>4</sub>.

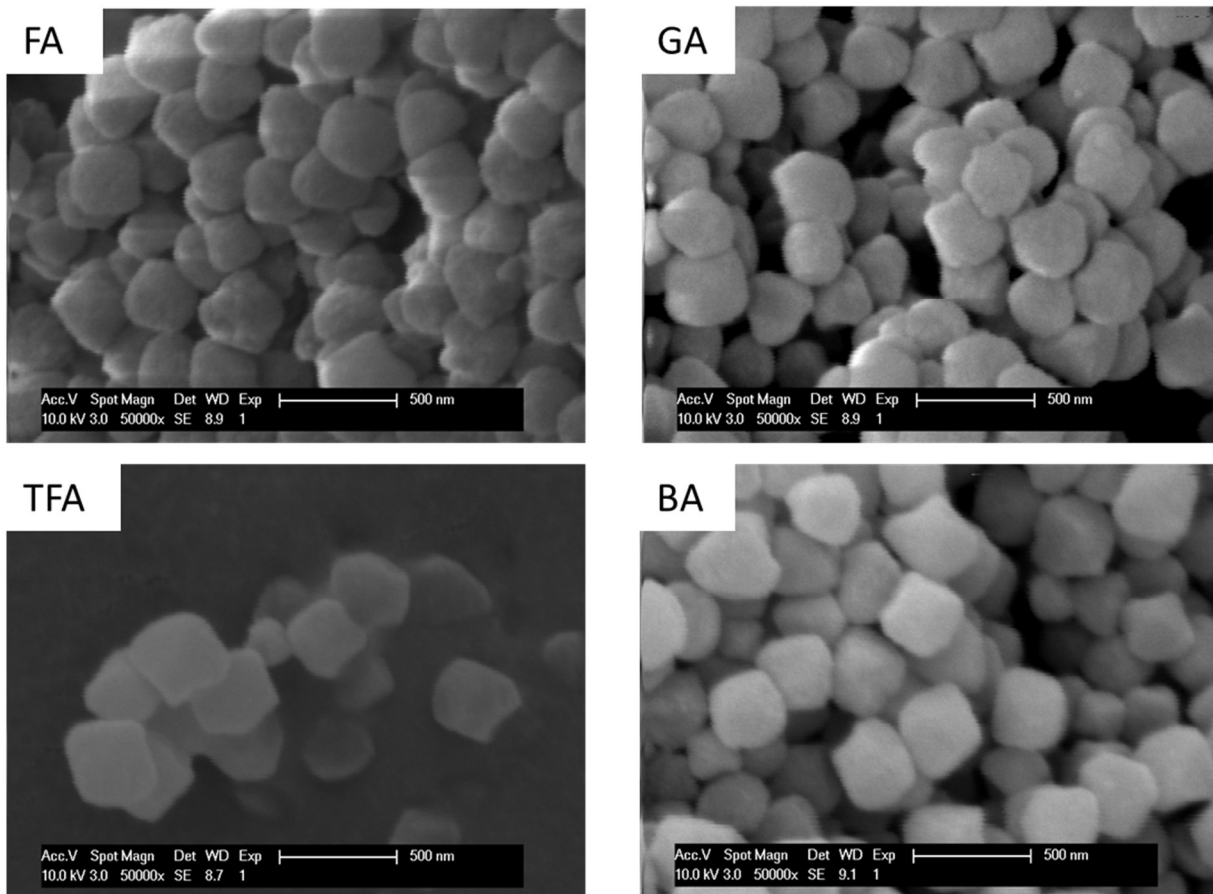


Figure A 7: SEM images of MOF-FA-u, MOF-GA, MOF-TFA and MOF-BA taken at a magnification (x50000). For MOF-His and MOF-Li<sub>2</sub>SO<sub>4</sub> no SEM images were recorded at this magnification.

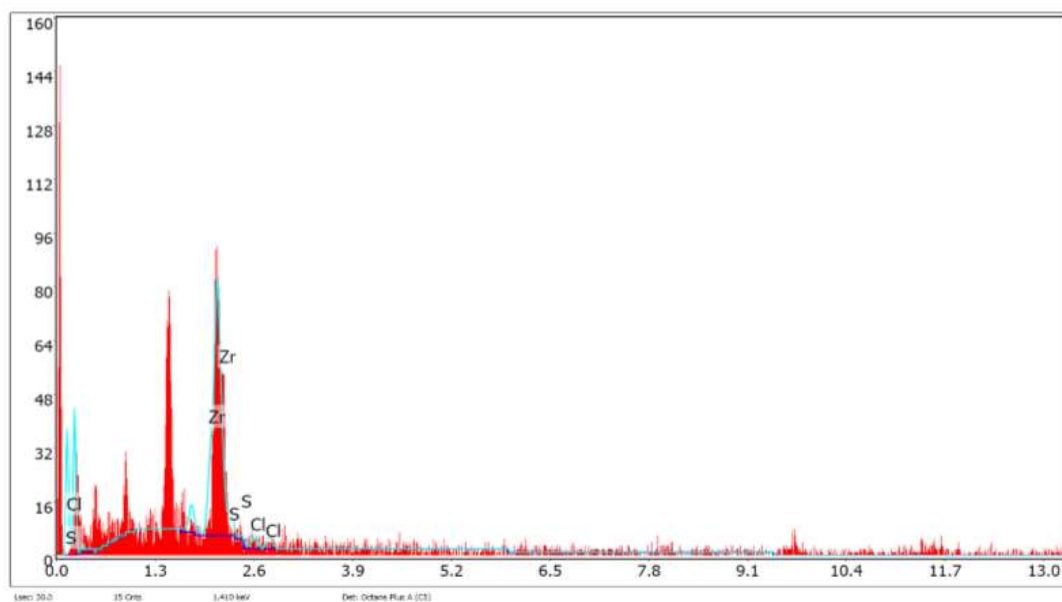


Figure A 8: EDX spectrum of MOF-Li<sub>2</sub>SO<sub>4</sub>.

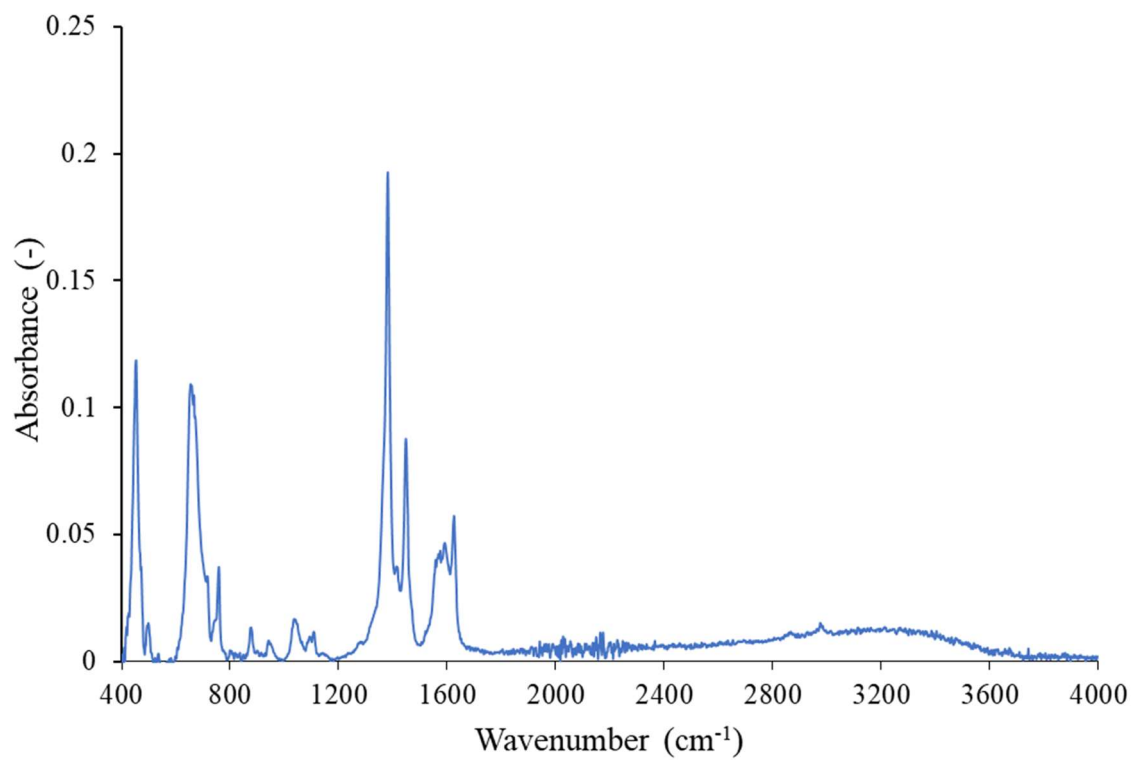


Figure A 9: ATR-FTIR absorbance spectrum of MOF-FA-u.

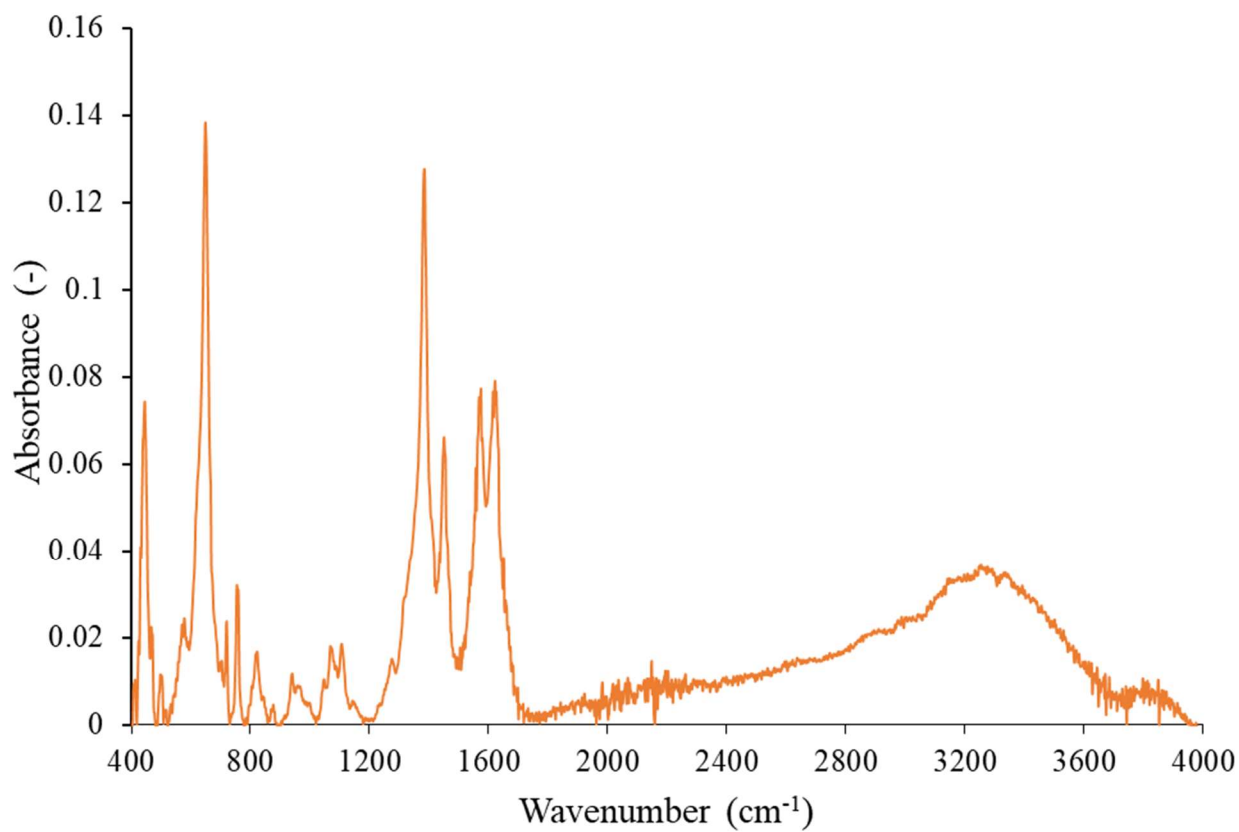


Figure A 10: ATR-FTIR absorbance spectrum of MOF-His.

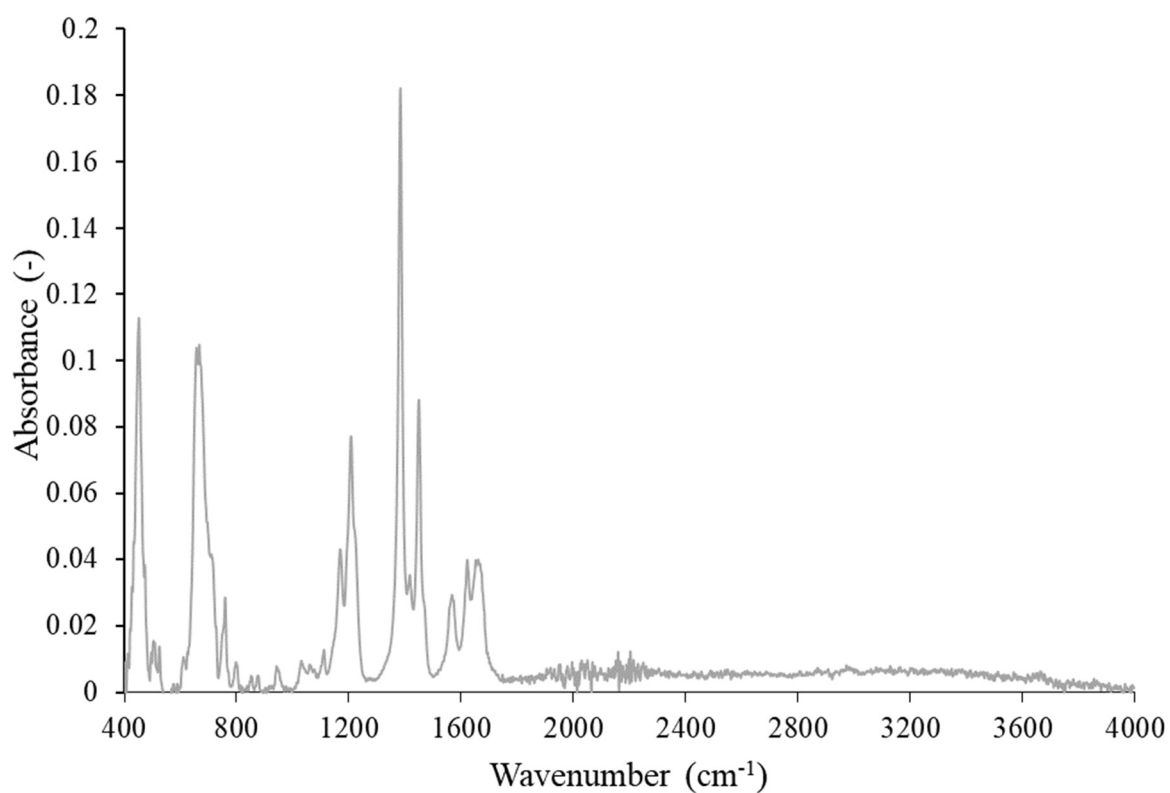


Figure A 11: ATR-FTIR absorbance spectrum of MOF-TFA.

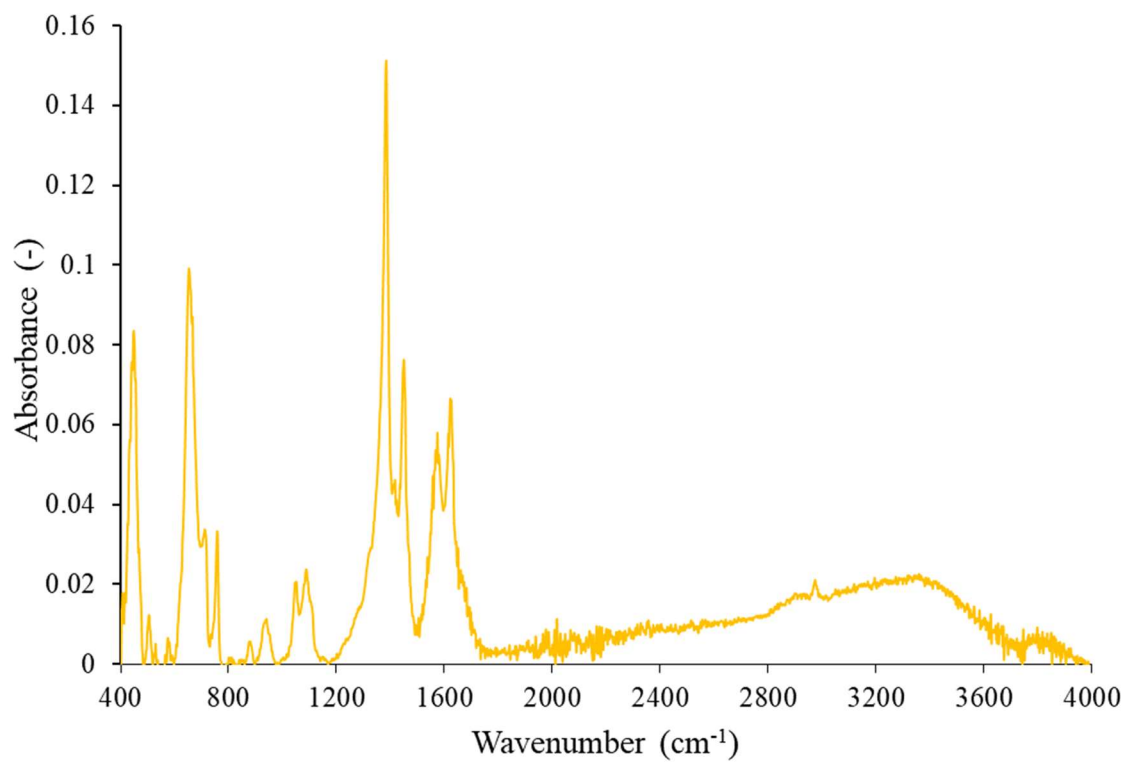


Figure A 12: ATR-FTIR absorbance spectrum of MOF-GA.

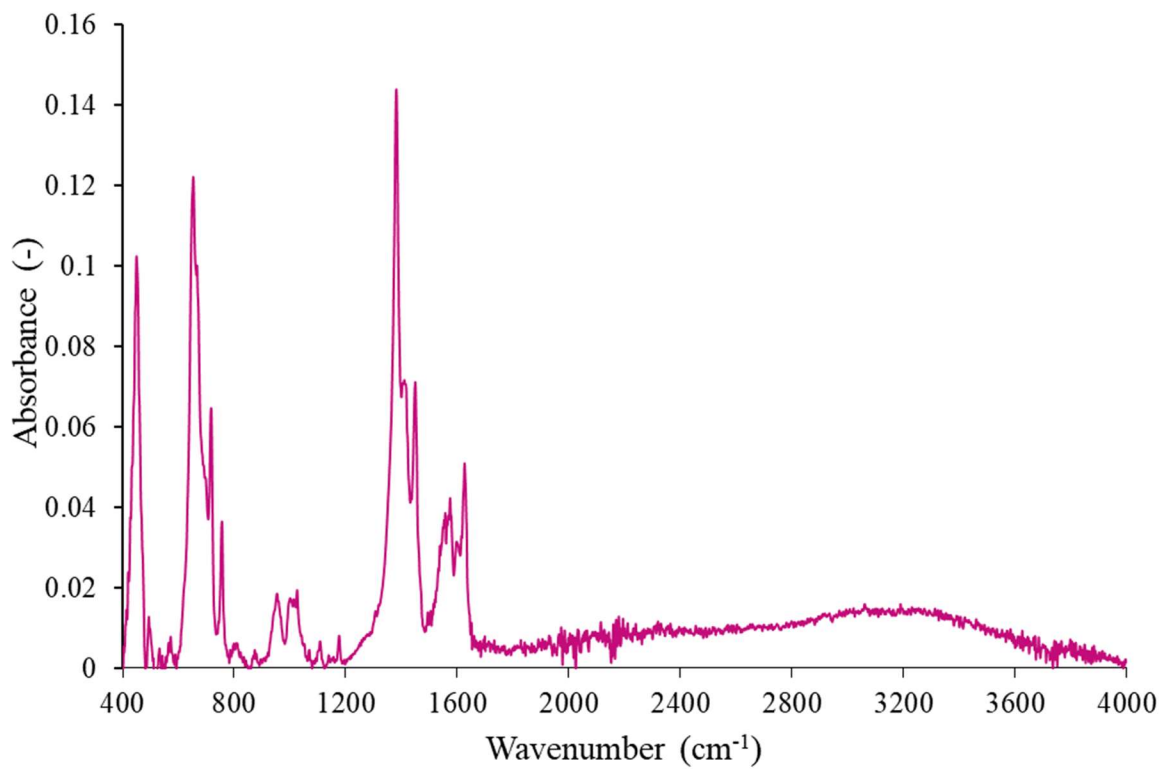


Figure A 13: ATR-FTIR absorbance spectrum of MOF-BA.

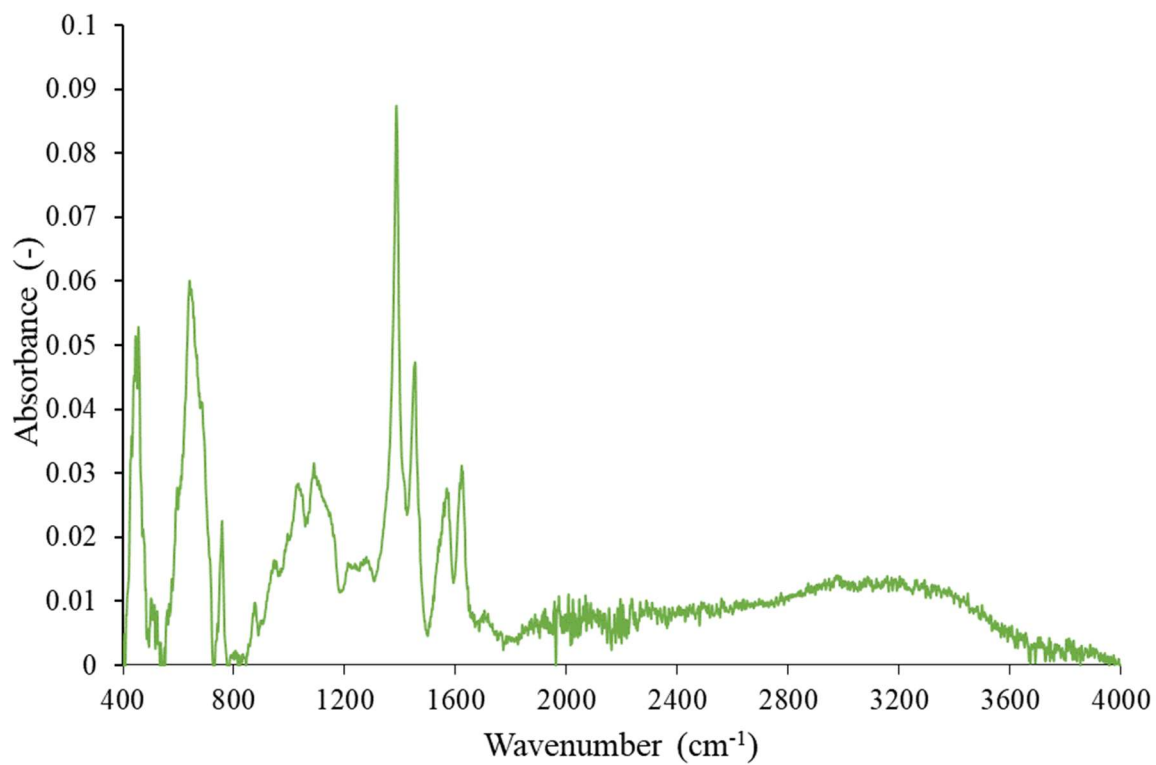


Figure A 14: ATR-FTIR absorbance spectrum of MOF-Li<sub>2</sub>SO<sub>4</sub>.

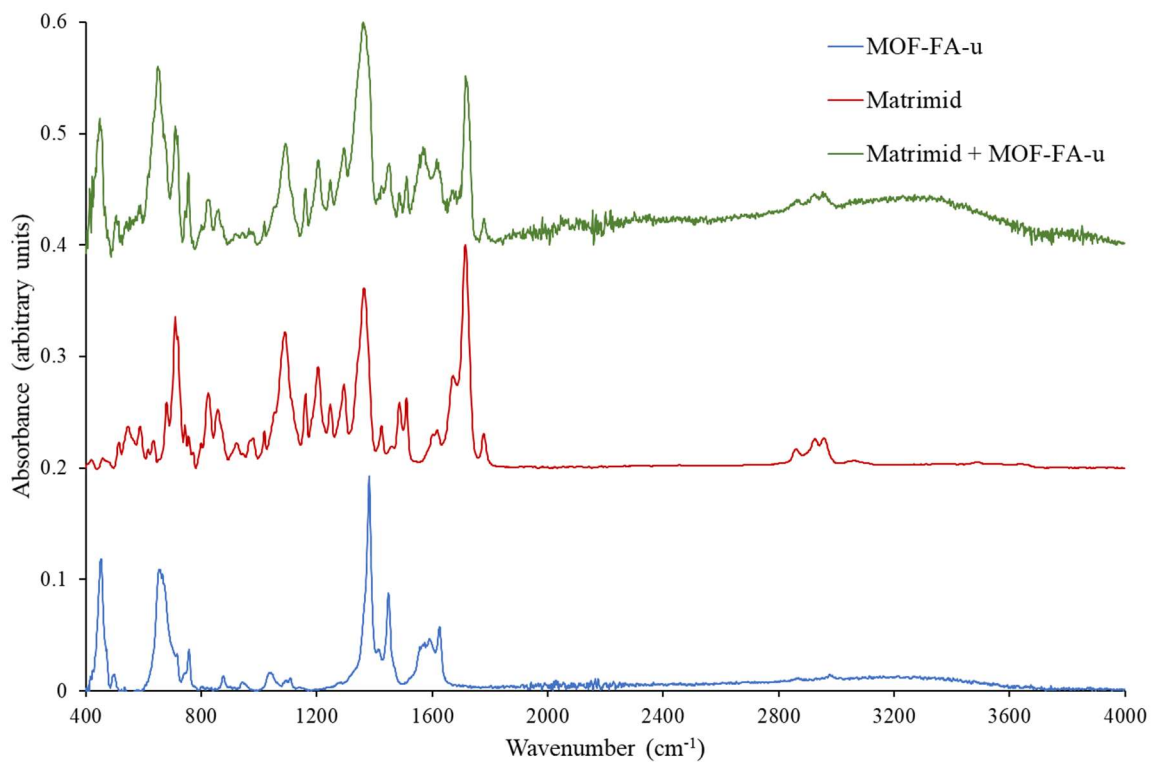


Figure A 15: ATR-FTIR absorbance spectrum of MOF-FA-u, Matrimid and Matrimid + MOF-FA-u MMM. Spectra were scaled to an identical intensity for the most intense absorption for clarity.

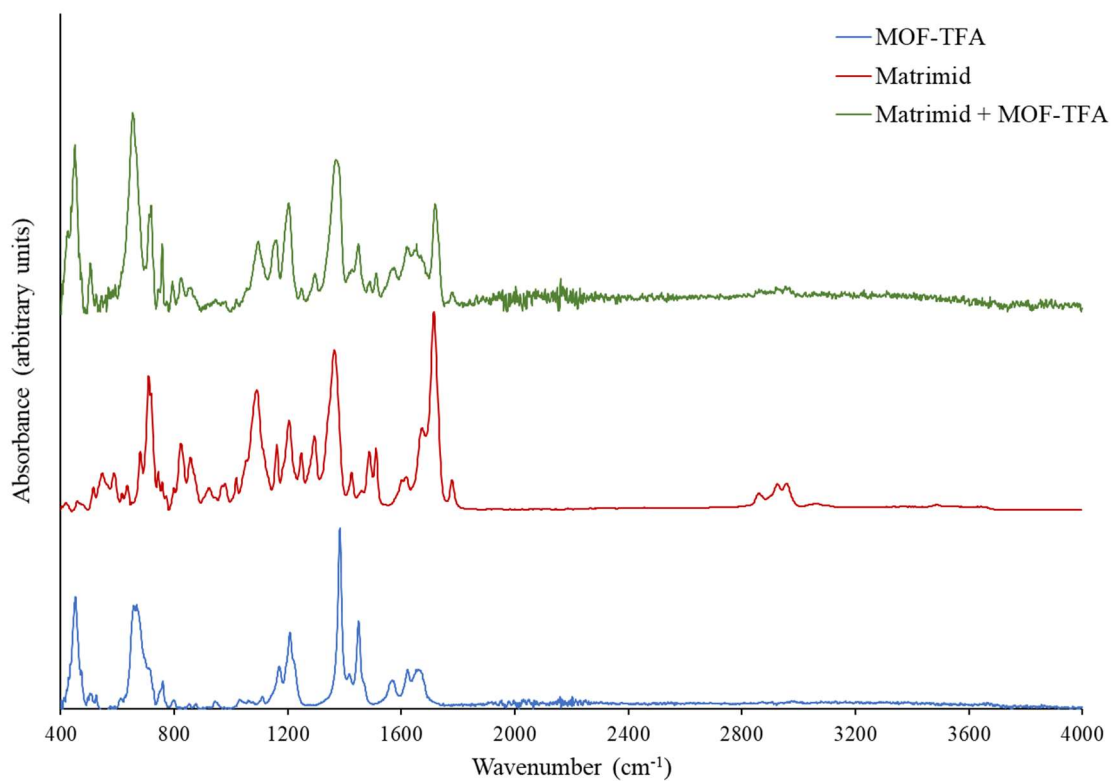


Figure A 16: ATR-FTIR absorbance spectrum of MOF-TFA, Matrimid and Matrimid + MOF-TFA MMM. Spectra were scaled to an identical intensity for the most intense absorption for clarity.

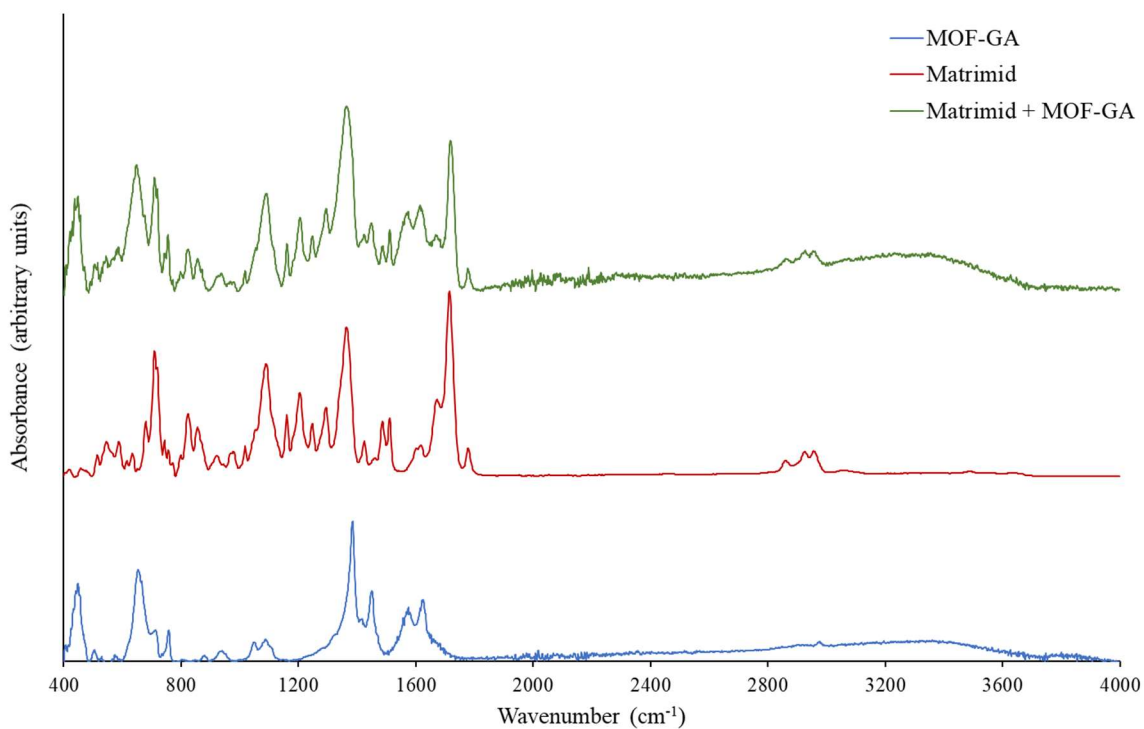


Figure A 17: ATR-FTIR absorbance spectrum of MOF-GA, Matrimid and Matrimid + MOF-GA MMM. Spectra were scaled to an identical intensity for the most intense absorption for clarity.

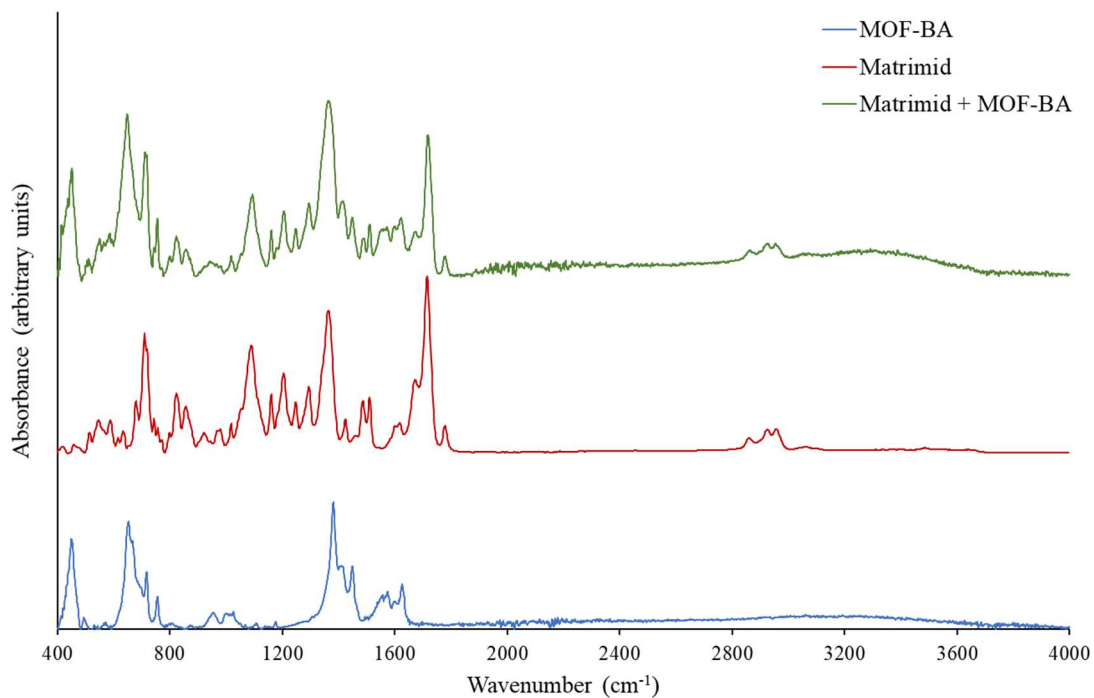


Figure A 18: ATR-FTIR absorbance spectrum of MOF-BA, Matrimid and Matrimid + MOF-BA MMM. Spectra were scaled to an identical intensity for the most intense absorption for clarity.

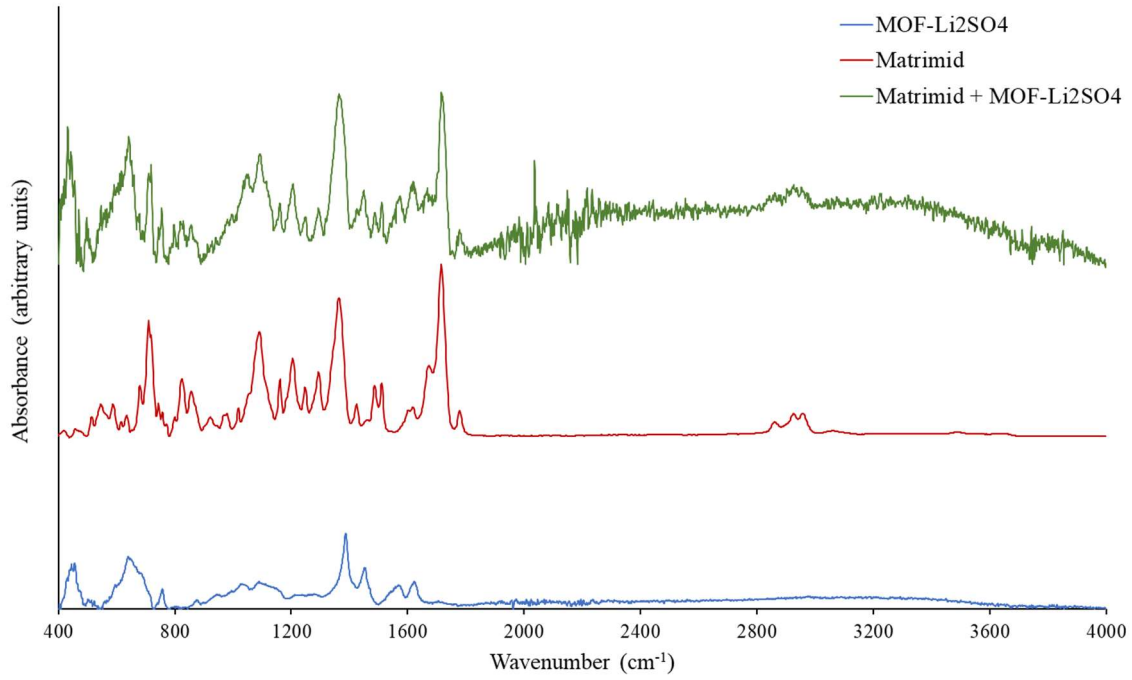


Figure A 19: ATR-FTIR absorbance spectrum of MOF-Li<sub>2</sub>SO<sub>4</sub>, Matrimid and Matrimid + MOF-Li<sub>2</sub>SO<sub>4</sub> MMM. Spectra were scaled to an identical intensity for the most intense absorption for clarity.

Fit Parameters									
	MOF-TFA			MOF-BA			MOF-FA-u		
	0 °C	20 °C	40 °C	0 °C	20 °C	40 °C	0 °C	20 °C	40 °C
$N_{m,a}$	0.4353	0.3309	0.1937	0.0210	0.0000	0.0009	0.3372	0.2932	0.0794
$N_{m,b}$	4.4420	4.6930	3.8160	4.9270	5.0540	5.7810	8.7370	7.7480	6.5000
$b_a$	0.0556	0.0203	0.0092	0.0333	0.0000	0.0027	0.0459	0.0172	0.0118
$b_b$	0.0007	0.0004	0.0003	0.0007	0.0004	0.0002	0.0004	0.0003	0.0002
$R^2$	1.0000	1.0000	1.0000	1.0000	0.9999	0.9995	1.0000	1.0000	1.0000
	MOF-GA			MOF-His			MOF-Li <sub>2</sub> SO <sub>4</sub>		
	0 °C	20 °C	40 °C	0 °C	20 °C	40 °C	0 °C	20 °C	40 °C
$N_{m,a}$	8.0850	5.9870	3.9260	5.6130	4.6390	3.0940	3.6320	3.2270	2.6520
$N_{m,b}$	0.3151	0.2123	0.1576	0.5914	0.3395	0.0668	0.3100	0.2227	0.0566
$b_a$	0.0003	0.0003	0.0003	0.0005	0.0005	0.0006	0.0006	0.0005	0.0005
$b_b$	0.0496	0.0184	0.0056	0.0201	0.0140	0.0195	0.0362	0.0436	0.0285
$R^2$	1.0000	1.0000	1.0000	0.9999	1.0000	1.0000	0.9999	1.0000	1.0000

Table A 1: Dual-site Langmuir fit parameters of the adsorption isotherms measured at 0 °C, 20 °C and 40 °C for each of the functionalized MOFs.

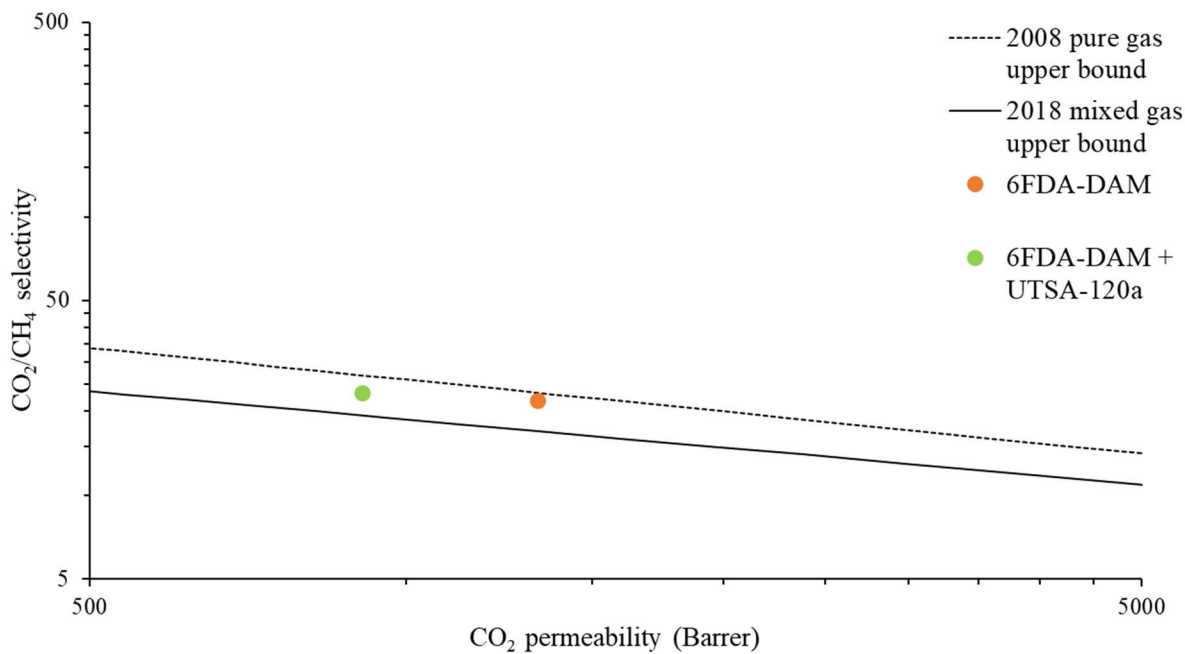


Figure A 20:  $CO_2/CH_4$  Robeson plot for 6FDA-DAM and UTSA-120a 6FDA-DAM MMM[69,229]. The datapoints for a 50/50  $CO_2/CH_4$  feed gas mixture are shown.

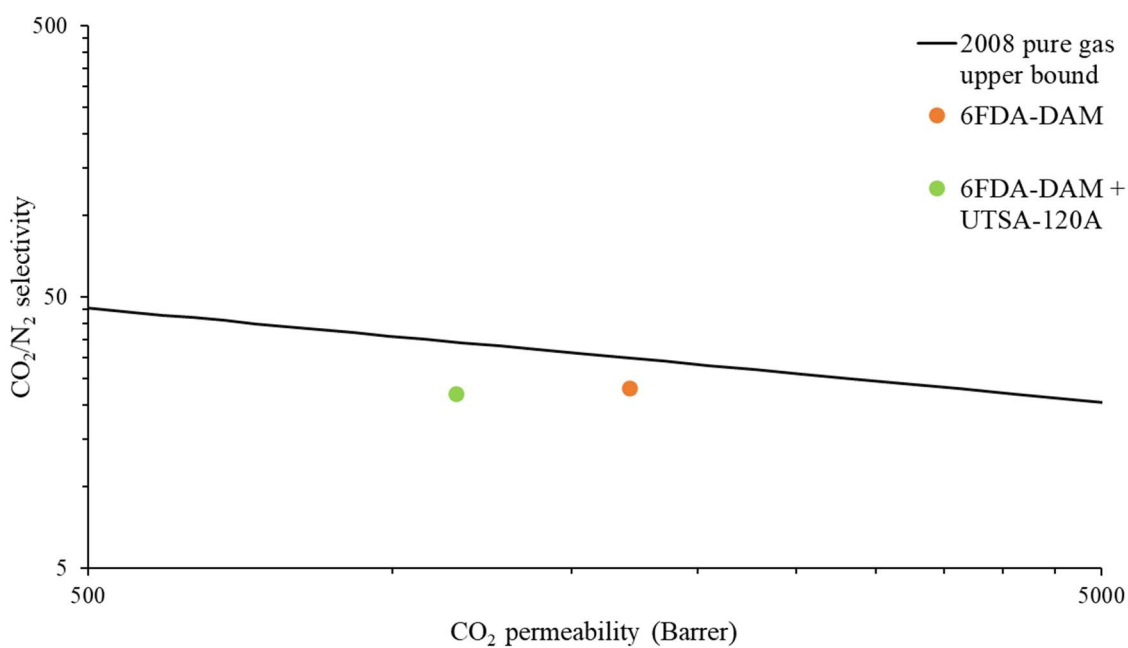


Figure A 21:  $CO_2/N_2$  Robeson plot for 6FDA-DAM and UTSA-120a 6FDA-DAM MMM[69]. The datapoints for a 15/85  $CO_2/N_2$  gas mixture are shown.

# Risk analysis



DIENTEN ALGEMEEN BEHEER  
DIRECTIE STAFDIENSTEN ALGEMEEN BEHEER  
DIENST VGM  
W. DE CROYLAAN 58 BUS 5530  
3001 LEUVEN, BELGIË



## RISICOANALYSE VOOR EEN EXPERIMENT MET CHEMISCHE PRODUCTEN VAN RISICOKLASSE E3 EN E4 EN NANOPARTIKELS

Vul dit formulier elektronisch in, in overleg met uw VGM-antennelid Chemische Veiligheid (CV)<sup>1</sup>.

### 1. Identificatie van de eenheid (gebruikers)

Aanvrager/contactpersoon:	Daan Van Havere	Eenheid:	cMACS
Tel:	0471133109	Magazijncode <sup>2</sup> :	IVG
E-mail adres:	daan.vanhavere@student.kul euven.be	Leidinggevende <sup>3</sup> :	Ivo Vankelecom
		Promotor:	Ivo Vankelecom

Personen die het experiment zullen uitvoeren (enkel van toepassing bij een *nieuwe* risicoanalyse):

Naam – voornaam:	u-/s-nummer/...:	Personeelsgroep:
Thür Raymond	u0111855	<input checked="" type="checkbox"/> KU <input type="checkbox"/> Student KU <input type="checkbox"/> UZ <input type="checkbox"/> VIB <input type="checkbox"/> Externen:
Van Havere Daan	R0757209	<input type="checkbox"/> KU <input checked="" type="checkbox"/> Student KU <input type="checkbox"/> UZ <input type="checkbox"/> VIB <input type="checkbox"/> Externen:
		<input type="checkbox"/> KU <input type="checkbox"/> Student KU <input type="checkbox"/> UZ <input type="checkbox"/> VIB <input type="checkbox"/> Externen:
		<input type="checkbox"/> KU <input type="checkbox"/> Student KU <input type="checkbox"/> UZ <input type="checkbox"/> VIB <input type="checkbox"/> Externen:
		<input type="checkbox"/> KU <input type="checkbox"/> Student KU <input type="checkbox"/> UZ <input type="checkbox"/> VIB <input type="checkbox"/> Externen:
		<input type="checkbox"/> KU <input type="checkbox"/> Student KU <input type="checkbox"/> UZ <input type="checkbox"/> VIB <input type="checkbox"/> Externen:
		<input type="checkbox"/> KU <input type="checkbox"/> Student KU <input type="checkbox"/> UZ <input type="checkbox"/> VIB <input type="checkbox"/> Externen:

### 2. Identificatie van het experiment

2.1. **Titel** (benaming) (max. 40 karakters): Synthese en testen van GS membranen

2.2. **Deze risicoanalyse betreft:**

- een nieuw experiment,
- een bestaand experiment zonder eerder ingediende melding,
- een wijziging/uitbreiding van een bestaand experiment met eerder opgestelde risicoanalyse,
  - Deze wijziging/uitbreiding betreft (gelieve aan te duiden en verder in het formulier te beschrijven):
    - lokalen waar het experiment plaatsvindt
    - agentia
    - verlenging
    - andere risico's (beschrijf kort):
  - Dossiernummer of referentienummer eerder ingediende melding (indien gekend):
- de stopzetting van het experiment met dossiernummer

2.3. **Activiteiten voor het VGM-dossier** (in overleg met VGM-antenne en Promotor/Leidinggevende<sup>3</sup>):

- Bestaande* activiteit: Geef het nummer van de activiteit, zoals opgenomen in KU Loket:
- Nieuwe* activiteit voor het VGM-dossier: Geef een naam voor de activiteit (max. 40 karakters):

<sup>1</sup> U vindt de leden van uw lokale VGM-antenne terug via uw [KU Loket > VGM & Ruimtes > Mijn VGM > Mijn VGM-antenne](#)

<sup>2</sup> Indien u de magazijncode niet kent, [contacteer dan uw VGM-antenne](#)

<sup>3</sup> Dit is de hiërarchisch verantwoordelijke volgens het officiële organigram.



2.4. Gewenste Startdatum: 01/09/2019 Geplande einddatum : 30/09/2020

### 3. Identificatie van agentia:

#### 3.1. Beschrijving van al de aangewende (of gevormde) chemische agentia:

Vervang indien mogelijk de zeer gevaarlijke agentia of processen door minder gevaarlijke alternatieven.

Productnaam	Cas-nummer	Fysische toestand (gas/vloeibaar/vast)	Aangewende hoeveelheid	Aangewende concentratie	Chemische risicoklasse product (E4/E3/E2/E1)
1. polysulfon	25154-01-2	vast	5g	10-20 wt%	E1
2. N-methylpyrrolidon	872-50-4	vloeibaar	10g	82 wt%	E4
3. polydimethylsiloxaan	9016-00-6	vast	5g	1-20wt%	E1
4. hexaandiamine	124-09-4	vast	1.25g	0.5 wt%	E3
5. m-fenyleendiamine	108-45-2	vast	5g	2wt%	E3
6. natriumdodecylsulfaat	151-21-3	vast	0.25g	0.1wt%	E1
7. triethylamine	121-44-8	vloeibaar	5g	2wt%	E3
8. n-hexaan	110-54-3	vloeibaar	25ml	+99%	E3
9. zirconiumtetrachloride	10026-11-6	vast	50 g	97%	E3
10. dimethylformamide	68-12-2	Vloeibaar	250 ml	+99%	E4
11. Tolueen	108-88-3	Vloeibaar	250 ml	+99%	E3
12. ethanol	64-17-5	Vloeibaar	250 ml	+99%	E3
13. ethylacetaat	141-78-6	Vloeibaar	250 ml	+99%	E3
14. koolstofdioxide	124-38-9	Gas	Continu	5	E1
15. methaan	74-82-8	Gas	Continu	5	E4
16. stikstof	7727-37-9	Gas	Continu	5	E1
17. Ethaan	74-84-0	Gas	Continu	5	E4
18. Etheen	74-85-1	Gas	Continu	5	E4
19. Propaan	74-98-6	Gas	Continu	5	E4
20. Propyleen	115-07-1	Gas	Continu	5	E4
21. Chloroform	67-66-3	Vloeibaar	250 ml	+99%	E4
22. polyimide	62929-02-6	Vast	Continu	Pure	E1
23. tetrahydrofuraan	109-99-9	Vloeibaar	100 ml	+99%	E4
24. zirconyl chloride hydraat	15461-27-5	Vast	100 g	+97%	E3
25. 1,3,5-benzeentricarbonsuur	554-95-0	Vast	5g	99%	E1
26. azijnzuur	64-19-7	Vloeibaar	50 ml	Pure	E3
27. zoutzuur	7647-01-0	Vloeibaar	100 ml	37wt% in water	E3
28. zirconyl nitraat hydraat	14985-18-3	Vast	5 g	99%	E3
29. mierenzuur	64-18-6	Vloeibaar	250 ml	99%	E3
30. trifluorazijnzuur	76-05-1	vloeibaar	100 mL	97%	E3
31. L-histidine	71-00-1	Vast	5g	Pure	NVT
32. L-lysine	56-87-1	Vast	5g	Pure	NVT
33. L-methionine	63-68-3	Vast	5g	Pure	NVT
34. L-arginine	74-79-3	Vast	5g	Pure	E1
35. L-cysteïne	52-90-4	Vast	5g	Pure	E1
36. glycine	56-40-6	Vast	5g	Pure	NVT
37. L-proline	147-85-3	Vast	5g	Pure	NVT
38. L-serine	56-45-1	Vast	5g	Pure	NVT
39. L-alanine	56-41-7	Vast	5g	Pure	E1



40. L-glutaminezuur	56-86-0	Vast	5g	Pure	NVT
41. natriumgluconaat	527-07-1	Vast	5g	Pure	NVT
42. Citrazinezuur	99-11-6	Vast	5g	97%	E1
43. 2-Chloropyridine-4-carboxylzuur	6313-54-8	Vast	5g	97%	Geen gegevens
44. 2-mercatopyridine-3-carboxylzuur	38521-46-9	Vast	5g	97%	Geen gegevens
45. 2,5-dichlorothiophene-3-carboxylzuur	36157-41-2	Vast	5g	97%	Geen gegevens
46. D-Penicillamine	52-67-5	Vast	1g	98%	E3
47. valeriaanzuur	109-52-4	Vloeibaar	5mL	99%	E3
48. hexaanzuur	142-62-1	Vloeibaar	5mL	99%	E3
49. heptaanzuur	111-14-8	Vloeibaar	5mL	99%	E3
50. para-tolylzuur	99-94-5	Vast	5g	98%	E1
51.9-anthraceencarboxylzuur	723-62-6	Vast	5g	99%	Geen gegevens
52. 1-pyreencarboxylzuur	19694-02-1	Vast	1g	97%	Geen gegevens
53. 4-(trifluoromethyl)-benzoezuur	455-24-3	Vast	5g	98%	E1
54. Dimethylsulfoxide	67-68-5	Vloeibaar	2 L	puur	NVT
55. Benzoezuur	65-85-0	Vast	100 g	99.5%	E3
56. Glycolzuur	79-14-1	Vloeibaar	100 mL	70 wt% in H2O	E3
57. Lithiumsulfaat monohydraat	10377-48-7	Vast	100 g	99%	E3
58. Zwavelzuur	7664-93-9	Vloeibaar	1 L	99%	E3
59. Methanol	67-56-1	Vloeibaar	5 L	Puur	E4
60. polyimide (Matrimid 5218)	62929-02-6	vast	continu	puur	E1
61. Tereftaalzuur	100-21-0	Vast	500 g	99%	NVT
62. Copper-hexafluorosilicate	12062-24-7	Vast	1 g	99%	E1
63. 3,6-Di(4-pyridyl)-1,2,4,5-tetrazine	57654-36-1	Vast	5 g	99%	E1

### 3.2. Gevaren verbonden aan het gebruik van chemische agentia:

Duid voor producten van risicoklasse **E3** en **E4** de gevaren aan.

Zorg dat bij gebruik van chemische producten de H- of R-zinnen steeds gekend zijn. U kan deze opzoeken in de Databank gevaarlijke stoffen (via [KU Loket > VGM & Ruimtes > VGM > Databank gevaarlijke stoffen](#)) of op de veiligheidsinformatiebladen van de fabrikant.

	Naam chemisch product:					
	N-methyleendaamine	hexaandiamine	m-fenyleendaamine	triethylamine	hexaan	1,3,5-benzotriazine
<b>Explosie- en brandgevaar:</b>						
Zeer licht of licht ontvlambaar (H220, H222,224, H228, H225) / (R11, R12)	<input type="checkbox"/>	<input type="checkbox"/>	<input type="checkbox"/>	<input checked="" type="checkbox"/>	<input checked="" type="checkbox"/>	<input type="checkbox"/>
Ontvlambaar gas, aerosol, vaste stof (H221, H223, H226)	<input type="checkbox"/>	<input type="checkbox"/>	<input type="checkbox"/>	<input type="checkbox"/>	<input type="checkbox"/>	<input type="checkbox"/>
Ontvlambaar door zelfverhitting (H251,H252)	<input type="checkbox"/>	<input type="checkbox"/>	<input type="checkbox"/>	<input type="checkbox"/>	<input type="checkbox"/>	<input type="checkbox"/>
Brand, ontploffing met scherfwerking (H204, H202, H203), massa-explosie bij brand (H205)	<input type="checkbox"/>	<input type="checkbox"/>	<input type="checkbox"/>	<input type="checkbox"/>	<input type="checkbox"/>	<input type="checkbox"/>
Explosief (EUH001, EUH006, H200, H201) / (R1,R2,R3,R5)	<input type="checkbox"/>	<input type="checkbox"/>	<input type="checkbox"/>	<input type="checkbox"/>	<input type="checkbox"/>	<input type="checkbox"/>



+ oxiderende stoffen (H271, H272)/(R9) + T†(H240, H241), afgesloten en T† (EUH044)/(R44)						
Ontvlambaar damp/lucht mengsel (EUH018)	<input type="checkbox"/>					
Ontploffbare peroxiden (EUH019)	<input type="checkbox"/>					
Incompatibel met water (EUH014, H260)/(R14,R15)	<input type="checkbox"/>					
Vat spontaan vlam in contact met lucht (H250)	<input type="checkbox"/>					
Explosief + metalen (R4) + O2 (R6)	<input type="checkbox"/>					
Incompatibel met oxiderende stoffen (R16)	<input type="checkbox"/>					
Instabiel product (R17, R18, R19)	<input type="checkbox"/>					
<b>Acuut gevaar voor gezondheid:</b>						
Zeer giftig (H300, H330, H310) / (R26, R27, R28) + zuur (EUH032)/(R32)	<input type="checkbox"/>	<input type="checkbox"/>	<input checked="" type="checkbox"/>	<input type="checkbox"/>	<input type="checkbox"/>	<input type="checkbox"/>
Giftig (H311, H331, EUH070) / (R23, R24) + water (EUH029) / (R29) + zuur (EUH031) / (R31)	<input type="checkbox"/>	<input type="checkbox"/>	<input checked="" type="checkbox"/>	<input type="checkbox"/>	<input type="checkbox"/>	<input checked="" type="checkbox"/>
Ernstige brandwonden (H314) / (R35)	<input type="checkbox"/>	<input checked="" type="checkbox"/>	<input type="checkbox"/>	<input checked="" type="checkbox"/>	<input type="checkbox"/>	<input checked="" type="checkbox"/>
<b>Gevaar voor gezondheid op langere termijn:</b>						
Kankerverwekkend of kanker niet uitgesloten (H350, H350i, H351) / (R40, R45, R49)	<input type="checkbox"/>					
Teratogeen (H361d, H360D) / (R61, R63) en schade aan vruchtbaarheid (H361f, H360F) / (R60, R62), beide (H361fd, H360FD, H360Df, H360Fd)	<input checked="" type="checkbox"/>	<input type="checkbox"/>	<input type="checkbox"/>	<input type="checkbox"/>	<input checked="" type="checkbox"/>	<input type="checkbox"/>
Mutageen (H341, H340) / (R46)	<input type="checkbox"/>					
Schade aan bepaalde organen (H371, H372, H370) bij herhaalde of langdurige blootstelling (H373)	<input type="checkbox"/>	<input type="checkbox"/>	<input type="checkbox"/>	<input type="checkbox"/>	<input checked="" type="checkbox"/>	<input type="checkbox"/>
Ernstige onherstelbare effecten (mogelijks) (R39, R68), Gezondheidsschade bij langdurige blootstelling (R48)	<input type="checkbox"/>					
<b>Alle andere relevante intrinsieke gevaren oplijsten per product (incl. E1- &amp; E2-producten):</b>						
<p>ik krijg niet alle producten in de tabel:</p> <p>dimethylformamide: teratogeen (H360D), giftig (H331)</p> <p>tolueen: licht ontvlambaar (H225), teratogeen (H361d), schade aan bep. organen bij herh. of langd. blootstelling (H373)</p> <p>ethanol: licht ontvlambaar (H225)</p> <p>acetonitril: licht ontvlambaar (H225), giftig (H311)</p> <p>ethylacetaat: licht ontvlambaar (H225)</p> <p>Methaan: zeer licht ontvlambaar gas (H220), kan ontploffen bij verwarming (H280)</p> <p>Ethaan: zeer licht ontvlambaar gas (H220), kan ontploffen bij verwarming (H280)</p> <p>Propaan: zeer licht ontvlambaar gas (H220), kan ontploffen bij verwarming (H280)</p> <p>Etheen: zeer licht ontvlambaar gas (H220), kan slaperigheid of duizeligheid veroorzaken (H336)</p> <p>Propeen: zeer licht ontvlambaar gas (H220), kan ontploffen bij verwarming (H280)</p> <p>zirconiumtetrachloride: H302 (schadelijk bij inslikken), H314 (ernstige brandwonden en oogletsel), H317 (allergische huidreactie), H334 (bij iandeming kans op allergie- of astmasymptomen of ademhalingsmoeilijkheden), H335 (irritatie van de luchtwegen), H41 (giftig voor in water levende organismen met langdurige gevolgen)</p> <p>chloroform: H302 (Schadelijk bij inslikken), H315 (huidirritatie), H319 (ernstige oogirritatie), H331 (giftig bij inademing), H351 (mogelijk kankerverwekkend), H361d (wordt ervan verdacht ongeboren kind te schaden), H372 (schade aan organen (lever, nieren) bij langdurige blootstelling)</p> <p>tetrahydrofuraan: H225 (Licht ontvlambaar), H319 (Ernstige oogirritatie), H335 (irritatie van de luchtwegen), H351 (mogelijk kankerverwekkend)</p> <p>zirconylchloride hydraat: H314 (ernstige brandwonden en oogletsel)</p> <p>azijnzuur: H225 (Licht ontvlambaar), H319 (Ernstige oogirritatie), H335 (irritatie van de luchtwegen), H351 (mogelijk kankerverwekkend)</p> <p>zoutzuur: H314 (ernstige brandwonden en oogletsel), H335 (Irritatie van de luchtwegen)</p> <p>zirconyl nitraat hydraat: H272 oxiderend, H314 ernstige brandwonden en oogletsel, H317 allergische huidreactie veroorzaken, H334 kan ademhalingsmoeilijkheden veroorzaken.</p>						



mierenzuur: H226: ontvlambare vloeistof, H314: ernstige brandwonden en oogletsel  
 trifluorazijnzuur: H314 Veroorzaakt ernstige brandwonden en oogletsel, H332 Schadelijk bij inademing, H412 Schadelijk voor in het water levende organismen, met langdurige gevolgen.  
 D-Penicillamine: H341 Verdacht van het veroorzaken van genetische schade.  
 Valeriaanzuur: H314 Veroorzaakt ernstige brandwonden en oogletsel, H412 Schadelijk voor in het water levende organismen, met langdurige gevolgen  
 Hexaanzuur: H314 Veroorzaakt ernstige brandwonden en oogletsel.  
 Heptaanzuur: H314 Veroorzaakt ernstige brandwonden en oogletsel.  
 Benzoëzuur: H315 Veroorzaakt huidirritatie, H318 Veroorzaakt ernstig oogletsel, H372 Veroorzaakt schade aan organen bij langdurige of herhaalde blootstelling bij inademen  
 Glycolzuur: H314 Veroorzaakt ernstige brandwonden en oogletsel, H332 Schadelijk bij inademing  
 Lithiumsulfaat monohydraat: H302 Schadelijk bij inslikken, H315 Veroorzaakt huidirritatie, H319 Veroorzaakt ernstige oogirritatie, H335 Kan irritatie van de luchtwegen veroorzaken, H341 Verdacht van het veroorzaken van genetische schade.  
 Zwavelzuur: H317 Veroorzaakt ernstige brandwonden en oogletsel.  
 Methanol: H225 Licht ontvlambare vloeistof en damp, H301 + H311 + H331 Giftig bij inslikken, bij contact met de huid en bij inademing, H370 Veroorzaakt schade aan organen (centraal zenuwstelsel, ogen (blindheid)).  
 3,6-Di(4-pyridyl)-1,2,4,5-tetrazine: H315 Veroorzaakt huidirritatie. H319 Veroorzaakt ernstige oogirritatie.  
 Copper-hexafluorosilicate: H302 Schadelijk bij inslikken.

3.3. Bijkomende informatie voor werken met nanopartikels:

	Naam nano-product:					
	MCF-808	UiO-67	UiO-66	MCM-41	ZrO <sub>2</sub>	UTSA-120A
<b>Aggregatietoestand</b>						
Suspensie	<input checked="" type="checkbox"/>					
Poeder	<input checked="" type="checkbox"/>					
Matrix	<input checked="" type="checkbox"/>					
Andere:	<input type="checkbox"/>					
<b>Gevaarlijke eigenschappen moedermateriaal</b>						
Kankerverwekkend	<input type="checkbox"/>					
Mutageen	<input type="checkbox"/>					
Giftig	<input type="checkbox"/>					
Andere: Mogelijk schadelijk bij inademen	<input checked="" type="checkbox"/>					
<b>Vorm</b>						
Kubus	<input type="checkbox"/>					
Vezel	<input type="checkbox"/>					
Sferisch	<input type="checkbox"/>	<input type="checkbox"/>	<input type="checkbox"/>	<input checked="" type="checkbox"/>	<input checked="" type="checkbox"/>	<input type="checkbox"/>
Andere: Octaeder	<input checked="" type="checkbox"/>	<input checked="" type="checkbox"/>	<input checked="" type="checkbox"/>	<input type="checkbox"/>	<input type="checkbox"/>	<input type="checkbox"/>
<b>Partikelgrootte (aspect/ratio)</b>						
1-10nm	<input type="checkbox"/>					
11-40nm	<input type="checkbox"/>	<input type="checkbox"/>	<input type="checkbox"/>	<input checked="" type="checkbox"/>	<input checked="" type="checkbox"/>	<input checked="" type="checkbox"/>
41-100nm	<input checked="" type="checkbox"/>					



## 4. Beschrijving van het experiment en de risicoanalyse

### 4.1. Beschrijving van de handelingen, de aangewende technieken en de locatie:

Nummer deel-experiment	Beschrijving handelingen en technieken	Gebruikte uitrusting	Nummers <sup>4</sup> gebruikte producten
1	afwegen en mengen van de polymeeroplossing & MOF suspensies  Spincoaten TFC membranen Centrifugatie Annealen van membranen in muffle oven	Geijkte weegschaal (492-31_04-225#BAL1_00001), centrifuge (492-31_04-225#CENTRIF_00001), 492-31_04-225#MO1, 492-31_04-221#SPINCOATER	1-13, 16, 21-23
2	MOF synthese: afwegen, mengen en reactie op temperatuur	Geijkte weegschaal (492-31_04-225#BAL1_00001), oven (492-31_04-225#O2_00001	9, 14, 16, 24-63
3	voedingsmengsel en druk aanbrengen, filtratie (drukken tot 34 bar, temperatuur tot 60 °C, gebruikte gassen: CH <sub>4</sub> , N <sub>2</sub> , CO <sub>2</sub> , ethaan, propaan, etheen, propeen)	HTGS (492-31_04-310_U3#HTgas) en HTGS 2.0 (492-31_04-310_U3#HTgas2)	Gassen 14-20, membranen na deexperiment 1 en 2
4			
5			

<sup>4</sup> Nummer van product zoals aangeduid in sectie 3.1.



Nummer deexperiment	Gebouw	Lokaal	Inperkings-niveau	Specificaties lokaal <sup>5</sup>
1.	492.31	04.225	2	<input checked="" type="checkbox"/> eigen eenheid <input type="checkbox"/> ruimte toegewezen aan andere eenheid:
2.	492.31	04.310	3	<input checked="" type="checkbox"/> eigen eenheid <input type="checkbox"/> ruimte toegewezen aan andere eenheid:
3.	492.31	04.225	2	<input checked="" type="checkbox"/> eigen eenheid <input type="checkbox"/> ruimte toegewezen aan andere eenheid:
4.				<input checked="" type="checkbox"/> eigen eenheid <input type="checkbox"/> ruimte toegewezen aan andere eenheid:
5.				<input type="checkbox"/> eigen eenheid <input type="checkbox"/> ruimte toegewezen aan andere eenheid:
6.				<input type="checkbox"/> eigen eenheid <input type="checkbox"/> ruimte toegewezen aan andere eenheid:

- 4.2. **Frequentie uitvoering experiment:**  Dagelijks  
 Wekelijks  
 Maandelijks  
 Minder dan maandelijks

4.3. **Hier kan u meer informatie toevoegen die essentieel is voor het uitvoeren van de risicoanalyse (bv. beschrijving, foto's, reactieschema) of verwijzen naar een bijlage:**

4.4. **Risico's verbonden aan het experiment:**

**Risico's verbonden aan het gebruik van chemische agentia of nanopartikels**

- Kans op inademing overgieten, verwarming, ...  
 Kans op spatten  
 Kans op verdamping en verspreiding door verwarming  
 Kans op snijden door gebruik van naalden / scherpe materialen  
 Kans op drukopbouw in recipiënt door reacties  
 Transport van chemisch materiaal of nanopartikels  
 binnen gebouw of gebouwencomplex: Beschrijf de maatregelen Gesloten verpakking, transportemmer  
 tussen KU Leuven gebouwen (niet op de openbare weg): Beschrijf de maatregelen Gesloten verpakking, enkel gedroogde SEM preparaten:  
 extern transport (over de openbare weg)  
 Andere:

**Andere risico's verbonden aan het experiment**

- Verbranden, bevroren ( hoge of lage temperaturen,  cryogene stoffen, ...)  
 Implosie, explosie ( hoge drukken,  lage drukken,  onderdruk, ...)  
 Brand ( ovens,  verwarmingsspiralen,  bunsenbrander,  oliebaden ...)  
 Niet-ioniserende straling ( NMR,  lasers,  UV-lampen, ...)  
 Elektrocutie ( naakte contacten,  vochtige omgeving,  hoge vermogens, ...)  
 Afgezonderde tewerkstelling afgelegen lokaal of plaats.  
 Beschrijf de voorwaarden (bv. met 2 aanwezig, dodemans alarm, ...):  
 Valgevaar ( opstellingen op hoogte,  in de hoogte,  moeilijk bereikbaar, ...)  
 Biologisch risico ( pathogene  $\mu$ -organismen (specificeer): ,  GGO (specificeer gastheer-vector-insert): ,  
 cellen (specificeer type en oorsprong): ,  bloed (specificeer oorsprong): ,  proefdieren (specificeer soort, wild-type/knock-out, ...): , ...)  
 Gassen: CO<sub>2</sub>, CH<sub>4</sub>, N<sub>2</sub>, ethaan/etheen, propaan/propeen  
 Ioniserende straling (X-stralen, radio-isotopen, ...) Specificeer:

<sup>5</sup> Indien manipulaties worden uitgevoerd in een ruimte toegewezen aan een andere eenheid, dan moet deze risicoanalyse ook naar de betrokken leidinggevende gestuurd worden (in cc.).



- De kans bestaat dat bij een ernstig incident **NIET** zelfstandig alarm kan gegeven worden (bv. gebruik van zeer toxische dampen of gassen, explosierisico, aanwezigheid verstikkend gas, ...)
- Andere:

## 5. Toe te passen voorzorgsmaatregelen

Indien niet alle voorzorgsmaatregelen toegepast kunnen worden, adviseert de Dienst VGM om de activiteiten niet te starten.

### 5.1. Collectieve beschermingsmiddelen:

Nummer deelexperiment <sup>6</sup> :	1	2	3	4	5
Gesloten systeem (specifieer type):	<input type="checkbox"/>	<input type="checkbox"/>	<input type="checkbox"/>	<input type="checkbox"/>	<input type="checkbox"/>
Zuurkast (trekkast)	<input checked="" type="checkbox"/>	<input checked="" type="checkbox"/>	<input type="checkbox"/>	<input type="checkbox"/>	<input type="checkbox"/>
Geventileerde omkasting	<input type="checkbox"/>	<input type="checkbox"/>	<input checked="" type="checkbox"/>	<input type="checkbox"/>	<input type="checkbox"/>
Reactor kabinet	<input type="checkbox"/>	<input type="checkbox"/>	<input type="checkbox"/>	<input type="checkbox"/>	<input type="checkbox"/>
Bioveiligheidskabinet met extractie naar buiten	<input type="checkbox"/>	<input type="checkbox"/>	<input type="checkbox"/>	<input type="checkbox"/>	<input type="checkbox"/>
Plaatselijke afzuiging	<input checked="" type="checkbox"/>	<input checked="" type="checkbox"/>	<input type="checkbox"/>	<input type="checkbox"/>	<input type="checkbox"/>
Ruimtelijke afzuiging	<input checked="" type="checkbox"/>	<input checked="" type="checkbox"/>	<input checked="" type="checkbox"/>	<input type="checkbox"/>	<input type="checkbox"/>
Veiligheidsscherm	<input type="checkbox"/>	<input type="checkbox"/>	<input type="checkbox"/>	<input type="checkbox"/>	<input type="checkbox"/>
Opvangbakken onder opstelling	<input type="checkbox"/>	<input type="checkbox"/>	<input type="checkbox"/>	<input type="checkbox"/>	<input type="checkbox"/>
Gasdetectie (type) brandbare of giftige gassen:					
- Draagbare	<input type="checkbox"/>	<input type="checkbox"/>	<input type="checkbox"/>	<input type="checkbox"/>	<input type="checkbox"/>
- Ruimtelijk	<input type="checkbox"/>	<input type="checkbox"/>	<input checked="" type="checkbox"/>	<input type="checkbox"/>	<input type="checkbox"/>
- Branddetectie (ruimtelijk)	<input type="checkbox"/>	<input type="checkbox"/>	<input type="checkbox"/>	<input type="checkbox"/>	<input type="checkbox"/>
- Andere:	<input type="checkbox"/>	<input type="checkbox"/>	<input type="checkbox"/>	<input type="checkbox"/>	<input type="checkbox"/>
Andere:	<input type="checkbox"/>	<input type="checkbox"/>	<input type="checkbox"/>	<input type="checkbox"/>	<input type="checkbox"/>

### 5.2. Persoonlijke beschermingsmiddelen<sup>7</sup>:

Nummer deelexperiment <sup>6</sup> :	1	2	3	4	5
Algemene bescherming:					
- Laboschort/werkkledij	<input checked="" type="checkbox"/>	<input checked="" type="checkbox"/>	<input checked="" type="checkbox"/>	<input type="checkbox"/>	<input type="checkbox"/>
- Wegwerp overschoenen	<input type="checkbox"/>	<input type="checkbox"/>	<input type="checkbox"/>	<input type="checkbox"/>	<input type="checkbox"/>
- Wegwerp hygiëne haarnetje	<input type="checkbox"/>	<input type="checkbox"/>	<input type="checkbox"/>	<input type="checkbox"/>	<input type="checkbox"/>
- Wegwerp overall	<input type="checkbox"/>	<input type="checkbox"/>	<input type="checkbox"/>	<input type="checkbox"/>	<input type="checkbox"/>
- Wegwerp laboschort	<input type="checkbox"/>	<input type="checkbox"/>	<input type="checkbox"/>	<input type="checkbox"/>	<input type="checkbox"/>
- Andere:	<input type="checkbox"/>	<input type="checkbox"/>	<input type="checkbox"/>	<input type="checkbox"/>	<input type="checkbox"/>
Gelaatsbescherming:					
- Veiligheidsbril	<input checked="" type="checkbox"/>	<input checked="" type="checkbox"/>	<input checked="" type="checkbox"/>	<input type="checkbox"/>	<input type="checkbox"/>
- Ruimtezichtbril	<input type="checkbox"/>	<input type="checkbox"/>	<input type="checkbox"/>	<input type="checkbox"/>	<input type="checkbox"/>
- Gelaatsscherm	<input type="checkbox"/>	<input type="checkbox"/>	<input type="checkbox"/>	<input type="checkbox"/>	<input type="checkbox"/>
- Andere:	<input type="checkbox"/>	<input type="checkbox"/>	<input type="checkbox"/>	<input type="checkbox"/>	<input type="checkbox"/>
Ademhalingsbescherming:					
- Wegwerp stofmasker P1	<input type="checkbox"/>	<input type="checkbox"/>	<input type="checkbox"/>	<input type="checkbox"/>	<input type="checkbox"/>
- Wegwerp stofmasker P3	<input type="checkbox"/>	<input type="checkbox"/>	<input type="checkbox"/>	<input type="checkbox"/>	<input type="checkbox"/>
- Wegwerp hygiënemasker/chirurgisch masker	<input type="checkbox"/>	<input type="checkbox"/>	<input type="checkbox"/>	<input type="checkbox"/>	<input type="checkbox"/>
- Andere: Laminare flowkast voor NPs kleiner dan 100 nm	<input checked="" type="checkbox"/>	<input checked="" type="checkbox"/>	<input type="checkbox"/>	<input type="checkbox"/>	<input type="checkbox"/>
Handschoenen:					
- Wegwerp nitrile EN 374	<input checked="" type="checkbox"/>	<input checked="" type="checkbox"/>	<input checked="" type="checkbox"/>	<input type="checkbox"/>	<input type="checkbox"/>
- Wegwerp vinyl EN 374	<input type="checkbox"/>	<input type="checkbox"/>	<input type="checkbox"/>	<input type="checkbox"/>	<input type="checkbox"/>
- Nitrile EN 374	<input type="checkbox"/>	<input type="checkbox"/>	<input type="checkbox"/>	<input type="checkbox"/>	<input type="checkbox"/>

<sup>6</sup> Nummer van het deelexperiment zoals aangeduid in sectie 4.1.

<sup>7</sup> Richtlijnen over het verkrijgen van Persoonlijke beschermingsmiddelen (PBM's): via uw VGM-antenne of [de website van de Dienst VGM](#).



- Cryogene handschoenen	<input type="checkbox"/>				
- Andere:	<input type="checkbox"/>				
Gehoorscherming:					
- Wegwerp oordopjes	<input type="checkbox"/>				
- Gehoorbeugel	<input type="checkbox"/>				
- Oorkappen	<input type="checkbox"/>				
- Andere:	<input type="checkbox"/>				

### 5.3. Specifieke preventiemaatregelen:

- Controle werking zuurkast
- Controle glaswerk op barsten
- Bevestigen spanningen aan koelsslangen
- Automatisch uitschakelen verwarmingssysteem bij defecte koeling
- Overdrukbeveiligingssysteem
- Brandblusser voor metaalbranden (D-blusser) aanwezig
- Zuurstofkit aanwezig (verplicht bij het werken met cyaniden)
- Aanwezigheid gasmasker met specifieke filters (interventie)
- Aanwezigheid calciumgluconaatzalf (werken met waterstoffluoride)
- Interventiekits aanwezig
- Specifiek neutralisatieproduct aanwezig nl. vermiculite
- Aanwezigheid van een tweede persoon in de buurt vereist
- Automatisch alarmsysteem (bv. dodemansalarm)
- Andere:

### 5.4. Werkpraktijken

- [Code Goede Laboratoriumpraktijk](#) toepassen
- Interne opleiding en begeleiding
- Selectieve inzameling van afval – chemisch afval
- Andere:

## 6. Afvalverwerking - Chemisch afval

### 6.1. Duid aan welke afvalfracties u verwacht en duid per afvalfractie de categorie van het chemisch afval aan:

Afvalfractie	Afvalcategorie	Recipiënt aanwezig
<b>Zuivere stoffen:</b>		
basisch anorganisch afval	<input checked="" type="checkbox"/> 1 - <input type="checkbox"/> 2 - <input type="checkbox"/> 3 - <input type="checkbox"/> 4 - <input type="checkbox"/> 5 - <input checked="" type="checkbox"/> 6 - <input type="checkbox"/> Andere:	<input checked="" type="checkbox"/>
zuur anorganisch afval: 27, 58	<input type="checkbox"/> 1 - <input checked="" type="checkbox"/> 2 - <input type="checkbox"/> 3 - <input type="checkbox"/> 4 - <input type="checkbox"/> 5 - <input checked="" type="checkbox"/> 6 - <input type="checkbox"/> Andere:	<input checked="" type="checkbox"/>
niet-gehalogeneerd organisch afval: 2,3,6,8,11,12,13,23,25,26,28,29,31-42,47-52,55,56,59,61,63	<input type="checkbox"/> 1 - <input type="checkbox"/> 2 - <input checked="" type="checkbox"/> 3 - <input type="checkbox"/> 4 - <input type="checkbox"/> 5 - <input type="checkbox"/> 6 - <input type="checkbox"/> Andere:	<input checked="" type="checkbox"/>
gehalogeneerd organisch afval: 21, 30,43,45,53	<input type="checkbox"/> 1 - <input type="checkbox"/> 2 - <input type="checkbox"/> 3 - <input checked="" type="checkbox"/> 4 - <input type="checkbox"/> 5 - <input type="checkbox"/> 6 - <input type="checkbox"/> Andere:	<input checked="" type="checkbox"/>
speciaal afval (amines): 4,5,7,46 speciaal afval (zirconiumtetrachloride): 9 speciaal afval (zirconylchloride hydraat): 32	<input type="checkbox"/> 1 - <input type="checkbox"/> 2 - <input type="checkbox"/> 3 - <input checked="" type="checkbox"/> 4 - <input checked="" type="checkbox"/> 5 - <input type="checkbox"/> 6 - <input type="checkbox"/> Andere:	<input checked="" type="checkbox"/>



speciaal afval (zirconyl nitraat hydraat):28 speciaal afval (DMF): 14 Speciaal afval (DMSO): 54 Speciaal afval (Lithiumsulfaat monohydraat): 57		
vast afval: 1,22, 60, 62	<input type="checkbox"/> 1 - <input type="checkbox"/> 2 - <input type="checkbox"/> 3 - <input type="checkbox"/> 4 - <input type="checkbox"/> 5 - <input type="checkbox"/> 6 - <input checked="" type="checkbox"/> Andere: chemisch vast afval	<input checked="" type="checkbox"/>
<b>Mengsels:</b>		
Hoofdcomponent: water met 4-8,10,9,24,28,55-58,61	<input type="checkbox"/> 1 - <input type="checkbox"/> 2 - <input type="checkbox"/> 3 - <input type="checkbox"/> 4 - <input checked="" type="checkbox"/> 5 - <input type="checkbox"/> 6 - <input type="checkbox"/> Andere:	<input checked="" type="checkbox"/>
Hoofdcomponent: water met 4,5,7,46	<input type="checkbox"/> 1 - <input type="checkbox"/> 2 - <input type="checkbox"/> 3 - <input type="checkbox"/> 4 - <input checked="" type="checkbox"/> 5 - <input type="checkbox"/> 6 - <input type="checkbox"/> Andere:	<input checked="" type="checkbox"/>
Hoofdcomponent: met	<input type="checkbox"/> 1 - <input type="checkbox"/> 2 - <input type="checkbox"/> 3 - <input type="checkbox"/> 4 - <input type="checkbox"/> 5 - <input type="checkbox"/> 6 - <input type="checkbox"/> Andere:	<input type="checkbox"/>
Hoofdcomponent: 10met 9,24-29	<input type="checkbox"/> 1 - <input type="checkbox"/> 2 - <input type="checkbox"/> 3 - <input type="checkbox"/> 4 - <input checked="" type="checkbox"/> 5 - <input type="checkbox"/> 6 - <input type="checkbox"/> Andere:	<input checked="" type="checkbox"/>
Hoofdcomponent: water met 30,43,45,53	<input type="checkbox"/> 1 - <input type="checkbox"/> 2 - <input type="checkbox"/> 3 - <input checked="" type="checkbox"/> 4 - <input type="checkbox"/> 5 - <input type="checkbox"/> 6 - <input type="checkbox"/> Andere:	<input type="checkbox"/>
Hoofdcomponent: 59 met 62,63	<input type="checkbox"/> 1 - <input type="checkbox"/> 2 - <input type="checkbox"/> 3 - <input type="checkbox"/> 4 - <input checked="" type="checkbox"/> 5 - <input type="checkbox"/> 6 - <input type="checkbox"/> Andere:	<input type="checkbox"/>
<b>Andere:</b>		
	<input type="checkbox"/> 1 - <input type="checkbox"/> 2 - <input type="checkbox"/> 3 - <input type="checkbox"/> 4 - <input type="checkbox"/> 5 - <input type="checkbox"/> 6 - <input type="checkbox"/> Andere:	<input type="checkbox"/>
	<input type="checkbox"/> 1 - <input type="checkbox"/> 2 - <input type="checkbox"/> 3 - <input type="checkbox"/> 4 - <input type="checkbox"/> 5 - <input type="checkbox"/> 6 - <input type="checkbox"/> Andere:	<input type="checkbox"/>

## 7. Maatregelen in bijzondere situaties

### 7.1. Bij falen en terug activeren van nutsvoorzieningen (incl. afwijken van specificaties):

Nutsvoorziening:	Gevolg(en) bij falen/uitvallen:	Is dit een VGM-probleem, ja/nee?	Indien ja, omschrijf de maatregelen:
Elektriciteit	MFCs worden uitgeschakeld -> geen gas flow, verwarming wordt uitgeschakeld	Nee	
Ventilatie	MFCs worden uitgeschakeld -> geen gas flow, verwarming wordt uitgeschakeld	Nee	
Gasvoorziening	Nee	Nee	
(Koel)water	Nee	Nee	
Perslucht	Geen GC meting mogelijk	Nee	
Inerte atmosfeer	Nee	Nee	
Vacuüm	Nee	Nee	
Andere:			

Nutsvoorziening:	Gevolg(en) bij het terug activeren:	Is dit een VGM-probleem, ja/nee?	Indien ja, omschrijf de maatregelen:
Elektriciteit	Manuele activatie vereist van MFCs en verwarming	Nee	
Andere:			

### 7.2. Kan het experiment doorgaan indien de opstelling onbewaakt wordt achtergelaten (= doorlopende proeven)?



- Niet van toepassing: de opstelling wordt nooit onbewaakt achtergelaten.  
 Ja.  
In dit geval wordt de procedure "[Doorlopende activiteiten - onbewaakt](#)" toegepast.  
 Neen, bijkomende maatregelen zijn nodig.  
Omschrijf de bijkomende maatregelen:  
Bovendien wordt de procedure "[Doorlopende activiteiten - onbewaakt](#)" toegepast.

7.3. **Is werken buiten de normale werkuren toegelaten?**

- Neen  
 Ja. Beschrijf welke bijkomende maatregelen hiervoor zijn genomen (vb: ventilatie, tweede persoon aanwezig, dodemansalarm, ...): ventilatie, tweede persoon aanwezig

7.4. **Beschrijf uw procedure voor snelle *shutdown* of de maatregelen die u neemt bij evacuatie van het gebouw:**

deelexperiment 1: reagentia enkel onder trekkast  
deelexperiment 2: noodstop + shutdown als ventilatie uitvalt, druk aflaten, brandbare gassen afsluiten  
deelexperiment 3: opstelling afzetten  
deelexperiment 4: oven uitschakelen

7.5. **Beschrijf de richtlijnen bij een morsincident:**

groot morsincident: vermiculiet, eventueel eerste hulp indien nodig  
klein morsincident: spillage opruimen

## 8. Besluit / Opmerkingen / Vragen

---

Noteer hier eventueel bijkomende opmerkingen of vragen:

**Bezorg het ingevulde risicoanalyseformulier aan uw VGM-antennecoördinator en leidinggevende.**

Indien acuut gevaarlijke producten van klasse E4 voorkomen, dan legt de VGM-antennecoördinator deze risicoanalyse voor aan de Dienst VGM.

## 9. Advies Dienst VGM

---

Deze ruimte is voorbehouden voor het advies van de Dienst VGM:

## Popularized summary

Carbon dioxide (CO<sub>2</sub>) is an important greenhouse gas and strong contributor to global warming. Therefore, CO<sub>2</sub> capture from power plants and industrial exhaust gas streams has recently gained attention. Next to environmental reasons, CO<sub>2</sub> removal from energy streams, such as natural gas and biogas, is imperative in industry to prevent damage to transport infrastructure and maintain the quality of the energy stream. Membrane gas separation is a promising technology for these CO<sub>2</sub> separations. This technique makes use of a membrane, a sort of filter, that separates the various components of the gas stream. One component will pass favorably through the membrane resulting in a relatively larger concentration of this component at the side of the membrane opposite to the side in contact with the original gas mixture. Membrane gas separations are advantageous compared to other separation processes due to their relatively low energy consumption and lower cost. However, traditional membranes face a trade-off between desirable membrane properties, making them less efficient in separating CO<sub>2</sub>.

A possible strategy to overcome this setback is the incorporation of various ‘filler’ materials in the membranes with separation enhancing properties, resulting in so-called mixed matrix membranes (MMM). The development of new fillers as well as understanding which filler properties result in enhanced MMM gas separation performance are crucial for the evolution of this field of research. Through a series of modifications of the filler MOF-808, this thesis aims at addressing both simultaneously. The filler itself (MOF-808) is a particle with a porous structure, meaning there is a lot of ‘unoccupied’ volume within its structure. These pores have specific sites which can interact with certain types of molecules. By varying the molecule interacting with these sites, the affinity of the filler for CO<sub>2</sub> can be changed. The modified fillers showed differences in their capacity to store CO<sub>2</sub> and in how strongly they interact with CO<sub>2</sub>. Furthermore, MMM based on some of these modified fillers were better at separating CO<sub>2</sub> from N<sub>2</sub>, the other component in flue gas, than MMM based on the unmodified MOF-808. Remarkably, there was no linear relationship between the CO<sub>2</sub> storage capacity of the filler and the gas separation performance of the MMM based on this filler. The only linear relationship observed was for the strength of interaction of CO<sub>2</sub> with the filler and the CO<sub>2</sub> permeability (a measure of the amount of CO<sub>2</sub> passing through the membrane surface per unit of time).

Finally, the effect of a new filler, UTSA-120a, for MMM was investigated. MMM based on this filler were better at distinguishing between CO<sub>2</sub> and methane (CH<sub>4</sub>) but had a lower CO<sub>2</sub> permeability. Both effects were most likely caused by the interaction of the filler with the polymer, rather than properties of the filler itself.